Interaction of bubbles with vortical structures

Narsing Kumar Jha

Department of Mechanical Engineering

Indian Institute of Science

This dissertation is submitted for the degree of

Doctor of Philosophy

Indian Institute of Science July 2015

I would like to dedicate my thesis to my late grandfather, loving parents and siblings . . .

Declaration

I hereby declare that except where specific reference is made to the work of others, the contents of this dissertation are original and have not been submitted in whole or in part for consideration for any other degree or qualification in this, or any other university. This dissertation is my own work.

Narsing Kumar Jha
July 2015

Acknowledgements

"Gratitude is the memory of the heart"

- Jean Baptiste Massieu

I would like to thank the institute and people who have played key roles in the successful completion of this research work.

I sincerely wish to thank my research supervisor Dr. R. N. Govardhan for accepting me as his student, imparting his knowledge and guiding me through the turbulent research. I would also like to acknowledge him for his constant support, continuous motivation and teaching me some of the basic human intellects. Throughout my PhD, I cherished the freedom I had while working with him and it was an experience of a lifetime. I have walked down to his cabin for discussions and always he found time for it.

I would like to thank Prof. Jaywant H. Arakeri, Prof. Vijay H. Arakeri, Dr. M. S. Bobji and Dr. G. Tomar for valuable discussions and suggestions about my research work.

I would also like to take this opportunity to thank my teachers, in particular, Prof. V Kumaran, Prof. Jaywant H. Arakeri, Dr. O. N. Ramesh, Nengaru master (school teacher) and my fantastic undergraduate teacher Arindam Samanta for their untiring and honest efforts in teaching the subject fundamentals.

I gratefully acknowledge the support of MHRD, for providing the resources and financial assistance throughout the duration of my study at IISc. I also thank department of mechanical engineering team, Mrs. Somavathi and Mrs. Sulochana for all the administrative related help.

Again I'd thank my advisor for giving me the opportunity to undertake a challenging work and for his belief in my ability from the beginning. I earnestly thank him and my lab mates for their keen participation in weekly meetings/presentations and important suggestions at crucial points in my research. Special thanks goes to Jim, JP-1, Prashant, Pankaj Nadge, Anil, Nithiyaraj, Pawar (PRSP), Saurabh and Prahallada for healthy and helpful research discussions and timely help with experiments. The long talks with Varghese and Prashant on random topics were really enjoyable and will be sorely missed. I thank Nithiyaraj, Prahallada and others, who have made my time in the lab most enjoyable. I also thank Sulochana and her family for their friendly gestures and for the fish meals at their home.

I also wish to thank the Project assistants and interns, in particular, Naresh, Anubhav Bhat, Abhilash, Amlesh, Anchal, Prem, Vaishnavi, Adithya, Rajkamal, Aman, Nafih, Prashanth and Keerthana for their help and highly enthusiastic nature.

The support extended by M/s Amritha Enterprises, M/s Vacuum systems, M/s Puronics systems and M/s Sreevallabha Enterprises, Bangalore for the fabrication of experimental facility is gratefully acknowledged. I must specially thank Suresh for timely availability and friendly gestures.

My special thanks go to my dear friends Anubhav, Snehesh, Ayush, Anil, Navneet, Khatta, Pramod, Subrata, Patel (PP), Varun, Akhilesh, Sachan, Aditya, Kishore, Shyam sir, Prapanj, Ramnath, Shrikant, Biswajit and Kamakhya. I wish to thank them for scientific and non scientific discussions, which has helped me in becoming a better human. Tea sessions and outings with them are some of the most memorable times spent at IISc. I also wish to thank Snehesh for all outings and also to Khatta for keeping me motivated for long running.

Finally but the most importantly, I would like to thank my parents and family for their unwavering support. Timely advice from Ojhaji is thankfully acknowledged.

Abstract

Bubbly turbulent flows occur in a variety of industrial, naval and geophysical problems. In these flows, the bubbles in the flow interact with turbulence and/or vortical structures present in the continuous phase, resulting in bubble motion and deformation, and at the same time modifying the turbulence and/or vortical structures. Despite the fact that this has been a subject of interest for some time, mechanisms of bubble break-up due to turbulence and turbulence modulation due to bubbles are not well understood. To help understand this two-way coupled problem, we study in this thesis, the interaction of single and multiple bubbles with vortical structures; the thesis being broadly divided in to three parts. In the first part, we study the interaction of a single bubble with a single vortical structure, namely a vortex ring, formed in the continuous phase (water). This may be thought of as a simplified case of the interaction of bubbles with vortical structures in any turbulent flow. We then increase the complexity and study the interaction of a single bubble with naturally occurring vortical structures present in a fully developed turbulent channel flow, and then finally to the case of a large number of bubbles injected in to a fully developed turbulent channel. The bubble motions and deformations in all three cases are directly imaged using high speed visualizations, while the flow field information is obtained using time-resolved Particle-Image Velocimetry (PIV) in the first two cases, and from pressure drop measurements within the channel in the latter case.

The interaction of a single vortex ring with a bubble has been studied for a large range of vortex ring strengths, represented in terms of a Weber number (We). We find that in all cases, the bubble is first captured by the low pressure within the core of the ring, then stretched azimuthally within the core, and gradually broken up in to a number of smaller bubbles. Along with these bubble deformations, the vorticity within the core of the ring is also modified significantly due to bubble capture. In particular, at low We, we find that the core of the ring fragments as a result of the interaction resulting in a large reduction in the enstrophy of the ring and its convection speed. In the second part of the thesis, interaction of a single bubble with naturally occurring vortical structures present in a fully developed turbulent channel is studied. In this case, single bubbles of different sizes are injected either from bottom or top wall into a channel at Reynolds number of about 60,000. We study the

trajectories of the single bubble, and also investigate the effect that such bubbles have on the naturally occurring vortical structures present in these flows. The injected bubble is found to have three broadly different types of bubble paths when injected from the bottom wall, which are sliding along the wall, bouncing motions and vertical escape from the vicinity of the wall. Even at the same bubble diameter D_b and channel flow Re, we find that different realizations show considerable variations, with all three bubble paths being possible. PIV measurements of a bubble captured by a naturally occurring vortical structure in the flow, shows a more rapid decrease in enstrophy compared to naturally occurring structures in the absence of bubbles, as seen in the interaction of a bubble with a vortex ring. We also find that the bubble can interact with multiple vortical structures, depending on their strength and spatial distribution in the flow, resulting in a complex bouncing bubble motion. In the third part of the study, a large number of bubbles are injected in to the channel through porous plates fixed at the top and bottom channel walls. The main parameters here are the channel Re, bubble void fraction (α) and the orientation of injection. In this case, in addition to bubble visualizations, the pressure drop through the channel is measured at different vertical locations. These measurements show large vertical variations in the measured pressure drop due to the presence of bubbles. The overall drag reduction in these cases is obtained from an integral of the pressure drop variation along the vertical direction. The visualizations show a number of bubble dynamics regimes depending on the parameters, with possibilities of both increased and decreased drag compared to the reference no bubble case. From simultaneous measurements, we relate the variations in drag reduction to the different bubble dynamics regimes. We find that at the same void fraction (α), the drag reduction obtained can be very different due to changes in bubble dynamics regimes caused by changes in other parameters. Top wall injection is observed to give good drag reductions over a wide range of flow Re and α, but is seen to saturate beyond a threshold α. In contrast, the bottom wall injection case shows that drag reduction continuously increases with α at high Re. The present study shows a maximum of about 60% increase and a similar 60% reduction in wall drag over the entire range of conditions investigated.

Table of contents

List of figures

List of tables

Chapter 1

Introduction

"Either write something worth reading or do something worth writing."

- Benjamin Franklin

Bubbly turbulent flows occur in a variety of industrial, naval and geophysical problems. Some examples of practical problems where these occur are in ship hydro-dynamics, transportation of oil, chemical reactors and processes at the ocean surface. In these applications, the bubbles in the flow interact with the turbulence and/or the vortical structures present in the continuous phase, resulting in bubble motion and deformation, and at the same time modifying the turbulence and/or the vortical structures. The motion of bubbles in inhomogeneous flow has been extensively studied as discussed in the review by Magnaudet and Eames [50], which focuses primarily on the different forces acting on the bubble in such flows. Lagrangian properties of particles in turbulence has also been studied for a long time and Toschi and Bodenschatz [79] have reviewed the work on the physics of particle acceleration, Lagrangian velocity structure functions, and pairs and shapes evolution and also discussed the ongoing work for non-ideal particles. They comment that the interaction becomes more complex in multiphase and particle-laden flows, where particles react back on the fluid, interact with each other, or collide. Turbulence modulation due to the presence of particles or bubbles has been reviewed by Balachandar and Eaton [5], where they state that mechanisms of such turbulence modulation are poorly understood. At the broader level, the presence or injection of bubbles in turbulent flow can be beneficial in enhancing mass, momentum and energy transfer, and this is utilized extensively in the chemical industry. A relatively different beneficial effect of the presence or injection of bubbles is in the reduction or suppression of turbulence. This could be of use in a number of turbulent flows, but one which has received considerable attention is in the possibility of drag reduction in internal liquid pipe flows and in external flows around bodies in water.

The presence of a second phase (bubble) in vortical flow of the continuous phase can have a dramatic effect on the flow field and on flow stability [see, for example, 30, 46, 49]. Interaction of vortical structures with bubbles occur in many places, example of this include injection of micro-bubbles in turbulent flow for drag reduction [49, 69, 84], tip vortex cavitation [4, 11, 12] and bubble cloud dynamics generated by breaking wind waves close to the sea surface [77]. Reduction of frictional drag on external bodies through gas or bubble injection has recently been reviewed by Ceccio [9] and Murai [58], where they discuss about parametric dependence of drag reduction and different physical mechanisms. In these applications, gas or micro-bubbles are injected into a liquid flow resulting in the formation of a bubbly mixture near the body surface, which can significantly modify the turbulent boundary layer, thereby reducing drag. This type of bubble injection into a turbulent boundary layer is of engineering interest from the perspective of drag reduction of ships and submarines, apart from the reduction in pumping costs for oil pipelines.

Turbulent flows have multiple scale of eddies/vortical structures ranging from largest scale to the Kolmogorov scale [75, 80]. Figure 1.1 shows typical 3-D vortical structures in a turbulent boundary layer, the structures being visualized here by iso-surfaces of swirling strength shown in black colour [16]. The interaction of bubbles with turbulence may therefore be thought of as the interaction of bubbles with the vortical structures present in turbulent flows. For example, in the case of bubbles injected in to a turbulent boundary layer, the bubbles interact with the vortical structures, such as those in figure 1.1. Presence of low pressure at the center of the core of vortical structures captures the bubble inside the vortex core [50], due to which we find preferential bubble concentration near the vortex centre in turbulent flow [79]. It is however very difficult to comment on the modification of individual vortical structures due to their interaction with multiple bubbles, as formation and decay of vortical structures within say a boundary layer is a spontaneous process. Structures in turbulent flows are statistically distributed in the flow field having very high number density, which adds further complexity to the study of their interactions with bubbles.

Review article by Balachandar and Eaton [5] compiles the work on turbulent dispersed multiphase flow. The review mainly focuses on three aspects of these flows: the preferential concentration of particles, droplets, and bubbles; the effect of turbulence on the coupling between the dispersed and carrier phases; and modulation of carrier-phase turbulence due to the presence of particles and bubbles. In the future directions, they state that “mechanisms of turbulence modulation due to second phase are poorly understood and are wide open for fundamental investigations”. They also suggest that experimental techniques capable of yielding simultaneous fully resolved measurements of both the carrier and dispersed phases should be developed and role of fine-scale turbulence in the preferential concentration of

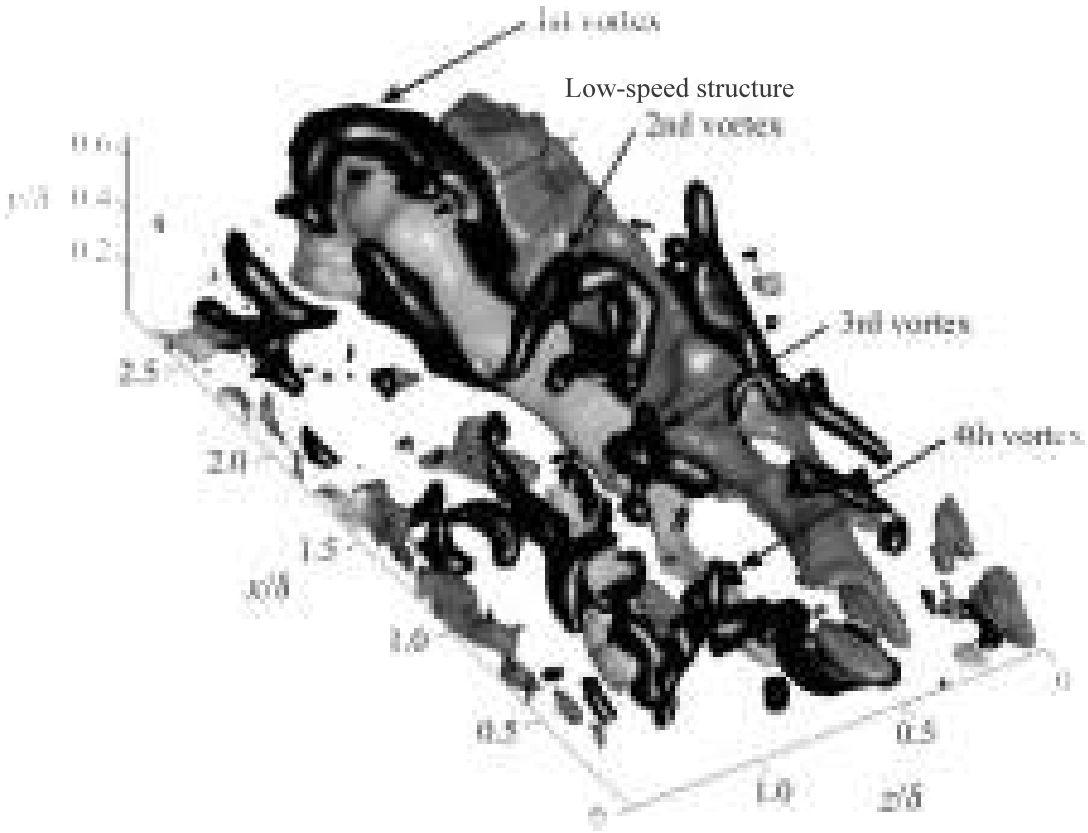

Fig. 1.1 Figure shows the 3-D visualization of vortical structure in turbulent boundary layer. Black colour represents iso-surface of swirling strength (λ_{ci}), which is the imaginary part of the complex Eigen-value of the velocity gradient tensor. Blue and red are iso-surface for negative and positive stream-wise velocity respectively. The figure is reproduced from Dennis and Nickels [16].

bubbles requires further attention. Keeping these points in mind and to better understand the problem of two phase turbulence in particular bubbles in turbulence, we experimentally study three different aspects of bubbles in turbulent flow in the present work.

In the present thesis, we experimentally investigate the interaction of vortical structures with bubbles. This is done in three parts with increasing amount of complexity in the vortical structures and the number of bubbles, with the focus being both on the bubbles and the vortical structures. In the first part of the work, we investigate the interaction of a single bubble with a single vortical structure, namely a vortex ring, formed in the continuous phase (water). This could be thought of as an idealization of the interaction of a bubble with a vortical structure present in a turbulent flow. There appears to be no prior experimental work that systematically investigates the two-way coupled nature of this interaction. In the second part of the work, we study the interaction again of a single bubble, but with the more complex vorticity field of a fully developed turbulent channel flow, which would have 3-D time dependent vortical structures. The focus here is on the interaction of a bubble with realistic vortical structures present in a turbulent flow, and we shall attempt to show connections with the more idealized case of a vortex ring studied in the first part. We then proceed in the third part of the study to investigate the effect of multiple bubbles with multiple eddies in the fully developed channel flow. In this part, we try to relate the different bubble dynamics regimes observed, with measurements of pressure drop and wall drag in the channel.

In the rest of this chapter, we present an overview of the literature relevant to the three parts of the work presented in this thesis, each in a separate sub-section, followed by an outline of the present thesis work.

1.1 Literature overview

Two phase turbulence has been an area of interest from decades but due to the complexity of the field, it still lacks fundamental understanding. We will present some relevant work related to each of the three parts of the present thesis work and justify the need of the present study.

1.1.1 Interaction of a bubble with a vortex ring

Turbulent flows have multiple scale of eddies/vortical structures ranging from largest scale to the Kolmogorov scale [75, 80]. Many investigators have recently shown that structures in turbulent boundary layers are mostly in the form of hairpins [2, 16]. The interaction of bubbles with turbulent structures within the boundary layer may therefore be thought of as the interaction of bubbles with these hairpin structures. It is however very difficult to comment on

the modification of individual hairpin vortex structures due to their interaction with bubbles, as formation and decay of hairpins is a spontaneous process. Hairpins in turbulent boundary layers are statistically distributed in the flow field having very high number density, which adds further complexity to the study of their interactions with bubbles. These structures also regenerate new structures before it die, which is an important mechanism for self sustaining turbulence. Interactions of multiple bubbles with multiple structures have further complexity due to the non-linear interaction between eddy-bubble, eddy-eddy and bubble-bubble. A simplified way to understand the interaction of such vortical structures with bubbles for better understanding of the underlying physics is to study the interaction of a single vortical structure with a single bubble. Perhaps the most simple and robust vortical structure that one can think of is a vortex ring, as “it is fairly robust, as well as simpler to generate, analyze, and isolate from end-effects than other configurations" [71].

A simple and common methodology to generate a vortex ring in the laboratory is by pushing a slug of fluid using a piston-cylinder mechanism. Gharib et al. [28] and Linden and Turner [44] have shown that there exists a maximum circulation that such a vortex ring can attain. The vortex rings formed can have thin or thick cores, this being indicated by a non-dimensional core radius (ε = (core area/πR^2)$^{0.5}$, where R = vortex ring radius); one limit being thin vortex rings with ε tending to zero, and the other limit being the Hill’s spherical vortex with $\varepsilon = \sqrt{2}$ [60]. Vortex rings can be laminar, transitional or turbulent depending on the ring Reynolds number ($Re = \rho\Gamma/\mu$) and non dimensional piston stroke (L/D_0) [29]. The laminar rings typically become unstable due to the azimuthal short wave instability of the vortex core, resulting in the formation of Kelvin waves [88]. Non dimensional core radius (ε) is also an important parameter that affects vortex instability with thicker core rings being more prone to instability, as shown by O’Farrell and Dabiri [61]. Vortex pairs or single vortices can also undergo other instabilities leading to distortion or fragmentation of the core. These include, for example, instabilities of annular vortices [18], elliptic instabilities of vortex pairs [43], fragmentation and unraveling of vortex loop due to twist waves [24], and instabilities in a vortex due to density stratification [17].

On the interaction of a vortex with a bubble, Chahine [10] asks the questions: “How does a microscopic bubble interact with a vortex?" and “how and to what extent does it modify the flow field of vortex?" In his numerical study, he observes extreme bubble elongation and wrapping around the viscous core region for bigger bubble sizes. In the review of Magnaudet and Eames [50], they state that only a few quantitative experiments have been attempted to explore the bubble motion interacting with a single vortex. Sridhar and Katz [73] investigated the drag and lift force on the bubble in a vortex and compared the bubble trajectory measured from experiments with numerical modeling. In the follow up work by Sridhar and Katz

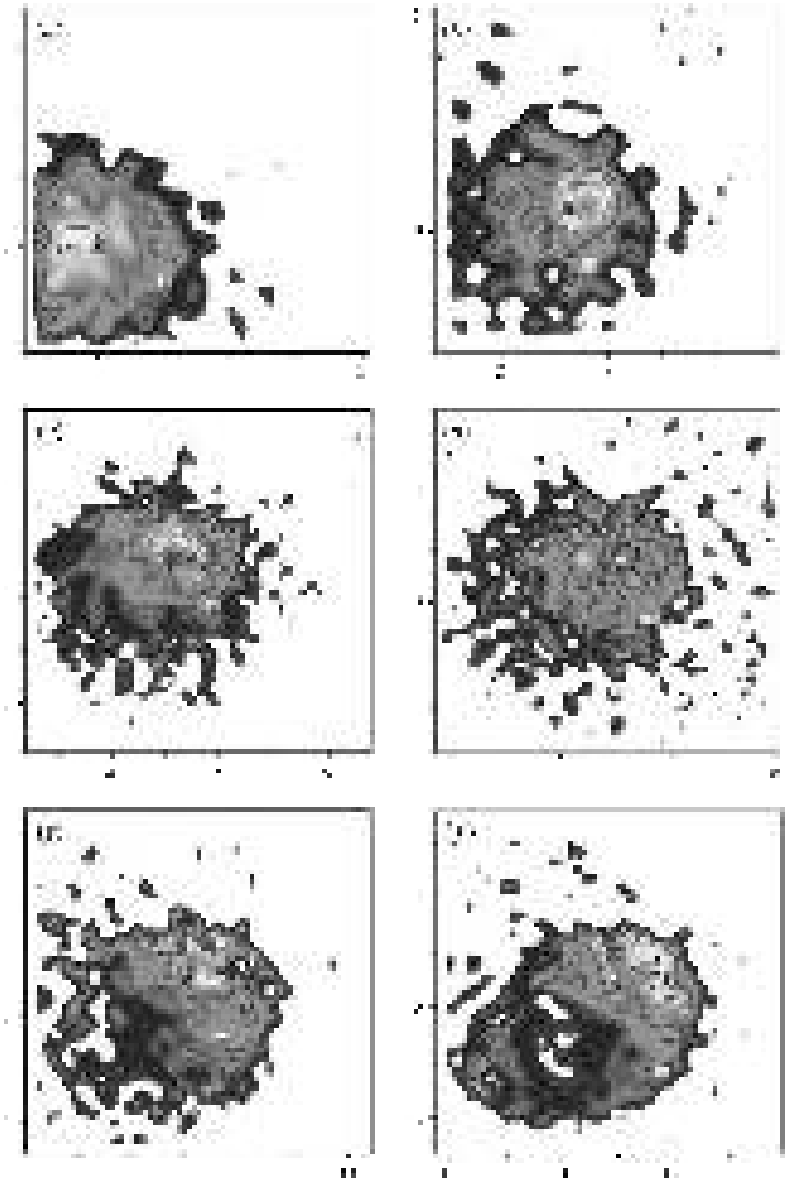

Fig. 1.2 Figure shows the time sequence of vorticity plots of the core of a vortex ring entraining 512 μm bubbles. Entrained bubbles affect the vorticity distribution of the core and at later times, core is no more intact. Entrained bubbles are represented by the solid circles. Results are reproduced from the experimental study by Sridhar and Katz [74]

[74], they looked into the effect of a set of relatively small bubbles on the structure of a relatively large vortex ring. As shown in figure 1.2, they showed that under certain conditions, a set of about 5 bubbles interacting with a vortex ring can distort the vortex core, with the vortex core returning to the initial state after the bubbles escape from the ring. During the interaction time, they observed that the circulation was nearly constant with about 20% increase in peak vorticity. In their experiments, the ratio of bubble volume to vortex core volume ($V_R = (\pi {D_b}^3/6)/(2\pi^2 R a^2)$) was very small ($\sim 10^{-6}$). In the current study V_R is of the order of 0.1, which is closer to the (V_R) observed in bubbly turbulent boundary layer used for drag reduction. More recently, a few numerical studies have attempted to understand the two ways coupling between the flow and the bubble. Cihonski et al. [13] studied the reaction force on the liquid due to the summation of bubble lift, drag, added mass, pressure and gravity forces, and found these to be very small and hence unable to distort the core as observed in the experiments of Sridhar and Katz [74]. They showed that vortex distortion can however be explained by accounting for volume displacement by the bubble. They observed around 10% increase in circulation and about 20% increase in peak vorticity of the vortex. There have also been studies of interaction of vortex ring with large number of minute size microbubbles. Interaction of vortex ring with bubble plume has been studied experimentally by Uchiyama and Kusamichi [82] and they observed increase in the upward convection speed, as vortex ring passes in an upward flow generated by the bubble plume. Numerical simulation using two-fluid approach of the effect of minute size microbubbles in Taylor-Green vortex with a volume fraction of about 0.01 and bubble number of around10^5 have been done by Ferrante and Elghobashi [23]. They observed that bubbles settle in the core of the vortex, which causes reduction in the vorticity magnitude at the vortex centre, but no noticeable change anywhere else. They explained that this is caused by local positive divergence of the fluid velocity due to entrainment of bubble. They also further state that the accumulation of bubbles in the highest enstrophy region reduces the vorticity and enstrophy.

There have also been many studies on the break-up of a bubble in a turbulent flow. Kolmogorov [40] and Hinze [35] showed in their pioneering works that bubbles or droplets break when the non dimensional number N (N = ratio of either viscous or dynamic forces to surface tension force) exceeds a critical value; the critical value itself being dependent on the amount of dispersion between the two phases. Shinnar [72] proposed from Kolmogorov's theory that the mean size of the droplet (or bubble) in isotropic turbulent flow varies as $We^{-0.6}$. In their microgravity experiments, where turbulence is the only cause of bubble breakup, Risso and Fabre [68] observed that the second mode is dominant in bubble break-up. Martínez-bazán et al. [51] suggest that binary breakup takes place at low *We*, but at larger *We* tertiary breakup dominates. Revuelta [66] has numerically studied the break-up of a single

Fig. 1.3 Three-dimensional numerical simulations of bubble break-up patterns observed for a single bubble interacting with a vortex ring at different Weber numbers performed by Revuelta [66]. In the simulations Re = 1000, R/R_b= 1.5, and a/R_b = 0.05.

bubble due to the induced velocity of a vortex ring; the bubble always being outside the vortex ring, which is shown in figure 1.3. He observed binary breakup at low *We*, and large deformations followed by break-up into multiple fragments at high *We*.

1.1.2 Interaction of a bubble with vortical structures in turbulent flow

There are many studies which focus on effect of bubbles on integral properties of turbulence. This includes investigations on the effect of bubbles on structure function, acceleration PDF [53], preferential concentration [41, 74], energy redistribution and scaling law [42, 47, 53, 57, 83]. Figure 1.4*a* shows the decrease in energy at the large scale and increase at small scale caused by interaction with bubbles, while figure 1.4*b* shows the preferential concentration of smaller bubbles in high enstrophy region. As suggested by Perry and Chong [64], such statistical/global properties of turbulence are constructed from vortical structures present in turbulent flow. However, despite the existence of studies about the effect of bubbles on turbulence from the macroscopic view point, there are very few studies about the microscopic view, which is the effect of bubbles on vortical structures in turbulent flow [46, 67]. Figure 1.5 shows results from the simulations of Lu et al. [46] showing suppression of vortical structures by bubbles. In the recent review article by Balachandar and Eaton [5]

on turbulent dispersed multiphase flow, they discuss important areas that should be addressed in the future. The stated areas are simultaneous experimental measurements of both the carrier and the dispersed phases to better understand the two-way coupled interaction, role of fine-scale turbulence in the preferential concentration of bubbles and the mechanisms of turbulence modulation and their parametric dependence. They emphasize that these areas are not well understood and are wide open for fundamental investigations to help understand the two-way coupling between the bubbles and the flow.

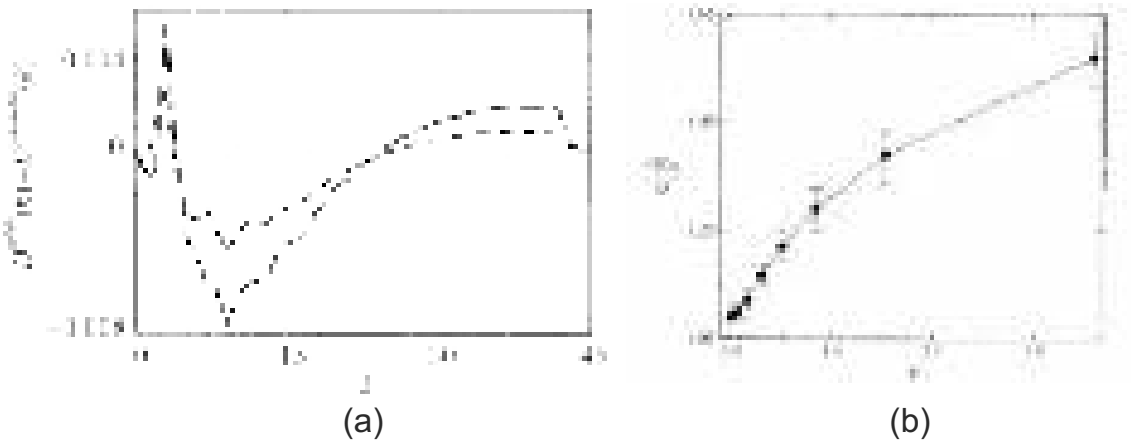

Fig. 1.4 Effect on bubbles on distribution of energy at different scales in the flow and also preferential concentration of smaller bubbles in the high enstrophy region. Numerical study by Mazzitelli et al. 2003 discusses the two-way coupled nature of bubbly turbulent flow.

Existence of coherent structures in turbulent flows dates back to at least Theodorsen [76], and has been widely discussed in [80]. These kind of structures have been used to construct statistical models of the turbulent boundary layer and is a very successful tool (e.g. [64]). Vortex packets are statistically significant structures for Reynolds stress and transport processes in the logarithmic region of the flow [52]. The presence of such small scale structures cause trajectories of particles or bubbles in the flow to be complex. Figure 1.6 shows the streak-line of 25 μm tracer particles and it shows the random nature of Lagrangian particle motion. The complex motion of a fluid tracer trapped in a small-scale vortex filament is shown figure 1.7*a* [6, 78] and in figure 1.7*b*. In these figures, the trajectory of the particle motion is shown along with the acceleration magnitude captured at 70,000 fps.

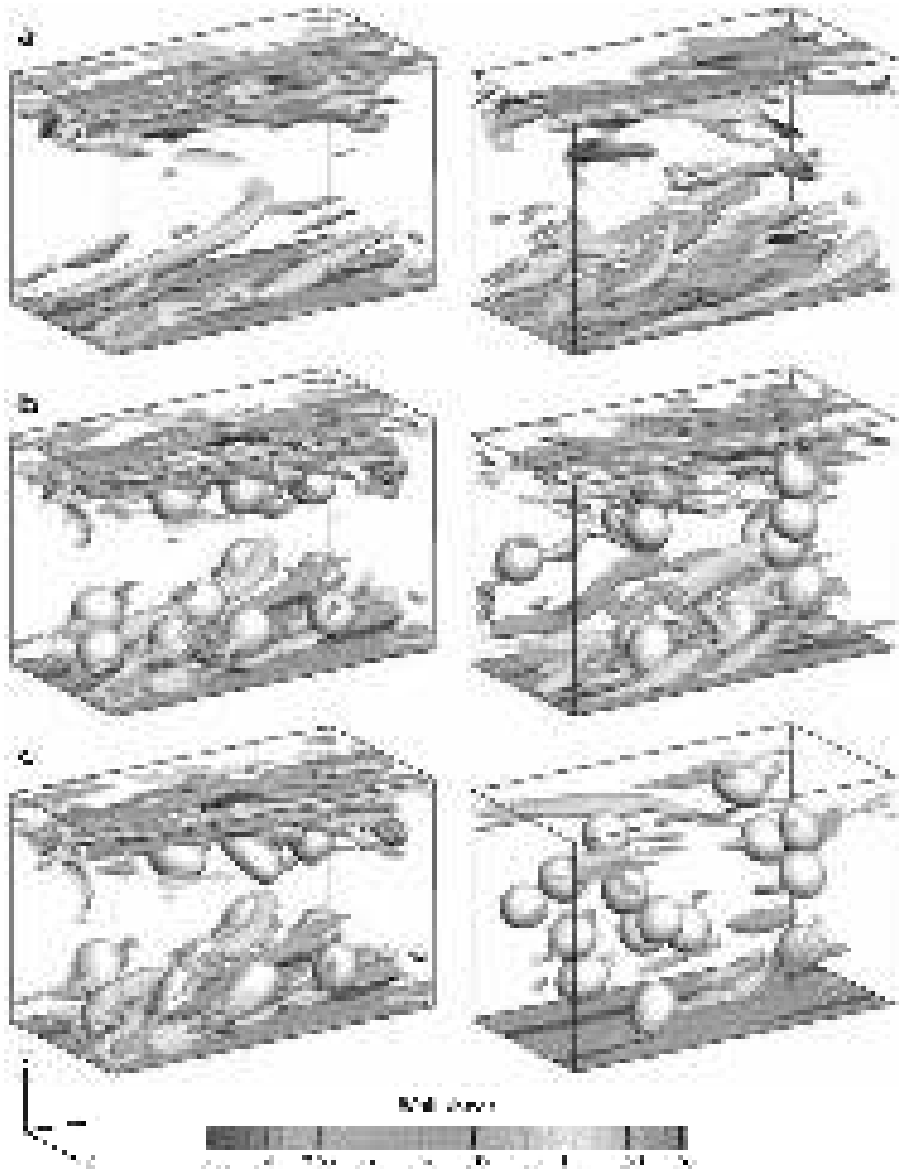

Fig. 1.5 Simulation of bubble-flow interactions in a turbulent channel leading to frictional drag reduction: (a) the baseline flow, (b) bubbles with $We = 0.203$, and (c) $We = 0.405$. The left column is for early time, and the right is for later time. Iso-contour of stream-wise vorticity are shown along with shear on the bottom wall. Figure is taken from Lu et al.[46].

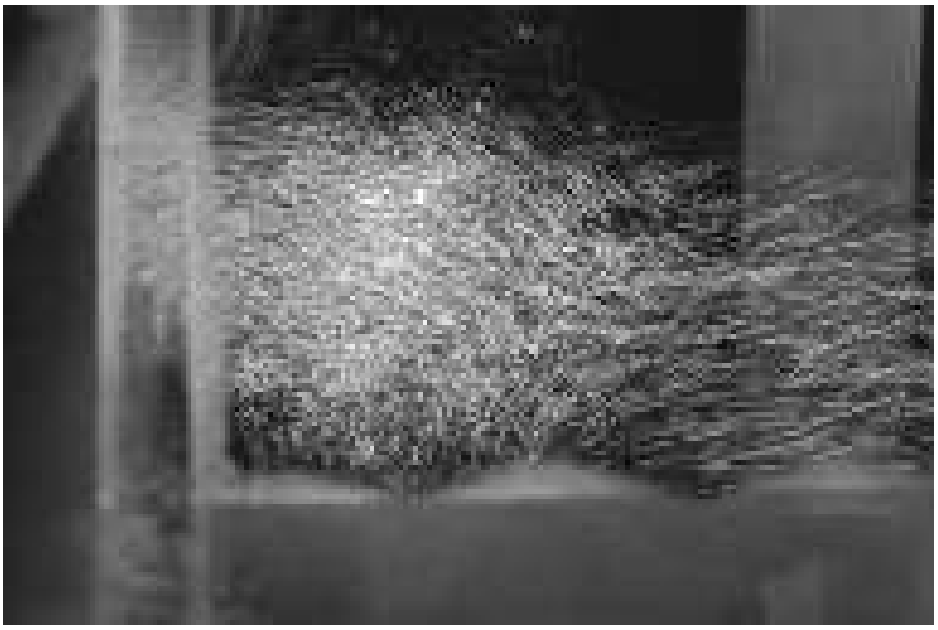

Fig. 1.6 Polystyrene spheres of diameter 25 μm are used as tracers in experiments and illuminated by a green YAG laser with a mean output power as high as 35 W. Image is taken at high exposure to capture streak of tracer particles. Figure taken from Toschi and Bodenschatz [79].

Richter and Sullivan [67] numerically studied modification of near-wall structures by inertial particles in a turbulent planar Couette flow. They show that conditional eddies near the wall are weakened substantially by the presence of the dispersed phase, and that this effect is further enhanced with increasing Re_b, (Re_b = bulk Reynolds numbers, based on the plate velocity difference and separation distance). They also propose a mechanism where particles, by interfering with the hairpin regeneration process near the wall, can influence turbulent fluxes. At the same time, turbulent momentum flux concentrated at higher wave-numbers with increasing Re_b allows small particles to be effective agents for altering turbulent transport [67].

In another study, role of coherent structures in bubble transport in turbulent shear flow is studied numerically by Sene et al. [70]. Discrete vortex model is used to simulate the mean flow, and Auton's force law is used for the unsteady motion of the spherical bubble. They mainly talk about two non-dimensional numbers, which decide trapping of a bubble. These numbers include a trapping parameter, which is the ratio of velocity difference across the vortex (or shear layer) to the terminal slip speed of the bubble or particle, and a relaxation parameter that is the ratio of inertia to buoyancy force. Bubbles are trapped in the mixing layer, if the trapping parameter exceeds a critical value. Trapping parameter is about 10 for relaxation parameter tending to zero and about 3 for relaxation parameter of around 0.5. For

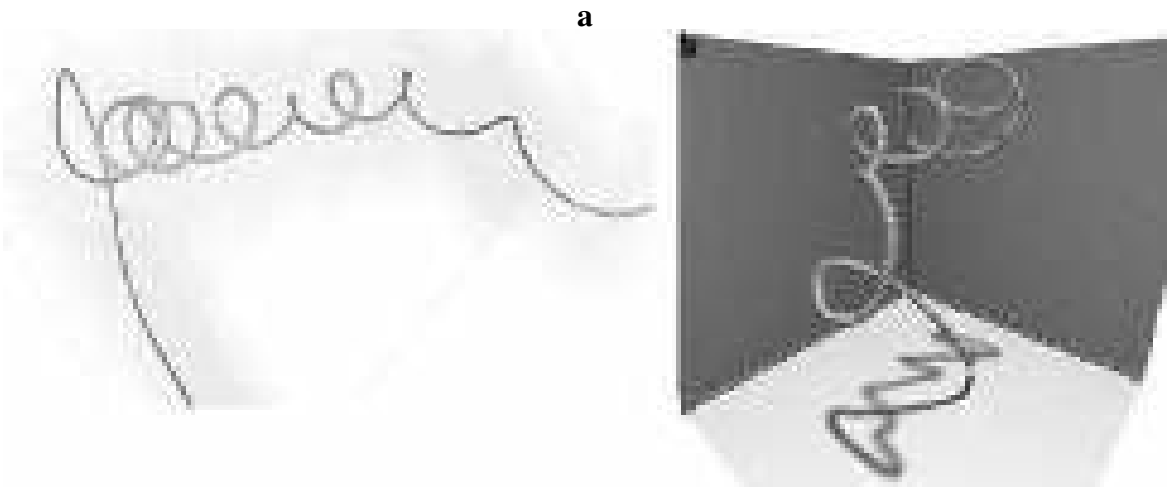

Fig. 1.7 (a) Plot shows the trajectory of a fluid tracer in a small-scale vortex filament in turbulent flow from a numerical simulation. Colors and arrows indicate the magnitude and direction of the velocity (Biferale et al. [6], Toschi et al. [78]). (b) Trajectory of a high acceleration event of a tracer particle in turbulence recorded at a frame rate of 70,000 frames per second. The position of the particle at each of the 278 frames is represented by a sphere. Figure reproduced from Voth et al. [85].

the same trapping parameter, decreasing the relaxation parameter increases the probability of escape. Huang et al. [36] measured bubble-induced velocity fluctuations close to the wall. The sink and source are clearly recognized in the downstream and upstream regions of bubbles respectively, as shown in figure 1.8. The pair of sink and source in the boundary layer corresponds to the ejection and sweep events along the wall. It was confirmed with spectral analysis that only small bubbles modify coherent structures.

1.1.3 Effect of bubbles and its distribution on wall drag in turbulent flow

Micro-bubble injection into a turbulent boundary layer has been studied for a long time, starting from the pioneering work of McCormick and Bhattacharyya [54]. It is now well established that drag reduction in these flows is a strong function of bubble void fraction near the surface [9, 49, 69]. However, the physical mechanisms responsible for frictional drag reduction using microbubbles in turbulent boundary layers is not yet completely understood [22, 58]. Broadly speaking, drag reduction by bubbles can either be caused by direct modification of fluid properties like density and viscosity, or through the relatively more complex interaction of bubbles with turbulent structures within the boundary layer. Murai [58] and L'vov et al. [48] have pointed that large reductions in drag cannot be explained

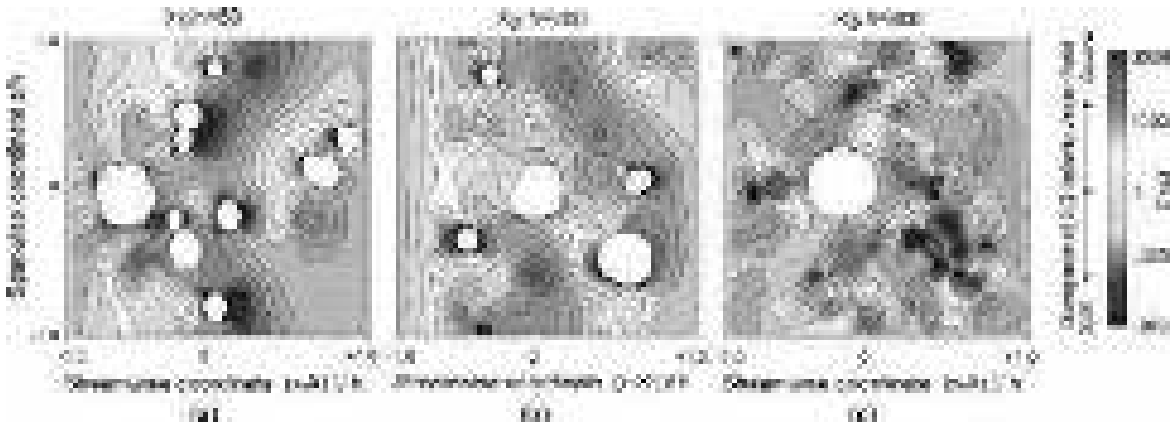

Fig. 1.8 Liquid velocity fluctuation induced by bubbles of various sizes in a horizontal turbulent channel flow. The bulk mean liquid velocity is 2 m/s and Re of 8,800. The two-dimensional divergence of velocity vector field at 1.50 ± 0.15 mm from the wall is visualized at (a) 250 mm, (b) 1 m, and (c) 4 m from the bubble injection point [36].

only through modification of fluid properties, and that the other mechanism is very likely to be playing an important part. In particular, Murai [58] highlights the fact that coherent structures present in turbulent flow can be modified by the presence of bubbles resulting in drag reduction; the mechanism being dependent on the bubble size and flow speed. Direct numerical simulations (DNS) have been done to understand the physical mechanism of drag reduction by Ferrante and Elghobashi [22] and Lu et al. [46] and these studies show that drag reduction can indeed be attributed to the interaction of bubbles with turbulent eddies. Lu et al. [46] also observed that presence of bubbles suppress stream-wise vortices and enstrophy, which in turn reduces the wall shear stress. The experiments of Jacob et al. [38] showed that injection of micro-bubbles into a turbulent boundary layer resulted in decrease of the characteristic dimension of the turbulent scale involved in production of kinetic energy. Van Gils et al. [84] have shown experimentally in a turbulent Taylor-Couette flow that bubble deformability is a crucial and important mechanism for drag reduction. Aliseda and Lasheras [3] studied the effect of microbubbles on a vertical flat plate turbulent boundary layer. In this case, bubbles were confined within the boundary layer, as convection by the carrier flow and rise due to buoyancy are both in the vertically upward direction. They find that secondary flows are generated due to the presence of bubbles.

Figure 1.9 shows composite data of the bubble drag reduction in a turbulent boundary layer, both from zero pressure gradient flat plate and fully developed channel flows [9]. Large variations among different experiments are clearly evident from the plot. This points to the fact that there could be better ways to scale bubble induced drag reduction data, which in turn suggests the lack of complete understanding of the physical mechanism of drag reduction.

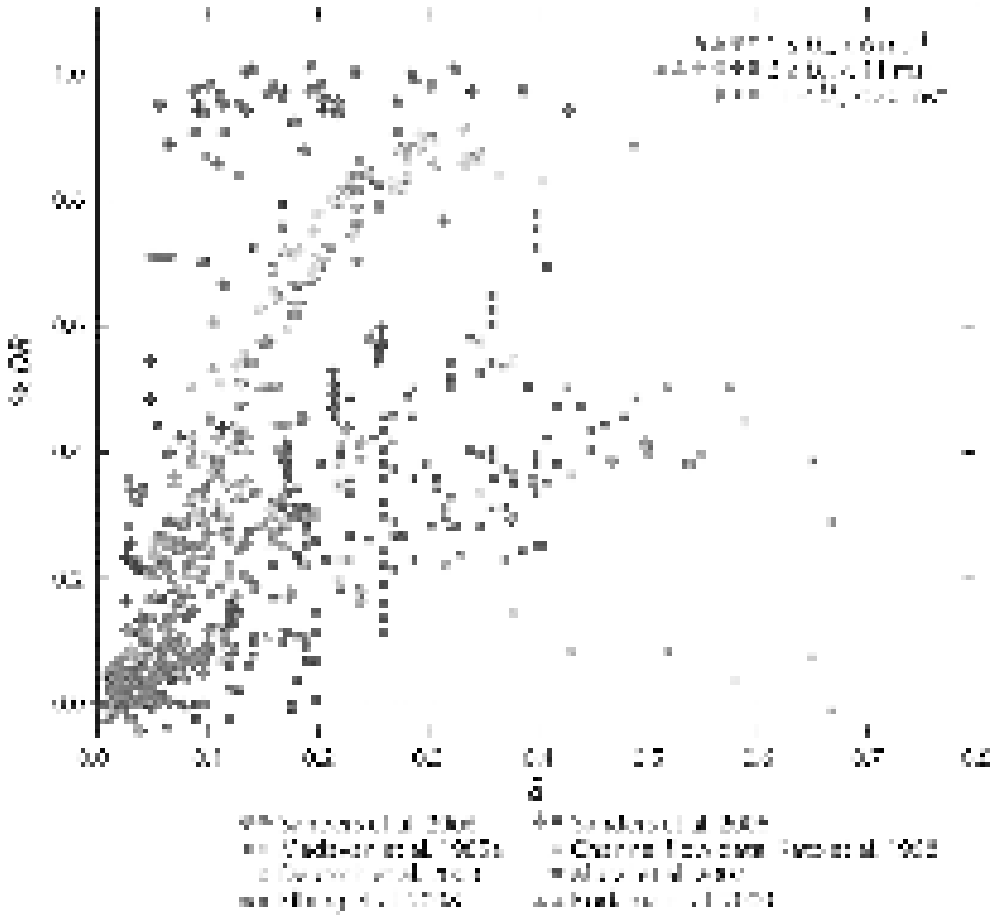

Fig. 1.9 Data for bubble–drag reduction from different experiments is compiled for flat plate and channel. Large scatter among different experiments are clearly evident, which suggests a scope for future investigation. Plot reproduced from the review article by Ceccio [9].

Fig. 1.10 Schematic of the one possible drag reduction mechanism in a bubbly turbulent boundary layer: (a) Single-phase flow, (b) bubble-laden flow. Vortical structures lift-up due to presence of bubbles and reduces the turbulence production and flow drag. Schematic is reproduced from Ferrante and Elghobashi [23].

Drag reduction using bubbles is highly dependent on the bubble distribution very close to the wall [20, 31, 49, 69] as most of the turbulent transport responsible for the production of wall drag takes place within the few tens of wall units near the surface [65]. There are a few broad mechanisms that affect wall drag in bubbly turbulent flows. Firstly, there is the modification of fluid properties like density and viscosity of the effective flow [48]. Secondly, there is the effect of compressibility of the bubble on the flow [45]. Thirdly, the bubble will interact with the turbulent flow and may affect the turbulent transport either by lifting the structure away from the wall and affecting the production [22] as shown in figure 1.10, or by suppressing the vortical structure [46, 74]. Fourthly, there can be bubble-bubble interaction and bubble splitting affecting the eddy distribution and properties [55]. Besides these four, there is also the possibility of the formation of an air layer close to the wall changing the boundary condition [20]. Different kind of bubble dynamics, bubble size distribution and coalescence time scale will also affect the physical mechanism responsible for drag reduction [58]. A parameter that is useful to measure the effectiveness of bubble induced drag reduction is the “Gain factor” defined as the drag reduction per unit void fraction [58]. This parameter is naturally a function of the physical mechanism responsible for drag reduction. It is important to note here that the effect of bubbles on drag is a function of bubble size and flow speed, and depending on these parameters, one can have drag reduction, increase or no change at all as shown in figure 1.11 [58].

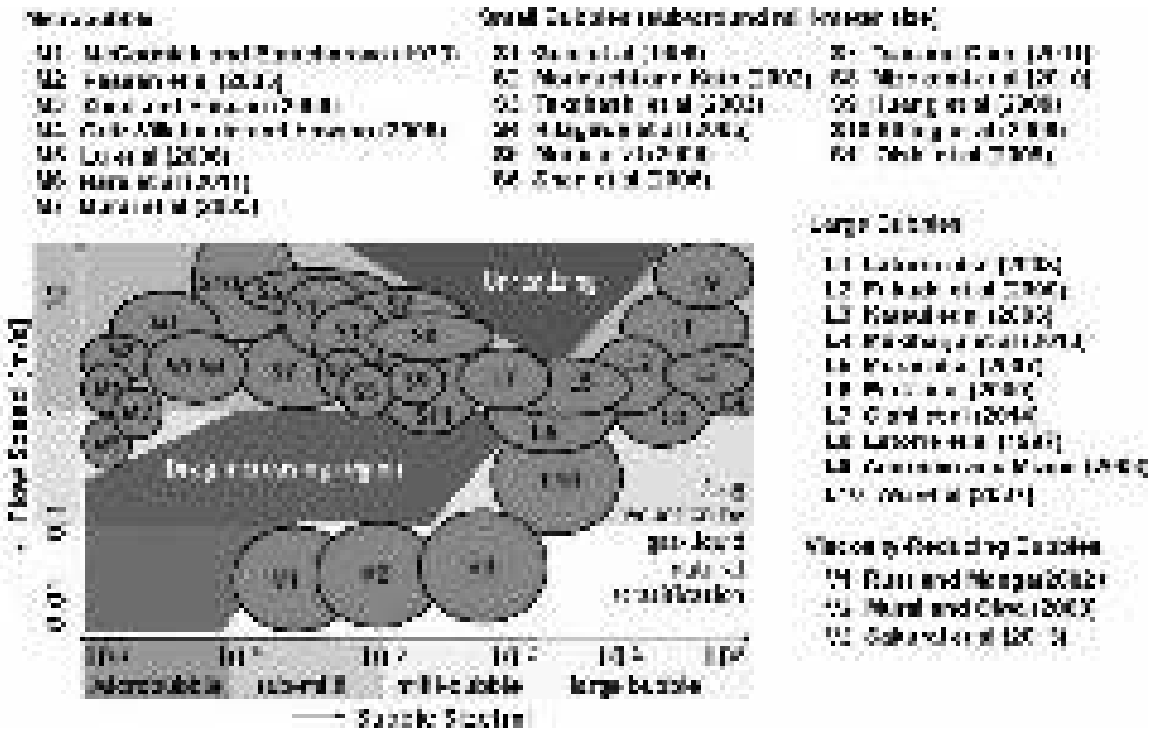

Fig. 1.11 Figure shows the distribution of studies on drag reduction plotted on flow speed-bubble size plane. The central position and diameter of each ellipse indicate the average conditions and the approximate range. Figure taken from Murai [58]

1.2 Present work

The focus of the present work is the interaction of single and multiple bubbles with vortical structures. Towards this broad goal, we study three related problems with increasing complexity in terms of the vortical structures and the number of bubbles. In all the three cases, our interest is the two-way coupled problem of the bubbles and the vortical structures, and as such we are interested in both the bubbles and the vortical structures. Hence, in all the problems, we measure/visualize both the bubble side and the flow side to help us better understand the interaction between the bubble and the vortical structures in the flow.

We first study the interaction of a single bubble with a single vortical structure, namely a vortex ring, formed in the continuous phase (water). This may be thought of as a simplified case of the interaction of bubbles with vortical structures in any turbulent flow. In our experiments, the vortex ring is generated by using a piston–cylinder arrangement in water, and the bubble is generated by a capillary connected to an air pump. The ring travels vertically upwards while interacting with the bubble, as shown schematically in figure 1.12(a). In this case, we directly visualize bubble motion and deformation using high speed imaging, while the vorticity field is measured using time-resolved Particle Image Velocimetry to enable us to comment on both the bubble and the vortical structure. Due to the low pressure within the core of the vortex ring, the bubble is drawn towards the ring, leading to capture of the bubble by the ring. This sets in motion a strong interaction between the two, which results in both bubble break-up and under the right conditions, permanent fragmentation of the vortex core. Although interactions of multiple bubbles with a vortex ring have been studied previously, this perhaps more simple case has not been studied previously.

We then proceed to study the interaction of a single bubble with vortical structures present in a fully developed turbulent channel flow. The focus of the work here is to measure and understand the interactions of a single bubble with the naturally occurring vortical structures within the turbulent channel. For this problem, a single bubble is injected in to a fully developed turbulent (water) channel flow, as illustrated schematically in figure 1.12(b). We again visualize the bubble with high speed imaging to track it, as it interacts with the naturally occurring unsteady vortical structures in the channel, which are visualized using time-resolved Particle Image Velocimetry. The simultaneous measurements of both bubble and vortical structures enable us to comment on their interactions.

We finally study the case of a large number of bubbles injected in to a fully developed turbulent channel flow, as illustrated in figure 1.12(c). The focus of the work here is to determine the different bubble dynamics regimes that exist in this case, and to relate them to measurements of the pressure drop in the channel. In this case, bubbles are generated and injected in to the flow by sending air though a porous bed and in to the channel. The

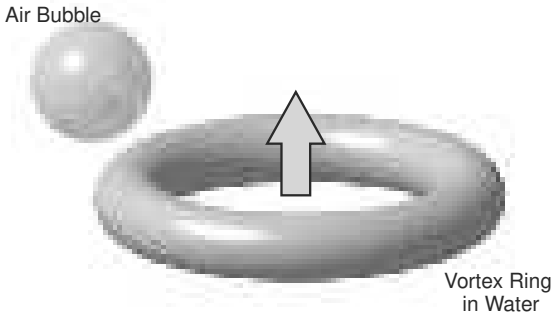

(a) Interaction of a single bubble with a vortex ring

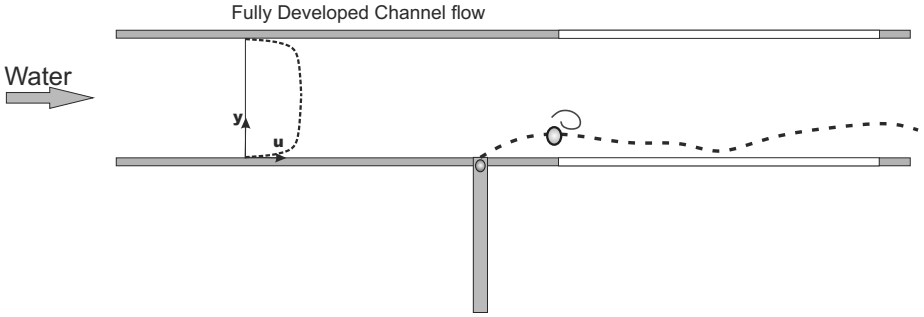

(b) Interaction a single bubble with vortical structures in turbulent boundary layer

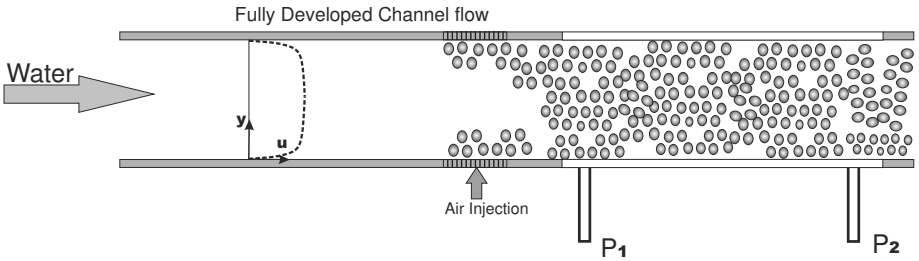

(c) Interaction of multiple bubbles with vortical structures in turbulent boundary layer

Fig. 1.12 (a) Schematic showing a vortex ring and bubble. The vortex ring convects vertically upward towards the bubble and interaction begins with the entrainment of the bubble in to the low-pressure vortex core. (b) Schematic of a single bubble injected from the wall into a fully developed turbulent channel flow. Bubble in the boundary layer interacts with the eddies and motion of it is decided by the interaction of the bubble and the flow field. (c) Schematic showing the injection of multiple bubbles into a fully developed turbulent channel flow. Effect of bubbles on overall flow drag is measured using pressure drop along the channel length.

main parameters that we vary in this case is the bubble void fraction in the flow, the channel Reynolds number and the orientation of bubble injection i.e. top or bottom wall injection. We visualize as in other problems, the bubble dynamics directly using high speed imaging, while on the flow side, we obtain information from time-averaged pressure drop measurements across the channel length. From pressure drop measurements, which are done at different vertical locations, we can obtain overall wall drag data, which depending on the parameters is found to either increase or decrease compared to the reference no bubble case.

The layout of the thesis is as follows. In chapter 2, we present details of the different experimental setup used in the present work, and give details of the measurement techniques used to make visualizations and quantitative measurements. In chapter 3, we present results from the study on the interaction of a single bubble with a vortex ring from both the bubble dynamics and vorticity dynamics perspective. This includes the effect of changes in the strength of the vortex ring and in the core size of the ring, both of which, we will show, have a profound impact on the interaction. Following this in chapter 4, we present results from the study on the interaction of a single bubble with the eddies present within a fully developed turbulent channel flow. We shall present here results of both the bubble trajectories within such a flow, and also discuss the effect of the bubble on vortical structures in this flow. In chapter 5, we present the results for multiple bubbles injected in to a fully developed turbulent channel flow. Here, we show the different bubble dynamics regimes that are possible as a function of the bubble void fraction, the Reynolds number and the orientation of bubble injection. We also present overall pressure drop/wall drag data as a function of these parameters, and relate them to the different observed bubble dynamics regimes. Finally, we shall present our conclusions from the study, providing an overview of how the above study helps in better understanding of bubbly turbulent flow.

Chapter 2

Experimental Methods

"It is the weight, not numbers of experiments that is to be regarded."

- Isaac Newton

The focus of the present thesis is an experimental study of the interaction of bubbles with vortical structures in different kind of flow environments. In this chapter, we present details of the experimental set-ups used and the different experimental techniques used to characterize the flow. We also present here details of the characterization of the base flow for the fully developed turbulent channel flow in the absence of bubbles. Different methods for bubble generation used in the present work are also described here.

2.1 Interaction of a single bubble with a vortex ring

The vortex ring was generated in a water tank and an air bubble was generated near it to study the interaction of the two. Schematic of the experimental setup for the this study is shown in figure 2.1. The experiments were conducted in a glass tank of dimensions 0.6 m $\times$ 0.6 m $\times$ 1.2 m. Vortex rings were generated by actuating a piston-cylinder mechanism within water, such that the resulting vortex ring convects vertically upwards against gravity. The ring generator had a diameter D_0, which was 15 mm for all the thin core vortex ring cases. The rings generated with this generator were relatively thin with non dimensional core radius (ε) of around 0.25. For the few thicker ring cases studied with non dimensional core radius (ε) of around 0.75, a ring generator having diameter (D_0) of 3 mm was used. Vortex rings were generated by impulsively pushing out a slug of water from the generator resulting in a vortex ring of strength Γ, ring radius R, and vortex core radius a, these parameters being measured from PIV velocity fields. In each case, these ring parameters were measured

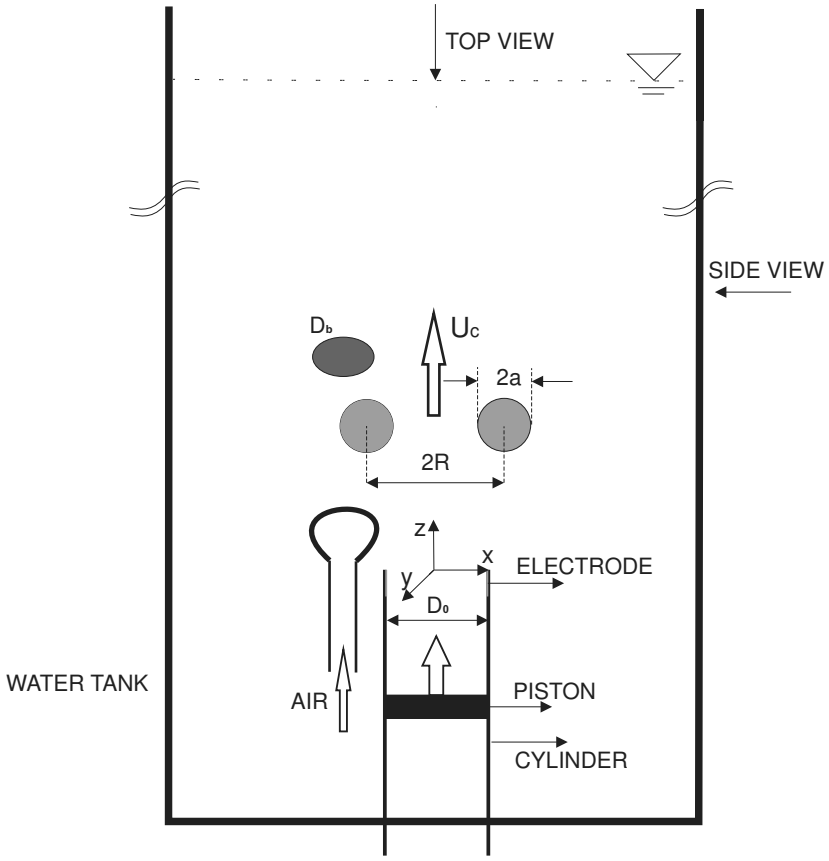

Fig. 2.1 Schematic showing the experimental set-up and the main parameters of the vortex ring and bubble. The vortex ring is generated by a piston-cylinder mechanism with generator diameter D_0. The resulting vortex ring has radius R with core size a and convects vertically upwards with convection velocity U_c, while the bubble is of size D_b. Camera orientation for imaging and position of electrode used to visualise the vortex ring are also indicated.

from a set of about three experiments conducted in the absence of the bubble. Circulation (Γ) was measured using the line integral of velocity around a large closed loop enclosing the vortex core. The core radius (a) and ring radius (R) were then determined from the measured vertical velocity along a horizontal line passing through both the vortex centers. Both these parameters were obtained from a least-squares fit of the vertical velocity induced by the superposition of two Lamb-Oseen vortices with the measured velocity in a manner similar to that of Leweke and Williamson [43]. Non-dimensional time scale (L/D_0, where L is the piston stroke length) was always kept less than 4, such that there was no trailing jet behind the ring [28]. The circulation strength of vortex rings was varied by changing the piston velocity. The resulting vortex ring strengths varied from 30-500 cm ^{2}/s, covering the laminar, transitional and turbulent vortex ring regimes. All the interaction experiments reported with the bubble were performed after the complete formation of the vortex ring. In order to visualize the vortex ring, micron sized air bubbles were generated at the metallic tip of the vortex generator by electrolysis. These bubbles were much smaller than the millimeter sized main bubble of diameter D_b and the core radius a, and hence their effects on the vortex ring were negligible. This was confirmed by comparing the convection speed of the ring tracked with dye and with these micron sized bubbles (both in the absence of the main large bubble), the convection speed being within experimental error between the two cases. The initial convection speed of the ring before interaction with the bubble was measured from position-time information and denoted as U_c. This velocity along with the initial ring radius R has been used to define a non-dimensional time, $t^* = tU_c/R$, and non-dimensional vorticity, $\omega R/U_c$, which are used throughout the chapter 3 to present results.

The bubble diameter D_b was 6 mm for the rings generated with the vortex ring generator of D_0 = 15 mm, while the bubble diameter D_b was about 1.5 mm for the few cases studied with the generator of D_o = 3 mm. In both cases, the bubbles were ellipsoidal before the interaction with the ring, as expected, with the average large to small axis ratio, as measured from the side view, being about 2. The bubble was released just prior to the generation of the vortex ring using a valve in the air line. Volume ratio ($V_R = (\pi {D_b}^3/6)/(2\pi^2 R a^2)$), defined as the ratio of bubble volume to the vortex core volume, was maintained to be of the order of 0.1 for all the experiments. The circulation of the vortex ring (Γ) was varied as stated above, resulting in a range of Weber numbers ($We = 0.87\rho(\Gamma/2\pi a)^2/(\sigma/D_b)$) from 3 to 400. For all measurements, with and without bubbles, three repetitions of the experiments were done, and the average of these is shown in plots with error bars used to indicate the variation between the runs. Parameters for the experiments are shown in table 2.1.

The origin of the coordinate system is at the centre of the exit plane of the vortex generator, as shown in figure 2.1. The vertical direction (upwards) is denoted by z, and x, y are in the

$R\ (mm)$	$a\ (mm)$	$\Gamma\ (cm^2/sec)$	ε	We	Re	$U_c\ (m/s)$
7.3	2.2	28	0.29	3	3430	0.13
9.4	2.3	98	0.24	33.3	11900	0.31
10.4	2.6	174	0.25	82	21200	0.47
11.5	2.9	245	0.25	131	29900	0.73
11.7	3.1	371	0.27	263	45200	0.95
12.1	3.4	505	0.28	406	61500	1.13

Table 2.1 Values of measured parameters and non-dimensional number for the thin core rings before interacting with a bubble. Ring generator diameter (D_0) and bubble diameter (D_b) for the present study are 15 and 6 mm respectively.

horizontal plane. We also use a radial coordinate r from the centre of the vortex ring core while describing, for example, the vorticity distribution within the core.

2.2 Fully developed turbulent channel flow

A fully developed turbulent channel flow facility was developed for the present work with water as the fluid medium. A schematic of the facility showing its main components is shown in figure 2.2, while the dimensions can be seen from the two views shown in figure 2.3. It consists of a 2000 liter capacity PVC tank that acts as the storage unit for water as well as the exhaust unit for injected air bubbles in the channel. Water was driven through the loop by a centrifugal pump from Kirloskar Brothers, model No. KDS 515+, capable of driving up to 23 liters/sec with 6 to 15m water head and rated at 3.7KW. The RPM of the motor and hence the flow rate was controlled through a frequency controller from Integrated Electric Co. Pvt. Ltd (ISAC05M, 3 phase, 6 KVA). In order to remove residual air from the channel during the initial engagement of the pump and prevent stray air pockets, three purge lines were provided at higher locations of the channel. As bubbles tend to rise to the highest point of the channel due to buoyancy, first purge outlet was positioned at the highest point of the channel in the settling chamber. Two other outlets were provided at critical points of the channel to enable rapid and complete removal of air from the system.

From the pump, water was connected to the channel main line through a flexible rubber coupling that acts as a vibration damper, minimizing the vibrations conveyed to the channel from the pump. All subsequent sections were joined together by flange couplings using

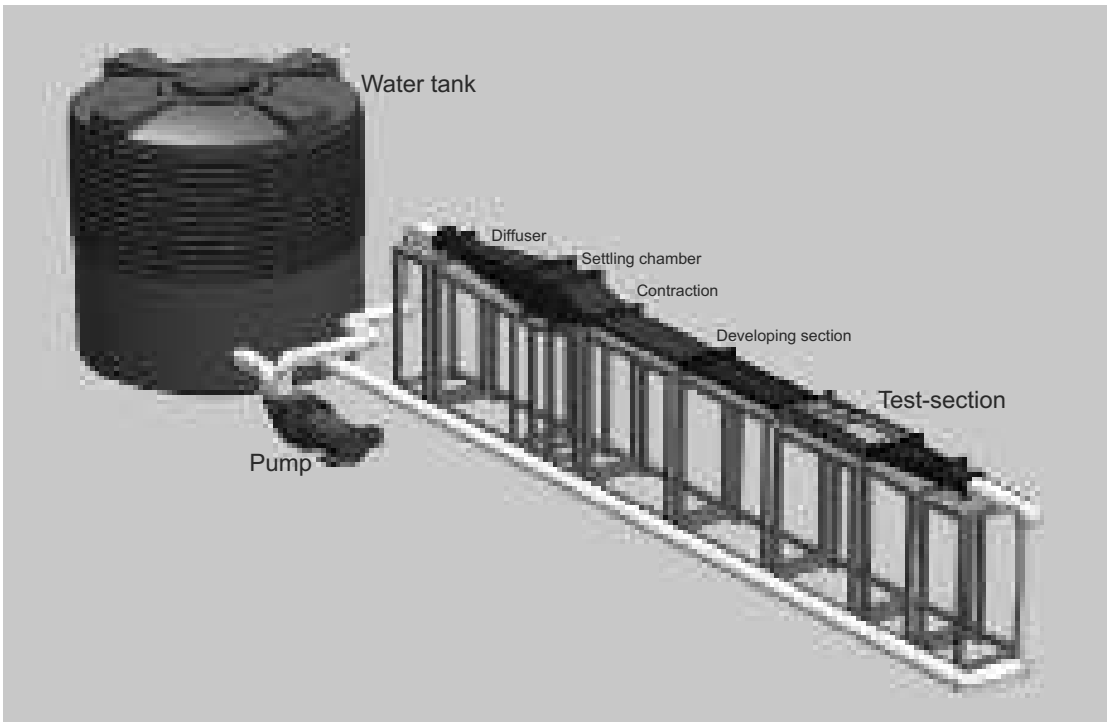

Fig. 2.2 Isometric view of the 3-D model of the fully developed horizontal turbulent channel flow facility developed for the present study.

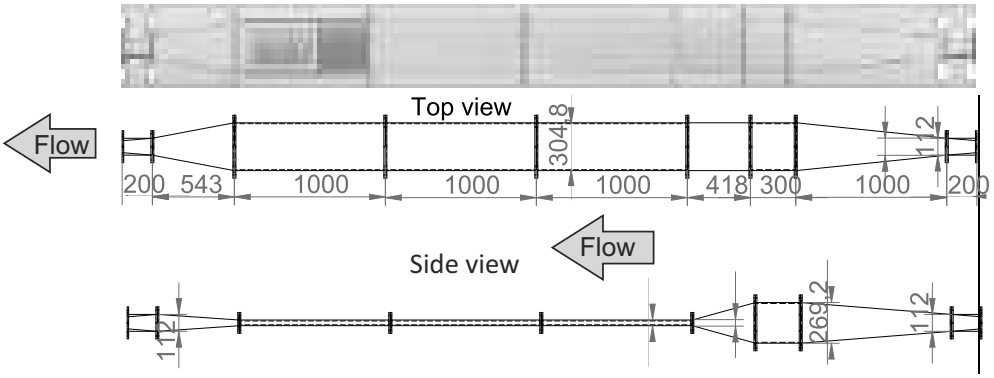

Fig. 2.3 Top and side views of the fully developed turbulent channel flow facility showing the major dimensions of the different sections of the channel.

regular hex-bolts and 1mm thick rubber gaskets to effectively seal the joints. The entire assembly was supported by a mild steel base table fixed to the ground.

The working fluid (water) from the pump enters the diffuser through a 200 mm long transformation section that transforms the cross-section from a circular one of the pipe to a square duct, as shown in the right end of figure 2.3. After this transformation section water enters a one meter long diffuser section, whose diffusing angle is kept small to minimize chances of flow separation. Water then reaches the 300 mm long settling chamber that has a rectangular cross-section section packed with 5 mm diameter straws, which is then followed by a 418 mm long convergent section. The settling unit and converging section helps in reducing incoming turbulence level prior to entry into the long development channel. The converging section is connected to a 2 meter long development channel, which is long enough to allow the flow to become fully developed by the time it enters the test-section, as will be shown later in this chapter. For measuring center-line velocity (U_c) of the undisturbed fully developed channel flow, a pitot-tube was fitted at the end of the development channel, just prior to the entry into the test-section. Measurements from this pitot tube were used to adjust the pump controller to ensure that necessary flow rate was achieved prior to any experiment with or without bubble injection. For example, if the flow rate was adjusted for the without bubble case, the pump setting had to be readjusted (increased) when bubbles were being injected to again achieve the same flow rate.

The test section was 871 mm long, 304.8 mm wide and had a height of 27.5 mm. At the time of final assembly the channel height was measured at several stream-wise and span-wise locations and variations were to be within 1.5%. The channel wall was smoothed before final assembly such that there was no large scale roughness on the surface. The test-section was made with a stainless steel framework with transparent perspex observation windows on the top, bottom and the two sides. Rubber gaskets in conjunction with screws to tighten the optical windows to the stainless steel framework were used to seal the section. In the initial (upstream) part of the test-section two porous plates were placed on both the top and bottom walls to enable bubble injection into the channel flow. Small air chambers were created on the outer side of these porous plates, which was pressurized with air from an external air source. The pressurized chambers forced air through the porous plates forming bubbles that then entered the main air flow. After the test section, water flows into a 543 mm long convergent section, which then terminates into another 200 mm long square to circular transformation section. Finally, water flows into the discharge pipeline and reaches the storage tank, from where water is drawn into the pump. A photo of the assembled and operating fully developed channel flow facility is shown in figure 2.5. For all the experiments, carrier fluid was tap water and dispersed fluid was air.

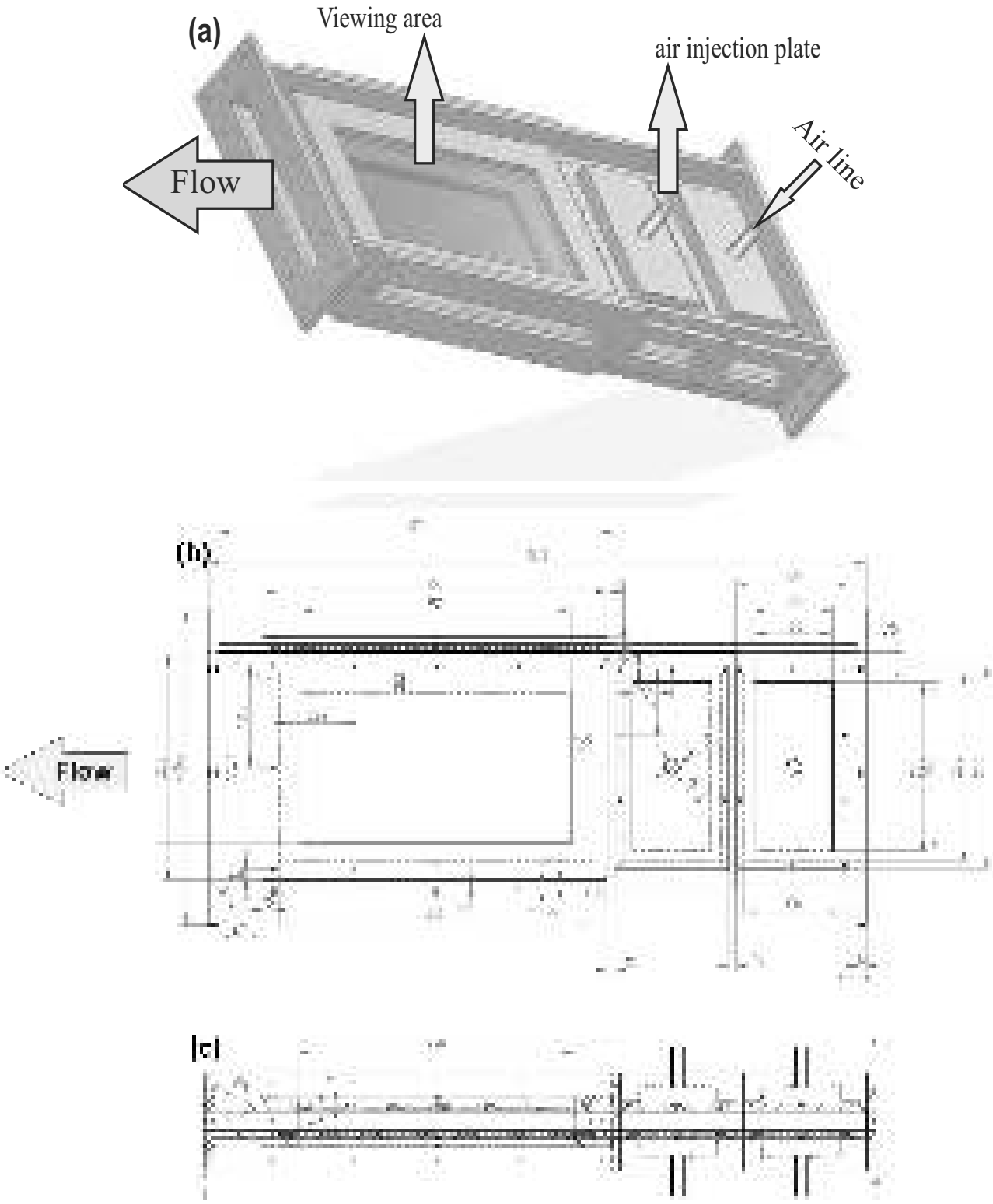

Fig. 2.4 Figure showing the test section of the fully developed turbulent channel flow. Iso view (a), Top view (b) and side view (c) are shown in the figure with dimensions.

Fig. 2.5 Photograph of the fully developed turbulent channel flow set-up.

2.3 Injection of single and multiple bubbles

2.3.1 Single bubble generation for the vortex ring-bubble interaction

Bubble of diameter D_b was generated from a small diameter tube connected to an air pump, which was placed close to the vortex ring generator. Before experiments with the vortex ring, the bubble size was measured separately from a series of zoomed in visualizations of the bubble immediately after detachment. From these experiments, the (equivalent) spherical bubble diameter (D_b) was calculated from measurements in two perpendicular planes, which gave the three axis lengths of the ellipsoidal bubble. The resulting values of equivalent bubble diameter were then averaged over about 10 runs to obtain the nominal equivalent spherical bubble diameter (D_b), which typically was found to vary by less than about 1.5% over the different runs.

2.3.2 Single bubble generation and injection in to turbulent channel flow

Single bubbles were injected into the channel from the bottom wall at the mid-section of the span of the test-section through a transparent water-filled pipe of 3 mm internal diameter. A bubble of 1.5 to 2mm diameter was generated in the pipe using a simple syringe. Schematic of the complete injection mechanism is shown in figure 2.6. Once the bubble was detached from the needle of the syringe, it rises slowly in the pipe due to buoyancy and enters the channel from the bottom wall and comes in contact with the flow. The actual bubble diameter in the flow is then decided by the incoming turbulence and the surface tension. We find that the interaction results in bubble diameters ranging from 0.2 to 1.5 mm in the flow. For the top wall injection of a single bubble, a similar system was employed, except that the bubble after detachment within the pipe needed to be pushed into the channel with a very small flow rate in the connecting pipe.

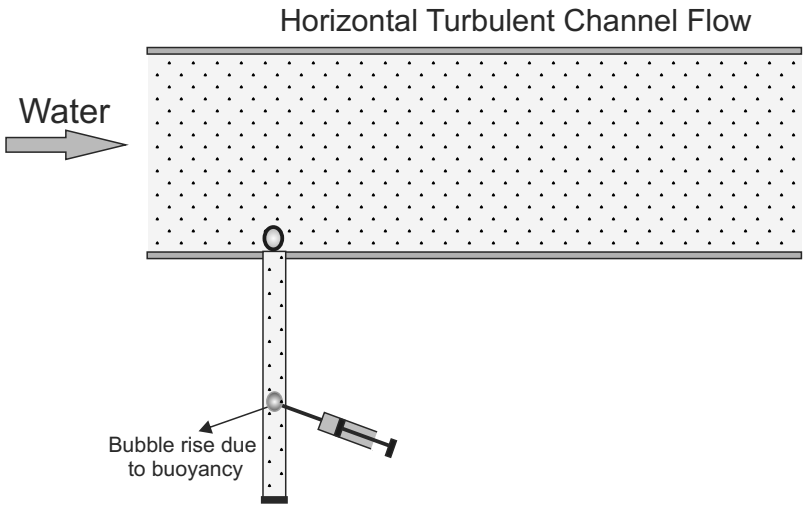

Fig. 2.6 Schematic showing single bubble generation and injection for interaction with eddies in turbulent channel flow.

2.3.3 Multiple bubble injection in turbulent channel flow

Inside the test section two porous plates were placed at the top and bottom walls for bubble injection, as shown in the schematics and drawings in figure 2.4. The porous plates were procured from Puronics system, Bangalore, and were made up of bronze spherical balls sintered at high temperature. The mean equivalent ball diameter used was 30 μm resulting in a mean pore size of about 10 μm with 33% porosity. A zoomed in optical image of the porous plate, and bubble generation through it is shown in figure 2.7(a) and (b), respectively. The porous-plates were placed in a cavity within the wall of the test section and firmly fitted

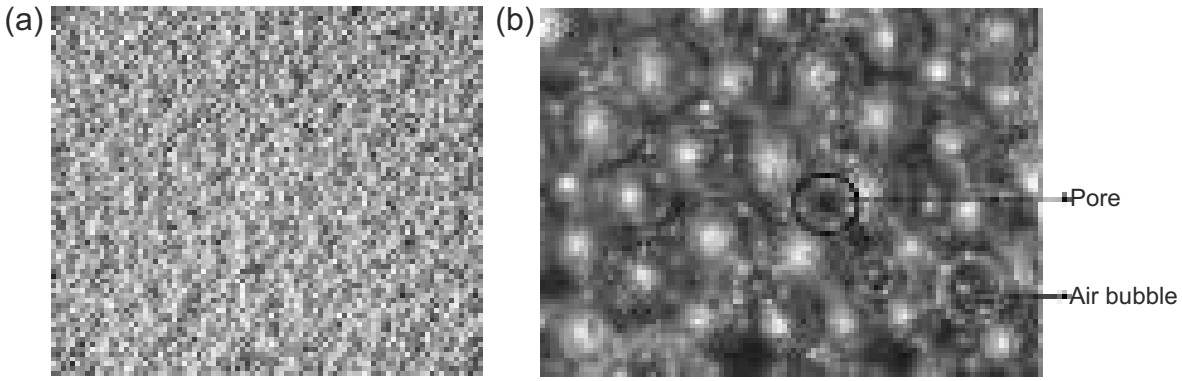

Fig. 2.7 Optical zoomed in images taken with a microscope of (a) the porous sintered plate, and (b) the air bubbles formed as air is pushed through the porous plate.

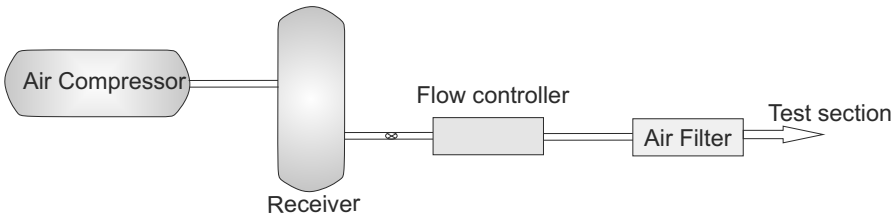

Fig. 2.8 Schematics of air supply line from compressor to the test-section.

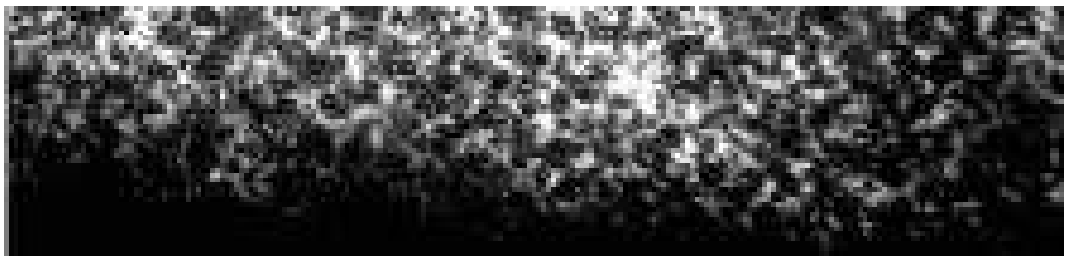

Fig. 2.9 Bubble visualisation at bottom wall porous plate at a channel Reynolds number of 67,500.

by a cadmium coated holding-plate. In order to avoid any stray bubbling from the edges of the porous plate, the face of the plate (from the extended edge) was coated with a thin layer of araldite. The sintered porous plates were pressurized through air chambers, and bubbles were generated as the air was pushed through the pores of the plate in to the flowing water in the channel. Each of these porous plates was 100mm wide, 250mm long and 10 mm thick. The details of the air supply used to supply pressurized air to the air chambers with porous plates is shown in figure 2.4a. Air was first compressed by an air compressor and was passed through a drier and oil filter before storing in a large receiver. An Alicat Scientific (Serial 92944) air-flow controller was used to supply a measured amount of air as shown in figure 2.8. The controller was used to vary and measure the flow rate of air injected in to the channel through the air chambers and porous plates. Visualization of the generated bubbles close to the surface of the bottom wall porous plate is shown in figure 2.9 at channel Reynolds number of 67,500, the bubble diameter varying from 100 to 400 μm.

2.4 Instrumentation and measurements

In the present work, we have extensively used high speed imaging of the bubble along with time-resolved Particle Image Velocimetry measurements of the flow. In chapter 5, extensive pressure drop measurements have been done to assess the impact of injection of a large

number of bubbles in to a turbulent channel. The following sub-sections give details of the measurement techniques used.

2.4.1 High speed bubble imaging

Top and front views of the bubble-vortex ring interaction were captured using a high speed Photron SA5 camera at framing rates of about 2000 fps with an exposure time of about 1/4000 sec. These two views were captured independently due to the different illumination requirements, after ensuring that the broad features were repeatable. Illumination for the bubble dynamics visualization was done with a high intensity halogen lamp. Apart from the bubble dynamics, the front view could also be directly used to measure the vertical location of the vortex ring with time. For the purpose of vertical location measurement of the ring, a relatively large field of view of about 300 mm $\times$ 300 mm was used, while a zoomed in field of view of about 50 mm $\times$ 50 mm was used to capture the details of entrainment of the bubble into the ring.

In the turbulent channel experiments, the bubble dynamics were imaged from both the top and front views simultaneously using two Phantom Miro-M110 cameras. Both the cameras were triggered simultaneously by a function generator (Stanford research system) at a framing rate of 1600 fps and exposure time of about 5 μsec. The cameras field of view for the side imaging was about 55 mm, while in the top view it was about 55 mm for the single bubble injection studies and 140 mm for the multiple bubble injection studies. A 1000 W halogen lamp was used in conjunction with a diffuser sheet to achieve uniform background illumination.

2.4.2 Time Resolved Particle Image Velocimetry (TRPIV)

Velocity and vorticity fields were obtained from time resolved PIV measurements for vortex ring-bubble injection and single bubble injection in turbulent channel flow studies. PIV was done at repetition rates between 1000 to 5000 Hz. For this purpose, the flow was seeded with silver coated hollow glass spheres with a mean diameter of about 14 microns. The seed particles were illuminated by a laser sheet from a high repetition double-pulsed LDY-301 Litron PIV laser with a maximum energy of 10 mJ/pulse. Delay between two laser pulses was typically about 0.2 ms, decided by the requirement to keep the mean pixel displacement to be about $1/4^{th}$ of the correlation box size. PIV images were captured using a Photron SA5 high speed camera with a resolution of 1024 $\times$ 1024 pixels. The images obtained had scattered light from both the relatively small seed particles and the larger bubble. The light from the bubble was masked out prior to PIV processing. The resulting image contained only

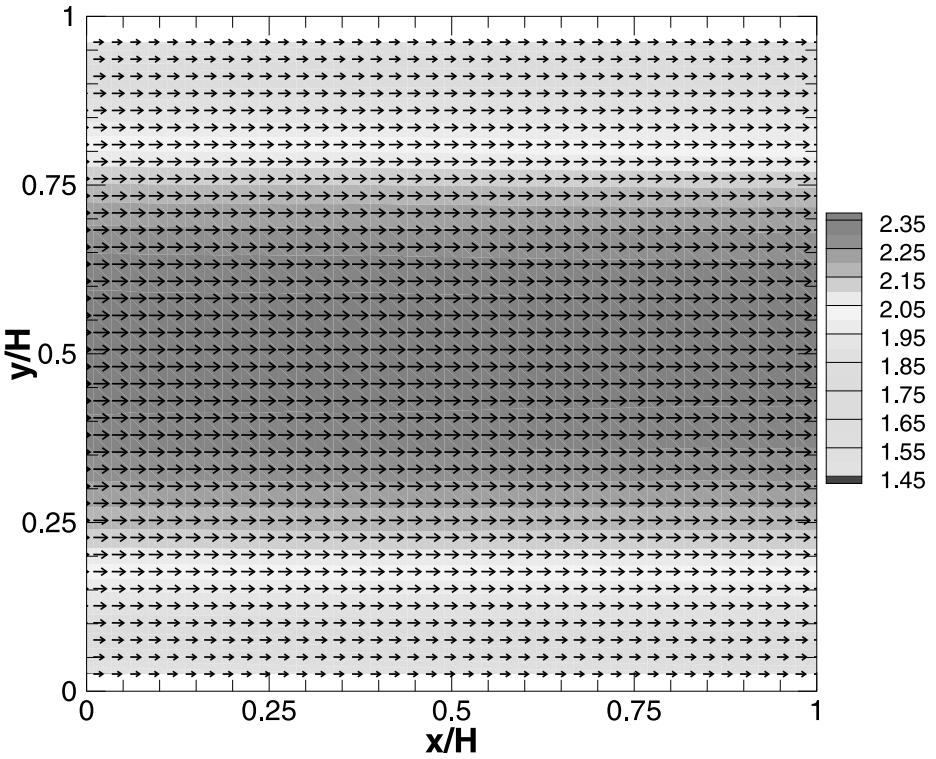

Fig. 2.10 Mean velocity field in the fully developed turbulent channel at a Reynolds number of 67,500. The mean field was obtained from averaging 2000 instantaneous PIV fields. Apart from the mean vectors, the mean stream-wise velocity contours (in m/s) are also shown. In the figure, the stream-wise (x) and wall-normal (y) directions are normalized by the channel height(H).

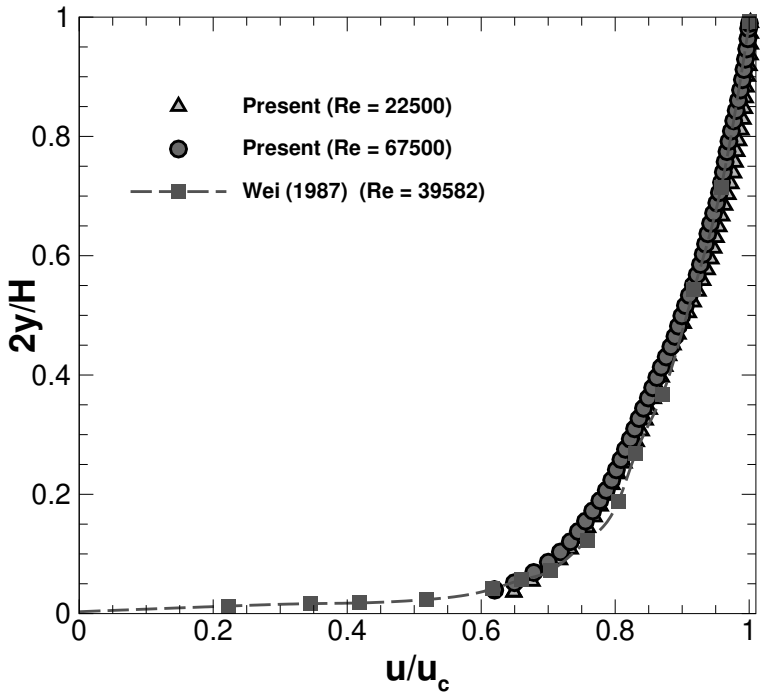

Fig. 2.11 Mean stream-wise velocity (u) profile across the channel height measured using PIV. Present measurements at two channel Reynolds numbers are compared with the measurements of Wei (1987) at Re=39,582. In the figure, the stream-wise velocity is normalized by the center-line velocity, while the vertical distance is normalized by the half-channel height (h). For comparison and validation, the data from Wei [86] for two-dimensional fully developed turbulent plane-channel flow is also shown in the figure, with reasonable agreement between that data and ours.

scattered light from seed particles, which was typically unaffected by the scattered light from the bubble. In a few cases, bubble scattering/reflections were found to be strongly affecting the image of nearby seed particles, and these images were not processed. The resulting images were then processed with Dantec PIV software using adaptive correlation with 2 step box size refinement with the final box size being 32 $\times$ 32 pixels and 16 $\times$ 16 pixels for the thin and thick core rings, respectively. Correlation box overlap was maintained at 50% in all cases, with each box having roughly at least 6 to 8 particles to ensure strong correlations.

2.4.3 Pressure drop measurement in channel

In fully developed channel flow, wall drag can be directly calculated from the measured pressure drop by force balance on a control volume. Hence, pressure drop was measured to study the effect of bubbles on flow drag in turbulent channel flow. It was measured using a Ashcroft pressure sensor (GC52; Wet/Wet Differential Pressure) having response time of 100 msec and range of 0 to 4 inches of water column. The pressure drop was measured between two stream-wise locations separated by a stream-wise distance of 332 mm. This was done at different vertical locations across the channel height, as the pressure drop was found to vary significantly with vertical location, as will be discussed in chapter 5.

2.5 Characterization of fully developed horizontal turbulent channel flow

Particle image velocimetry (PIV) and pressure drop measurements were done for the fully developed turbulent channel without bubbles to validate the base case flow field. For PIV measurements, the field of view used was 4cm X 4cm, to enable flow field measurements with good resolution. For the mean velocity field, we take the average of 2000 instantaneous flow fields, and this is shown in figure 2.10. The figure shows both the mean vector field as well as the mean stream-wise velocity contours. As seen in the figure, the flow is fully developed with almost no variation in the mean velocity field in the stream-wise (x) direction. There is, as expected, only a variation in the wall-normal (y) direction, which is shown in figure 2.11. The mean stream-wise velocity profile in this plot is normalized by the centre-line velocity (u_c), and is shown at two channel Reynolds numbers. For comparison and validation, the data from Wei [86] for two-dimensional fully developed turbulent plane-channel flow is also shown in the figure, with reasonable agreement between that data and ours. Figure 2.12 shows the mean streamwise velocity profile in the traditional log-law form above the buffer

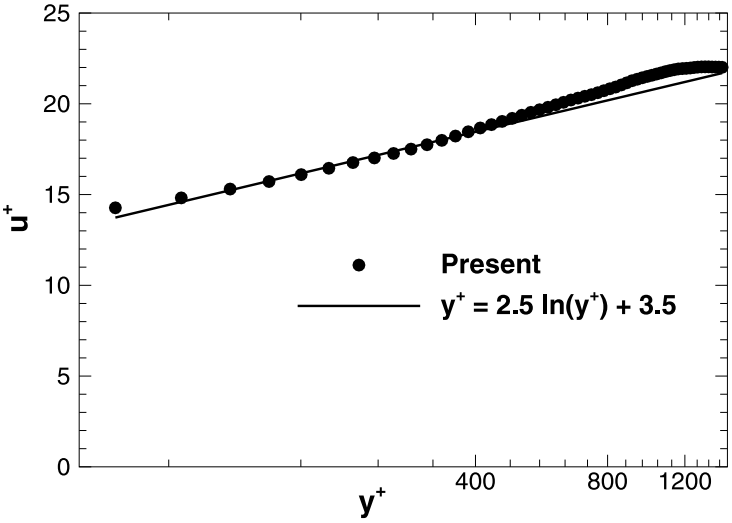

Fig. 2.12 Stream-wise mean velocity profile in the traditional log-law form for flow *Re* of 67500 at bottom wall of the channel. Von Karman and additive constant is also shown in the plot. For comparison and validation, the data from Wei and Willmarth [87] for two-dimensional fully developed turbulent plane-channel flow is also shown, with reasonable agreement between that data and ours.

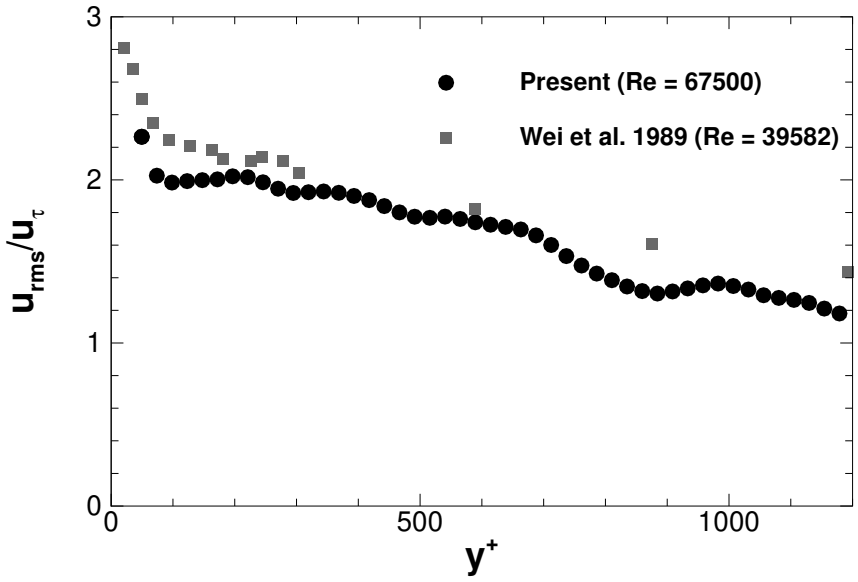

Fig. 2.13 Stream-wise turbulent intensity profile, non-dimensionalised by friction velocity plotted with vertical distance scaled by inner length scale (u_τ/ν). For comparison and validation, the data from Wei and Willmarth [87] for two-dimensional fully developed turbulent plane-channel flow is also shown, with reasonable agreement between that data and ours.

region. For log law of the wall, Von Karman constant and additive constant is 0.4 and 3.5 respectively, which is very similar to the high resolution data of [89].

After presenting the mean flow field, we now proceed to show the fluctuating flow quantities along with corresponding prior experimental data for fully developed turbulent channel flow. Stream-wise turbulent intensity profile scaled by friction velocity (u_τ) is plotted against vertical height non-dimensionalised by inner wall length scale ($y^+ = yu_\tau/\nu$) as shown in figure 2.13. This data has reasonable match with Wei and Willmarth [87] as seen in figure. Reynolds stress is scaled with u_τ^2 and plotted against y/H in figure 2.14. It can be observed in the plot that trend of Reynolds stress distribution is similar to Wei and Willmarth [87] but absolute value has some differences. This difference is probably due to the effect of Reynolds number on distribution [87] or limitation of spatial resolution in PIV. Present values are consistently low as compared to Wei and Willmarth[87], which may be probably due to the inability of PIV to capture the smallest scale in the flow [16].

The pressure drop was measured by differential pressure sensor as discussed earlier. Then, the wall shear stress was estimated from the pressure drop and it was used for C_f calculation. Variation of C_f with flow *Re* is plotted in figure 2.15 along with well established empirical relation given by Dean [15]. Experimental uncertainty in C_f is also plotted to get an estimate

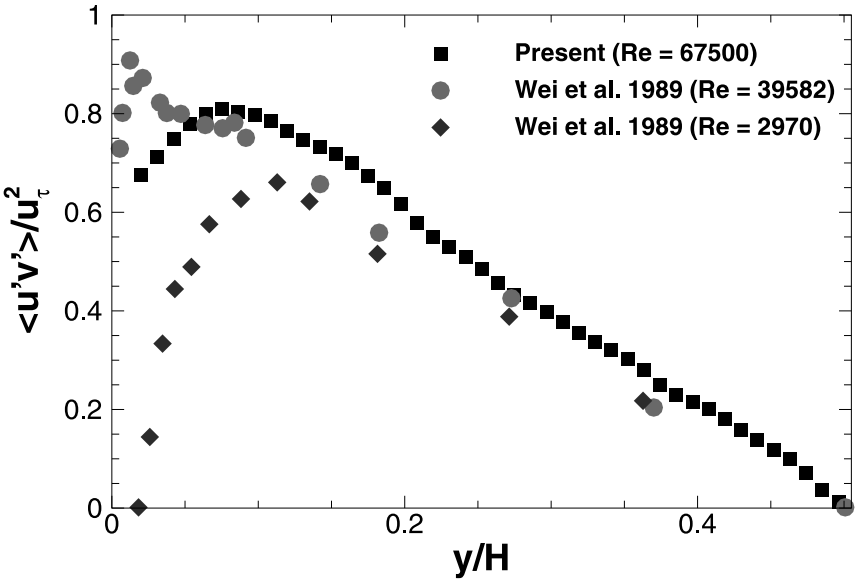

Fig. 2.14 Variation of Reynolds stress non-dimensinalised by friction velocity with respect to wall normal distance scaled by channel height (H).

of confidence in the measured skin friction co-efficient. From the plot, it is obvious that it can measure skin friction with reasonable accuracy.

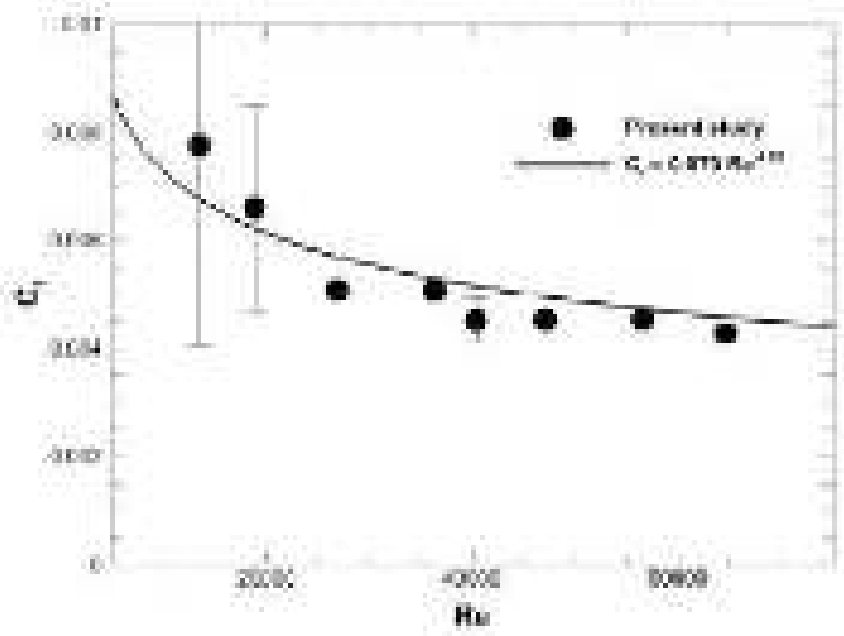

Fig. 2.15 Dependence of wall shear stress on flow *Re* plotted along with Dean [15]. It matches reasonably well with empirical relation.

Chapter 3

Interaction of a vortex ring with a single bubble: Bubble and vorticity dynamics

"Nature is our kindest friend and best critic in experimental science if we only allow her intimations to fall unbiased on our minds."

- Michael Faraday

In this chapter, we study the idealized case of the interaction of a single bubble with a single vortex ring. This may be thought of as a simplified case of the interaction of bubbles with for example the hairpin structures seen in turbulent boundary layers, or indeed of vortical structures in any turbulent flow. As part of this study, we are interested in, and shall present results from both the bubble dynamics perspective, as well as the modifications induced in the vortex ring due to the interaction.

The parameters in this interaction problem comprise naturally the properties quantifying the vortex ring and the bubble. Figure 3.1) shows the schematic presentation of a vortex ring approaching towards a bubble and parameters for this interaction. On the vortex ring side, this encompasses, the circulation (Γ), the vortex ring radius (R), the equivalent vortex core radius (a), the latter being represented by the non-dimensional core radius ($\varepsilon = a/R$), and there is also the ring Reynolds number, $Re = \Gamma/\nu$ (ν = kinematic viscosity). On the bubble side, there is the equivalent spherical bubble diameter (D_b) and the surface tension (σ). In terms of the interaction between the ring and the bubble, the two main parameters are the ratio of the bubble volume to vortex core volume ($V_R = (\pi {D_b}^3/6)/(2\pi^2 R a^2)$), and the Weber number (We) based on the circulation strength of the ring (Γ). We define here the We as $We = 0.87\rho(\Gamma/2\pi a)^2/(\sigma/D_b)$, along the lines used in Oweis et al. [63], which may be thought of as the ratio of the pressure difference ($\Delta P = 0.87\rho(\Gamma/2\pi a)^2$) between the vortex core and the far field to the Laplace pressure (σ/D_b) for a spherical bubble. In our studies, V_R

is kept fixed at about 0.1, this being representative of the kind of volume ratio (bubble volume to eddy core volume) seen in bubbly turbulent boundary layers used in drag reduction studies, as discussed later. The *We* number is varied by changing the circulation (Γ), and the effect of changes in the non-dimensional core radius (ε) is also presented. In our experiments, the vortex ring of radius (R) is generated by using a piston-cylinder arrangement in water, and the bubble is generated by a capillary connected to an air pump. The ring travels vertically upwards while interacting with the bubble.

The layout of the chapter is as follows. In section 3.1, we present results for the initial stages of interaction from both the bubble dynamics and vorticity dynamics perspective. This includes the bubble capture, bubble expansion and vorticity field modification processes for different vortex ring strengths (Γ), or equivalently the *We*. In section 3.2, we present results for the later stages of interaction, where the bubble has already been broken down into a set of smaller bubbles, and the bubble has reached a quasi-steady state with the smaller bubbles no longer breaking-up. We present here the vorticity distribution in the cores at this later stage, including integral measures of it such as the circulation and enstrophy. This is followed by section 3.3, where we present results for the interactions of a bubble with a thicker vortex ring $(\varepsilon \sim 0.75)$, where the results can be even more dramatic compared to the thinner core rings $(\varepsilon \sim 0.25)$ discussed in sections 3.1 and 3.2. The possible physical mechanisms for the observed reduction in convection speed and fragmentation of the vortex core and the relevance of the present experiments to drag reduction through bubble injection in turbulent flows are discussed in section 3.4.

3.1 Thin core rings: Initial stages of interaction

We begin by presenting an interaction between a bubble and a vortex ring at large *We* to show the type of effects that can occur before presenting more detailed results in later sections. For this case, the ring diameter $(2R)$ is about 23 mm, ring core radius (a) is about 3 mm, its circulation (Γ) is about 245 cm^2/s, and the bubble size (D_b) is about 6 mm, which results in a bubble to vortex core volume ratio (V_R) of about 0.1 and corresponds to a reasonably large Weber number of 131. We present in figures 3.2 and 3.3, time sequences of the top and front view of the bubble dynamics from two independent experiments, to get a three-dimensional perspective of the interaction. In order to visualize the vortex ring, micron sized air bubbles are generated at the metallic tip of the vortex generator by electrolysis, these bubbles being much smaller than the millimeter sized main bubble of diameter D_b. In figure 3.2(a) and 3.3(a), one can see the bubble outside the ring just as the interactions begin. The bubble is then entrained into the low pressure vortex core of the ring following a spiral

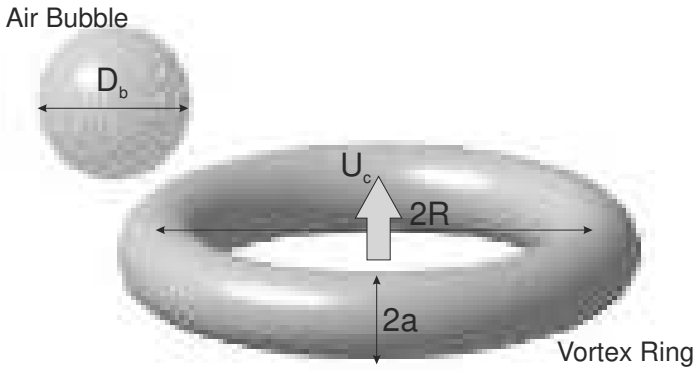

Fig. 3.1 Schematic showing the experimental set-up and the main parameters of the vortex ring and bubble. The resulting vortex ring has radius R with core size a and convects vertically upwards with convection velocity U_c, while the bubble is of size D_b.

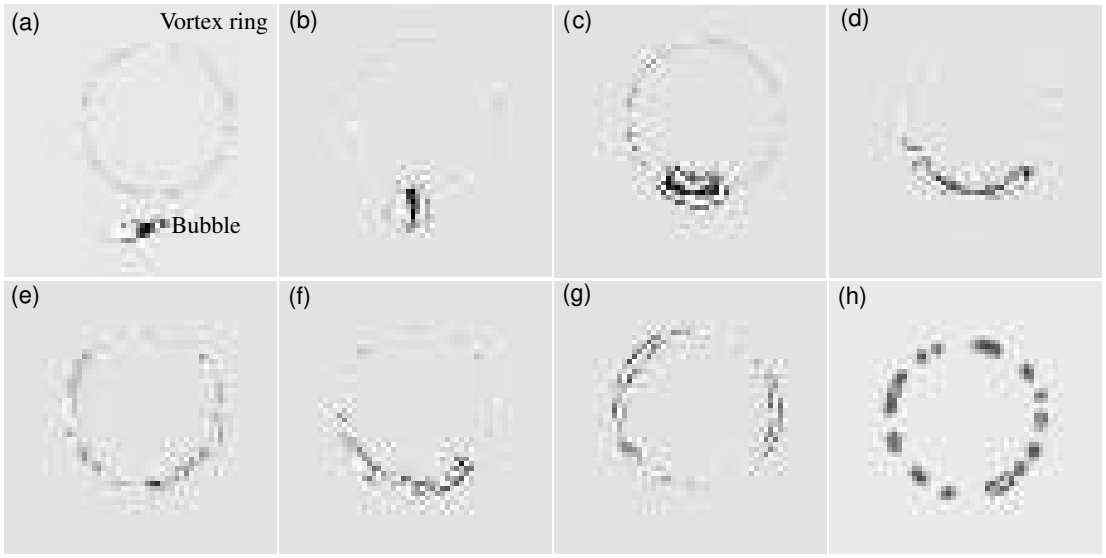

Fig. 3.2 Time sequence of top view visualization images showing the interaction of a single bubble with a vortex ring. In this case, the bubble diameter D_b is 6 mm, the vortex ring circulation Γ is 245 cm^2/s with ring Re of 29900 and the corresponding Weber number ($We = 0.87\rho(\Gamma/2\pi a)^2/(\sigma/D_b)$) is 131. The non-dimensional time ($t^* = tU_c/R$) corresponding to each of the images shown is (a) 3.36, (b) 3.93, (c) 4.37, (d) 4.63, (e) 6.09, (f) 7.17, (g) 8.98 and (h) 12.37, where U_c and R are the convection speed and radius of the ring before interaction with the bubble.

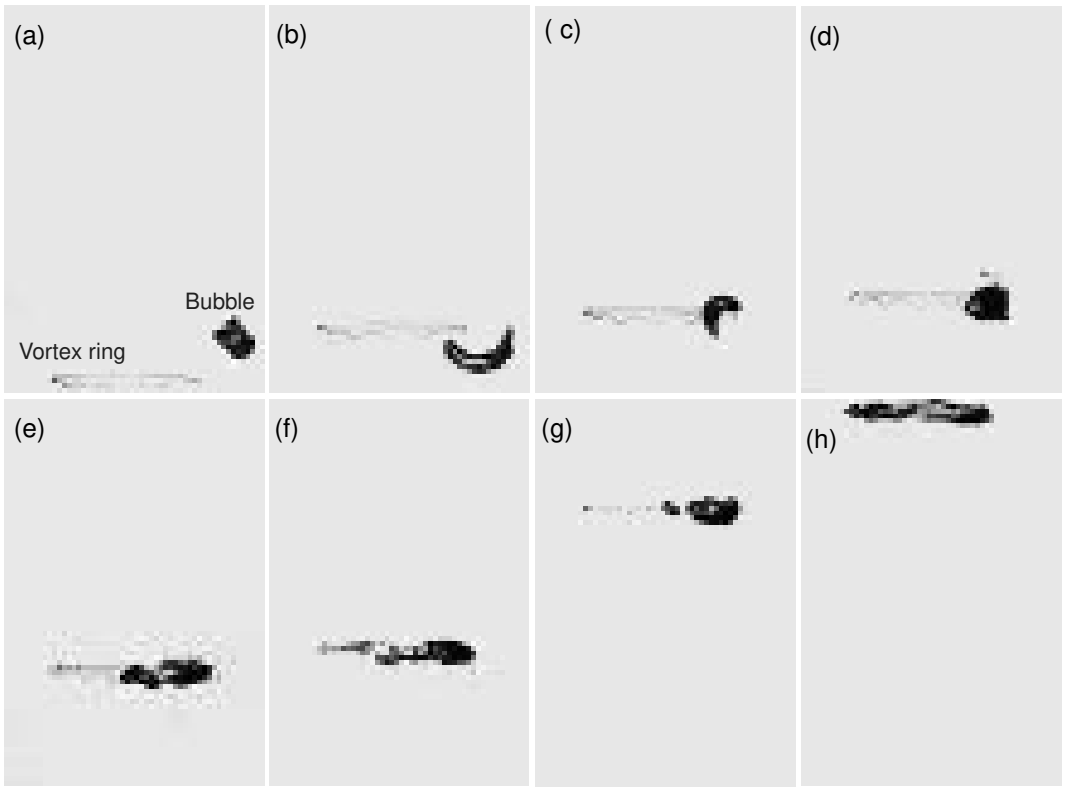

Fig. 3.3 Time sequence of side view visualization images showing the interaction of a single bubble with a vortex ring. All parameters are same as in figure 1. The non-dimensional time ($t^* = tU_c/R$) corresponding to each of the images shown is (a) 3.36, (b) 3.99, (c) 4.28, (d) 4.44, (e) 4.72, (f) 6.06, (g) 7.13 and (h) 8.88.

path, with the bubble being elongated along the spiral path, as seen in 3.2(b) and 3.3(b) & (c). Once the bubble enters into the core completely, it starts expanding in the azimuthal direction along the core, as seen in 3.2(c) to (e) and also 3.3(d) to (f). This is followed by a contraction of the bubble in 3.2(f) and re-expansion in 3.2(g) & 3.3(h). During this time, surface perturbations can be seen to be growing on the bubble, which leads to progressive break-up of the initial bubble. Given sufficient time this leads to the state shown in 3.2(h) comprising of a set of smaller bubbles of roughly equal size, which does not further break-up. As seen in figure 2, the ring convects vertically upwards during this entire interaction with convection speed, this speed being a good indicator of the coherence of the vortex ring. We shall see later that the convection speed can be significantly reduced by the interactions.

Observation of bubble dynamics is accompanied by the measurement of the principal azimuthal vorticity of the vortex ring using 2D time resolved PIV, as shown in figure 3.4. In these plots, the bubble is marked as a hatched area with magenta colour (online). Figure 3.4(a) shows the vortex ring before the interactions with the bubble begin. In (b), the bubble is

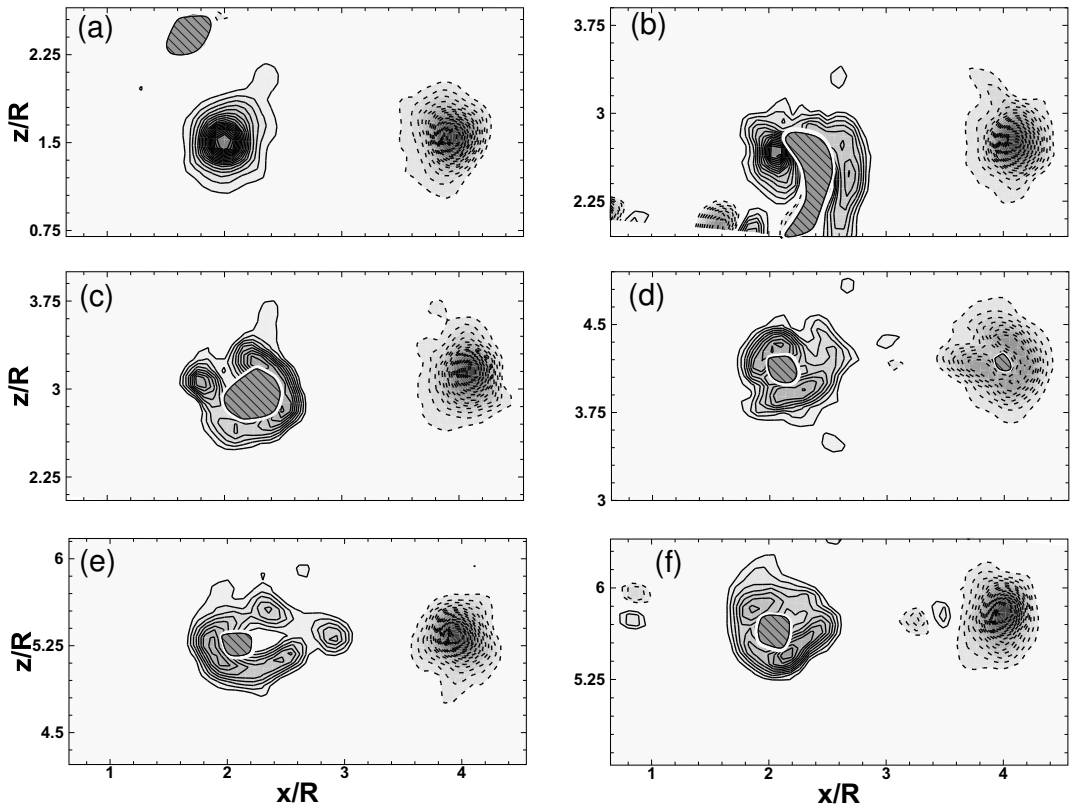

Fig. 3.4 (Colour online) Time sequence of principal azimuthal vorticity within the ring measured using time-resolved PIV showing the interaction of a single bubble with a vortex ring. In each image, the bubble is marked as a hatched area with magenta colour. Solid and dashed line contours represent positive and negative signs of vorticity, respectively. The non-dimensional time ($t^* = tU_c/R$) corresponding to each of the images shown is (a) 3.3, (b) 3.99, (c) 4.37, (d) 5.96, (e) 7.04 and (f) 8.75. All parameters are same as in figures 1 and 2. Non-dimensional vorticity contour levels ($\omega R/U_c$) shown are $\pm 1.57, 2.75, 3.93, ...$

elongated as it is being entrained into the ring, with significant distortion of the vortex core. After entrainment in (c), the bubble sits in the centre of the vortex core, and vorticity at this instant is distributed like an annulus outside the bubble. The bubble then gets elongated azimuthally along the ring, so that the bubble cross-sectional area reduces in the core on the left in (d), with the stretched out bubble being also visible in the right side (dashed) core in (d) with some resultant modification to this core. Figure 3.4(e) and (f) show the vorticity contours for minimum azimuthal shrinkage and maximum re-expansion of the bubble. As may be seen from these set of plots, significant changes can occur in the vorticity distribution within the core, which can in turn lead to a significant reduction in the convection speed of the ring as we shall see later.

In all cases presented in this and the following section, the non dimensional core radius (ε) was about 0.25, which we refer to as thin, in comparison with the thicker core ring (ε = 0.75) results presented in section 3.3. The vortex ring in the present experiment convects vertically upwards, and its vertical position (z) as a function of time (t) can easily be tracked from side view visualizations. The circulation (Γ) of the vortex ring has been systematically varied in the experiments, while keeping the bubble size (D_b) fixed, resulting in a relatively large range of Weber numbers ($We = 0.87\rho(\Gamma/2\pi a)^2/(\sigma/D_b)$) from 3 to 406.

We present in figure 3.5 an overview plot showing the normalized vertical position (z/R) of the vortex ring as it interacts with the bubble for different *We* (or Γ) cases. The data (solid symbols) is plotted versus time normalized by the vortex ring time-scale (R/U_c), where U_c and R are the convection speed and ring radius of the baseline ring at initial time. Also, shown in the inset with open symbols is the data for the respective base line cases for the vortex ring (with same Γ) in the absence of the bubble. As one might expect, in the absence of the bubble, the ring location for all the different cases studied collapses onto a single line, which also agrees well with the viscous vortex ring model of Fukumoto and Moffatt [25], also shown in the inset by a dashed line. This same dashed line representing the baseline cases is also shown in the main plot for reference. The interacting case data in the main plot includes the entire time of interaction between the vortex ring and the bubble starting from entrainment of the bubble into the ring, bubble break-up and in some cases bubble escape from the ring. This figure is therefore useful to delineate the different stages in the interaction, and accordingly we demarcate four broad stages in the interaction. In stage I, at the bottom left corner of the plot, the bubble is outside the ring, as in figure 3.2(a) & (b), and is drawn in towards the vortex ring. Entrainment of the bubble into the ring occurs at the line demarcating stage I and II. Within stage II, the bubble elongates in the azimuthal direction along the core, followed by contraction and then begins to gradually break-up into a set of smaller bubbles, as in figure 3.2(c to g). In stage III, the break-up is complete and the set of

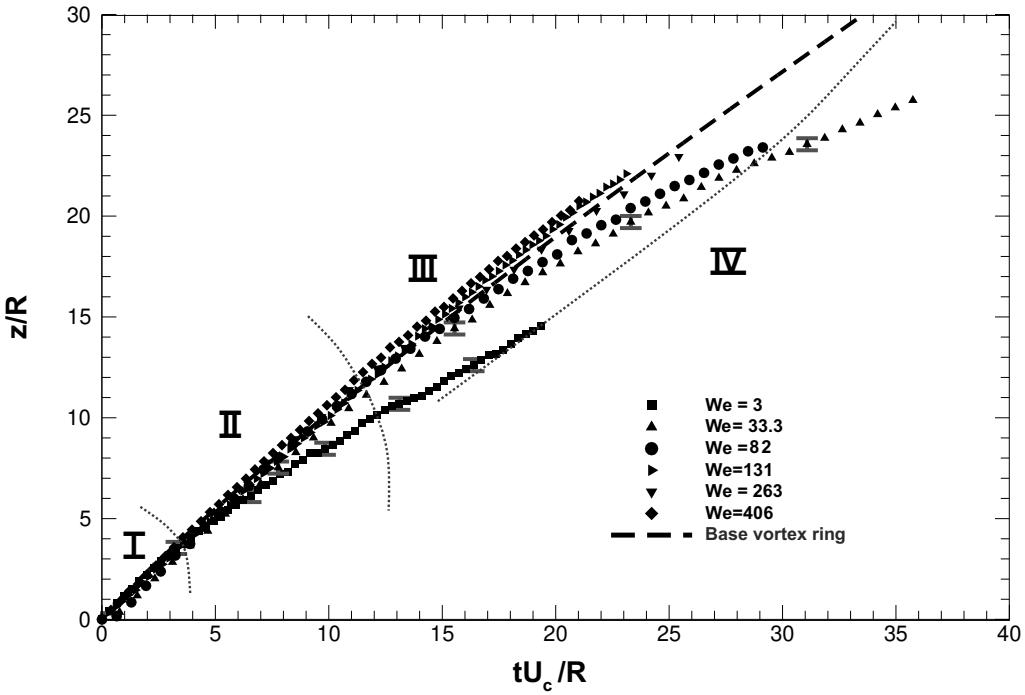

Fig. 3.5 Plot showing the vertical position (z/R) of the vortex ring as a function of time when the ring is interacting with a bubble of diameter (D_b). Results are shown for 6 vortex ring strengths (Γ) represented in terms of a Weber number, $(We = (0.87\rho(\Gamma/2\pi a)^2/(\sigma/D_b))$. The inset shows the motion of the same rings in the absence of the bubble. The plot is used to demarcate four stages (I, II, III and IV) during the interaction of the bubble and vortex ring. Data for the ring interacting with the bubble is shown in the main plot with filled symbols, while the corresponding open symbols shown in the inset represent the motion of the same ring in the absence of the bubble. ■, *We* = 3, *Re* = 3430; ▲, *We* = 33.3, *Re* = 11900; ●, *We* = 82, *Re* = 21200; ►, *We* = 131, *Re* = 29900; ▼, *We* = 263, *Re* = 45200; ♦, *We* = 406, *Re* = 61500; −−, Base vortex ring.

smaller broken bubbles slowly move around in the azimuthal direction within the ring (figure 3.2(h)). In some cases, as we shall see later, the bubbles eventually escape from the ring, and this is denoted as stage IV, with the line between the two demarcating the time of escape. It may be noted that the data shown for each of the vortex ring cases with and without bubble in figure 3.5 were obtained as an average of three independent runs with variation between runs being indicated by error bars at certain locations, which is seen to be about $0.5R$. The convective speed at any given instant normalized by the initial convection speed may be easily ascertained from figure 3.5 as the slope of the position-time data shown."

One of the most striking features visible from the plot is the difference between low and high *We* number interactions. In high *We* cases, like *We* = 131 shown in figure 3.2, the differences in vertical location between the vortex ring that is interacting with the bubble

(►) and the baseline ring in the absence of the bubble, represented by the dashed line, is very small. As the *We* is decreased, the difference in convection speed and hence the vertical location between the interacting ring and the baseline ring increases. In particular, in the*We* of 3 case, there is a very significant drop (about 30%) in the convection speed of the ring at later times when it is interacting with a bubble. This is a first indication that the interaction between the bubble and the ring is having a significant impact on the vortex ring as well. As the small *We* indicates, the significant impact on the vortex ring occurs when the surface tension forces are comparable to the inertial forces. We shall discuss this in more detail later in this section.

We shall present in the rest of this section, results from both the bubble dynamics and vortex dynamics perspective of the initial stages of interaction comprising stages I and I, while stages III and IV are discussed in the next section.

3.1.1 Bubble Dynamics

We now begin by presenting results from the bubble dynamics perspective for the initial stages of interaction comprising stages I and II. We shall present here visualizations and analysis of the processes of bubble entrainment into the ring, and its subsequent deformations leading to break-up, as a function of the vortex ring strength or equivalently the Weber number (*We*).

Bubble capture by the vortex ring (Stage I)

Bubble capture is the beginning of the vortex ring-bubble interaction. The low pressure within the core of the vortex ring induces motion of the bubble into the vortex core in a spiralling path, as seen in figures 3.2 and 3.3. During this capture process, the bubble undergoes extreme elongation and wraps itself around the core, before reaching an equilibrium radial position within the vortex core. This type of bubble capture process has been observed for example in the numerical study of Chahine [10], and in the experiments of Oweis et al. [63] and Sridhar and Katz [73].

An important quantity related to the capture process is the capture time (t_c) of the bubble. We define this capture time (t_c) here along the lines of Oweis et al. [63], as the time taken for the bubble to move to a location within the core ($r = a/4$) from an initial radial location $r = 3a$ from the centre of the core (a=core radius). We have experimentally measured this capture time (t_c) from time sequences of the bubble visualization (as in figure 3.3) for the different *We* number cases, and this is shown in figure 3.6 by the solid symbols. The data in the figure is normalized by the vortex ring time-scale (R/U_c) and also includes error bars

obtained from three repetitions of the experiment. We find as one might expect that the capture time (t_c) decreases as the ring circulation or *We* is increased.

The capture time can be modelled by doing a radial balance of the dominant forces acting on the bubble, as done for example by Oweis et al. [63]. Along their lines, we neglect the bubble acceleration and shear lift force in this balance, as these are small compared to the pressure gradient and drag induced forces, due to the low air density and the negligible vorticity outside the vortex core, respectively. Hence, the radial force balance reduces to a balance between the pressure gradient induced force (F_P) and the drag force (F_D) on the bubble outside the vortex core. Further, assuming that the largest component of bubble velocity is in the radial direction $(u_{b,r})$, the radial force balance can be written as:

$$\frac{\rho u_\theta^2 V_b}{r} = \frac{1}{2}\rho C_D \left(\frac{\pi}{4}\right) D_b^2 u_{b,r}^2 \tag{3.1}$$

where u_θ is the azimuthal bubble velocity and V_b is the bubble volume. In our case, where we consider a relatively thin vortex ring, the azimuthal velocity u_θ may be approximated by the induced velocity of a line Gaussian vortex. The radial velocity, $u_{b,r}$, at any given radial location (r), can then be obtained from the above radial equilibrium equation using an appropriate expression for C_D valid over a large range of bubble Reynolds numbers $(Re_b = u_{b,r}D_b/\nu)$, $C_D = (24/Re_b)\left(1 + 0.197Re_b^{0.63} + 0.00026Re_b^{1.38}\right)$ [32]. The capture time (t_c) can then be found by integration of the thus obtained radial velocity $(u_{b,r})$ from an initial location, $r = 3a$, to $r = a/4$.

The above simple model is similar to that of Oweis et al. [63], except for the fact that we use a more complete expression for C_D due to the much larger bubble Reynolds numbers (Re_b) in our study. The capture time (t_c) can be evaluated from this model given the bubble size (D_b), the vortex strength (Γ), and its core size (a). Shown in figure 3.6 in open symbols is the capture time (t_c) evaluated using this model. As may be seen from the figure, the qualitative trend of the values obtained from this simple model are in reasonable agreement with the experimental values. The quantitative values are however not close, with the model always under-predicting the experimental values, this being similar to the case in Oweis et al. [63]. We find that at low *We*, the model gives values about 25% lower than the measured values, while at higher *We*, the difference increases to about 50%, consistent with the fact that bubble deformations that have not been modeled, increase with *We*. Besides bubble deformations, the observed differences are also likely linked to other features observed in the experiments that have not been modeled. This includes, for example, the effects of added mass and lift forces that become more important as the bubble approaches the vortex core [63], apart from the fact that the bubble modifies the vorticity distribution.

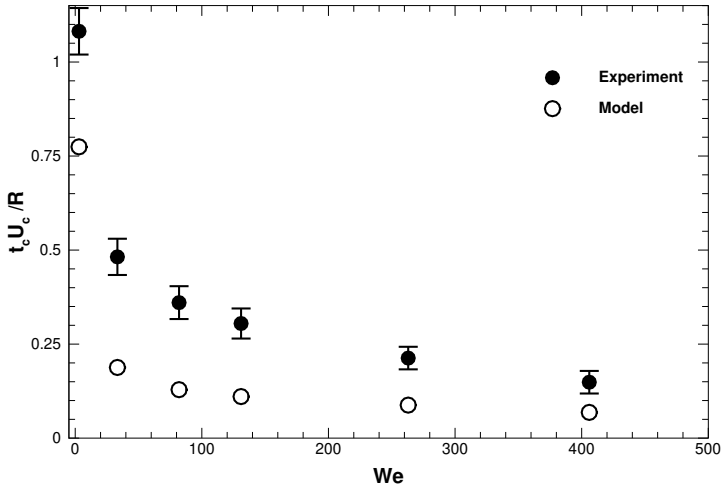

Fig. 3.6 Plot showing the variation of normalised capture time $(t_c U_c/R)$ with Weber number (We). Filled circle is for experimental data and open circle is from a simple model based on radial force balance. Ring Reynolds number for the data points from left are 3430, 11900, 21200, 29900, 45200 and 61500.

As the ring circulation, or equivalently the *We*, is varied, the appearance (or shape) of the captured bubble and the radial equilibrium location of the captured bubble also change. This is illustrated in figure 3.7, where we present top view visualization of the bubble after it has been captured by the vortex ring. In each case, the visualization corresponds to an instant in time when the bubble has reached a radial equilibrium position, with further deformation of the bubble with time being purely in the azimuthal direction. We shall first discuss the shape and surface waves on the bubble at this instant, and then discuss the radial equilibrium position. One can see from the images that the bubble in figure 3.7(a) has a relatively smooth surface, while the bubble in figure 3.7(b) has a lot of wrinkling or small scale features, with the complete bubble surface having a wrinkled appearance in figure 3.7(c). It appears that this change in the nature of the bubble surface is linked to the vortex ring going unstable, as the change in appearance corresponds well to the critical or transition *Re* for the vortex ring. Based on the experimental results of Glezer [29], and also from our own visualizations, the critical *Re* for the rings occur at $Re = \Gamma/\nu \sim 11,000$, which corresponds to the $We \sim 33$ case in our studies. Hence, the ring in figure 3.7(a) at a *Re* = 3430 is laminar, while the cases in (b) and (c) corresponding to *Re* well above the critical value are turbulent. It is thus clear that the nature of the bubble surface at capture depends on whether the ring is laminar or turbulent, with the latter showing a wrinkled surface with much smaller scale features.

We shall now proceed to discuss the radial location of the bubble in figure 3.7 (a to c). The picture in figure 3.7(a) is striking as it shows that the captured large bubble is distinctly

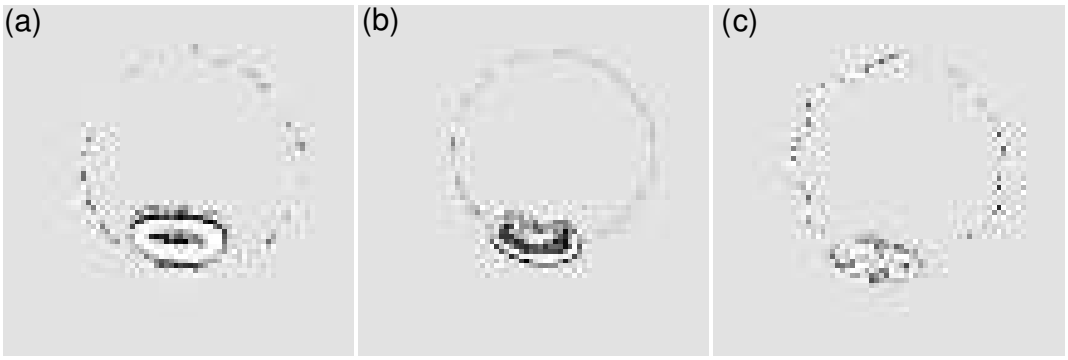

Fig. 3.7 Bubble visualization immediately after bubble capture for different vortex ring strengths (Γ), and correspondingly different ring Reynolds numbers (Γ/ν). In each case shown, the bubble has reached its radial equilibrium position. The three cases shown correspond to (a) Re = 3430, We = 3, t^* = 4.63, (b) Re = 29900, We = 131, t^* = 4.44, (c) Re = 61500, We = 406, t^* = 3.88; the times being with reference to figure 3.5. In (a), one can see that the large bubble is displaced from the micro-bubbles that mark the centre of the vortex core, while in (b) and (c) the large bubble is at the centre of the micro-bubbles.

displaced from the small bubbles that presumably mark the centre of the vortex core. It should be stressed here that the bubble shown in figure 3.7(a) has reached a radial equilibrium position with further motion/deformation of the bubble occurring only in the azimuthal direction, as may be seen from the corresponding time sequence shown in figure 3.8 (c-d). The fact that larger bubbles have a radial equilibrium position away from the core has been seen earlier in the work of Sridhar and Katz [74], who discuss this point based on the radial force balance. As discussed by them, the radial equilibrium location within the vortex core can be found from the balance between the radially inward pressure gradient induced force $\left(F_P = \rho u_\theta^2 V_b/r\right)$ and the radially outward lift force $\left(F_L = (1/2)\,\rho C_L\,(\pi/4)\,D_b^2 u_\theta^2\right)$ where $u_\theta = \Gamma r/2\pi a^2$ is the azimuthal velocity of the bubble, and V_b is the bubble volume. Substituting for the azimuthal velocity into the expressions, it is clear that F_P is proportional to $(\Gamma^2 r D_b^3)$ while F_L is proportional to $(\Gamma^2 r^2 D_b^2)$. Hence, as the bubble gets larger, the pressure gradient induced force gets much stronger, and the balance requires that the equilibrium radial location (r) of the bubble be larger. This of course does not take into account the modification of the vorticity field, but gives a broad indication that larger bubbles would have an equilibrium radial position away from the vortex center. As the strength of the ring increases, as in figure 3.7(b) and 3.7(c), the experimental visualization shows that the equilibrium radial location of the bubble shifts to the centre of the core, as marked by the smaller micro-bubbles. It is not possible to explain this using the radial force balance in the form discussed above, as both F_P and F_L have the same Γ^2 dependence. This is hence likely to be related to the modification of vorticity, as suggested above, and as will be shown later

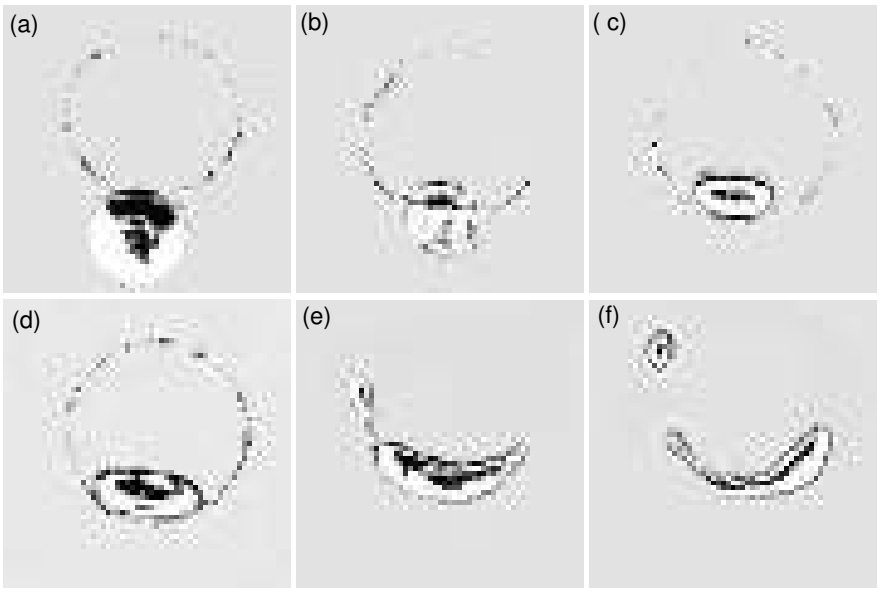

Fig. 3.8 Time sequence of bubble visualization images showing the capture and deformation of a bubble for the low *We* of 3 case. The non-dimensional time (t^*) corresponding to each of the images shown is (a) 3.19, (b) 4.41, (c) 4.61, (d) 4.74, (e) 6.47, and (f) 7.27; the times being with reference to figure 3.5.

in this section. In summary, we find that at lower vortex strengths (lower *We*), the bubble is displaced from the vortex centre, while at higher vortex strengths, the bubble pierces through the vortex core and sits in the centre of the vortex.

Bubble dynamics within the vortex ring (Stage II)

We shall now proceed to present results of the bubble deformations following capture, in what we refer to as stage II (as defined in figure 3.5). Top view bubble visualizations beginning from bubble capture is shown in figure 3.8 for the *We* = 3 case. Figures 3.8(a) to (c) show capture, with 3.8(c) being the same as figure 3.7(a); this figure showing that the captured large bubble is displaced from the micron sized bubbles that mark the vortex core. Following capture in (c), one can see pure azimuthal growth of the bubble in (d) showing that (c) is indeed the radial equilibrium position. After this, in (e) and (f), one can see further elongation of the bubble in the azimuthal direction. This elongation occurs as a result of the azimuthal pressure difference resulting from the modified vorticity distribution in the presence of the bubble, as discussed in more detail later in this section. This azimuthal pressure difference stretches the bubble, which in turn leads to gradual break-up of a small bubble from the large bubble through necking as seen in figure 3.8(e) and (f).

As the ring strength is increased, the *We* increases, and the same broad features of bubble capture and azimuthal expansion are seen. We have already discussed the *We* of 131 case that was shown in figure 3.2, where we can see capture of the bubble and bubble elongation as seen in the *We* = 3 case in figure 3.8. In the *We* = 131 case (figure 3.2), one can however see surface perturbations on the bubble that are absent at lower *We*, which continue to grow as the bubble expands following capture. Following expansion, the bubble also contracts azimuthally with the surface perturbations continuing to grow. This gradually leads to the formation of a number of small bubbles as seen in figure 3.2(h).

From visualizations such as those in figures 1 and 8, we can extract bubble size information at different times. In particular, we can extract the azimuthal length of the bubble (L_b) following capture, and this is shown in figure 3.9, where L_b is normalized by the vortex ring circumference $(2\pi R)$. It may be noted that the azimuthal bubble expansion length shown for each of the vortex ring cases in figure 3.9 were obtained as an average of three independent runs with variation between runs indicated by error bars. In the figure, the time (t') starts from the instant of bubble capture and is normalized by a pressure gradient based time-scale (t_P) discussed below. The pressure difference between the core of a single Gaussian line vortex with core size (a) and the far field is $\Delta P = \{0.87\rho\,(\Gamma/2\pi a)^2\}$ [63], while it is expected to be closer to the far field pressure when the bubble sits in the centre of the vortex core, as discussed in more detail in the next section (see figure 3.11). Broadly speaking, the bubble is thus exposed to a pressure difference in the azimuthal direction, which is of the order of $\Delta P = \{0.87\rho\,(\Gamma/2\pi a)^2\}$ that is responsible for elongation of the bubble after capture. A time-scale (t_p) may be obtained from the above pressure difference, $t_p = (0.87\rho\Gamma)\,/(\Delta P\pi) = \pi(2a)^2/\Gamma$.

In figure 3.9, we plot the bubble elongation data against time (t') non-dimensionalised by this time scale t_p, and we can see that the initial azimuthal elongation $(t'/t_p < 4)$ in all the six *We* cases from 3 to 406 shown in figure 3.5 lie nearly along a single line. One can however see from the figure that there are differences in the data for $t'/t_p > 4$, which corresponds to the time after the bubble reaches its maximum elongation. The collapse of the data for $t'/t_p < 4$ with this non-dimensionalization does however validate the fact that the azimuthal elongation of the bubble is indeed decided by the azimuthal pressure difference given above. One can further see from figure 3.9 that the slope of the contraction in all cases is also similar with this non-dimensionalization. For the *We* of 3 and 33, the trend after first maximum bubble expansion is different as compared to higher *We* (*We*>50). For the *We* > 50, the trend of bubble expansion and contraction is similar for both expansion and contraction, which is shown by a dashed line in the plot. At later times, in all *We* cases, the bubble breaks-up into smaller ones, whose combined length is shown in the plot, and is seen

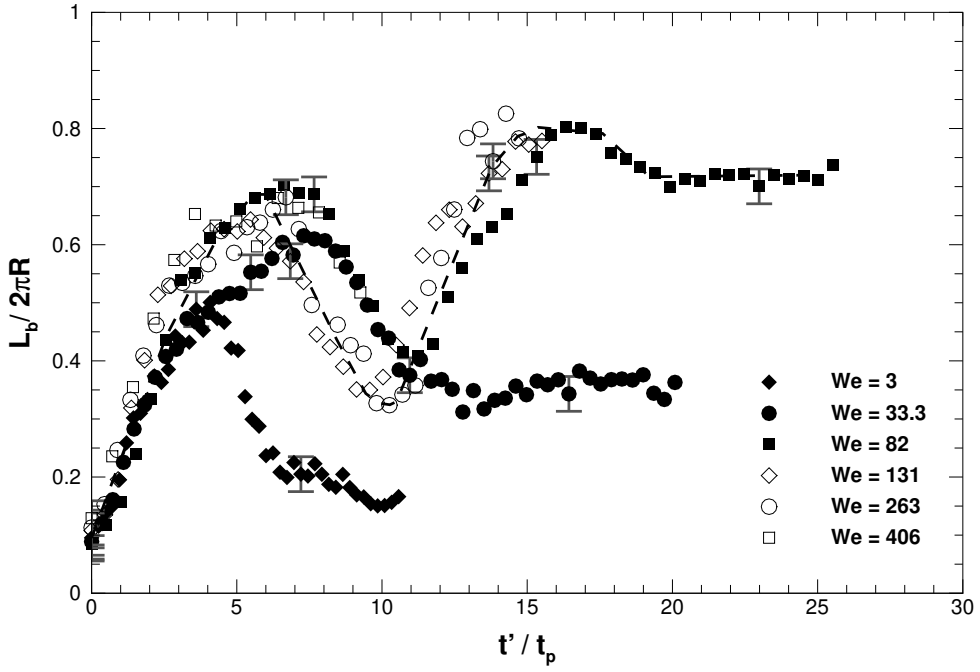

Fig. 3.9 Plot showing variation of bubble expansion length (L_b) along the azimuthal direction within the vortex ring with time starting from the instant of capture. The normalized bubble expansion length $(L_b/2\pi R)$ is plotted with time non-dimensionalised with an azimuthal pressure difference based time-scale (t_p). The initial bubble expansion data for the different *We* cases collapses on to a single line.

to reach an approximately constant value. It may also be seen from the figure that both the first maximum bubble elongation $(L_{b,\,max})$ at t'/t_p between 4 to 7 and the final steady bubble length at large time, increase with *We* at low *We*, and then saturate for $We > 200$. The first maximum bubble elongation $(L_{b,\,max})$ saturates at $(L_b/(2\pi R))$ of about 0.7, while the long time bubble length saturates at about 0.8, both corresponding to $We > 200$.

3.1.2 Vorticity Dynamics

We shall now present results from the vortex dynamics perspective for the initial stages of interaction between the ring and the bubble comprising of stages I and II. With this in mind, we present, as in figure 3.4, measurements of the azimuthal vorticity obtained from time resolved PIV in the $x-z$ plane cutting through the center of the vortex ring. The time sequence of the measured azimuthal vorticity for *We* number of 3 case is shown in figure 3.10, with the bubble in each plot being marked by a hatched area filled with magenta colour. In figure 3.10(a), the bubble is outside the vortex ring, and the vorticity distribution of the undisturbed vortex ring can be seen. In addition, vorticity can also be seen around

the approaching bubble, as seen in rising single bubble studies [7, 56]. At these low *We*, the vorticity shed from the bubble is of the same order as the strength of the ring and is hence clearly visible in the vorticity plots. As the bubble gets pulled into the ring, it elongates and pierces into the ring, as shown in figure 3.8(b) and in the process distorts the vorticity distribution as shown in figure 3.10(b). In this low *We* number case, as discussed earlier, the radial equilibrium position of the large bubble is not at the centre of the vortex, but is displaced radially outward from the centre of the vortex core. This may be seen in figure 3.10(c), where the higher vorticity contours of the right hand side core are bunched to the left of the bubble, indicating that the larger bubble is not sitting at the centre of the modified vortex core. After the bubble is captured, it elongates in the azimuthal direction, reaching maximum expansion and then contracts back as may be seen in figure 3.9. The vorticity plots corresponding to maximum elongation is shown in figure 3.10(d), and figure 3.10(e) and (f) correspond to later times, where the bubble length (L_b) reaches a constant value as may be seen from figure 3.9. There is no noticeable change in bubble size in figure 3.10(e) and (f), as there is not much change in the azimuthal length of the bubble after contraction. One can also clearly see from the figures that the left hand side core is relatively unaffected throughout the interaction process, as the bubble in the right hand core is not sufficiently stretched to reach the other side.

As the *We* is increased, the time sequence of vorticity snapshots show broadly similar features, although there are some important changes as well. The vorticity time sequence for the high *We* of 131 case was shown earlier in figure 3.4. A common feature in both the high *We* case (figure 3.4) and the low *We* case (figure 3.10) is the fact that the bubble pierces through the vortex core in (b), distorting the vorticity distribution as it enters the ring. Once the bubble is thus captured by the ring, the contours rejoin and the vorticity gets distributed in an annular form around the captured bubble. Apart from these similarities, there are also important differences between the high and low *We* cases, as seen for example in the radial location of the bubble after capture. In the high *We* case, the bubble is located roughly in the vortex centre, while in the lower *We* case, the bubble is clearly off the vortex centre, as seen earlier from the bubble dynamics in figure 3.7. The other difference is in frames (e) and (f) following maximum expansion of the bubble. In the higher *We* case, the expansion of the bubble is larger, and hence the stretched bubble, or some broken up pieces of it, reaches the other core as well, resulting in some noticeable distortion of the other core, unlike the lower *We* case.

The pressure field around the vortex core can be calculated from knowledge of the velocity field using the Navier-Stokes equation. This can be done by substitution of the velocity field into the Navier-Stokes equation to determine the pressure gradient term, which

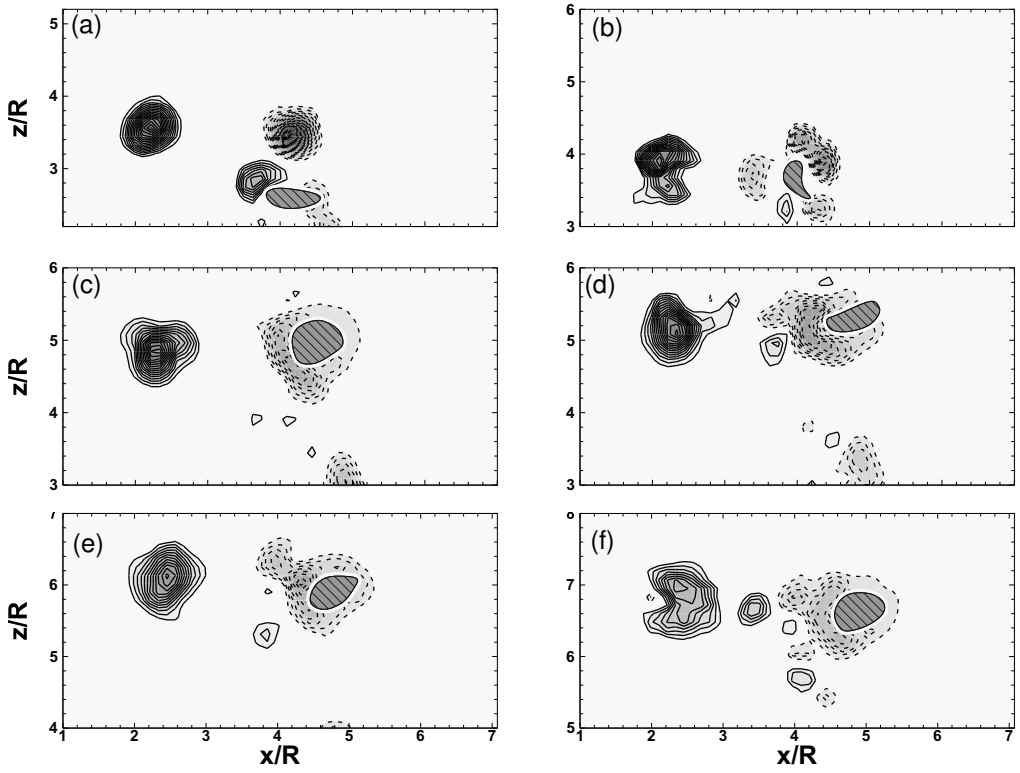

Fig. 3.10 (Colour online) Time sequence of principal azimuthal vorticity showing the different stages of vortex ring-bubble interaction for the low *We* of 3 case. In each image, the bubble is marked as a hatched area with magenta colour, while the solid and dashed line contours represent positive and negative signs of vorticity, respectively. The non-dimensional time (t^*) corresponding to each of the images shown is (a) 3.18, (b) 4.29, (c) 4.6, (d) 6.4, (e) 7.25 and (f) 7.8; the times being with reference to figure 3.5. Non-dimensional vorticity contour ($\omega R/U_c$) levels shown are $\pm 1.6, 2.2, 2.9, \ldots..$.

can in turn be integrated with respect to a reference pressure, say the far field value, to get the pressure field. As pointed out by Dabiri et al. (2014), there are issues in doing the above calculations with experimental PIV data that is inherently noisy, and they developed an appropriate algorithm to minimize these issues and implemented it into a code. Utilizing this code, we have determined the pressure field from our measured PIV velocity field, and this is shown in figure 3.11, the pressure being shown in non-dimensional form, $P^* = (P - P_\infty)/\Delta P$, where $\Delta P = 0.87\rho(\Gamma/2\pi a)^2$ is the pressure reduction at the centre of a 2D Gaussian vortex as discussed earlier and P_∞ is the far field pressure. The pressure fields shown correspond to the *We* = 406 case, with the core (lowest vorticity contour) being marked in each case by a dashed line, and the bubble by the hatched area. In figure 3.11(a), the bubble is outside the ring, and the non-dimensional pressure (P^*) in both cores is close to -0.9, indicating that the core pressures are low and close to the values for an equivalent 2D Gaussian vortex. On the other hand, the pressure field in figure 3.11(b) at bubble capture is significantly modified, with the pressure in the left core being much closer to the far field pressure at -0.3, while that in the right core remains nearly unaffected with a pressure of about -0.8. There is thus a large non-dimensional pressure difference of about 0.5 in the azimuthal direction, which is responsible for the azimuthal elongation of the bubble, discussed earlier. Figure 3.11(c) corresponds to maximum elongation of the bubble in the azimuthal direction and hence a relatively smaller bubble radius. In this case, the pressure on the left core with the bubble is a little lower with a value of about -0.4. The pressure fields shown highlight the differences in pressure caused by the distorted vorticity distribution within the core, which is broadly in an annular form within the water phase around the bubble. It may be noted that these pressure fields were calculated with the fluid velocity within the bubble set to zero, thus giving no variation in pressure within the bubble area, as one would expect in the real case due to the much smaller density of air compared to that of water. Further, it should also be noted here that in these cases, the change in pressure across the interface due to surface tension is very small compared to ΔP.

We have so far discussed the bubble and vorticity dynamics in stages I and II of the ring and bubble interaction. By the end of the second stage, the bubble has been completely broken up in to smaller bubbles, as shown for example in figure 3.2(h) for the high *We* case and figure 3.8(f) for the low *We* case. At the same instant in time, the vorticity fields in the high and low *We* cases are shown in figure 3.4(f) and figure 3.10(f), respectively. In both cases, the vorticity is distributed in an annular form within the water phase, caused by the presence of the bubble in the centre. A simple and robust measure of the integral effect of the vorticity distribution is the convection speed of the vortex ring, which is the slope of the ring position data in figure 3.5. At this instant (end of stage II), the convection speed data shows

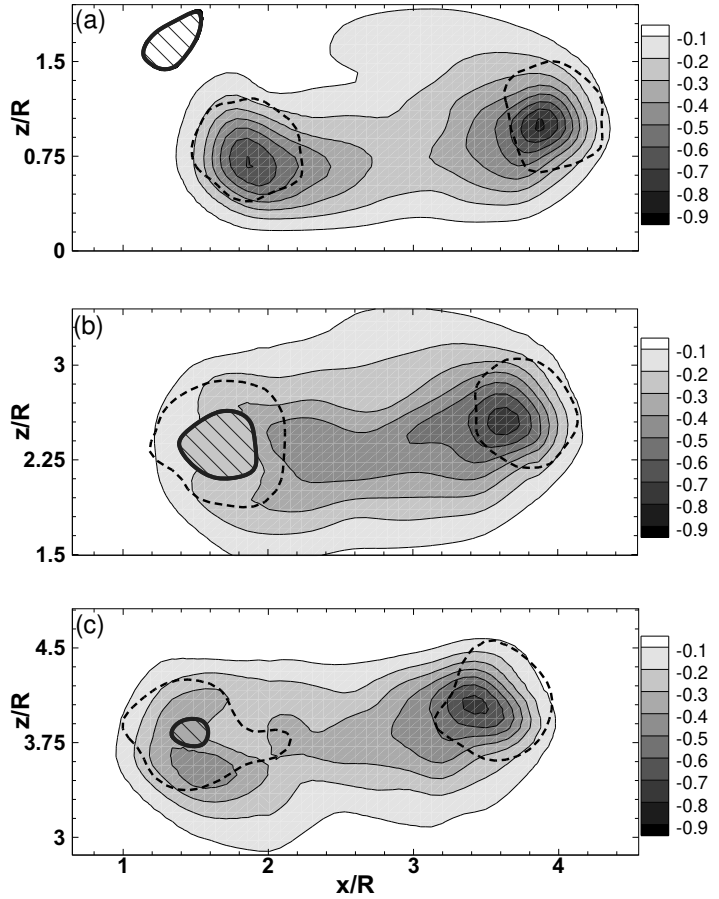

Fig. 3.11 Contour plots of the normalized pressure distribution P^* around the vortex ring calculated from the measured PIV velocity field. In each case, both the vortex cores are marked by a dashed line while the bubble location is indicated by the region with hatched slanting lines. The normalized pressure P^* is defined as $(P-P_\infty)/\Delta P$, where $\Delta P = 0.87\rho(\Gamma/2\pi a)^2$ is the pressure reduction at the centre of a 2D Gaussian vortex. As seen in (a), the pressure P^* at the centre of the vortex core before bubble capture is close to -1 indicating that it is similar to an equivalent 2D Gaussian vortex. In (b) and (c), one can see the large pressure difference between the two vortex cores, with the pressure in the left side core affected by the bubble being around -0.2 and that of the unaffected right core being around -0.9. Non-dimensional time (t^*) corresponding to (a), (b) and (c) are 1.77, 3.85 and 5.25 respectively ($We = 406$).

a distinct difference between the low and high *We* cases. In the high *We* cases, the data for the ring with the bubble is nearly the same as the baseline case, while in the lower *We* case ($We \sim 3$), there is a clear reduction in the convection speed of the ring. This is an indication of the fact that the ring has been considerably affected by the bubble at this time. This naturally raises the question of what could be possible mechanisms that may be responsible for the reduction in convection speed of the ring. One possible mechanism is related to the distorted annular vorticity field caused by bubble capture, which occurs at the line demarcating stages I and II in figure 5. Around this time, bubble capture occurs at a rapid rate, but there is no significant change in convection speed at this time, as seen in figure 3.5. This suggests that the modified annular vorticity distribution caused by bubble capture does not by itself directly affect the convection speed. The reduction in convection speed may then be caused by an instability of the modified vortex core at bubble capture (such as figure 3.10(c)), which then gradually develops. There are a few features of this modified vortex core at bubble capture that may be responsible for instability and reduction in the convection speed of the ring. This includes the annular form of vorticity distribution within the water phase, and the presence of sharp density and viscosity changes at the interface. For example, Dritschel [18] has shown that a single annular 2D distribution of constant vorticity in an incompressible (single) phase can be unstable to two-dimensional perturbations, which can lead to the formation of multiple vortices, or what they refer to as “break-up" of the vortex. We shall see in the next section that this is what happens in our case, although the precise reason for it in our case is not very clear.

A common feature of the distorted vorticity fields seen in the present interaction is the presence of vorticity in an annular form within the water phase, caused by the presence of the bubble in the centre, as seen for example in figure 3.4 and 3.18*b*. We present in figure 3.12 such an idealized 2D single core to highlight some of its key features, and to also broadly illustrate what may be happening within the bubble where measurements were not made. The variations in vorticity shown on the water side are based on our measurements. The corresponding velocity and pressure on the water side for this single core case are from simple calculations based on Biot-Savart law and radial force balance, respectively. On the other hand, the variation within the bubble is based on the boundary conditions at the interface that require velocity and shear stress continuity. For example, shear stress continuity at the interface dictates that the vorticity (or velocity gradient) just within the bubble at the interface would be much higher due to the much lower viscosity of air compared to that of water. This would suggest a rapid decrease in vertical velocity within the bubble, which must however come down to zero at the centre from symmetry considerations for this idealized (symmetric) case. From the far field values, the pressure reduces as we approach and enter

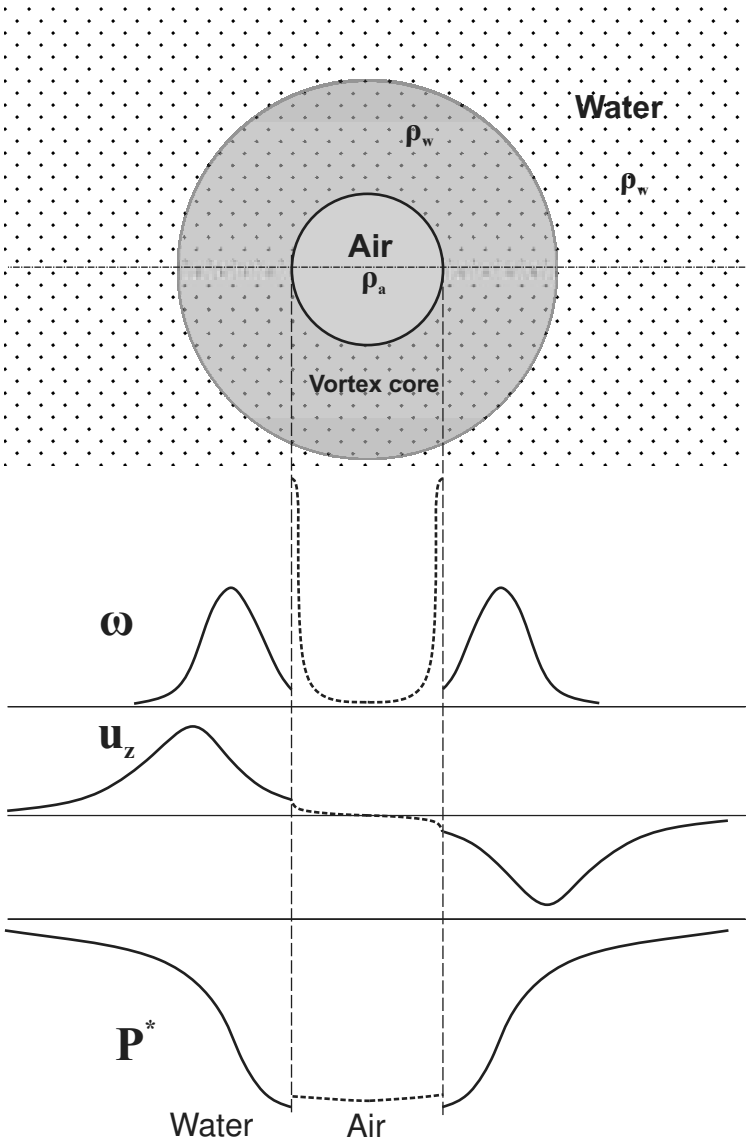

Fig. 3.12 Schematic of a single 2D vortex core in water with a cylindrical bubble in the centre. The vorticity within the water phase is in this case in an annular form with the profile being a Gaussian on either side of the bubble. The variations in vorticity (ω), vertical velocity (u_z) and pressure (P^*) shown are based on our measurements and calculations on the water side, while it is qualitatively illustrated on the bubble side based on the boundary conditions at the interface that require velocity and shear stress continuity.

the annular core, with the minimum pressure occurring at the interface on the water side. After this, there is a jump in pressure due to surface tension across the interface, with the pressure thereafter expected to be nearly constant within the bubble due to the much lower air density (ρ_a), as illustrated in the figure. Despite the relatively large values of vorticity and velocity that can exist within the bubble, one should note that angular momentum and energy within it would be negligibly small due to the much smaller density. We would also like to state here that the stability or rather the instability of this configuration could be a key to understanding the mechanisms responsible for some of our observations in this study. We shall see later in section 3.4, that stability analysis of such an annular vortex in a single phase scenario [18] do indeed show that it is susceptible to instabilities that can even lead to break up of the annular vortex into multiple vortices. We shall see in the following sections that such breakup of the vortex core occur in our experiments at later times.

3.2 Thin core rings: Later stages of interaction

We present in this section, the later stages of the bubble-vortex ring interaction discussed in the previous section. This comprises of stages III and IV as defined in figure 3.5; these two stages corresponding to the quasi-steady state, with a set of broken bubbles inside the ring, and the time after which the bubble escapes from the ring, respectively.

3.2.1 Bubble Dynamics

The break-up of the bubble into smaller bubbles is complete by the end of stage II, and hence there is almost no further break-up of the bubble within stage III. This stage may hence be referred to as a quasi-steady stage from the bubble dynamics perspective. This is shown by an example time sequence of bubble visualization within this stage in figure 3.13, that shows that the number of bubbles is almost the same. One of the smaller broken bubbles is marked in the first image, with the same bubble being marked in the other two images and angular position of it with respect to time t^* is shown in the same figure. This shows the gradual anti-clockwise azimuthal motion of the bubbles within the core during this stage, as also indicated by the arrow in the first image.

In each of the *We* number cases studied, there are a fixed number of smaller bubbles within stage III, as no further break-up occurs within this stage. Shown in figure 3.14(a) is the number of smaller broken bubbles in this stage as a function of the *We*. As may be seen from the plot, the number of smaller bubbles formed as a result of break-up increases with *We* starting from 3 at low *We*, and reaching about 16 at the higher *We* of 406. It should be

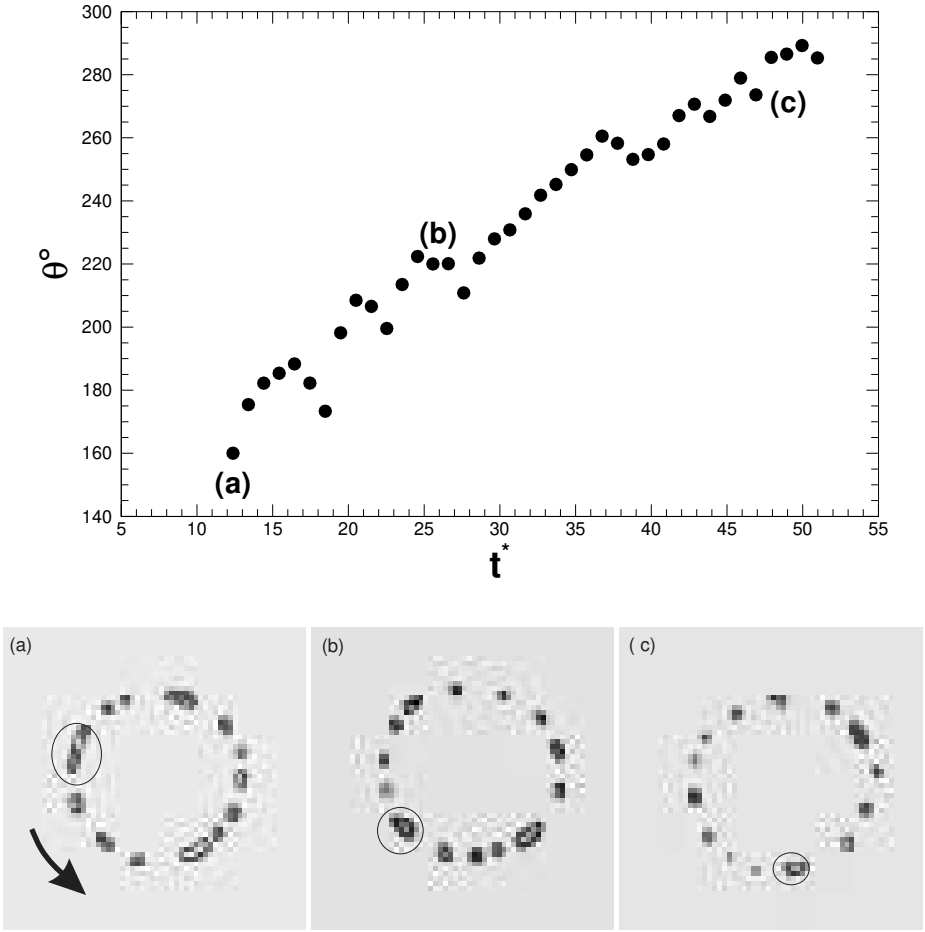

Fig. 3.13 The figure shows a time sequence of bubble visualization within stage III. As may be seen the number of broken bubbles remains nearly the same in all the three cases. One of the smaller broken bubbles is marked in the first image, with the same bubble being marked in the other two images, showing the gradual azimuthal motions of the broken bubbles within the core. The non-dimensional time (t^*) corresponding to (a), (b) and (c) are 12.69, 25.3 and 47.59 respectively ($We = 131$).

noted that all the values shown here are a result of the average of three experiments done for each *We* case, with the variation between the 3 runs indicated by the error bars in the plot. Associated with this increase in the number of smaller bubbles is a reduction in the average diameter of the bubbles formed (D_m), which is shown in figure 3.14(b) normalized by the nominal bubble size D_b before entrainment. We can fit a power law to the data, and we find that the average diameter of the formed bubbles varies as $We^{-0.124}$, as shown in the figure. This may be compared to the more well studied case of droplet/bubble break-up due to isotropic turbulence, where Shinnar [72] showed that the average droplet/bubble size formed after complete break-up by isotropic turbulent flow varies as $We^{-0.6}$ based on simple arguments; the *We* number here being defined as the ratio of kinetic energy of oscillating droplet/bubble to the surface energy. In these cases of bubble break-up due to isotropic turbulence, as discussed by Martínez-bazán et al. [51], bubble break-up occurs as a result of the combined effects of inertia, surface tension and turbulent energy dissipation per unit mass. Risso and Fabre [68] further suggest that the time response of the bubble controls the maximum amount of energy which can be extracted from each turbulent eddy and the viscous damping limits the energy that the bubble can accumulate during its fluctuating deformation. This problem has received a lot of attention due to its importance in bubbly turbulent flow where the average diameter of the completely broken up bubble decides the interfacial area, which in turn decides the rate of mass, momentum and energy transfer between the two phases. Our experiments suggest that the exponent is different in the present idealized case of a single vortex structure (ring) as compared to Shinnar [72], which is for isotropic turbulence. It should be noted here that the change in exponent is not unexpected, as in the isotropic turbulence case, the whole process of break-up is considerably more complex due to the multi-scale nature of turbulent structures. The differences between the two can be firstly attributed to the fact that bubble break-up in the turbulent case can not only occur due to an intense single eddy, but also through the combined action of a succession of different eddies [68]. This is in addition to the obvious fact that in the turbulent case, the broken bubbles are always exposed to eddies with smaller scales that they can interact with, unlike in the present case.

A close-up of the bubble break-up in our present case from side visualizations is shown in figure 3.15; this occurring in stage II. The visualizations show both the large bubble being deformed within the ring, as well as the micron sized bubbles tracking the vortex core. The smaller bubbles tracking the core clearly show the Kelvin waves in the core of the vortex ring, as discussed by Widnall et al. [88]. It is natural to then ask the question if the number of smaller bubbles is related to the number of Kelvin waves in the ring, which can be easily counted from the visualizations besides getting an estimate from the theory based on the

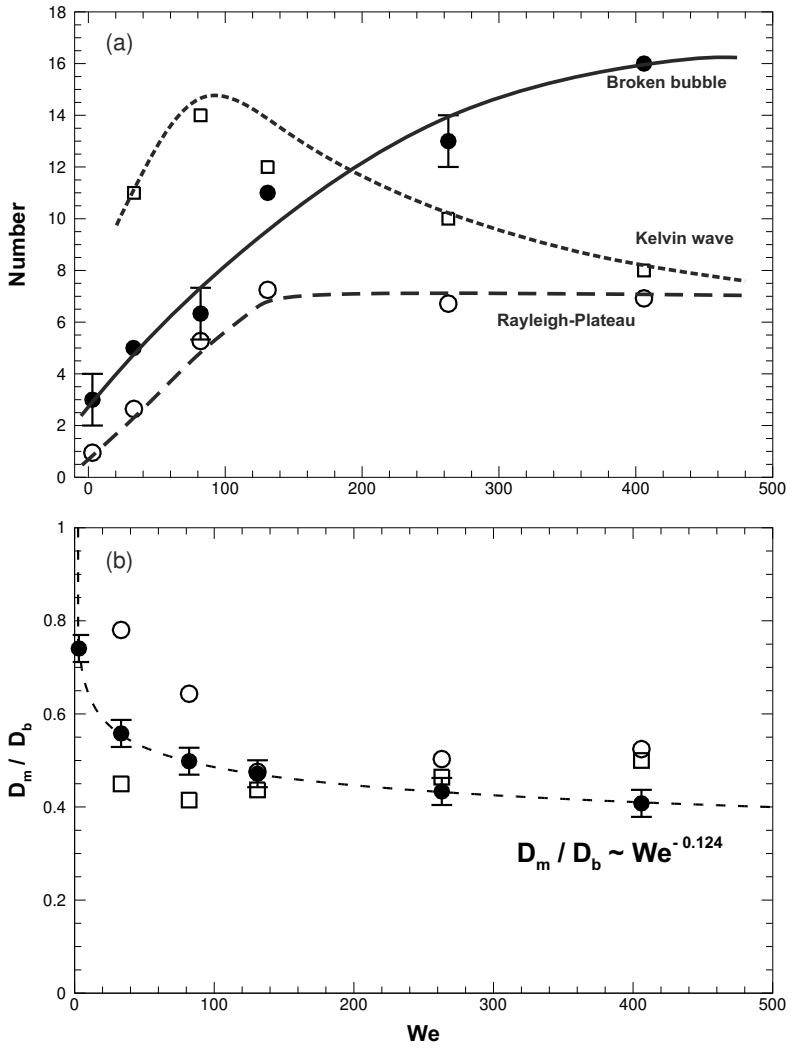

Fig. 3.14 Variation of (a) the number of broken bubbles, and (b) their diameter (D_m) with *We* after complete break-up of the bubble (stage III). The number of Kelvin waves seen from the visualizations is also shown in (a), and is found to be different from the number of broken smaller bubbles. The number of Rayleigh-Plateau instability waves that fit on the cylindrical bubble is also shown in (a), with the equivalent mean bubble diameter (D_m) shown in (b). The number of instability waves is close to the number of broken bubbles at low *We*, but deviates at larger *We*. •, Experiment; □, Kelvin wave; ○, Rayleigh-Plateau instability.

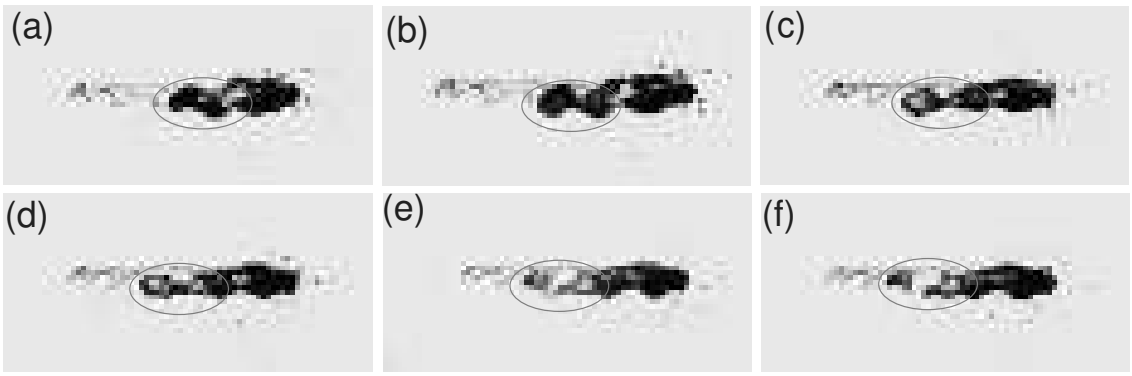

Fig. 3.15 Successive images of bubble break-up while interacting with the vortex ring illustrating 'pinch-off' of smaller bubbles (*We*= 131). Necking can be seen in figure (d). The non-dimensional time (t^*) corresponding to each of the images shown is (a) 4.72, (b) 4.75, (c) 4.82, (d) 4.85, (e) 4.88 and (f) 4.91; the times being with reference to figure 3.5.

relative core size [88]. We present in figure 3.14(a), the number of Kelvin waves as counted from the visualizations at each *We*, and it is clear that the number of Kelvin waves does not match the average number of bubbles formed after complete break-up. The Kelvin waves do however play some part in the break-up as seen in the images in figure 3.15, where the bubble appears to break-up due to these azimuthal waves, as may be seen by following the time-sequence of images. The process of necking can be seen in (b), which develops leading to the formation of a gas bridge in (e) and break-up in (f). However, the number of bubbles formed after complete break-up is clearly not decided by the Kelvin waves. Apart from the mismatch in numbers discussed earlier, there is also a time-scale issue, as these Kelvin waves are typically short lived as they rapidly grow and result in the ring becoming turbulent. The complete break-up of the bubble on the other hand takes much longer time.

Apart from the Kelvin waves, another possible mechanism that could determine the average size or number of broken bubbles would be the classical Rayleigh-Plateau instability of the stretched cylindrical bubble. The wavelength corresponding to maximum growth rate for this instability is about 4.5 times the diameter of the cylindrical bubble. In our case, if we use the minimum diameter of the stretched bubble ($d_{br,\,min}$), which corresponds to the first maximum azimuthal length ($L_{b,\,max}$), we can get a wavelength for each one of the different *We* cases, from the data set shown in figure 3.9. From this wavelength, we can get both the number of waves that can fit on the cylindrical bubble of length ($L_{b,\,max}$) and the diameter of the corresponding broken bubble, as shown in figure 3.14(a) and (b), respectively (open circle). As may be seen from the values in the plot, the number of these waves that fit into the stretched bubble and their variation with *We*, is reasonably in agreement with experimental data at low We ($We < 150$), although it is not very close. At $We > 150$, the

visualized number of broken bubbles continues to increase, while the number of instability waves is fixed as the bubble length and diameter saturate, as discussed earlier with reference to figure 3.9. The diameter of the broken bubble estimated from these waves is also shown in figure 3.14(b), showing a similar trend to those seen in the experiments, although the actual values are again not very close. It should be noted here that the number of broken bubbles seen in the experiments is typically larger than from the instability wavelength, and the difference increases for $We > 150$, where the *Re* of the ring is also larger. Although the reason for this is not very clear, the larger number of broken bubbles seen in the experiments may be caused by the increased level of turbulence as the ring *Re* increases. In addition, differences may be caused by the presence of rotational flow around the bubble.

3.2.2 Vorticity dynamics

We present here the azimuthal vorticity measurements during the later stages of interaction between the bubble and the vortex ring. In figure 3.16, we present the measured vorticity field for the *We* of 3 case, at non-dimensional time $t^* = 14.67$, where the convection speed of the vortex ring is substantially lower than the base case of the vortex ring without bubble, as may be seen from figure 3.5. The figure shows both the base case, in (a), and the case with bubble interaction in (b) with only lower level contours shown in both cases to highlight the edges of the vortex and shedding from it. As may be seen from the figure, there is a striking difference in the measured vorticity fields in the two cases. The vorticity field in (a), shows a clear circular vortex core with no shedding of vorticity from the ring, consistent with the fact that the ring is laminar. On the other hand, the vorticity contours for the case with bubble interactions in (b), shows a fragmented right core where the bubble is present, with significant shedding of vorticity from this core. The left hand side core is also affected, but not as significantly as the right, but the overall convection speed of the ring has been significantly reduced (about 30%) as seen in figure 3.5. Shortly after this, the bubble escapes from the ring, leaving behind a ring with a fragmented core that travels significantly slower. We would like to stress here that Sridhar and Katz [74] also noted vortex distortion in their study, but the vortex core regained its initial undistorted state in that case once the bubble escaped. On the other hand, the effect on the vortex core is a lasting one in our case and the core is left in a fragmented state even after bubble escape.

In contrast to the low *We* case, the vorticity distribution in the higher *We* number cases show lesser influence of the bubble on the core, as shown in figure 3.17 for $We = 406$ case. As in the low *We* case, both the base ring in the absence of the bubble (in (a)), and the ring after interactions with the bubble in (b) are shown. Both these fields are shown at non-dimensional time $t^* = 14.02$, where the convection speed is nearly the same as the base ring case, as may

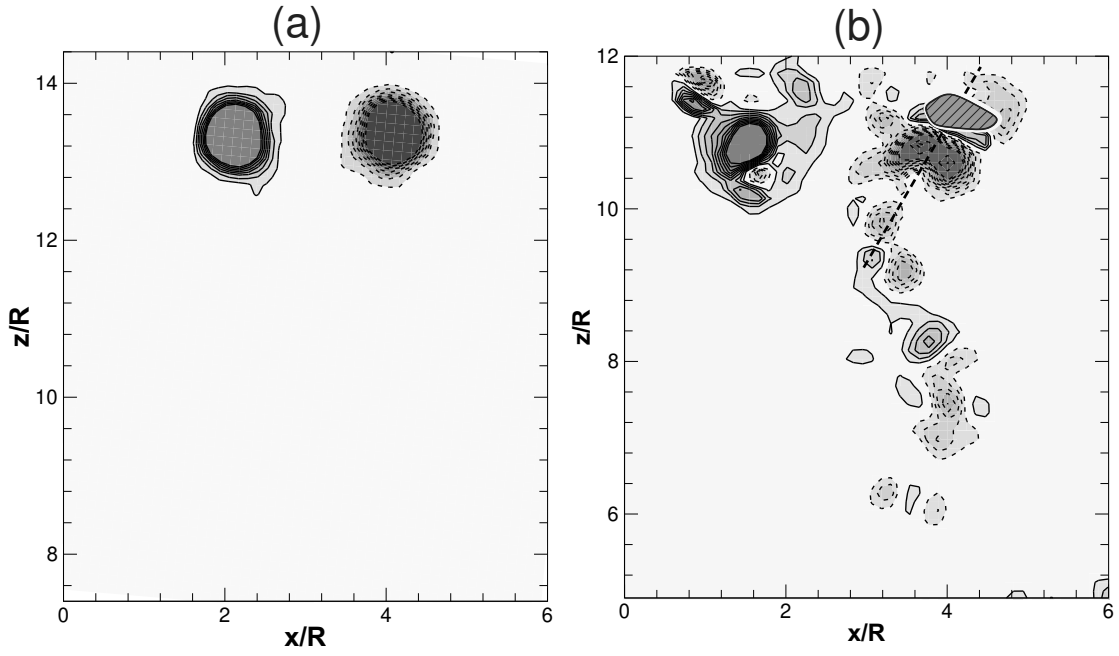

Fig. 3.16 (Colour online) Comparison of principal azimuthal vorticity distribution for a vortex ring with and without interactions with a bubble for *We* of 3 case at later times. In (b), the vorticity distribution for the ring interacting with a bubble is shown, which is markedly different from the identical ring in the absence of a bubble shown at the same time in (a). The vortex core in (b), particularly the one on the right with the bubble appears fragmented with significant shedding from it. The bubble is marked by hatched line filled with magenta colour, while the solid and dashed line contours represent positive and negative signs of vorticity, respectively. The non-dimensional time (t^*) with reference to figure 3.5 is 14.67. Non-dimensional contour levels shown are $\pm 0.16, 0.32, 0.48, \ldots\ldots$ 1.29.

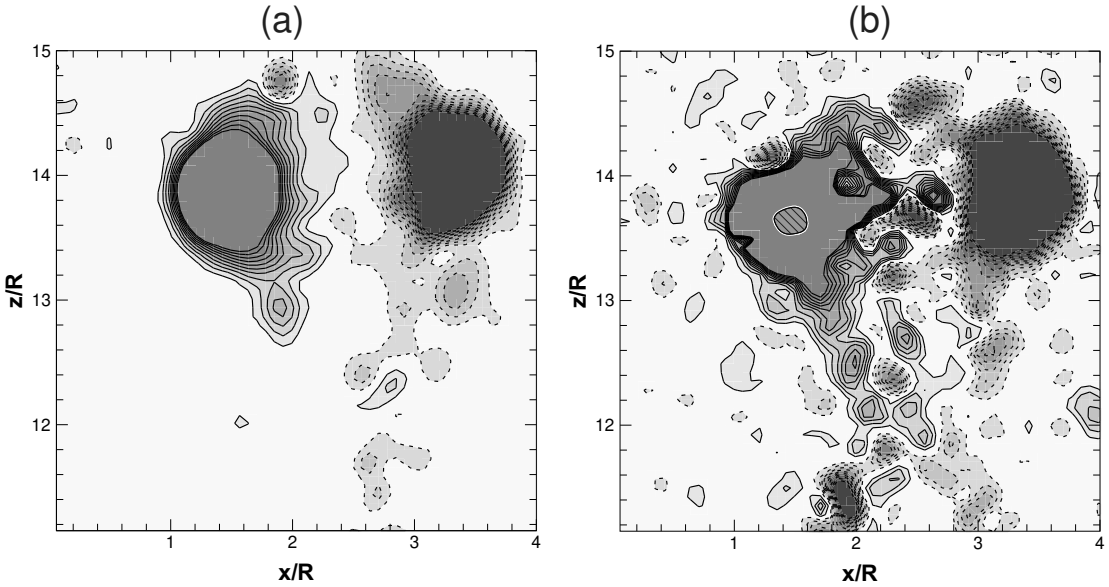

Fig. 3.17 (Colour online) Comparison of principal azimuthal vorticity distribution for a vortex ring with and without interactions with a bubble for *We* of 406 case at later times. In (b), the vorticity distribution for the ring interacting with a bubble is shown, which is again significantly different from the identical ring in the absence of a bubble shown at the same time in (a). The main difference here is the increased shedding from the ring. However, at this higher *We*, the core appears reasonably intact with no significant deformation, unlike in the lower *We* case in figure 3.16. Solid and dashed lines in the contours represent opposite signs of vorticity. The bubble is marked by hatched line filled with magenta colour, while the solid and dashed line contours represent positive and negative signs of vorticity, respectively. The non-dimensional time (t^*) with reference to figure 3.5 is 14.02. Non-dimensional contour levels shown are $\pm 0.1, 0.21, 0.32, \ldots\ldots$ 1.06.

be seen from figure 3.5. In this case, the base ring vorticity field (in (a)) shows inherent shedding from the ring, consistent with the fact that the ring in this case is turbulent [27], as discussed earlier. However, in the case of the ring with the bubble, as shown in (b), one can see a significant increase in the shedding from the ring compared to (a). Although the reason for this increased shedding from the vortex core with the bubble is not completely clear, it is likely caused by the shedding from the bubble present within the core, as has been discussed for example in Sridhar and Katz [74]. Despite this increased shedding, the core appears relatively intact in this high *We* case, unlike in the lower *We* case in figure 3.16. The convection speed in this high *We* case is also relatively unaffected consistent with the almost intact vortex core.

The vorticity distribution within the (single) vortex core for the low and high We cases is shown in figure 3.18 for both the ring interacting with the bubble, and the base case, to further highlight the differences. In figure 3.18(a), the vorticity distribution along a 45° line

through the core with the bubble is shown for the *We* = 3 case, as also marked on the image in figure 3.16(b). The vorticity distribution is clearly quite complex with the presence of multiple peaks; two positive vorticity peaks and one negative vorticity peak. As expected, the base vortex core in the absence of the bubble, shown by the dashed line, is a simple Gaussian profile. In the higher *We* number case shown in figure 3.18(b), the vorticity is distributed in an annular way around the bubble, the distribution being in the form of two Gaussian profiles with reduced peak vorticity. This type of reduced peak vorticity for cases where the bubble resides within the core is a common feature in these flows, which as we shall see below has consequences. The vertical induced velocity for both the low and high *We* cases across both vortex cores is shown in figure 3.19(a) and (b), respectively. In the low *We* case, a significant reduction in velocity compared to the base case can be seen due to the interaction with the bubble. This decrease in velocity is linked to the fragmented state of the vortex core and also consistent with the significant decrease in convection velocity of the ring at this instant, as may be seen from figure 3.5. In the higher *We* case, differences can be seen between the interacting ring and the base ring, but the differences are much smaller.

The convection speed of the ring is an integral effect of the vorticity distribution within it. Hence, one way to understand the underlying physics of the reduction of convection speed is to look at the enstrophy or volume integral of the square of the vorticity of the vortex ring. In the current study, as 2D time resolved PIV measurements have been done, the enstrophy (Z) is calculated as the area average of the square of the azimuthal vorticity, this being representative of the principal vorticity in the flow. For the purpose of enstrophy calculation, an area that is about 100 times the core area was used to ensure that all the vorticity corresponding to the vortex ring is included. There is some variation between runs, but this is within the experimental uncertainties, as may be seen by the variation in circulation between time instant and the variation between repetitions of the same experiment shown by the error bars in the plot. Figure 3.20(a) shows the variation of enstrophy (Z) with time for a low *We* and a high *We* number case, along with their respective base ring cases; the enstrophy (Z) being non-dimensionalised in each case by its respective initial value (Z_i). In both the base cases, in the absence of a bubble, a gradual reduction in enstrophy is seen with time due to viscous diffusion of the core, reaching a value of about 0.8 at $tU_c/R \approx 12$ due to diffusion of the core. In contrast, for the low *We* = 3 case, the enstrophy reduction with time is significantly enhanced in the case with bubble. At small times, the enstrophy reduction is similar to the base case, until $tU_c/R \approx 4$, where there is a sharp drop in enstrophy, due to the sudden capture of the bubble by the ring, which results in a sharp drop in peak vorticity. Subsequently, as the bubble expands azimuthally within the ring, the bubble diameter reduces, as may be seen in figure 3.9, and this leads to an increase in enstrophy, which almost reaches

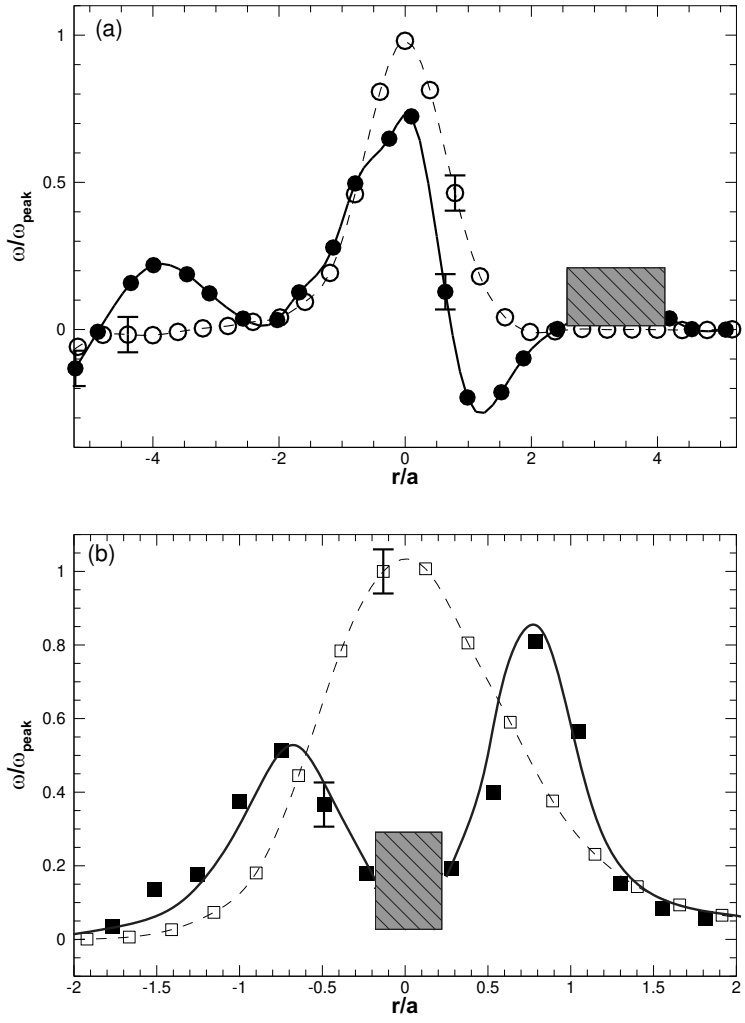

Fig. 3.18 Principal azimuthal vorticity (ω) profile along a radial line through the vortex centre at later times for (a) *We* = 3, and (b) *We* = 406. In each case, the vorticity profile in the absence of the bubble is also shown by open symbols, while interacting case data is shown by filled symbols. The non-dimensional time (t^*) with respect to figure 3.5 is 14.67 for (a), and 14.02 for (b); the times being with reference to figure 3.5. The data shown correspond to the vorticity fields shown in figure 3.16 and figure 3.17, respectively. All vorticity values in these plots are normalized by the peak vorticity of the base vortex ring (ω_{peak}). The bubble in the plot is marked by hatched line filled with magenta colour

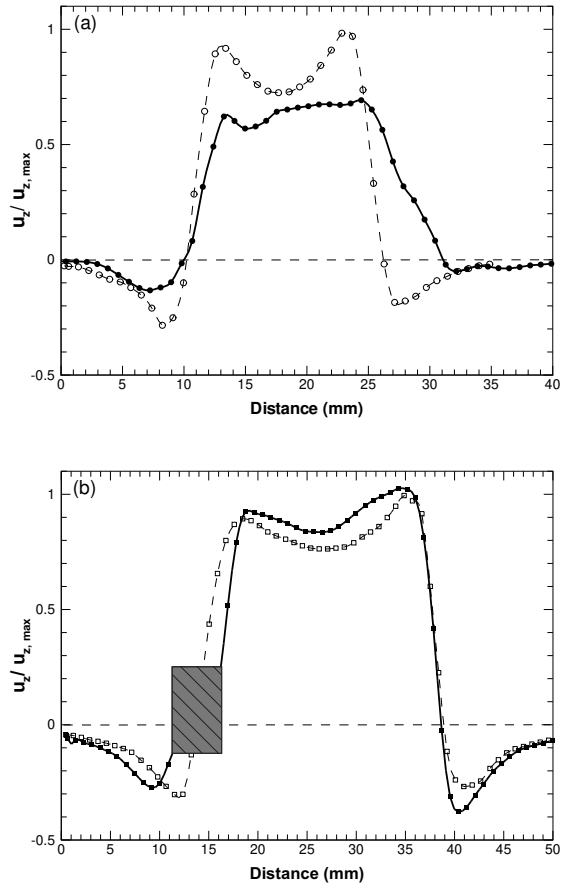

Fig. 3.19 Vertical velocity (u_z) profile along a radial line through the vortex centre at later times for (a) *We* = 3, and (b) *We* = 406. In each case, the velocity profile in the absence of the bubble is also shown by open symbols, while interacting case data is shown by filled symbols. The data shown correspond to the vorticity fields shown in figure 3.16 and figure 3.17, respectively.

the enstrophy of the base vortex ring at $tU_c/R \approx 5.4$. Following this, the enstrophy (Z/Z_i) reduces reasonably rapidly reaching what appears to be an asymptotic value of about 0.4, which corresponds to a large reduction of about 50% as compared to the base case at the same time. As stated earlier, this state continues even after the bubble escapes leaving behind a less coherent vortex ring, whose core appears fragmented as shown in figure 3.16. In contrast to this large reduction in enstrophy for the low *We* case, the reduction in enstrophy is relatively small for the higher *We* case of 263 also shown in figure 3.20(a). The enstrophy values for this case are in fact close to the base ring case, consistent with the negligible reduction in convection speed for this case, as may be seen from figure 3.5. It should be noted here that reduction in enstrophy of a vortex due to interaction with bubbles has been observed earlier. For example, Ferrante and Elghobashi [23] in their numerical study of the interaction of a Taylor-Green vortex with a large number of entrained small bubbles report a reduction in enstrophy of around 4% due to the modified vorticity distribution. For a turbulent channel flow with bubbles, Lu et al. [46] report a large reduction of about 60% in enstrophy in their DNS study, with suppression of structures. They attribute the observed drag reduction to the reduction in enstrophy and suppression of structures, with more drag reduction seen when their Weber number (We) is closer to 1. Van Gils et al. [84] for the case of bubbles in Taylor-Couette flow show that the We close to the inner wall is very important in determining drag reduction, with more drag reduction observed when the bubbles deform. Our results show similar reductions in enstrophy in the more basic interaction of a single bubble with a vortex ring when the $We \sim 3$.

The circulation of the vortex core is another integral quantity of interest. In our case, as is typical of many experiments, we calculate the circulation as the line integral of velocity around a sufficiently large closed curve around a core. The resulting values of circulation for the low and high *We* cases with corresponding base cases is shown in figure 3.20(b). As may be seen from the plot, there is some variation in circulation, but this is not significant compared to the variations in time, indicating that the observed variations are within the experimental error. Hence, at a broad level, we find that there is no significant change in the circulation around the core of the vortex ring, although some small variations may be present. It may be noted that Sridhar and Katz [74] also reported no noticeable change in circulation in their experimental study of a ring interacting with few smaller bubbles. On the other hand, Cihonski et al. [13] in their numerical study of the same case showed an increase in circulation of about 10%.

As discussed in the end of section 3.1, the convection speed of the ring was seen to have reduced significantly in the low *We* case by the end of stage II. We suggested that this reduction could be due to a possible instability of the modified vortex core that developed at

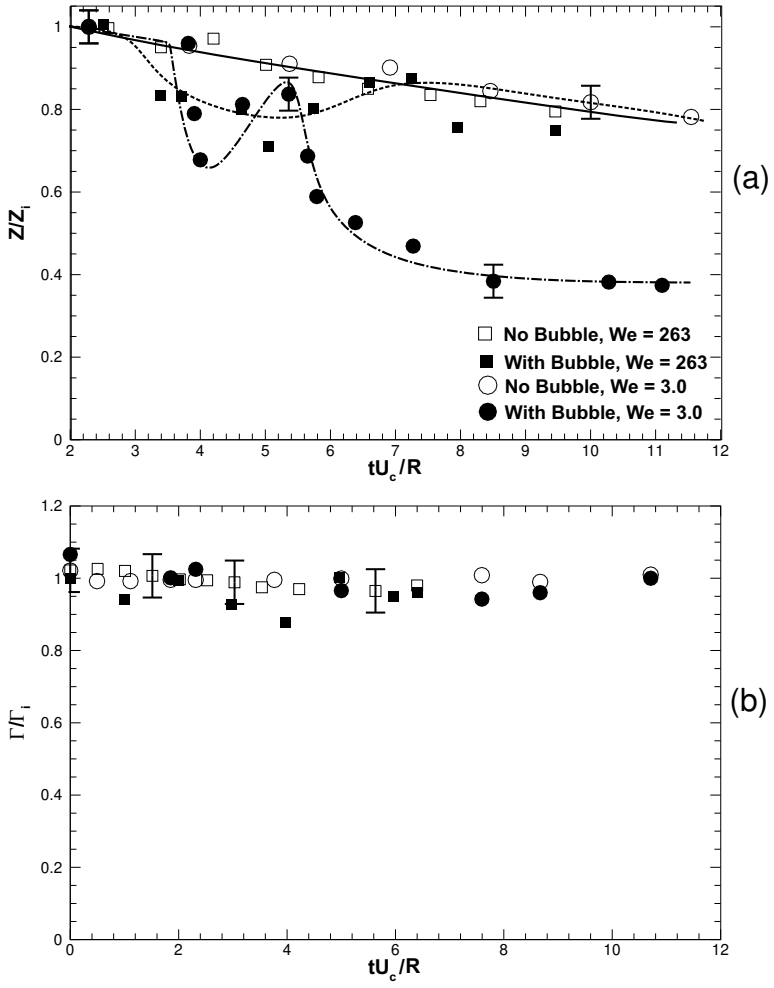

Fig. 3.20 Plot shows the variation of (a) enstrophy (Z) and (b) circulation (Γ) with time for vortex ring interacting with a bubble and for the base ring case in the absence of the bubble. The enstrophy (Z) and circulation (Γ) shown are non-dimensionalised by their respective values at $t = 0$, and time is non dimensionalised by the ring time scale (R/U_c). ○, *We* = 3 (with bubble); ●, *We* = 3 (without bubble); □, *We* = 263 (with bubble); ■, *We* = 263 (without bubble).

bubble capture, with the vorticity being distributed in an annular form around the bubble. As stated there, Dritschel [18] for example, has shown that a single annular 2D distribution of constant vorticity in an incompressible (single) phase, can be unstable to two-dimensional perturbations, leading to the formation of multiple vortices, which is what we observe in the present case at low We (figure 3.16(b)). We shall see in the following section that this deformation of the core leading to multiple vortices is even more dramatic in the thick ring case.

3.3 Thick core rings

In sections 3.1 and 3.2, results for bubble interactions with a relatively thin vortex ring of non-dimensional ring radius (ε) of 0.25 have been presented. In this section, we shall present some results for the case of a thicker vortex ring, with non dimensional ring radius (ε) of 0.75, interacting with a bubble. We shall see that thicker rings, which are inherently more unstable [61], show even more dramatic effects during interactions with a bubble, leading to clear fragmentation of the vortex core.

The thicker core rings studied here were generated using a smaller 3 mm diameter vortex generator, as compared to the 15 mm generator used for the thin core rings, as discussed in the experimental methods section. The bubble used here was correspondingly of smaller size, so as to maintain the volume ratio (V_R) of the bubble to the vortex core at about 0.1, as in the previous thin core experiments. In particular, two cases were studied, one corresponding to low *We* of 3, and the other corresponding to a high *We* of 387, the difference between the two cases being as before the circulation of the vortex ring. We begin as before by presenting a plot of the vertical location of these rings for the two *We* cases, along with their respective base cases in figure 3.21. As is clear from the plot, in this thicker core case, one can see significant reductions in convection velocity for the ring interacting with the bubble compared to the base ring case even at higher *We*. This reduction in convection speed of the ring is as before related to the effect of the bubble on the vorticity distribution within the vortex core. This can be seen from the vorticity plots also shown in figure 3.21, which show the measured vorticity distributions for the lower *We* case at later times, as marked on the vertical location plot (as (b)), along with the corresponding base case, marked as (a). As is clear from the vorticity plots, the vortex core after interaction with the bubble (in (b)) is dramatically modified, with each core having completely fragmented into two, while the base ring (in (a)) remains intact at the corresponding time. One can also see from the vorticity plots that the ring after interacting with the bubble has nearly stopped at a vertical location ($z/R = 14$), while the base vortex ring has in the same time traversed much further ($z/R = 25$) and is

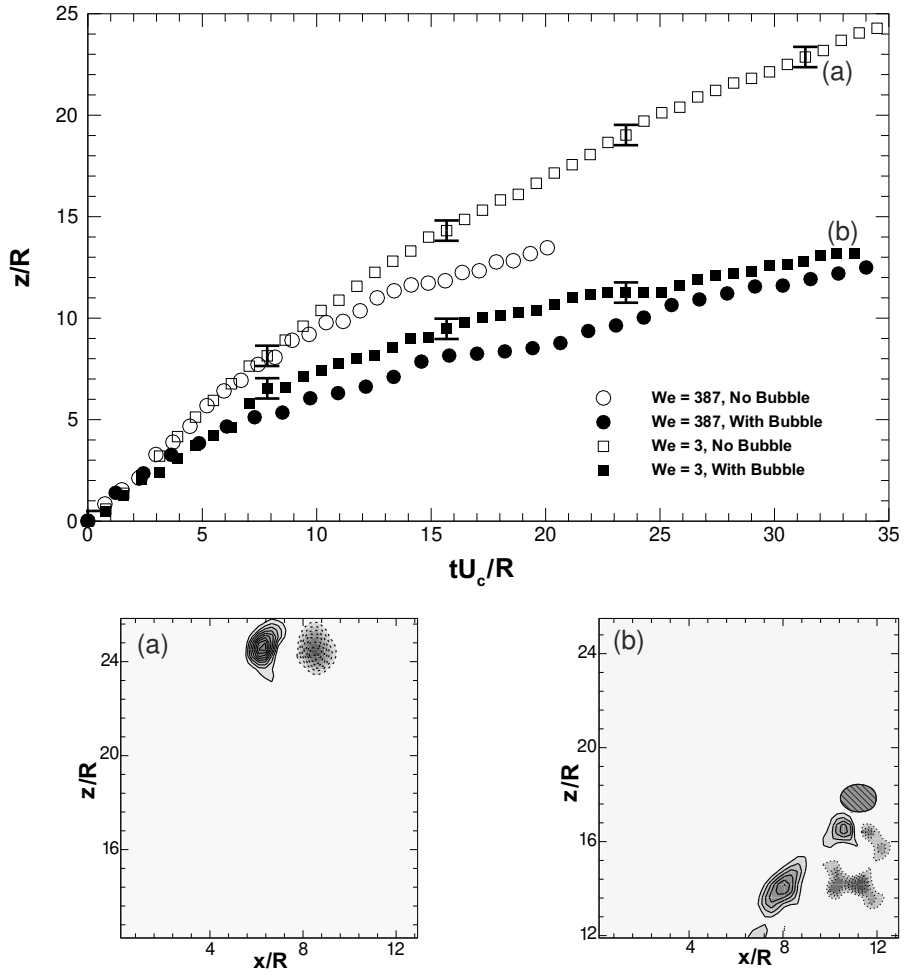

Fig. 3.21 (Colour online) Vertical location (z) of the vortex ring as a function of time for the thicker core ring for *We* of 3 and 387. The data for the ring interacting with the bubble is shown by the filled symbols, while the base case without bubble is shown by the open symbols. Vorticity plots corresponding to the time instants marked as (a) and (b) in the plot are also shown. □, *We* = 3 (with bubble); ■, *We* = 3 (without bubble); ○, *We* = 387 (with bubble); ●, *We* = 387 (without bubble).

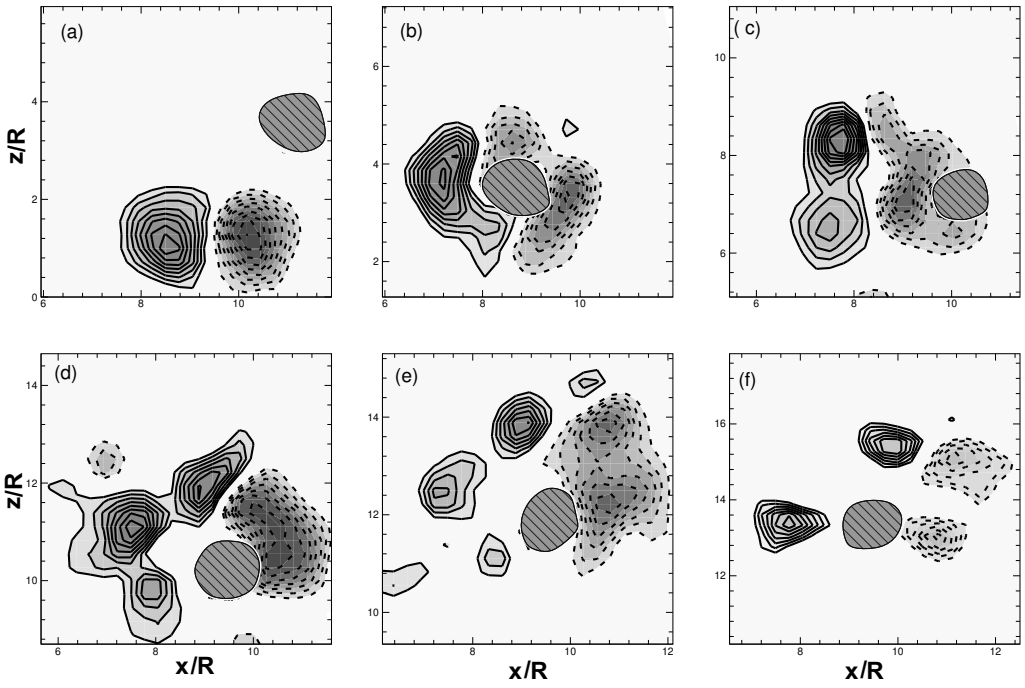

Fig. 3.22 (Colour online) Time sequence of azimuthal vorticity for thicker core ring showing the different stages of vortex ring-bubble interaction for *We* of 3 showing clear fragmentation of the core into two. The bubble is marked by a thick black boundary filled with grey colour, while the solid and dashed line contours represent positive and negative signs of vorticity, respectively. The non-dimensional time (t^*) corresponding to each of the images shown is (a) 0, (b) 4.06, (c) 8.36, (d) 16.72, (e) 21.73 and (f) 28.36; the times being with reference to figure 3.21.

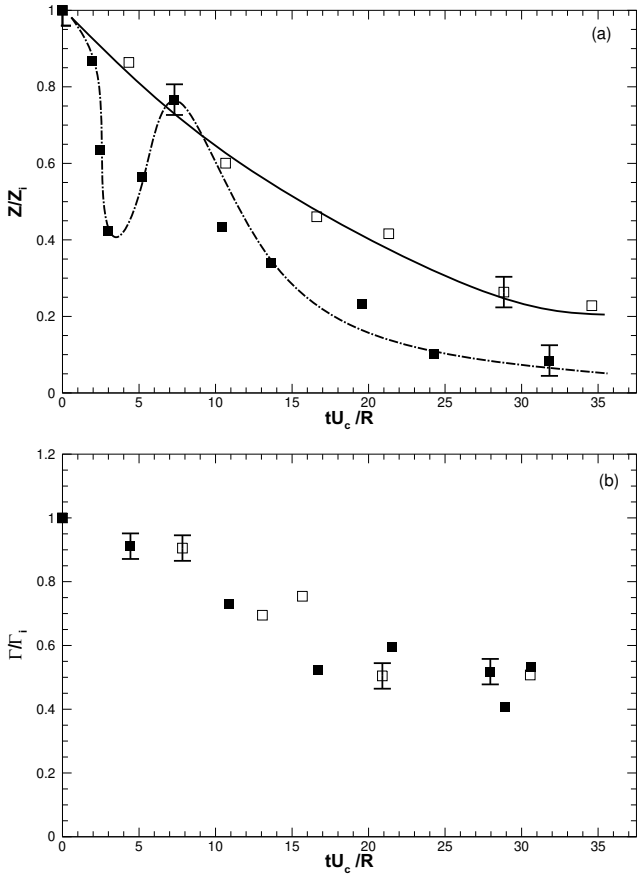

Fig. 3.23 Plot shows the variation of (a) enstrophy (Z) and (b) circulation (Γ) with time for vortex ring interacting with a bubble and for the base case in the absence of the bubble. The enstrophy and circulation shown are non-dimensionalised by their respective values at$t = 0$, and time is non dimensionalised by the ring time scale (R/U_c). ■, *We* = 3 (with bubble); □, *We* = 3 (without bubble).

continuing to move vertically upwards. These results clearly show that the effects of the interaction of these thicker rings with a bubble are more dramatic than for the thin core rings. This may be attributed to the inherently more unstable nature of the thicker core rings, as discussed by O'Farrell and Dabiri [61].

A time sequence of vorticity plots showing the interaction of the ring with the bubble for the *We* of 3 case is shown in figure 3.22. In each case, we present vorticity plots zoomed in around the core, with the vertical location being appropriately marked on the y-axis. As may be seen from the figure, the bubble is outside the ring in (a) and is captured by the ring in (b). In these thicker ring cases, visualizations show that the interactions can be more complex with the bubble in some cases jumping between cores of the ring. As may be seen from (c) to (f), the interactions of the bubble with the ring result in large-scale deformations of the

core. It appears that the presence and motion of the bubble within the ring adds perturbations to the vorticity field, which seems to make the vortex ring unstable, leading ultimately to the fragmentation of the core into two pieces in (f). By this time, the bubble escapes from the ring, leaving behind a fragmented core as seen in the vorticity plot in figure 3.22(f). It should also be noted that the whole process in this thicker ring case appears to be more three-dimensional, as one might expect.

The enstrophy (Z) as a function of time calculated, as before, as the area-averaged square of the azimuthal vorticity is shown in figure 3.23(a) for the low *We* case, with the enstrophy being non-dimensionalized by its initial value (Z_i). The solid symbols show the case for the ring interacting with the bubble, while the open symbols show the base ring case. In this thicker ring case, the enstrophy even for the base ring is seen to reduce with time due to viscous diffusion and resulting cancellation of vorticity. This may also be seen in the corresponding circulation plot shown in figure 3.23(b), where the circulation even for the base ring reduces with time. For the ring interacting with a bubble, the enstrophy variation is qualitatively similar to the thin core ring case shown earlier. There is first a sharp drop in the enstrophy of the ring, when the bubble is captured by the ring. This occurs at $tU_c/R \approx 4$ with a reduction of the normalized enstrophy (Z/Z_i) to about 0.4, a nearly 50% reduction compared to the enstrophy of the base ring at the same time. This is then followed by an increase in enstrophy that is linked to the decrease in diameter of the bubble, which is in turn caused by the azimuthal expansion of the bubble within the ring. The enstrophy (Z/Z_i) then decreases at a rate that is more rapid than the base case reaching values of less than 0.1, which is again a more than 50% reduction compared to the base ring case at the same time. From the corresponding circulation plot in figure 3.23(b), one can see that the total circulation of the core however remains nearly the same as that of the base ring case. There are some variations, but these are within the experimental uncertainties, as may be seen by the variations in circulation between time instants and the variations between repetition of the same experiment shown by the error bars in the plot. Hence, even though there is very severe distortion and even fragmentation of the core leading to a more than 50% reduction in enstrophy compared to the base case at the same time, the circulation remains nearly the same as for the base case.

In summary, we find that thicker core rings (ε =0.75) interacting with a bubble show more significant effects than in the thinner core case. In particular at low *We*, we find that such a thick core ring while interacting with a bubble fragments into two, leading to a large drop in enstrophy with a consequent large reduction in convection speed.

3.4 Discussions

We shall discuss in this section some of the possible physical mechanisms that may be responsible for our observed decrease in convection speed of the ring and fragmentation of the core. We shall also discuss the relations between the present idealized configuration of a single bubble and a vortex ring with previous studies of bubble interaction in turbulent flows, and highlight some of the similarities.

The interaction of the vortex ring with a bubble has been shown to result in significant distortion of the vortex core and even in fragmentation of the core. This in turn is responsible for the observed drop in convection speed and enstrophy of the ring. These observations naturally raise the question of what could be possible mechanisms or instabilities that may be responsible for the fragmentation of the core. Firstly, as noted at the end of section 3.1, there is no observed change in convection speed of the ring at bubble capture. This suggests that the modified vorticity distribution, with decreased enstrophy, at bubble capture, is not directly responsible for the reduction in convection speed, which develops later. The reduction in convection speed and fragmentation of the core, may thus be attributed to an instability of the modified vortex core formed at bubble capture.

There are a few features of this modified vortex core that may be responsible for instability and ultimately the fragmentation of the core. This includes the annular form of vorticity distribution within the water phase, and the presence of sharp density and viscosity changes at the interface. In the case of a single annular 2D distribution of constant vorticity in an incompressible (single) phase, Dritschel [18] and others, have shown that the vortex can be unstable to two-dimensional perturbations, which can lead to fragmentation of the vortex core. Their results show that the instability is dependent on the ratio of the inner and outer radii of the annular vortex patch with thinner annular regions typically being more unstable. It may also be noted that in our low *We* case, where fragmentation of the core is seen, the radial equilibrium position of the bubble at capture, and thereafter, is displaced from the centre of the vortex core. This results in the symmetry (circular) of the vortex core being broken, which could lead to a more unstable core. The sharp change in viscosity and density at the interface could also induce instabilities. This is discussed for example in Govindarajan and Sahu [30] and Dixit and Govindarajan [17], the latter showing that a vortex with a light core having a “stable density" stratification can still be unstable. Apart from these single core instabilities, the influence of the neighbouring oppositely signed core can also be important, as it overlays a strain field on the main vortex, as discussed for example by Leweke and Williamson [43] in the case of the “cooperative" instability of vortex pairs. The stability analysis of O’Farrell and Dabiri [61] further suggests that thicker core vortex rings are inherently more prone to instability than thinner core rings, as also observed in our study.

In summary, given all the features of the present modified vortex core at bubble capture, it is difficult to pinpoint the instability mechanism responsible for fragmentation of the core in the present case. It is clear that a detailed stability analysis of the modified annular vortex core at bubble capture (figures 3.4(c) or figure 3.10(c)) is needed and the result could be a combination of the above influences.

It is also useful to look at the interaction of the vortex ring and the bubble from the energy perspective. In particular, we can estimate the vortex ring kinetic energy, the buoyant energy fed by the bubble to the vortex ring during the interaction, and surface energy extracted by the bubble from the vortex ring due to stretching of the bubble. For example, for the thicker core ring with *We* of 3, where large reduction in convection speed and enstrophy are seen, the ring kinetic energy is an order of magnitude higher than both the buoyant energy and the surface energy. Further, it may be noted that the buoyant energy should ideally add to the ring energy as the bubble and ring rise, while increase in surface energy should result in a reduction in ring energy. However, considering that both of these are an order of magnitude smaller than the ring energy, it is difficult to explain the reduction in convection speed of the ring from this perspective. This again thus points to the fact that there is likely an instability of the modified vortex core (after bubble capture) that is responsible for both the fragmentation of the core and reduction in convection speed.

The present study of a single bubble interacting with a single vortical structure in the form of a ring may be viewed as an idealization of the interaction of micro-bubbles with turbulent structures (hairpin) in a boundary layer, as discussed in the introduction. This raises the question of whether non-dimensional numbers such as V_R and *We* (based on vortex strength) used in the present study are relevant in drag reduction studies using micro-bubbles. The volume of bubble to vortex core volume (V_R) used in boundary layer drag reduction studies for example of Ferrante and Elghobashi [22] can be determined based on the eddy area fraction measurements in turbulent boundary layer of Carlier and Stanislas [8]. The above mentioned bubble injection studies show large drag reduction of about 20% with overall bubble void fraction of about 0.02. Simple calculations based on Carlier and Stanislas [8] show that the corresponding bubble to eddy volume (V_R) is about 0.12 and thus V_R values of the order of 0.1, as used in the present study, appear reasonable. We can similarly see if the strength of the eddy structures or hairpins in turbulent boundary layers are amenable for eddy-bubble interactions based on the present work. From strength and length-scale measurements in boundary layers [16, 34], and a V_R of 0.1, we can estimate the *We* corresponding to a bubble interacting with a hairpin (eddy) structure in a boundary layer. Our estimations based on the above studies suggest that the *We* would be about 10. At such *We*, we clearly see large reductions in enstrophy of structures in the present work, suggesting that the structures in

turbulent boundary layers could also be suppressed with reduction in their enstrophy while interacting with bubbles. Inspite of these similarities, one should however note that there are important differences between the present idealized case of a single vortical structure interacting with a bubble and of a bubble in a turbulent flow. In the later case, the multi-scale nature of turbulence would imply that a bubble would in fact interact with eddies of different scales making the problem considerably more complex, and at the very least requiring studies with a range of volume ratios (V_R) to account for the many eddy sizes.

We can also make further connections between some results from the present study and observations from bubbles in turbulent boundary layer studies. In terms of hairpin vortices in a boundary layer, Zhou et al. [90] showed that primary hairpin vortices of peak vorticity above a certain threshold result in generation of secondary hairpin vortices. As seen in figure 3.18, presence of bubble in a vortex reduces peak vorticity, which could be lesser than the threshold needed for regeneration of hairpin thus resulting in reduction of the hairpin population. This reduction in number of such structures could in turn result in reduction of enstrophy and wall shear stress. Another observation for bubbles in turbulent flow, from both numerical [53] and experimental studies [83], is the enhancement of energy at small scales and reduction in energy at large scales. In the present context, the increase in energy at small scales can be related to the observed increase in shedding behind the vortex ring interacting with a bubble, as shown in figure 3.16(b). On the other hand, the reduction in energy at the large scales can be related to our observed fragmentation of the vortex core into smaller ones, as shown in figure 3.16(b) and 3.22(f). These connections between the present idealized interaction of a vortex ring and a bubble with turbulent bubbly flows suggest that the present work could be useful in understanding a variety of bubbly turbulent flows that are used in many engineering applications.

Chapter 4

Interaction of a single bubble with vortical structures in a turbulent channel flow

In the previous chapter, we have studied the interaction of a single bubble with a single vortical structure, namely a vortex ring. We now proceed to investigate the interaction of a bubble with naturally occurring vortical structures in a turbulent flow. In particular, we study the interactions of a single bubble with unsteady vortical structures present in a fully developed turbulent channel flow. We are interested here, as in the previous chapter, with both the bubble dynamics and the effect of the bubble on the vortical structures present in the turbulent channel flow. We thus study and report in this chapter on the trajectories of single bubbles injected in to a fully developed turbulent channel flow, and also look in to the effect that such bubbles have on vortical structures present in these flows. We are particularly interested to see if bubble capture by a vortical structure in the turbulent flow leads to a rapid decrease in enstrophy of the structure, as seen in the previous chapter for a simple vortical structure. Towards these broad goals, we use high speed visualizations to track injected bubbles in the flow, while simultaneously measuring the velocity/vorticity of the bulk (water) flow using time-resolved Particle Image Velocimetry (PIV). These simultaneous time-resolved measurements enable us to connect bubble trajectories with the small scale vortical structures present in the flow.

Felton and Loth [21] and Tran-Cong et al. [81] have previously studied the trajectories of a single bubble injected in a turbulent boundary layer. Both these studies report on the trajectories of bubbles in a vertical boundary layer, and in particular state the observation of the bubble bouncing on the wall as it moves up along the surface. They make the connection of this type of trajectory with turbulent structures in the boundary layer. In the case of

Tran-Cong et al. [81], they have time-resolved flow visualization pictures and use these to comment on the interaction of the bubble with large-scale structures of the boundary layer. Felton and Loth [21] use time-evolving flow fields to comment on the forces acting on the bubble. In the present work, we study the two-way interaction of a bubble with vortical structures in a horizontal turbulent channel flow. We shall comment both on the bubble trajectories in relation to such vortical structures, and also on the effect that such a bubble can have on these vortical structures.

Another line of thought to appreciate this problem is related to the fact that there are many studies which focus on effect of bubbles on integral properties of turbulence [41, 42, 47, 53, 57, 74, 83], but there are very few studies on the effect of bubbles on vortical structures in a turbulent flow [46, 67]. As stated by Perry and Chong [64], statistical/global properties of turbulence are a manifestation of the the vortical structures present in a turbulent flow. Hence, understanding the interaction of bubbles with vortical structures can help in understanding the modification of statistical/global properties of turbulence due to presence of bubbles.

For the present work, we have designed, fabricated and tested a fully developed horizontal large aspect ratio turbulent channel flow facility. The channel aspect ratio (span/height) is about 12, which is large enough to ensure a nearly two dimensional flow in the mean sense. The base flow field of the channel, in the absence of bubbles, has been measured with PIV, and the mean and fluctuating quantities have been validated with prior measurements, as discussed in chapter 2. We inject single bubbles in to this flow, taking care to minimize any effect on the incoming turbulent boundary layer as discussed in chapter 2 and as we shall see a little later. This is schematically shown in figure 4.1. The single bubble is injected at the mid-section of the span and interacts with the multiple vortical structures present in the incoming boundary layer. We measure the bubble trajectories using high speed visualizations, and also extract small scale structures from the instantaneous flow field obtained using time-resolved PIV. The injected bubble size varies from 0.3 to 1.5 mm in a channel of height (H) 27.5 mm. Experiments are done at two channel Reynolds number ($Re = u_m H/\nu$) of 43400 and 67500 (u_m = mean velocity, H = channel height and ν = kinematic viscosity).

4.1 Bubble trajectory

The single bubble was injected into the channel either from the top or bottom wall at the mid-section of the span through a transparent pipe of internal diameter 4 mm. One side of the pipe was connected to the channel while the other side was closed. The bubble was generated in the pipe through a syringe, with the bubble after detachment from the syringe moving upwards through the pipe due to buoyancy. The bubble then slowly entered the channel, with

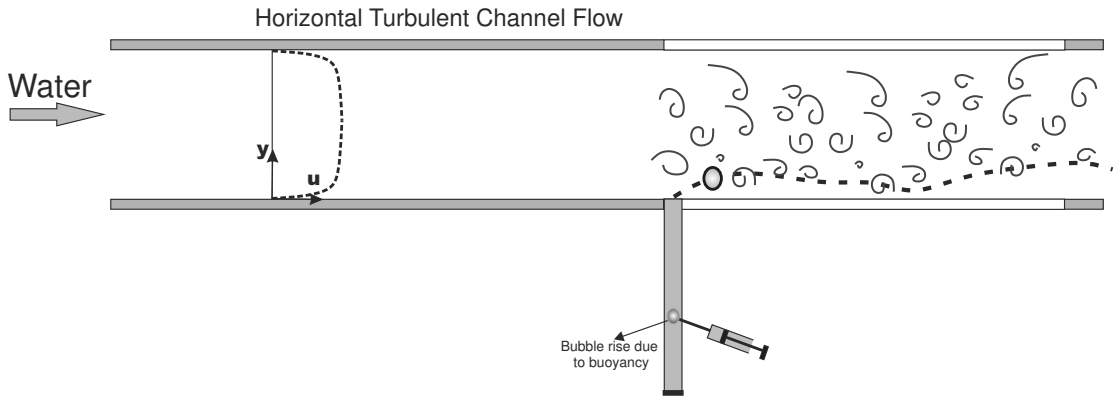

Fig. 4.1 Schematic showing the fully developed horizontal turbulent channel flow and single bubble injection from the bottom wall. It also shows the interaction of the injected single bubble with vortical structures in turbulent channel flow.

the diameter inside the channel being decided by the incoming turbulence parameters and the surface tension. We found the bubble diameter in the channel to vary between 0.3 to 1.5 mm. In this section, we shall present results from high speed bubble imaging done simultaneously in two perpendicular planes, the top and side views. Both visualizations were done at 1600 fps with an exposure time of 15 μs, to get a time resolved 3-D perspective of the bubble motion. The bubble size in the channel and the channel Reynolds numbers are the two main parameters in this case, and we shall discuss the effect especially of the bubble size. For each bubble size many realizations of the bubble path were done to see the variation between realizations.

4.1.1 Bubble injected from bottom wall

Bubbles can either be injected from the top or bottom wall of the horizontal channel. We present here the results for the case when the bubble is injected from the bottom wall, where buoyancy pushes the bubble away from the wall. The bubble diameter (D_b) in the channel varied from 0.3 to 1.5 mm, and we present a number of realizations of each size to show variations in bubble paths.

From the recorded high speed visualizations, we extracted the bubble shape and its location at successive instants in time, and created a composite image showing both shape and the location at all times. This was done for both views, and sample cases showing the three distinctly different types of bubble paths observed are shown in figure 4.2. The three kinds of bubble paths observed are, sliding, bouncing and escape, which is broadly similar to that reported by Felton and Loth (2001) for the case of a bubble in a vertical boundary layer. The main difference is the “escape” path observed here, which is likely linked to

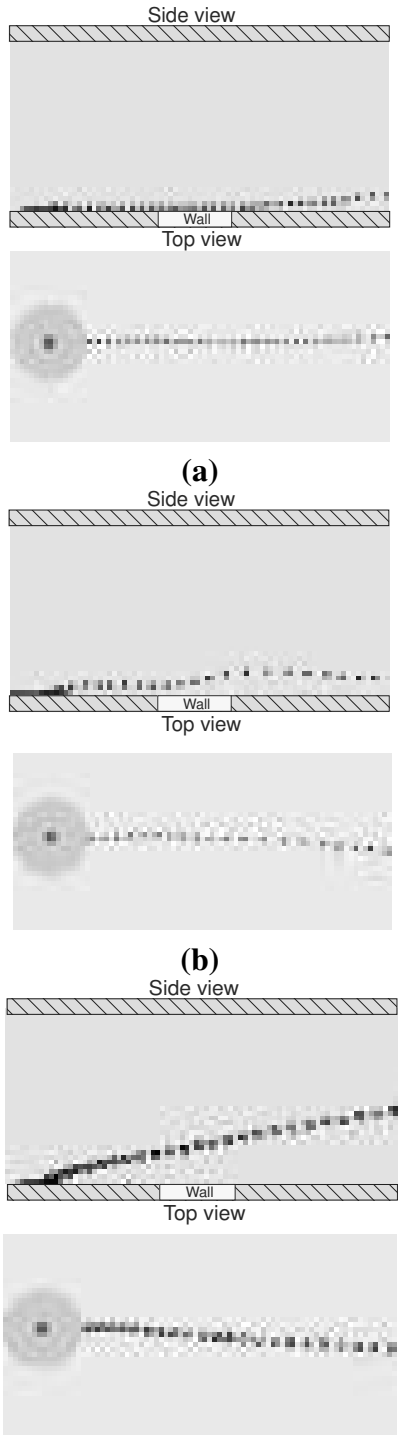

Fig. 4.2 Image showing simultaneous top and side views for different kinds of bubble path traced after injection in to a turbulent channel. In (a), we see the bubble sliding along the wall, while in (b), the bubble appears to bounce. In (c), the bubble escapes. In all cases, the bubble is injected from the bottom wall of the channel. The bubble diameter (D_b) and channel Reynolds numbers for the cases are (a)D_b = 1 mm, Re= 43400,(b)D_b= 1 mm, Re= 67500,(c))D_b= 1.5 mm, Re= 43400.

buoyancy taking the bubble away from the wall. In the first case in figure 4.2(a), we show a sliding bubble, where the bubble remains close to the wall and appears to slide along it for most of the field of view. The simultaneous top view visualization shows a nearly straight streamwise trajectory of the bubble. The bubble trajectory in (b) is distinctly different and shows bouncing behavior, with two bounces within the field of view in the particular case shown. As discussed by Felton and Loth [21], this bouncing is likely caused by the interaction of the bubble with the vortical structures within the turbulent channel. Finally, in (c), we present the case of a bubble that escapes from the wall, this corresponding to a case where the bubble was larger about 1.5 mm. In this case, one can see clear deformations of the bubble as it travels upwards away from the wall, and also at a small angle to the free-stream direction in the top view.

We shall now present bubble trajectories in the wall normal plane for different realizations of the same bubble size and flow *Re*. In figure 4.3, we show fourteen realizations while maintaining the bubble diameter (D_b) at 1 ± 0.05 mm, and the channel Reynolds number at 67500, respectively. In these plots, we show the locations of the bubble at successive time instants without the actual bubble image. It is clear from the figure that there can be considerable variation between realizations for the same D_b and *Re*. The bubble paths shown include sliding at the wall, bouncing on the wall, escape, and combination of the above three types of motions. For example, in figure 4.3*a*, the bubble initially slides for some distance along the wall, after which it moves away from the wall, and then appears to bounce further downstream.

The variations in bubble paths for different realizations, while maintaining parameters to be nearly the same, indicates that the bubble paths are significantly affected by local turbulent structures that can vary considerably. This will become more evident when we look into the interaction of vortical structures present in the flow with a bubble in the next section. In the case of a bubble in a boundary layer on a vertical flat plate, Tran-Cong et al. [81] observed that the bubble will either go near the wall and slide over it, or will migrate away from the wall, depending on the bubble diameter. On the other hand, in our case for a fully developed horizontal channel flow, we observe that even for the same bubble diameter, we see large variations in the kind of bubble motion unlike Tran-Cong et al. [81].

Statistics of bubble path is important to understand the mean and fluctuating nature of bubble motion in a turbulent flow and also to understand two-way coupled interaction between the bubble and the vortical structures. In figure 4.4, statistics of the bubble path in the wall normal plane are shown for flow *Re* and D_b of 67500 and 1 mm, respectively. As seen in (a), the streamwise velocity has a mean of about 1.38 m/s with a variation of about 15% between the difference realizations. On the other hand, the wall normal location (y) in

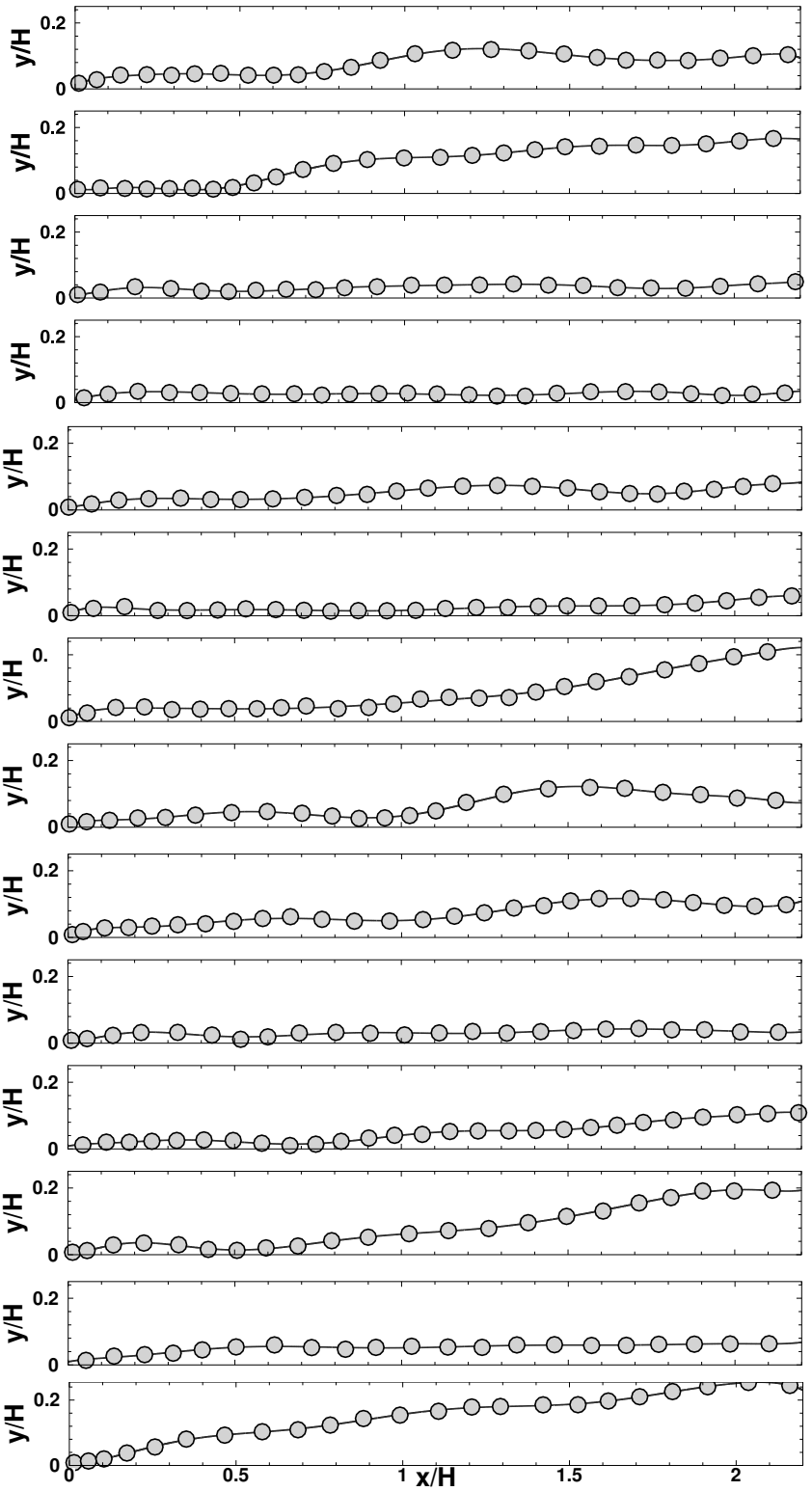

Fig. 4.3 Plot of bubble motions in wall normal plane for different realizations at the same Re = 67500 and bubble diameter (D_b) of 1 ± 0.05 mm. Large variations in bubble paths can be seen between different realizations due to differences in the incoming turbulent structure even at the same Re. Successive data points in the plot are separated by 1.875 ms.

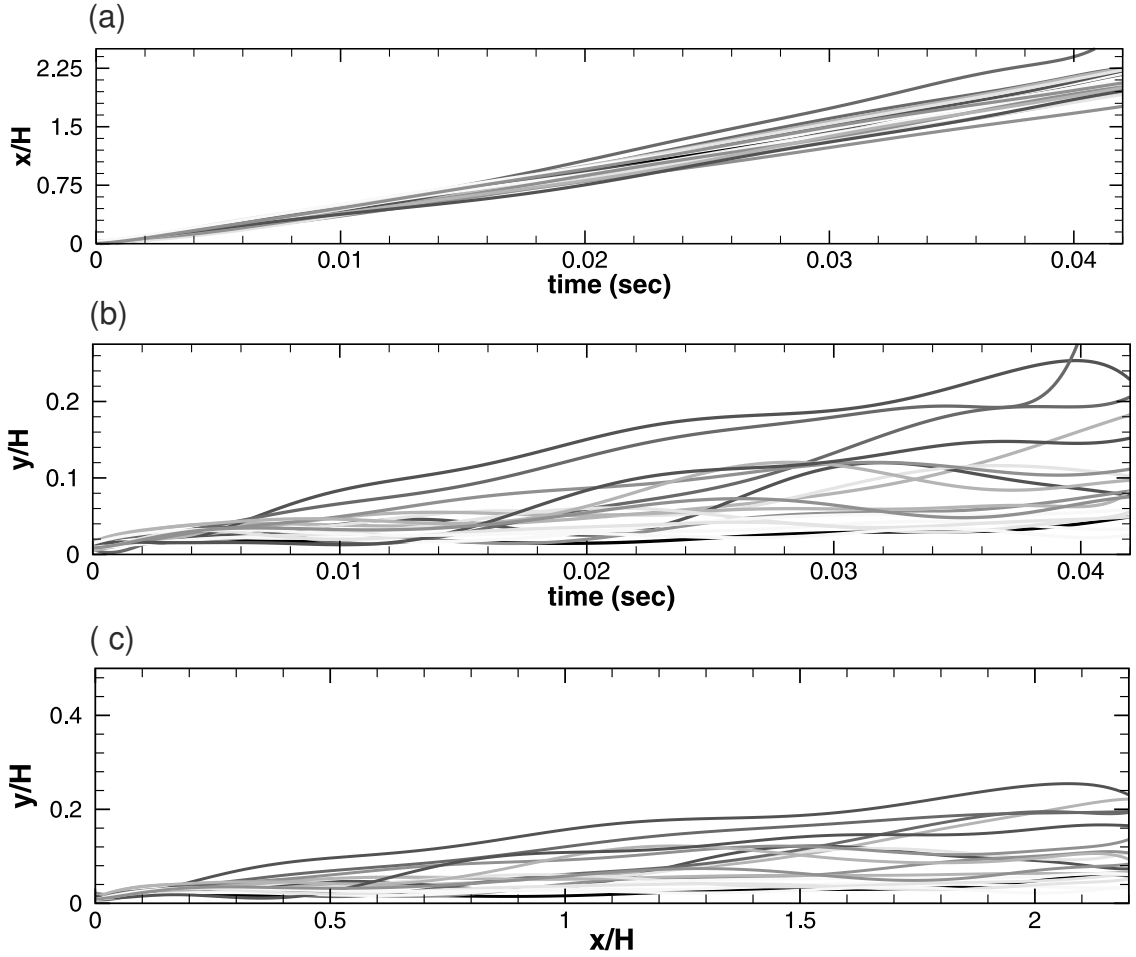

Fig. 4.4 Statistics of bubble motions in wall normal plane for Re = 67500 and bubble diameter of 1 ± 0.05 mm. The plots show a compilation of a large number of bubble trajectories. In (a), variation of streamwise location (x) with time is shown, while in (b), the wall-normal location (y) variations are shown with time. Bubble trajectory in the wall normal ($x-y$) plane is shown in (c). The plots show the large variations in bubble paths caused by the different incoming turbulent structures even at the same Re.

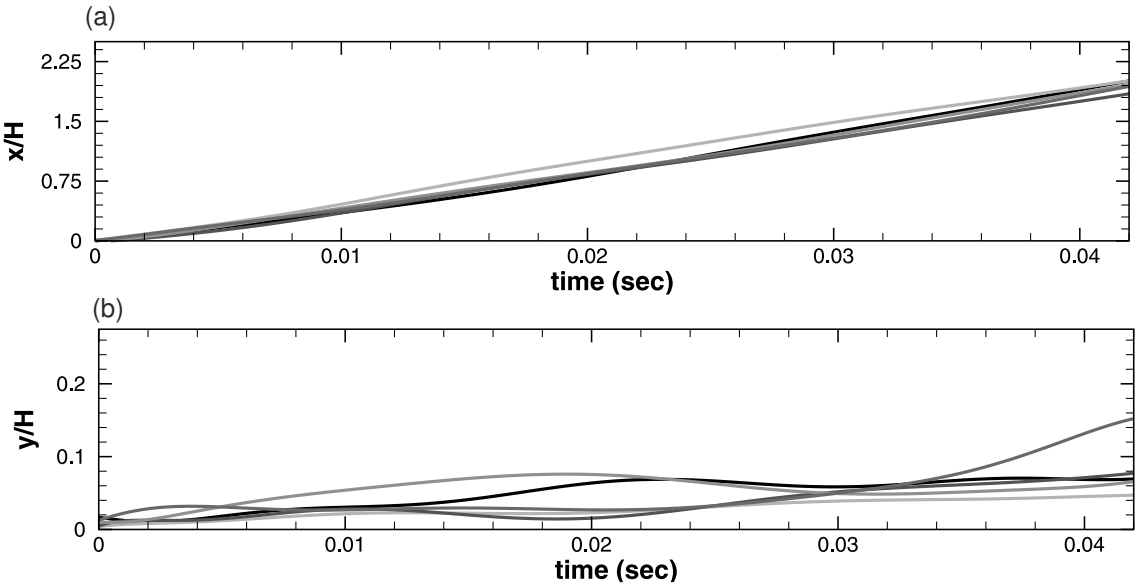

Fig. 4.5 Statistics of bubble motions in wall normal plane for Re = 67500 and bubble diameter of 0.3 mm.

(b), shows much larger variations. This is also clear in the trajectory plot shown in (c), where both x and y directions are normalized by the channel height (H). By the end of the field of view ($x/H = 2.2$), the y location of the bubble can vary anywhere from $y/H = 0.02$ very close to the wall, corresponding to bubble sliding, to $y/H = 0.23$ representing bubble escape.

We shall now present bubble statistics for different bubble sizes, but at the same *Re* as in figure 4.4. This is presented in figures 4.5 and 4.6, corresponding to bubble diameters of 0.3 mm and 1.5 mm, respectively. Comparison of the y location of the bubbles at the end of the field of view across the different bubble sizes in figures 4.3 to 4.5, suggests that the average y location is smallest for the smallest 0.3 mm bubble case. Correspondingly, the mean stream-wise velocity of the 0.3 mm bubble is smallest with a value of 1.28 m/s. The larger 1 mm and 1.5 mm bubbles migrate on average further from the wall probably due to increased buoyancy. This may be quantified by getting a probability of escape for a given bubble size, the escape being say defined as the bubble crossing (y/H) of 0.15 within the field of view. With this definition of escape, the probability of escape for D_b of 0.3, 1 and 1.5 mm is 0.2, 0.27 and 0.43, respectively. As expected, there is a clear increase in probability of escape with increase in bubble diameter. Correspondingly, we find an increase in the mean streamwise velocity from 1.28 m/s for the 0.3mm bubble, to about 1.38 m/s for both the larger 1 and 1.5 mm bubbles. Apart from the presented data at Re = 67,500, we have also done experiments at Re = 43,400 for the different bubble sizes. A sample of this is shown in figure 4.7 for a bubble diameter of 1 mm. The results are broadly similar to the Re = 67,500

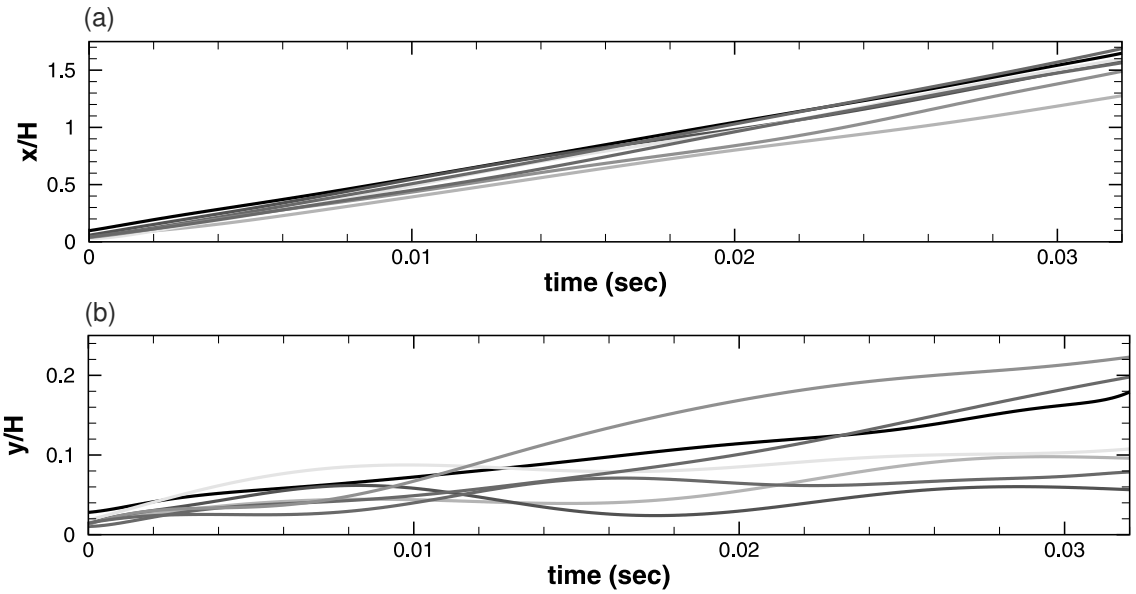

Fig. 4.6 Statistics of bubble motions in wall normal plane for Re = 67500 and bubble diameter of 1.5 mm.

case with the main difference being the larger vertical rise at the lower channel velocities corresponding to the lower Reynolds numbers.

4.1.2 Bubble injected from top wall

We now present results for a single bubble injected in to the horizontal channel from the top wall. In this case, buoyancy helps to keep the bubble close to the wall, unlike in the bottom wall injection case. Images of four realizations of the tracked bubbles in both top and side views are shown in figure 4.8. As seen in the figure, and from many other realizations, the only bubble trajectory seen in this top wall injection case was bouncing. Escape of bubbles is obviously not expected in this case, but perhaps surprisingly even sliding motions of the bubble were not seen for any of the bubble sizes investigated, which varied again from 0.3 mm to 1.5 mm. The only variation between realizations in this case is the variation in amplitude and wavelength of bounce (bubble path), which is again very likely linked to the location and strength of vortical structures in the vicinity of the bubble. In a dilute distribution of bubbles within a horizontal channel, Hara et al. [33] and Murai et al. [59] observe rare occurrence of bouncing of bubbles on the top wall and Hara et al. [33] suggest that this trajectory is likely associated with vortical structures near the wall.

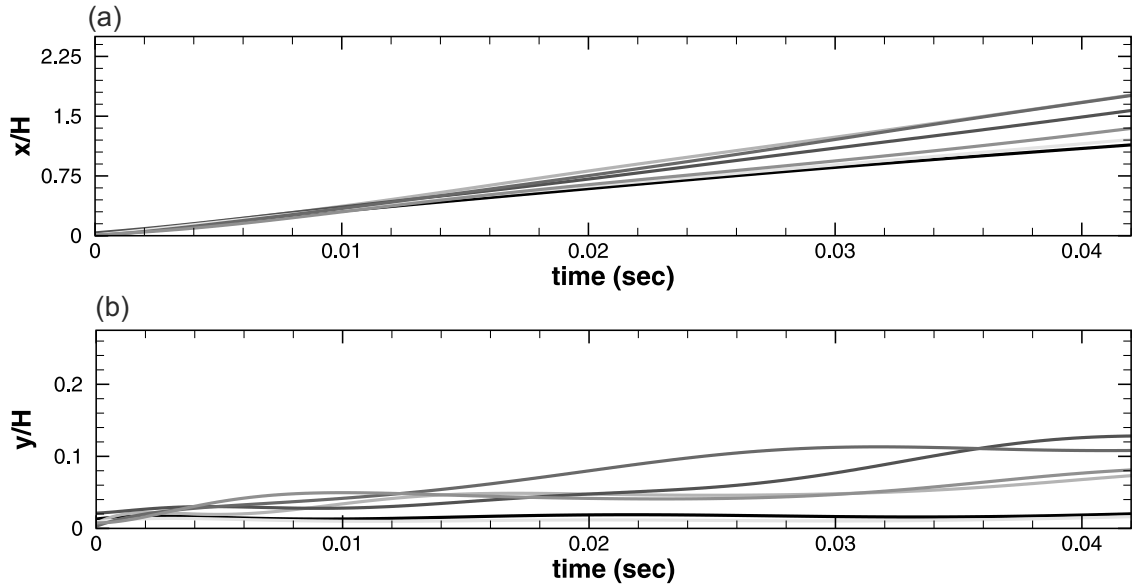

Fig. 4.7 Statistics of bubble motions in wall normal plane for Re = 43400 and bubble diameter of 1 mm.

4.2 Vorticity dynamics and two-way interaction

In the bubble imaging studies, we observed that the motion is predominantly in the wall normal $x-y$ plane. The present turbulent channel flow thus has an advantage over the more well studied homogeneous isotropic turbulence case, where the bubble tracking and the flow field measurements have a strong third dimension motion. In those cases, one has to do 3-D time resolved PIV to study the interaction between the bubbles and the vortical structures in the flow, which is not easy. In the present section, we present time-resolved measurements of the water (carrier phase) velocity/vorticity field to help understand the interaction of vortical structures present in the turbulent channel flow with the single bubble. For this, we do PIV at 1000 fps, which is found to be adequate to track the temporal evolution of vortical structures in the flow and the bubble. The vortical structures in the flow convect at roughly the local mean velocity, which at 1000 fps, gives us about 35 PIV velocity/vorticity fields to track the structures from the left to the right of the field of view. Two PIV snapshots are separated by 1 msec, which at highest *Re* of 67500 corresponds to the non-dimensional time ($t^+ = tu_\tau^2/\nu$) of 11.5, where u_τ and ν are the friction velocity and kinematic viscosity, respectively. A sample set of a time sequence of vorticity fields corresponding to a bouncing bubble path is shown in figure4.9. In the figure, roughly about every 9th vorticity field from the time sequence is shown. We can see from the figure that vortical structures can be captured with good spatial and temporal resolution, the latter is clear as we have about 8 more fields between each of the

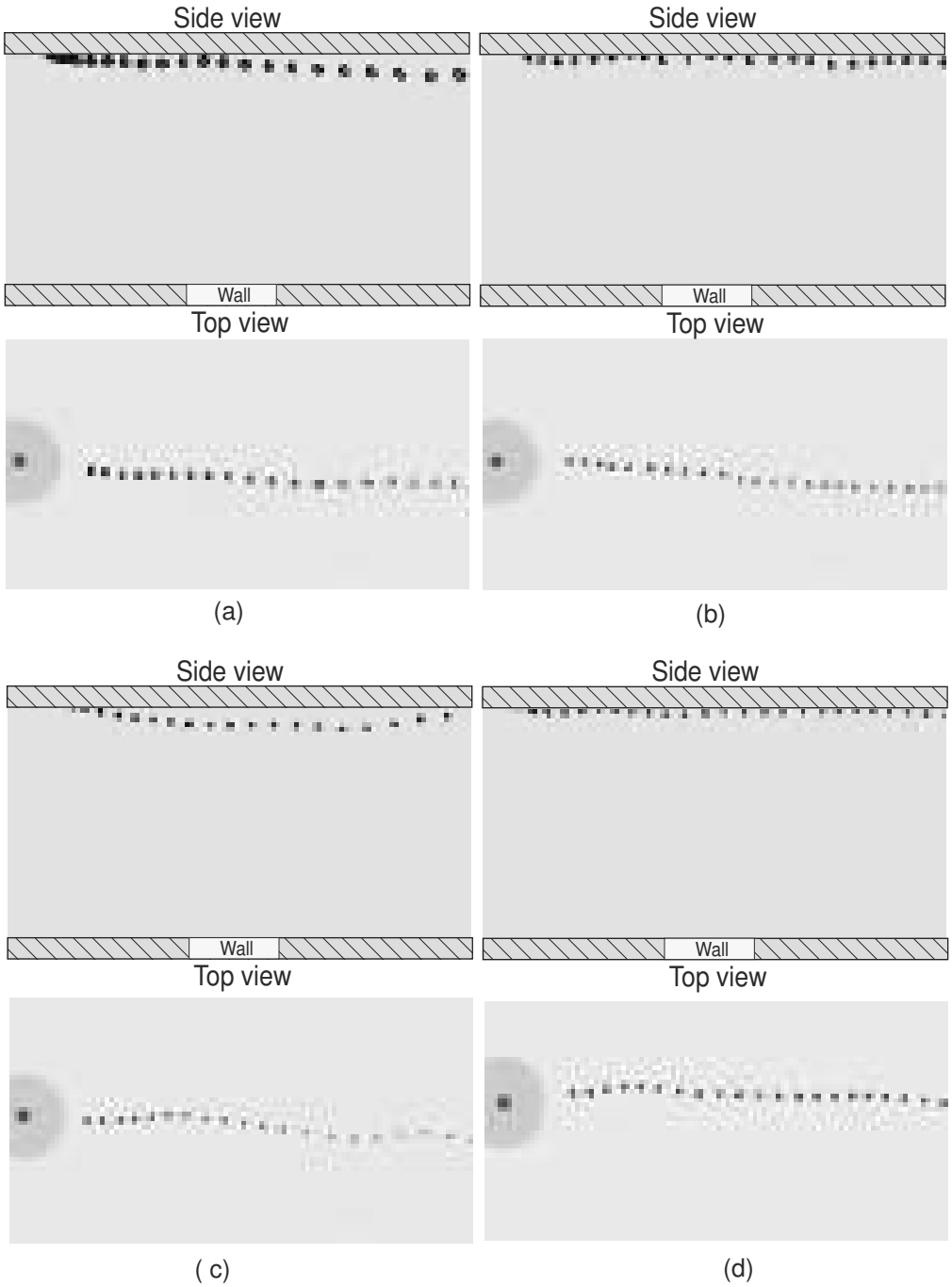

Fig. 4.8 Image showing simultaneous top and side views for single bubble injected from the top wall in to a turbulent channel. Four realizations are shown in (a) to (d), the bubble bouncing in all cases with variations in the bounce streamwise length-scale. The bubble diameter (D_b) and channel Reynolds numbers for the cases are (a) D_b= 1.5 mm, Re= 67500,(b)D_b= 1 mm, Re= 67500,(c) D_b= 0.85 mm, Re= 67500 and (d) D_b= 1 mm, Re= 67500.

successive fields shown in the figure. The non-dimensional numbers involved in the study are the Weber number, We = Inertia/Surface tension ($\sim$1), the Stokes number, St = Particle time scale/fluid time scale ($\sim 10^{-4}$), the Capillary number, Ca = Viscous force/Surface tension (~ 0.1), and the bubble Reynolds number, Re_b = Inertia/Viscous ($\sim$100).

Interest in the existence of vortical structures present in a turbulent boundary layer flow dates back at least to Theodorsen [76] and has been discussed widely in Townsend [80]. Such 'typical' structures have also been used to construct successful statistical models of the turbulent boundary layer (e.g. [64]). These structures are generally considered to be in the form of curved vortex tubes which extend from the wall, forming an arch-like shape, and appear as an inclined train of vortices in the wall normal plane [2]. These structures migrate away from the wall by self-induction, and play a dominant role in wall-normal momentum transport [2, 37]. Reynolds decomposition reveals small-scale vortices because these vortices frequently convect at velocities close to the local mean velocity [1]. It does not however reveal large scale structures, as they are intimately associated with the mean flow [1]. In figure 4.9, we plot the fluctuating velocity vectors and fluctuating span-wise vorticity, to look into the interaction of the bubble with small scale structures present in the turbulent channel flow. This velocity/vorticity field presentation is similar to the one adopted by Joshi et al. [39] to look into the suppression of structures due to a favorable pressure gradient in a turbulent boundary layer. Vorticity contours are kept constant for all cases presented in this section and are shown in figure 4.9a. In each image, the bubble is marked as a hatched area with magenta colour. Wake of the bubble is not seen in the PIV field, which may be either due to bubble Reynolds number (Re_b) being below the critical value or related to the strength of these shed vortices being too small compared to that of vortical structures present in the flow. The bubble convects along with the local vortical structure in figure a and b, and is completely entrained in to the vortical structure in c. The bubble then convects with the vortex core, the bubble being trapped within it till the end of the frame shown in figure 4.9d. Zoomed in and more temporal snapshots of the interaction are shown in figure 4.15 as we shall see later.

As discussed in the bubble dynamics section, the other possible bubble path type is an escape path, where the bubble escapes from the near wall region. In figure 4.10, we present time resolved PIV for the case of escape of the bubble. All the vorticity contours, bubble masking and plot presentation is similar to that in the previous vorticity fields shown for the bouncing case. Escape of the bubble may be either due to absence of strong structure in the vicinity of the bubble, in which case the bubble rises due to buoyancy, or the small scale vortical structure itself being lifted up due to the induced motion of other vortical structures. Bubble can also lift up due to Q_1 or Q_2 (ejection) events close to it. Sliding of

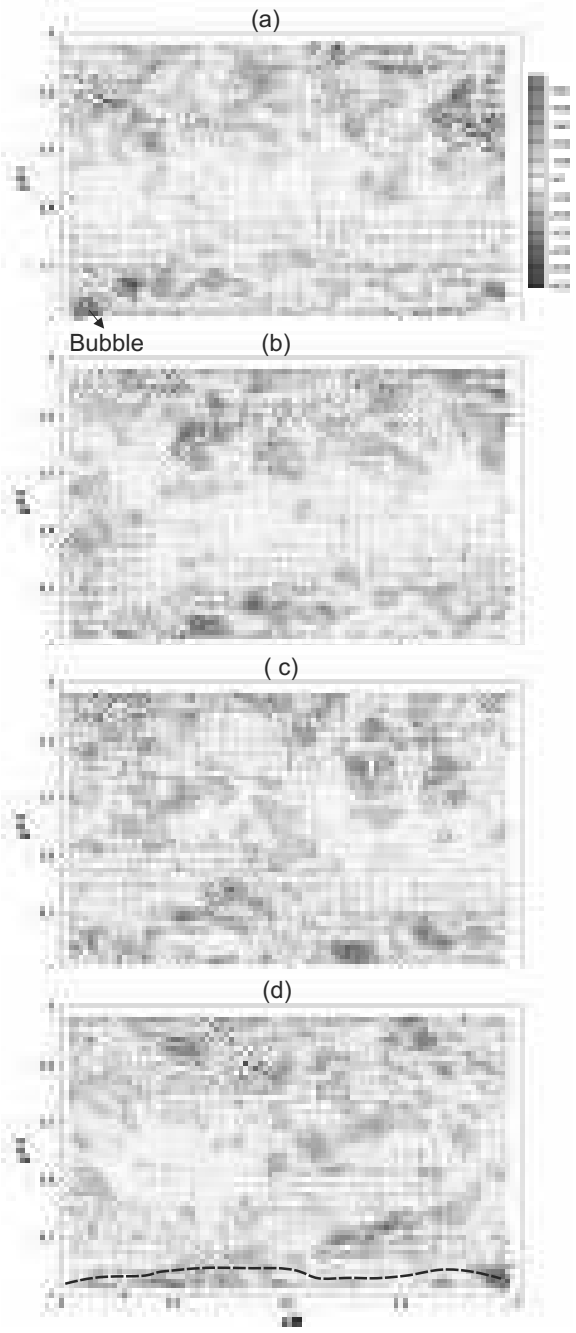

Fig. 4.9 Example time sequence of vorticity fields corresponding to a bouncing bubble path. In each of the plots, we show both the fluctuating velocity vectors and contours of the fluctuating spanwise vorticity, the latter being a good indicator of small scale structures. The location and shape of the bubble is also marked in each of the plots by a hatched magenta area, with the bouncing bubble path being shown by a dashed line in (d). The bubble diameter is close to 1 mm and the channel Reynolds number is 67,500. The non-dimensional time ($t^+ = tu_\tau^2/\nu$) corresponding to each of the images shown is (a) 11.5, (b) 92, (c) 195.5 and (d) 299, where u_τ and ν are the friction velocity and kinematic viscosity. When bubble enters the field of view corresponds to the time, t = 0 second.

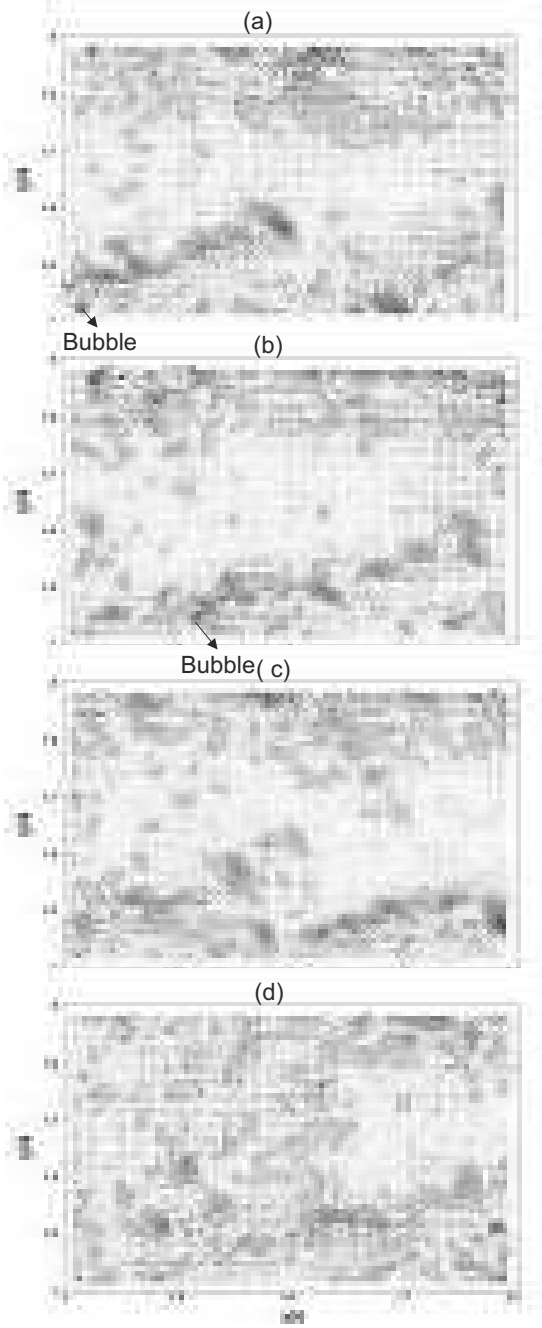

Fig. 4.10 Example time sequence of vorticity fields corresponding to an escaping bubble path. In each of the plots, we show both the fluctuating velocity vectors and contours of the fluctuating spanwise vorticity. The location and shape of the bubble is also marked in each of the plots by a hatched magenta area, with the escaping bubble path being shown by a dashed line in (d). The bubble diameter is close to 1 mm and the channel Reynolds number is 67,500. The non-dimensional time ($t^+ = tu_\tau^2/\nu$) corresponding to each of the images shown is (a) 11.5, (b) 126.5, (c) 241.5 and (d) 379.5, where u_τ and ν are the friction velocity and kinematic viscosity. When bubble enters the field of view corresponds to the time, t = 0 second.

bubble at the wall as observed in figure 4.11, can again be either due to the bubble entrained in some vortical structure near the wall or related to the downward Q_3 or Q_4 (sweep) events of the flow. Tran-Cong et al. [81] experimentally studied bubble migration within a turbulent boundary layer on a vertical flat plate. They observed that the bubble would either go near the wall and slide over it, or it could migrate away from the wall even with release at the wall, which is decided by the bubble diameter and large scale structures. Felton and Loth [21] studied the motion of spherical bubbles in a turbulent boundary layer. By knowing bubble motion and the flow field around it, they obtained instantaneous liquid forces acting on individual bubbles in a turbulent flow to ascertain drag and lift coefficients. Significant vorticity surrounding the bubble can cause a shear-induced lift force to drive the bubble towards the wall. Bubble path is either affected by single eddy or combination of many eddies. Bubble in the turbulent flow can even be surrounded by multiple structures. One such typical case of a zoomed in structure in a turbulent boundary layer is shown in figure 4.12. In this case, the bubble is surrounded by four eddies of different strength, size and relative distance with respect to the bubble. In such cases, when the bubble is surrounded by multiple eddies, it will have an induced pressure force due to individual structures, and the net force will be the summation of the contribution of these vortical structures.

The pressure field around a vortical structure can be calculated from velocity fields obtained from PIV. This can be done by substitution of the velocity field into the Navier-Stokes equation to determine the pressure gradient term, which can in turn be integrated with respect to a reference pressure, say the far field value, to get the pressure field similar to Dabiri et al. [14]. Along similar lines, we have determined the pressure field from our measured PIV velocity field, and an example of this is shown in figure 4.13(b), the pressure contour being $P - P_\infty$ (P_∞ is the far field pressure). This pressure field corresponds to the vortical structure near the top wall marked by a square region in figure 4.13(a). As one would expect, we find that the centre of the vortex corresponds to a minima in pressure. This pressure minima is similar to that observed in the previous chapter within the core of a vortex ring and for a single vortical structure in a turbulent boundary layer flow by Joshi et al.[39].

Now, we look at the different forces acting on a bubble inside a turbulent boundary layer. There are few forces which one finds even in the laminar boundary layer like lift force (shear lift, Magnus, shedding behind bubble), drag force and added mass force. Presence of vortical structures in a turbulent boundary layer, as in the present case, brings in additional forces. There is the pressure gradient based force towards the vortex center, which in the multiple eddies case, as in figure 4.12 results in a force towards each vortex centre. Distribution of structures in a turbulent boundary layer is random, which gives rise to a complex pressure gradient induced force. Further, as the bubble reaches the vortex core, it also experiences

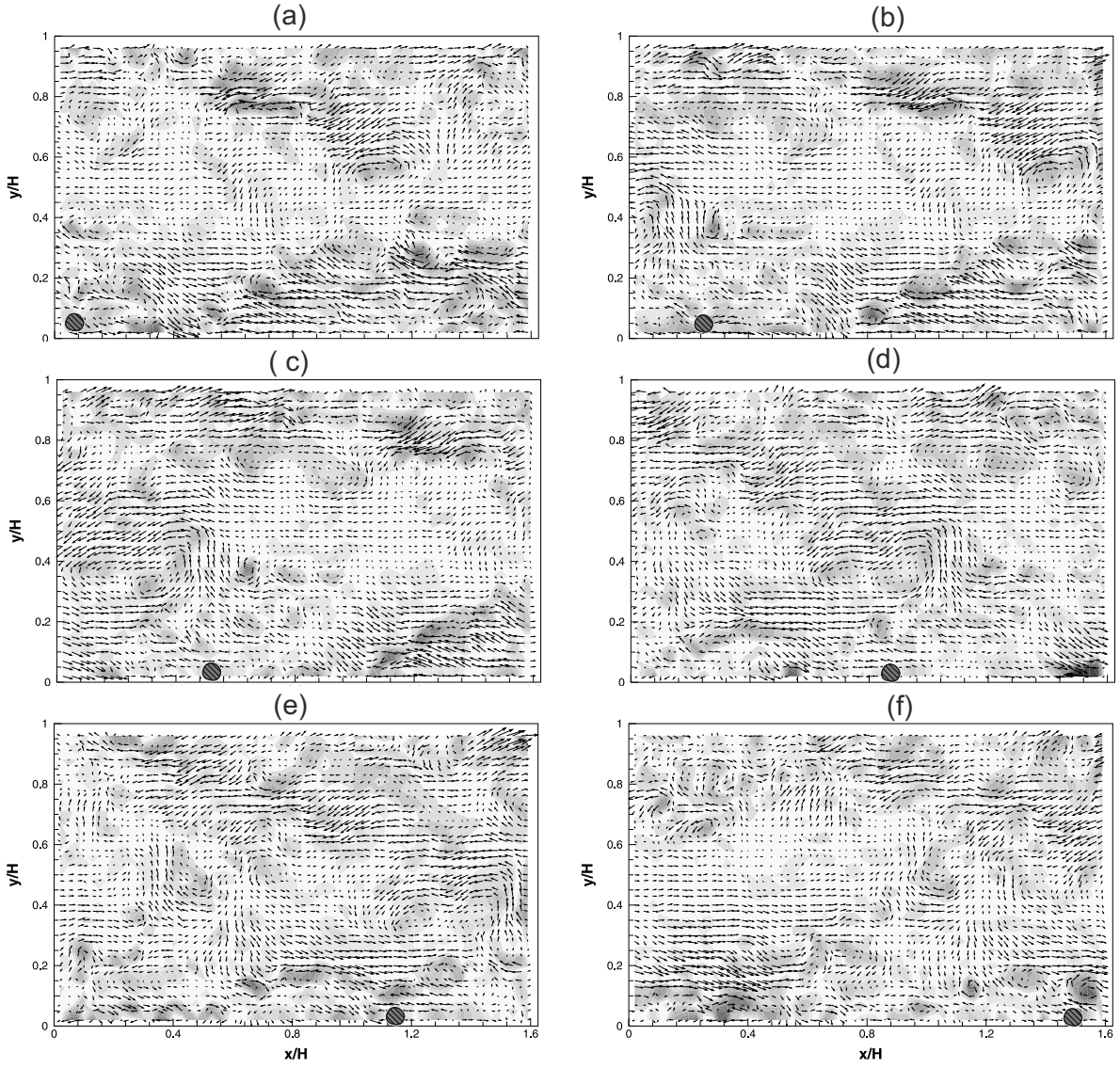

Fig. 4.11 Example time sequence of vorticity fields corresponding to a sliding bubble path. In each of the plots, we show both the fluctuating velocity vectors and contours of the fluctuating spanwise vorticity, which is a good indicator of small scale structure in boundary layer flows. The location and shape of the bubble is also marked in each of the plots by a hatched magenta area. The bubble diameter is close to 1 mm and the channel Reynolds number is 67,500. It shows the sliding of bubble near the wall along with the interaction with the flow field. The non-dimensional time ($t^+ = tu_\tau^2/\nu$) corresponding to each of the images shown is (a) 11.5, (b) 69, (c) 126.5, (d) 218.5, (e) 299 and (f) 391, where u_τ and ν are the friction velocity and kinematic viscosity. When bubble enters the field of view corresponds to the time,$t = 0$ second.

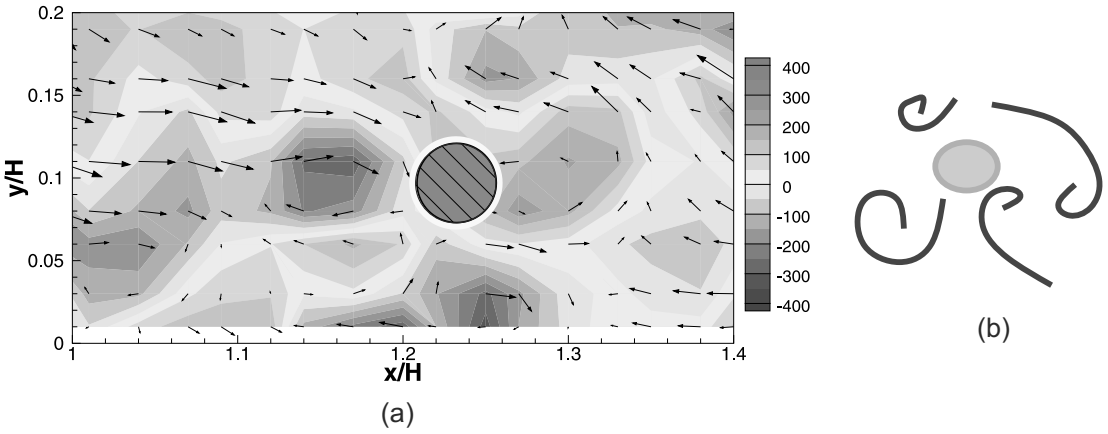

Fig. 4.12 Plot shows the zoomed in view of the fluctuating vorticity around a bubble in (a), showing the presence of multiple eddies. This is schematically shown in (b). The channel Reynolds is 67,500 and the bubble diameter is 1 mm.

a fluctuating shear lift force. The problem may be even more complex, as, it is a two-way coupled problem, with the vorticity distribution itself being affected by the bubble.

One way to estimate the total strength/life of vortical structures in a turbulent flow is to look at the enstrophy or volume integral of the square of the vorticity of the structures. Lu et al. [46] plots the enstrophy to look into the total vorticity present in the flow field and observes a suppression of enstrophy due to the presence of bubbles. In chapter 3, we also observe suppression of enstrophy of vortex ring due to its interaction with a bubble. In the numerical study for turbulent channel flow by Zhou et al. [90], they plot the volume integral of the fluctuating spanwise vorticity to help understand the evolution of a group of vortices. In the current study, as 2D time resolved PIV measurements have been done, the enstrophy is calculated as the area average of the square of the fluctuating spanwise vorticity, this being representative of the principal vorticity of the structure. For the purpose of enstrophy calculation, a rectangular area that covers the complete vortical structure was used in each time instant, as shown in the bottom of figures 4.14 and 4.15. Figure 4.14 shows the variation of enstrophy with time for a vortical structure present in the channel flow in the absence of a bubble; the enstrophy being non-dimensionalised in each case by its maximum value. A vortical structure in a boundary layer flow takes birth, grows and reaches an equilibrium state. At later times, the vortical structure decays down slowly, giving birth to newer structures. This process can be observed in figure 4.14, where enstrophy first increases, reaches a maxima and stays at the maximum value for about 60 wall units in time (t^+), before slowly decaying again down to a very small value. This can be seen from the vorticity plots also shown in figure 4.14, which show the measured vorticity distributions, as

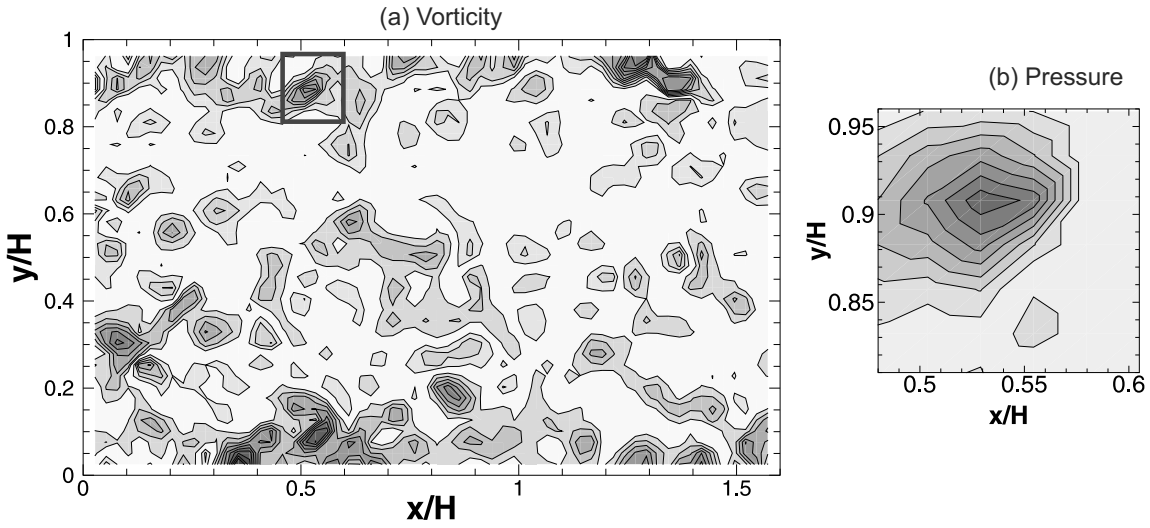

Fig. 4.13 The pressure field around a vortical structure marked in (a) is shown in (b).

marked on the enstrophy plot. As is clear from the vorticity plots, the vortex core initially become stronger, and reaches a maximum and then stays there for some time before decaying down slowly. We refer to the time spent within the maximum 10% of enstrophy (between 0.9 and 1.0) as the life time of the structure (t^+_{life}), which was typically found to between 60 and 65. Similar equilibrium state time scale is observed by Zhou et al.[90] in his numerical study of a turbulent channel flow.

Effect of a single bubble on the evolution of vortical structure is plotted in figure 4.15 for the bouncing bubble path. As seen in the vorticity plot, the bubble gets entrapped within a vortical structure from (c) to (h) and convects along with it. The enstrophy for this case is also shown in the figure. As in the previous figure, we can see the clear increase in the enstrophy realted to the growth of the structure. There is however in this case a significant difference once the bubble is captured by the structure at (d). Although the structure grows in strength, as noted by the enstrophy increase, it does not stay at the peak value for long. The lifetime of this structure, defined as before as the time when the enstrophy is within 10% of the maximum, is now found to be significantly smaller about 33 wall units as compared to 60 wall units for no bubble case. This suggests that as in the vortex ring case in chapter 3, we can see reasonably rapid decrease in enstrophy of the structure when it entrains a bubble.

The enstrophy plot in figure 4.15 while suggestive is not as strong as in the vortex ring case. The vortical structures in the turbulent channel flow are more complex in structure with large variations between them. Since no two structures are the same, it is not easy to compare the effect of a bubble on such structures, as there is no clear base vortical structure.

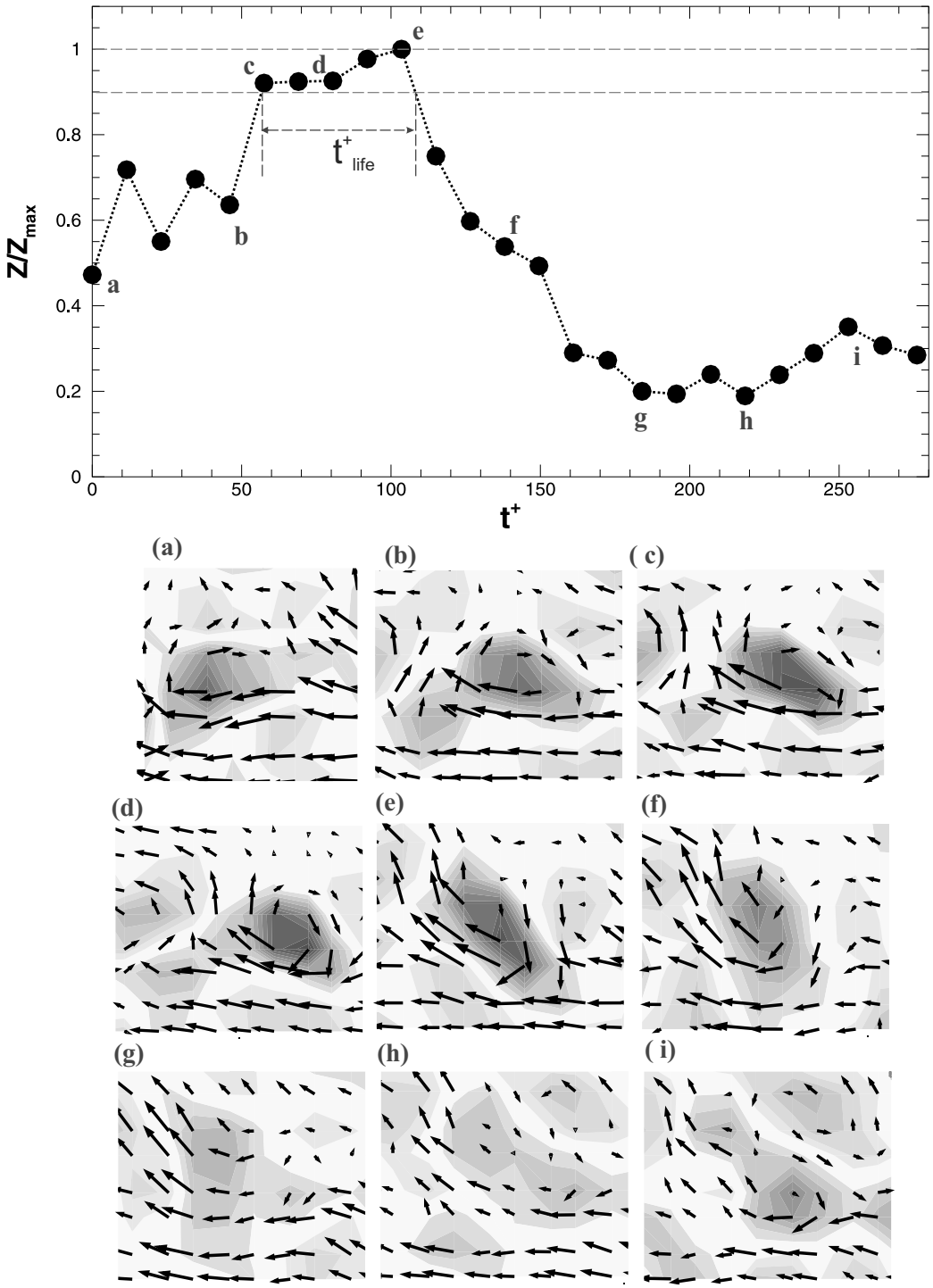

Fig. 4.14 Evolution of enstrophy (Z) normalised by maximum enstrophy (Z_{max}) for a single vortical structure in a turbulent boundary layer is shown with non dimensional time ($t^+ = tu_\tau^2/\nu$). There is no bubble within the structure in this case. Also shown are the fluctuating vorticity fields at different instants (a) to (i), as marked on the enstrophy plot.

These observations are therefore not very conclusive, but they do suggest that presence of a bubble can affect vortical structures that capture it, very similar to the idealized vortex ring structure studied in the previous chapter.

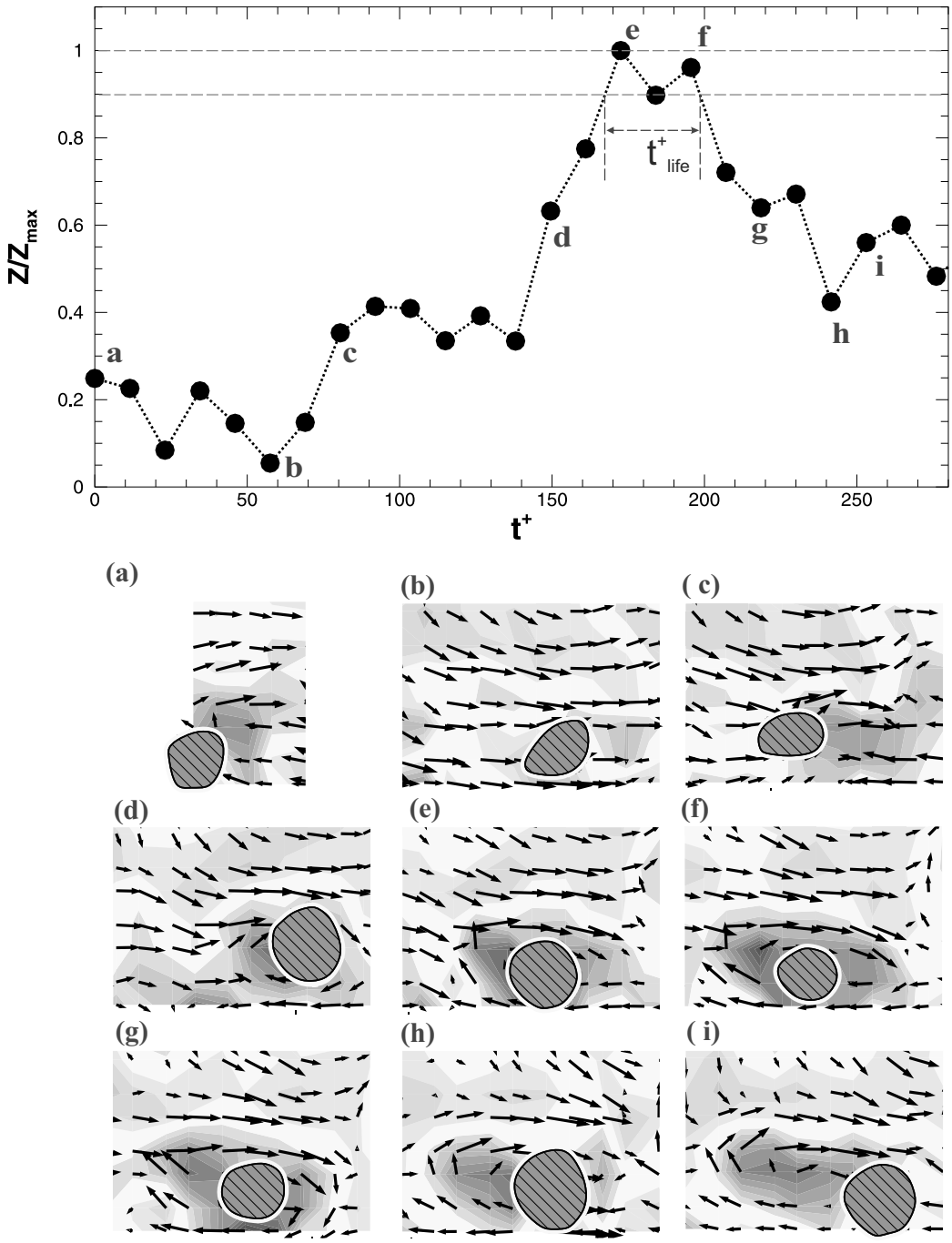

Fig. 4.15 Evolution of enstrophy (Z) normalised by maximum enstrophy (Z_{max}) for a single vortical structure in a turbulent boundary layer is shown with non dimensional time ($t^+ = tu_\tau^2/\nu$). Also shown are the fluctuating vorticity fields at different instants (a) to (i), as marked on the enstrophy plot. In the figure, the bubble is shown in magenta colour filled with hatched lines.

Chapter 5

Effect of bubble distribution and buoyancy on pressure field and drag in channel flow

We now proceed from the single bubble in a fully developed turbulent channel flow to the problem of a large number of bubbles injected in to the channel. This is directly linked to the problem of bubble injection in to a flat plate boundary layer, which has been studied for some time due to the possibility of using it for drag reduction in ships and other under water vehicles. Micro-bubble injection into a turbulent boundary layer has been studied for a long time, starting from the pioneering work of McCormick and Bhattacharyya [54]. It is now well established that drag reduction in these flows is a strong function of bubble void fraction near the surface [9, 49, 69]. There are however large variations in drag reduction among different studies in the literature, as reported in the recent review of Ceccio [9]. These variations are probably a reflection of the fact that there are many other parameters other than void fraction that can significantly influence the final drag reduction. Elbing et al. [20], Madavan et al. [49], Murai [58], Sanders et al. [69] have extensively studied drag reduction using bubble injection in various forms. In particular, Elbing et al. [20], Sanders et al. [69] have studied drag reduction at very high Reynolds numbers on a flat plate in a large-scale facility. In their experiments, the bubbles are injected from the bottom of the plate with buoyancy helping to keep the bubbles close to the wall. In contrast, the earlier studies of Madavan et al. [49] used injection from the bottom wall of the flat plate, where buoyancy helps in the migration of bubbles away from the wall. Murai [58] in his review summarizes the work of a number of studies on bubble injection in a horizontal channel. These studies generally report on injection from the top wall of the channel, where buoyancy helps to keep the injected air close to the top surface. A study on bubble injection from the lower wall of a channel was

done by Gabillet et al. [26], where the bubbles naturally migrate away from the wall, with the study reporting on measurements of both the water velocity and measurements of the void fraction and bubble diameter.

In the present work, we report results from our studies on bubble injection in to a horizontal channel. We are interested again in both bubble dynamics and in the vortical structures within the flow. In this study, we use pressure drop measurements at different vertical heights to ascertain the effect of the bubbles on the vortical structures, as it is not possible to obtain reasonable PIV measurements in flows with large amount of bubbles. The bubble dynamics are however again directly visualized using high speed visualization as in the previous chapter. The parameters that are varied in this work are the bubble void fraction (α), the channel Reynolds number (Re), and the orientation of injection in to the channel. The bubble void fraction, (α), which is the ratio of the volumetric flow rate of injected air from one wall (Q_a) to that of water flow rate in the channel (Q_w) is varied from 0 to about 0.2, this being measured and controlled by an air controller feeding air to the bubble injection system. Experiments are done at seven bubble void fraction (α) of about 0.025, 0.05, 0.075, 0.1, 0.125, 0.15, and 0.175. The experimental arrangement permits injection of bubbles through porous plates from either only the top wall, or only the bottom wall, or from both walls. We have studied and report results on all these three combinations. In addition, the channel Reynolds number has been varied over the range from about 22,500 to about 67,500 at four Reynolds number ($Re = \mathrm{u}_m\,\mathrm{H}/\nu$) of 22500, 43400, 54600, 67500. In all these cases, we visualize the bubble dynamics in two perpendicular views and also measure the stream-wise pressure drop at four vertical locations on the channel. From these systematic measurements over a range of parameters, we attempt to identify different bubble dynamics regimes and relate it to the pressure drop distribution and wall drag within the channel.

A schematic of the experimental arrangement is shown in figure 5.1. Bubbles are injected either from top or bottom walls or from both walls over a 100 mm porous plate section. The sintered porous plate is pressurized through an air chamber with bubble formation taking place at the porous surface in contact with the water in the channel. The bubble diameter near the porous plate varied from 200 to 400 μm depending on the conditions. Transparent window for visualising bubble dynamics and measuring pressure drop starts 85 mm after the end of the bubble injection section. The pressure drop measurements are done a little downstream (85 mm) of the porous plate over a stream-wise length of 332 mm, this pressure drop measurement being done at four vertical locations, as will be discussed later.

Top and side views of the bubble dynamics are captured using high speed cameras at 1600 fps and exposure time of 15 μs to study temporal and spatial bubble shape size evolution. Captured images have a stream-wise field of view of 56.5 mm for front view and 143.2

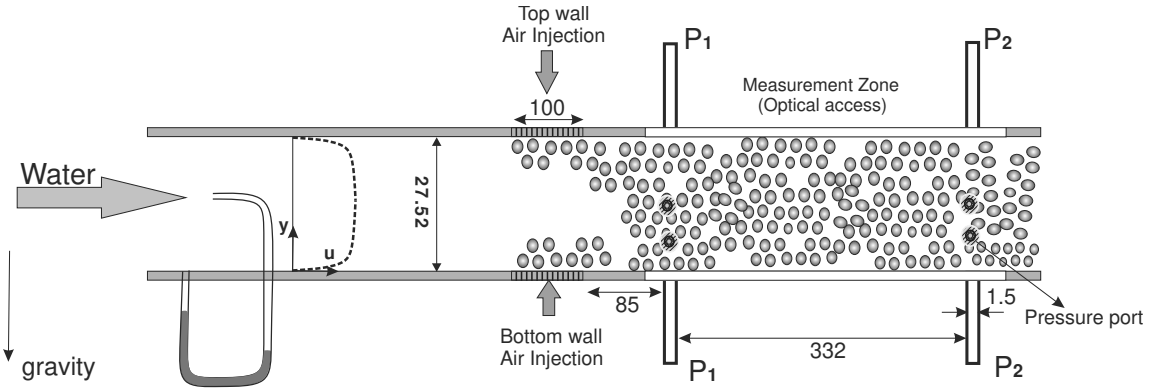

Fig. 5.1 Schematic showing the main components of the experimental set-up used for injection of a large amount of bubbles in to a fully developed channel test-section. The injection ports on both top and bottom walls, besides the transparent section for bubble visualization and pressure ports are shown along with the important dimensions. All dimensions shown are in mm.

mm for top view, starting from 100 mm after the end of the injection plate. Pressure drop is also measured to study the effect of bubbles on wall drag. Center-line velocity (U_c) for undisturbed fully developed channel flow was measured using a Pitot-tube at the end of the development section of channel as shown in figure 5.1. When we inject bubbles in the channel, the incoming water flow rate was affected and it was brought back to the required value by adjusting the pump controller. Pressure drop was measured at different channel height (y/H = 0, 0.25, 0.5, 1) to study the effect of bubbles on the vertical distribution of pressure drop. Of these measurements, y/H = 0 and 1 measurements were done on the top/bottom wall along the mid-span of the test-section, while the other two measurements at y/H = 0.25 and 0.5 were done on the side walls as shown in figure 5.1. Measurements indicated that there was little span-wise variation of the pressure drop, as suggested by comparison of the pressure drop values done at the centre-line (from top/bottom walls) and compared with side wall measurements done close to the top/bottom walls. We shall first present bubbly dynamics from direct imaging in section 5.1, and then present results from pressure drop measurements in section 5.2.

5.1 Bubble dynamics

Understanding two way coupling between the bubbling condition and resultant effect on integral flow properties explains about underlying physics of the interaction. The relation between two comprises of complex multi-variable interaction, which come from bubble (dispersed phase) properties, undisturbed flow (carrier phase) properties and two-way coupled

parameter. Physics of the single phase turbulent boundary layer is highly difficult to deduce as it is described by so many parameters (different length scales, different velocity scales, different *Re*). When one inject the bubbles, they give rise to a huge parametric space and makes the study complex and hence, to come-up with universal scaling/physics of the interaction between the two is a challenging task.

Spatio-temporal scale of bubbles near the surface and in the flow affects the mean and fluctuating flow and wall shear stress. In this section, we shall present results from high speed bubble imaging in two orthogonal views, namely the top and side views. A total of 36 cases were visualized corresponding to three void fraction (0.05, 0.1 and 0.15), three bubble injection orientations (top wall, bottom wall, and both walls), and four channel Reynolds numbers (22500, 43400, 54600, 67500). Due to the large amount of resulting visualizations, we present in this section only samples showing the different types of bubble dynamics regimes seen. A more systematic presentation of the bubble dynamics for the different cases is shown in Appendix *A*.

5.1.1 Discrete Bubbles distributed in flow

Broadly, we observe four kinds of bubble dynamics depending on the void fraction, the Reynolds number of the channel and orientation of bubble injection. These types are classified either by bubble size or relative position of bubble with respect to the wall. First of these different types is when the bubble is reasonably uniformly distributed in the flow field near the wall region where bubbles are injected. A sample visualization showing this type of bubble dynamics is shown in figure 5.2. This corresponds to flow *Re* and α of 67500 and 0.05, respectively, and for the both wall injection case. We see here discrete bubbles of mean diameter of about 1.7 mm distributed near the top and bottom walls, with the bottom wall injected bubbles migrating to about half the channel height. The present visualization may be compared with the different kind of bubble paths seen in chapter 4 for flow *Re* of 67500 and D_b of 1.5 mm. The variations in bubble vertical location seen in chapter 4 compare reasonably with vertical extent of the bubble distribution seen in the present multi-bubble case. This is likely related to the relatively low void fraction in the present multi-bubble case, which minimizes chances of bubble-bubble interactions, and hence vertical migration of bubbles in the two cases is comparable. Other examples of such discrete bubbles in the flow are shown in appendix figures A.4(a), A.8(a) and A.13(a). Broadly, we see such discrete bubbles near the wall at high *Re* and low void fraction cases. This is consistent with the observations of such bubble dynamics by Madavan et al. [49], Murai [58], Sanders et al. [69].

This type of discrete bubbles are possible when buoyancy and lift force is much smaller compared to the flow drag in the stream-wise direction. In other words, the wall normal

migration of bubbles is small compared to the stream-wise velocity, so that most of the bubbles stay in the near wall regime, where it affects wall drag the most. Buoyancy and lift force on the bubble is a function of the size of the bubble, which is decided by the flow characteristics at the point of detachment and the bubble coalescence characteristics. Coalescence probability inside the test-section is decided by coalescence time scale as compared to the flow time scale and the bubble void fraction. If these two parameters are such that coalescence is not strong then we find discrete small size bubbles in the channel and they stay close to the wall. Drag reduction for this particular bubble size is mainly decided by its interaction with the vortical structures present in the turbulent boundary layer. The parameters which encourage this type of bubble dynamics are high flow Re, small α, and either top or bottom wall injection orientations.

5.1.2 Coalesced large bubbles in the flow

Near the porous plate at the point of detachment, the size of the bubble is decided by the incoming flow characteristics. However, further downstream near the measurement/visualization section, the bubble size is predominantly decided by the turbulence characteristics and coalescence probability. Increasing the bubble void fraction increases the probability of coalescence, and hence of finding large coalesced bubbles. In figure 5.3, we show sample images of large bubbles near the centre of the channel for Re and α of 67500 and 0.15, respectively, for bottom wall injection. These bubbles slowly coalesce and rise away from the bottom wall by the mutual effect of buoyancy and lift force. The size of these bubbles is very large, of the order of about half the channel height. In figure 5.3, we can see small bubbles near the bottom wall and highly deformed coalesced bubbles of large size near the center of the channel. In the top view, we see different size of bubbles, which can also be seen in the side view at different vertical heights. We will see later that despite the presence of such large bubbles near the channel centre, there are large reductions in total drag for this condition. This type of large coalesced bubbles would be expected to occur in large void fraction cases, but are not easy to see in the flat plat cases in large facilities, where bubble visualizations are not easy. We are not aware of prior visualizations showing clearly such very large bubbles. The parameters which encourage this type of bubble dynamics are high flow Re, moderate to large α, and bottom wall injection.

5.1.3 Coalesced large bubbles at the top wall like an air layer

One other mechanism to reduce frictional drag is by sustaining an air layer near the surface, as discussed by Elbing et al. [20]. In this case, injection has to be done from the top wall

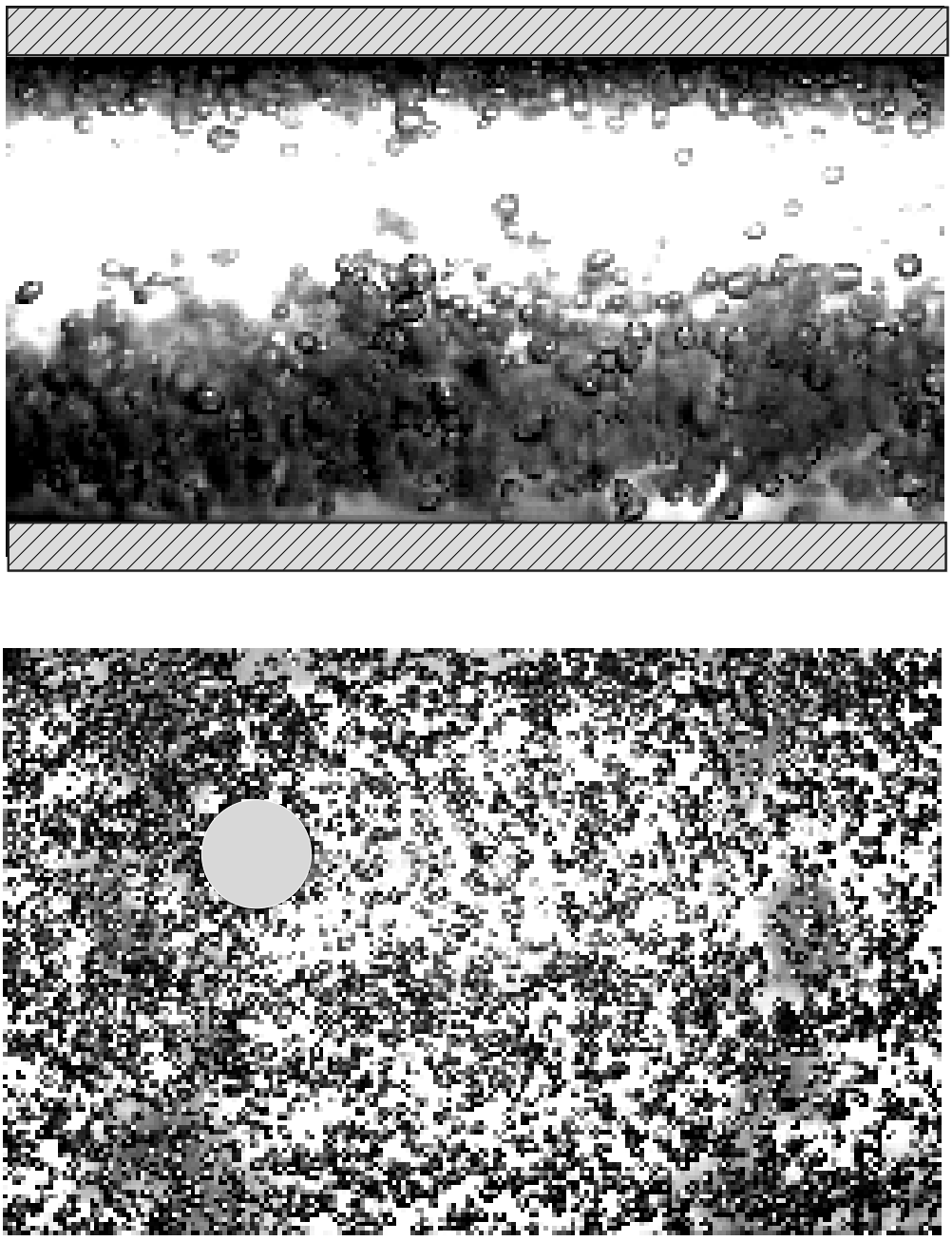

Fig. 5.2 Images of bubble dynamics for a sample case showing discrete bubbles. In this case, bubble void fraction (α) is 0.05 and *Re* is 67500 and corresponds to both wall injection. Scales for side can be found from wall to wall distance of 27.52 mm, where as the scales for top view is 14.32 cm in stream-wise direction and 8.96 cm in span-wise direction. Region marked with hatches in side view are the channel top and bottom wall. There are discrete bubbles in the flow field. Fluid flow is from left to right in both images. A circle filled with ash grey colour seen in top view is used to mask out the pressure port.

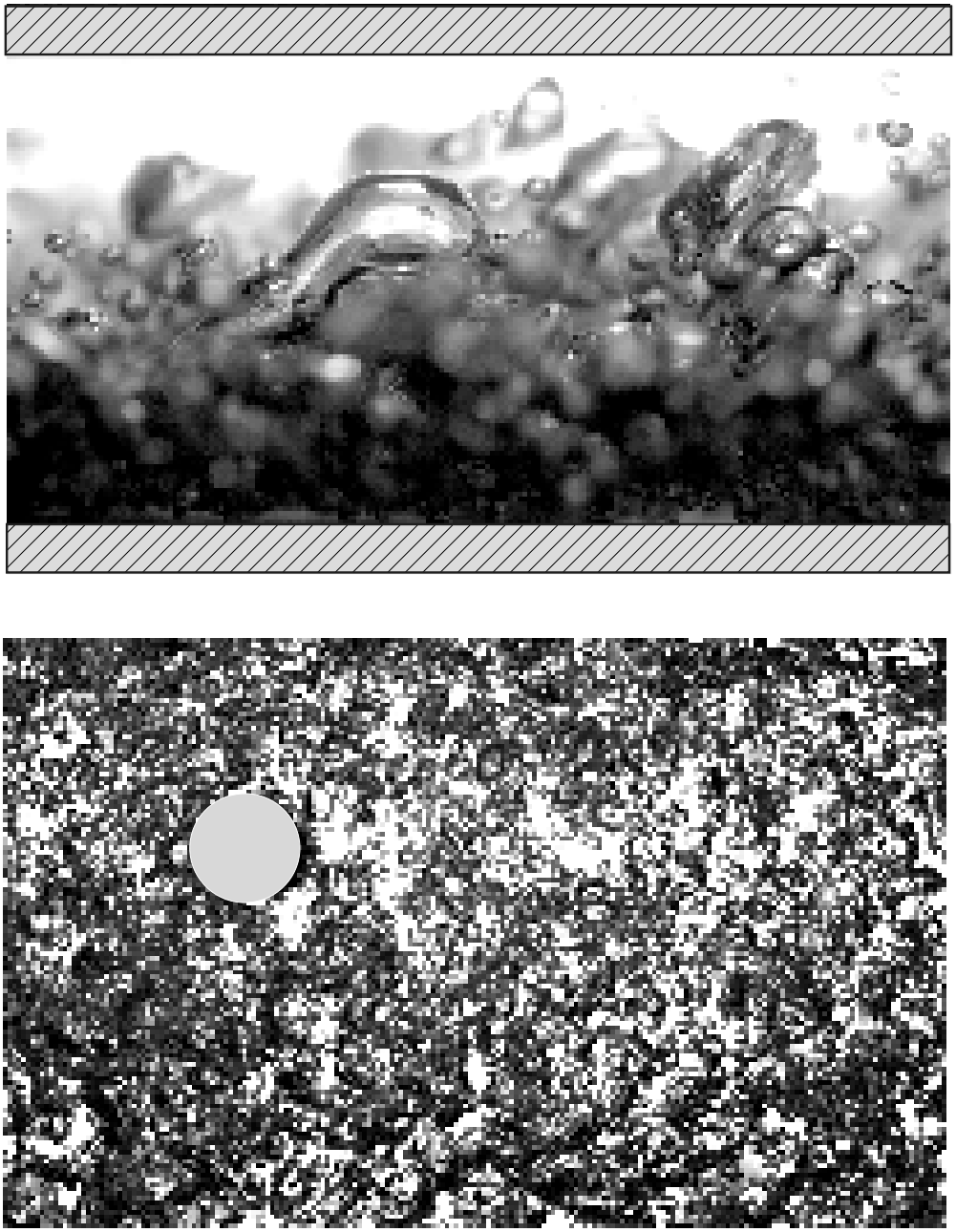

Fig. 5.3 Images of bubble dynamics for a sample case showing large coalesced bubbles. In this case, bubble void fraction (α) is 0.15 and *Re* is 67500 and corresponds to bottom wall injection. Field of view is same as previous figure. Region marked with hatches in side view are the channel top and bottom wall. Flow has large coalesced bubbles in the center and small bubbles near the wall. Fluid flow is from left to right in both images. A circle filled with ash grey colour seen in top view is used to mask out the pressure port.

in our channel, such that buoyancy helps to keep the bubbles close to the wall. An example visualization of such an intermittent air layer formed on the top wall is shown in figure 5.4 corresponding to a Re and α of 22,500 and 0.1, respectively. The side view in the figure clearly shows the fact that the bubbles/air layer are confined to a region close to the top wall. The side view on the other hand, shows a nearly contiguous air layer, with water in between at some regular intervals, which we refer to as an intermittent air layer. This intermittent air layer may be viewed as large flat bubbles on the top wall with some water in between the large flat bubbles. This intermittent or continuous air film is formed by coalescence of the injected air bubbles. Surface waves can be seen near the interfaces of two film (or flat air bubbles) and they sometimes join into a larger flat air bubble by breaking interfaces. In some interfaces, we even observed few trapped bubbles between two interfaces, which seemed to be comparatively stable. Small sized bubbles were also seen to float at the bottom edge of the air film. Further increase of the α to 0.15, lead to very large contiguous air layer or films with size of about $6H$ as shown in appendix A.5(c). The parameters which encourage this type of bubble dynamics are low flow Re, moderate to large α, and top wall injection.

5.1.4 Bubble waves in between the air layer

For top wall injection, at high void fraction and high flow speed, bubble waves were seen to form in between large flat bubbles or air layer. An example visualization of such a case is shown in figure 5.5, corresponding to $\alpha = 0.15$ $Re = 67500$ with only top wall injection. As seen in the top view, a stream-wise train of bubbles in the form of waves can be seen at regular span-wise spacing with relatively large nearly continuous air layers between them. Murai [58] observed few bubbles aligned in the flow for very low α and referred to it as void waves. We shall refer to the long bubble trains or waves seen here at high void fractions as bubble waves. We observe a periodic formation of stream-wise aligned bubble waves with air layers between them. In addition, discrete bubbles are also seen at the bottom of the air layer as seen in the side view of figure 5.5.

Figure 5.6 shows the temporal evolution of this phenomena. In (a), we observe bubble waves and after 75.6 msec, we observe that the waves are completely broken and random patches of bubbles and air layers are observed. The bubble waves or trains travel in the stream-wise direction with a lower velocity that the continuous air layers between them, as also observed by Murai [58] for small bubble wave in water at very small α. In the subsequent images, we find that the bubble waves keep forming and breaking at different spatial locations, and the whole configuration is very dynamic with large changes in time. As we shall see later, this configuration also results in a noticeable drag reduction. The

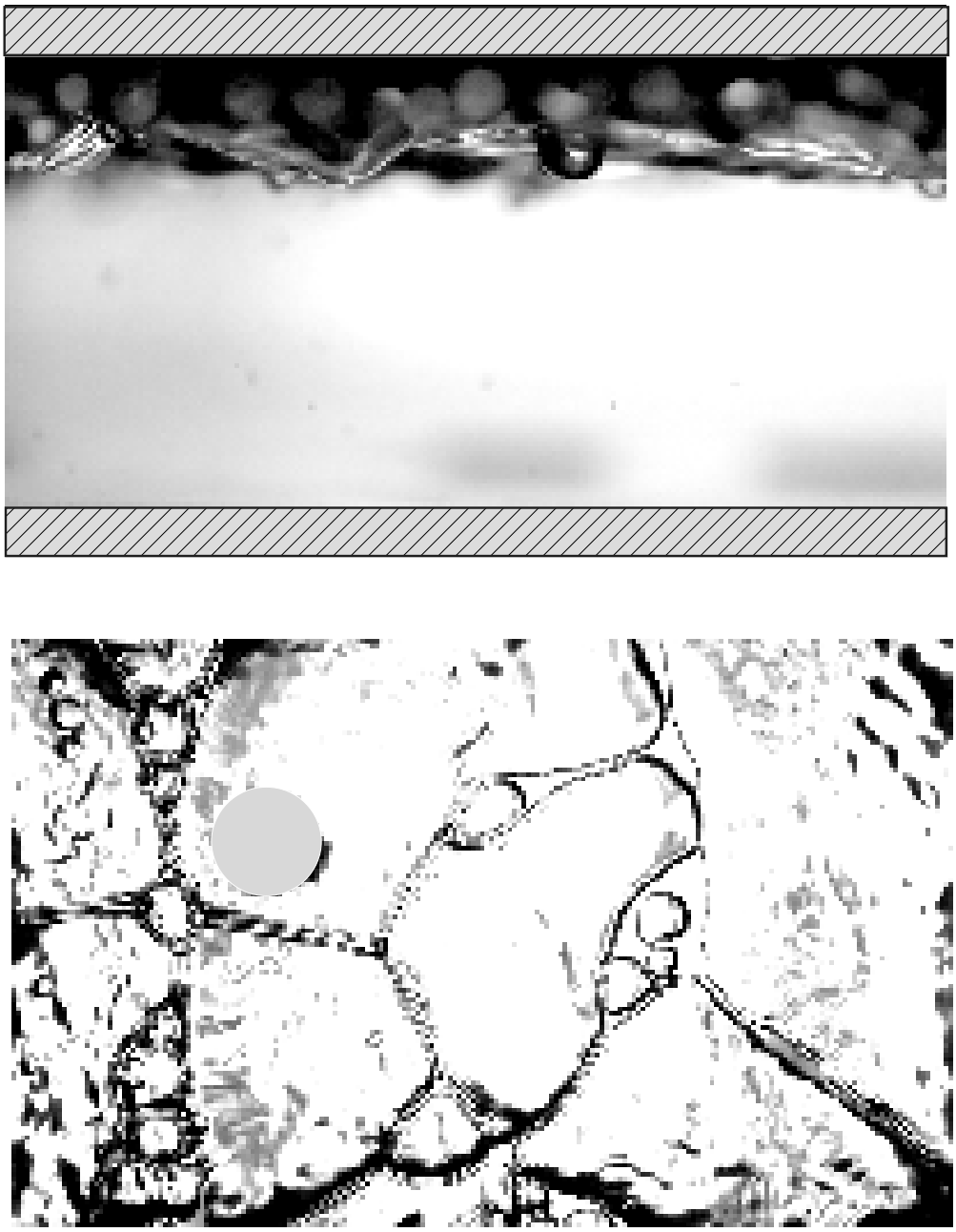

Fig. 5.4 Images of bubble dynamics for a sample case showing coalesced large flat bubbles at the top wall in the form of an air layer or film. In this case, bubble void fraction (α) is 0.1 and *Re* is 22,500 and corresponds to top wall injection. Field of view is same as figure 5.2. Region marked with hatches in side view are the channel top and bottom wall. There are intermittent air layer in the flow field. Fluid flow is from left to right in both images. A circle filled with ash grey colour seen in top view is used to mask out the pressure port.

parameters which encourage this type of bubble dynamics are high flow *Re*, moderate to large α, and top wall injection.

5.2 Effect of bubbles on skin friction

We have seen in the previous section that high speed visualizations of the bubbles shows distinctly different types of dynamics as the parameters are varied. The changes in the observed bubble dynamics have a direct impact on the drag or pressure drop within the channel, as one would expect. We shall see in this section that the wall drag in the channel can be both enhanced and reduced due to the injection of bubbles, and is related to the type of bubble dynamics seen.

In fully developed channel flow, wall drag can be directly calculated from the measured pressure drop along the stream-wise direction using momentum conservation on a control volume. In the present study, pressure drop is measured to study the effect of bubbles on frictional drag in turbulent channel flow. We shall soon see that the pressure drop varies in the wall normal plane after bubble injection. We therefore measure pressure drop at four vertical locations (y/H = 0, 0.25, 0.5, 1) and then integrate it over the control volume to estimate the wall drag. In this section, results are presented in three sub-sections, one corresponding to results for each of the three bubble injection orientations. Within each sub-section, we present results for systematic variation of channel *Re* and α.

Bubbles can reduce the turbulent flow drag either due to modification of fluid properties or due to its interaction with turbulence. Drag reductions to modification of fluid properties such as water density and velocity are relatively simple effects and not difficult to explain. In order to focus our attention on drag reduction from the more interesting and complex turbulence-bubble interaction, we normalize the wall drag using the modified density and velocity to remove any variations (reductions) caused by these changes in fluid properties. For the normalization of the wall shear stress in the presence of bubbles, to obtain the skin friction coefficient (C_f), we thus use the modified density and velocity as discussed below.

The primary assumption for getting the modified water properties in the presence of bubbles is that the bubbles (or air) is uniformly distributed in the water. It is then simple to obtain a relation for the effective density of the bubbly water (ρ_{eff}) in terms of the water density (ρ_w) as given below:

$$\rho_{eff} = \rho_w(1-\alpha), \tag{5.1}$$

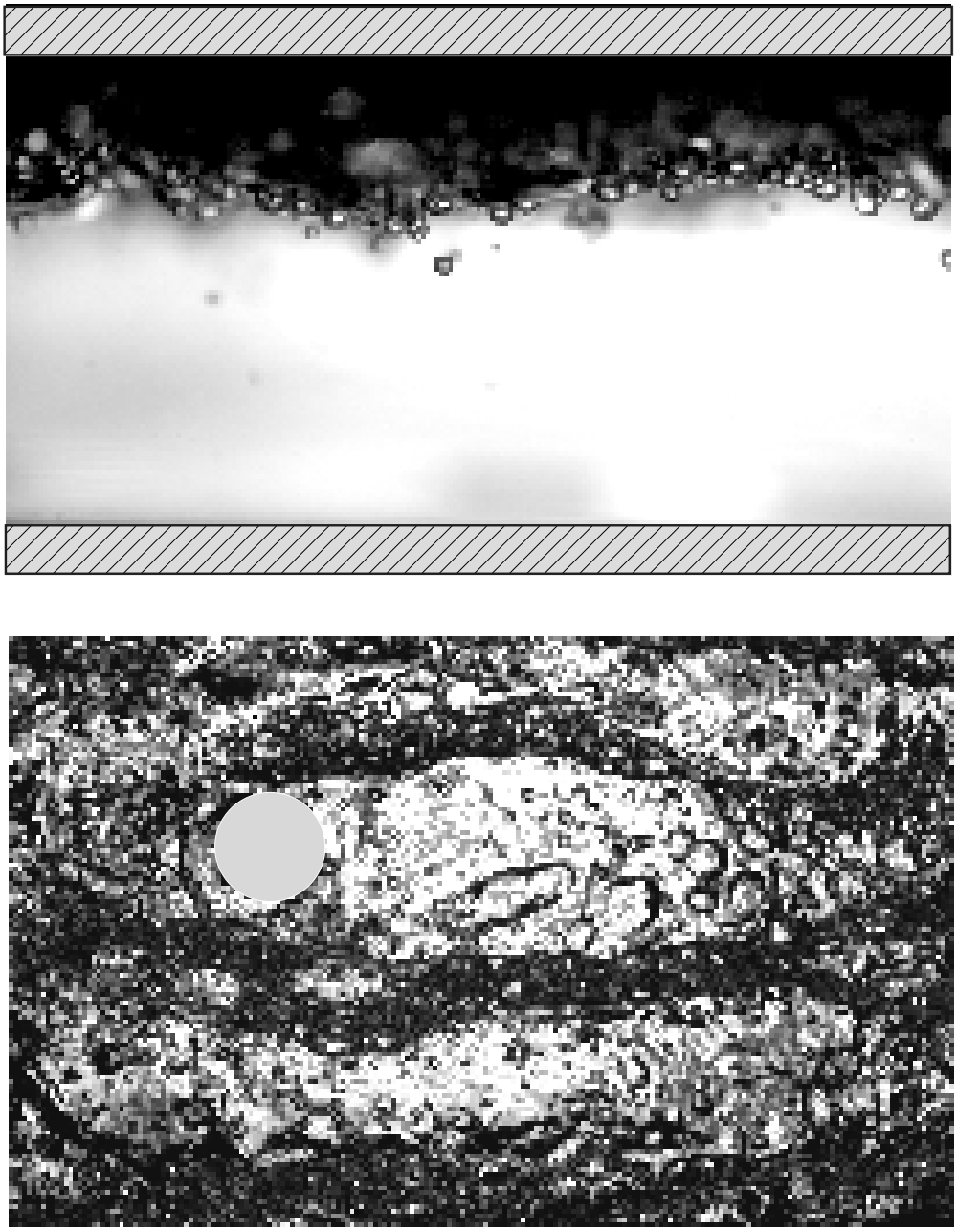

Fig. 5.5 Images of bubble dynamics for a sample case showing bubble waves between the air layer. In this case, bubble void fraction (α) is 0.15 and *Re* is 67,500 and corresponds to top wall injection. Field of view is same as figure 5.2. Region marked with hatches in side view are the channel top and bottom wall. There are bubble waves along with the air layer. Fluid flow is from left to right in both images. A circle filled with ash grey colour seen in top view is used to mask out the pressure port.

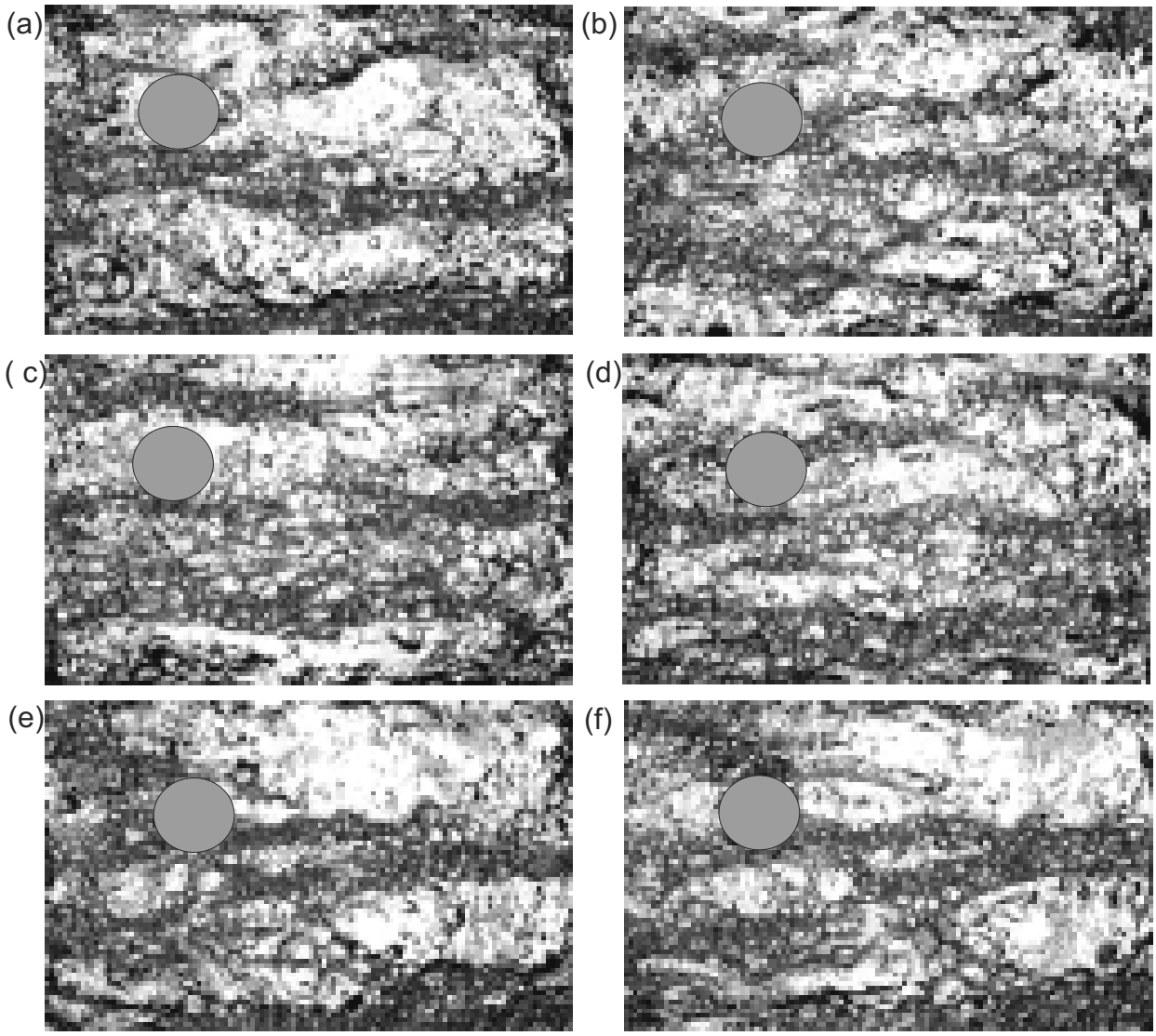

Fig. 5.6 Top view images of temporal evolution of bubble dynamics for bubble void fraction (α) of 0.15 and *Re* of 67500 for the top wall injection. Field of view is 14.32 cm in streamwise direction. There are bubble waves along with the air layer. Fluid flow is from left to right in the images. A circle filled with ash grey colour seen in top view is used to mask out the pressure port. The time corresponding to each of the images shown is (a) 0, (b) 75.6, (c) 119.4 , (d) 199.4, (e) 273.1, and (f) 287.5 msec.

The effective velocity of the bubbly mixture is higher due to the additional volumetric flow rate of injected air. This can be accounted for with a new effective mean velocity (u_{eff}), which can be obtained from volume conservation assuming that both air and water are incompressible, as given below:

$$u_{eff} = (Q_a + Q_w)/A = u_m/(1-\alpha), \tag{5.2}$$

where u_m is the mean velocity in the channel in the absence of bubble injection and A is the cross-sectional area of the channel.

For the non-dimensionalization of wall shear stress (τ_w) to find skin friction co-efficient (C_f), we thus now use the effective flow velocity (u_{eff}) and fluid density (ρ_{eff}) as defined above similar to the Oishi et al. [62]. We refer to the skin friction co-efficient in the absence of bubbles as C_{f0}. The ratio of the skin friction coefficient with bubbles to that of the base case is thus:

$$C_f/C_{f0} = (\tau_w/0.5\rho_{eff}u_{eff}^2)/(\tau_{w0}/(0.5\rho_w u_m^2). \tag{5.3}$$

In the above equation, the shear stress at the wall in the presence of bubbles can be found from integrals of the measured pressure drop at various vertical locations.

5.2.1 Bottom wall Injection

We shall begin with an example case of variation of pressure drop (ΔP) with channel height (y) for different bubble void fraction (α) for bottom wall injection, as shown in figure 5.7. The pressure drop (ΔP) is non-dimensionalised here by the pressure drop in the absence of bubbles (ΔP_0) with the top and bottom wall corresponding to y/H of one and zero, respectively. In the figure, $\Delta P/\Delta P_0$ is presented for flow *Re* of 22500, 43400, 54600 and 67500 in sub-figures (a), (b), (c) and (d), respectively. In each sub-figure, different symbols mark the effect of variation in void fraction (α). The most striking feature of all the plots is that substantial variations in pressure drop can be seen with the normalized vertical location y/H in all cases where there is bubble injection i.e. non-zero void fractions. This is in contrast to the no bubble or base case shown in each figure, corresponding to the $\alpha = 0$ case, where as expected there is no variation of pressure drop with the vertical location (y/H). The pressure drop variations also give spatial information about the effect of the bubbles. For example, in (d), there is substantial pressure drop reduction at the bottom wall ($y/H = 0$), and some reduction in pressure drop at the top wall ($y/H = 1$), but there is an increase in pressure drop in the

centre-line of the channel, this being the case for all non-zero void fractions in this case. From the pressure drop at different vertical location, as shown in figure 5.7, we can obtain the wall shear stress (τ_w) from a simple control volume analysis using the integral of the pressure drop over the channel height. This wall shear stress (τ_w) is non-dimensionalised to find skin friction (C_f) as stated earlier, and its ratio with C_{f0} calculated at each *Re* and α. A contour plot of the resulting (C_f/C_{f0}) values is shown in figure (figure 5.8) in the *Re* - α plane. Also shown in the figure are bubble visualization images at 6 different conditions (a) to (f), which are marked on the drag reduction plot to enable connections to be made between drag reduction or increase and the bubble dynamics, as discussed below.

For the flow *Re* of 22500 (figure 5.7a), we observe pressure drop and drag increase for all α. If we look at bubble dynamics for α of 0.05, we observe that there are flat bubbles near the top wall. These bubbles have migrated to the top wall after injection at the bottom wall due to buoyancy, with almost all bubbles reaching the top wall after traversing the vertical height of the channel. We should remember that the bubble is injected 100 mm upstream of the visualisation window. There are three probable reasons for faster vertical migration of the bubbles at low flow *Re*, as compared to higher *Re* cases. First, the bubble detachment diameter is larger due to the low flow velocity and turbulence near the porous plate. The second is the higher available coalescence time due to smaller mean flow velocity, which causes larger bubbles. thirdly, fluid inertia or flow drag on bubble is smaller compared to buoyancy. All this together gives rise to strong vertical migration of the bubbles. In the pressure drop plot, we observe higher drag at the top wall as bubbles reach the top wall after disturbing the top wall boundary layer. With increasing α, we observe bigger bubble sizes and a wall drag (C_f/C_{f0}) increase of 60%. Even at *Re* of 43400 in figure 5.7b, we observe a drag increase but relative increase in drag is less for *Re* of 43400. For this case, all the bubbles have not reached near the top wall as the flow velocity is larger here. With further increases in *Re* to 54600, we observe a reduction in pressure drop at bottom wall, whereas at other heights, we still find an increase in pressure drop. In the integral sense, we still find a drag increase. If we look at the bubble dynamics (figure A.3) in appendix, we observe that bubbles are near the centre of the channel. For the *Re* of 67500, we observe a reduction in pressure drop at the bottom wall. Most of the bubbles in this case are in the bottom wall boundary layer, but we still observe a reduction in pressure drop at the top wall also as seen in figure 5.7(d). This is probably linked to the fact that in channel flow, boundary layer/vorticity on top and bottom walls mutually affect each other and hence the pressure drop decreases at the top wall despite the absence of bubbles there. At the bottom wall, pressure drop becomes negative for $\alpha \geq 0.12$, which is a surprising result. These experiments have been repeated many times to gain confidence in our measurements, and the results were repeatable. This

probably means that close to the bottom wall, bubbles have suppressed drag completely and added extra energy to the flow. One possible reason for this surprising result may be due to the energy released during coalescence, which could be added to the flow. This argument is not very conclusive, but it is perhaps one possible mechanism to release energy in the flow. As there is variation in pressure drop in the vertical direction, the mean flow streamline will also be curved. We should keep in mind that locally near the wall, pressure drop is negative, but in the integral sense it still has a drag, which is 60% smaller than the base case for Re and α of 67500 and 0.16. The contour plot of C_f/C_{f0} in $Re-\alpha$ plane shows that drag is reduced only for the Re of 67500 case, and at this Re, drag reduction increases with α reaching about 50% drag reduction at the highest void fractions. For all the other Re and α, drag either increases or is insensitive to bubble injection. Drag increase is highest at small Re and large α, where all bubbles are near the top wall boundary layer and do not contribute to drag reduction.

5.2.2 Top wall Injection

When bubbles are injected from the top wall, buoyancy force is towards the wall and therefore bubbles stay near the top wall. We have seen in the bubble dynamics section that for the top wall injection, bubbles are very close to the top wall unlike in the bottom wall injection case. In figure 5.9a, we observe that there is pressure drop reduction at all heights and for all void fractions. The integrated pressure drop or wall drag (C_f/C_{f0}) at this Re (22,500) also shows drag reduction at all α. The variation of C_f/C_{f0} with α at each of the four Re values is shown as a line plot in figure 5.13. One can see here (for the top wall injection case) that the drag reduction saturates at higher void fractions in each Re case.

In figure 5.10(a), we can see flat bubbles near the top , while in (d), we see an intermittent large air layer at the wall, both these bubble dynamics helping to reduce the drag by changing conditions at and near the wall. The drag reduction is naturally higher for the nearly continuous air layer in (d), compared to the flat bubble case in (a), both at Re = 22,500. As the air flow rate is increased at this Re, the discrete flat bubbles (in (a)) change to a thin air layer (see Appendix A.5(b)), which then remains as a air layer with further increase in α with only the thickness of the layer increasing (in (d) or Appendix A.5(c)). This explains the saturation of drag reduction after certain flow rate, which is similar to the observation of Elbing et al. [19] for air layer drag reduction in zero pressure gradient turbulent boundary layer. We observe a maximum drag reduction of about 55% at this Re. For the flow Re of 43,400 and α of 0.05, there are discrete large bubbles near the top wall (figure 5.10(b)), which does not help in drag reduction. These are found to actually enhance the drag slightly (about 10%) as seen in figure 5.10. With increasing α values, the air layer forms (figure 5.10(e))

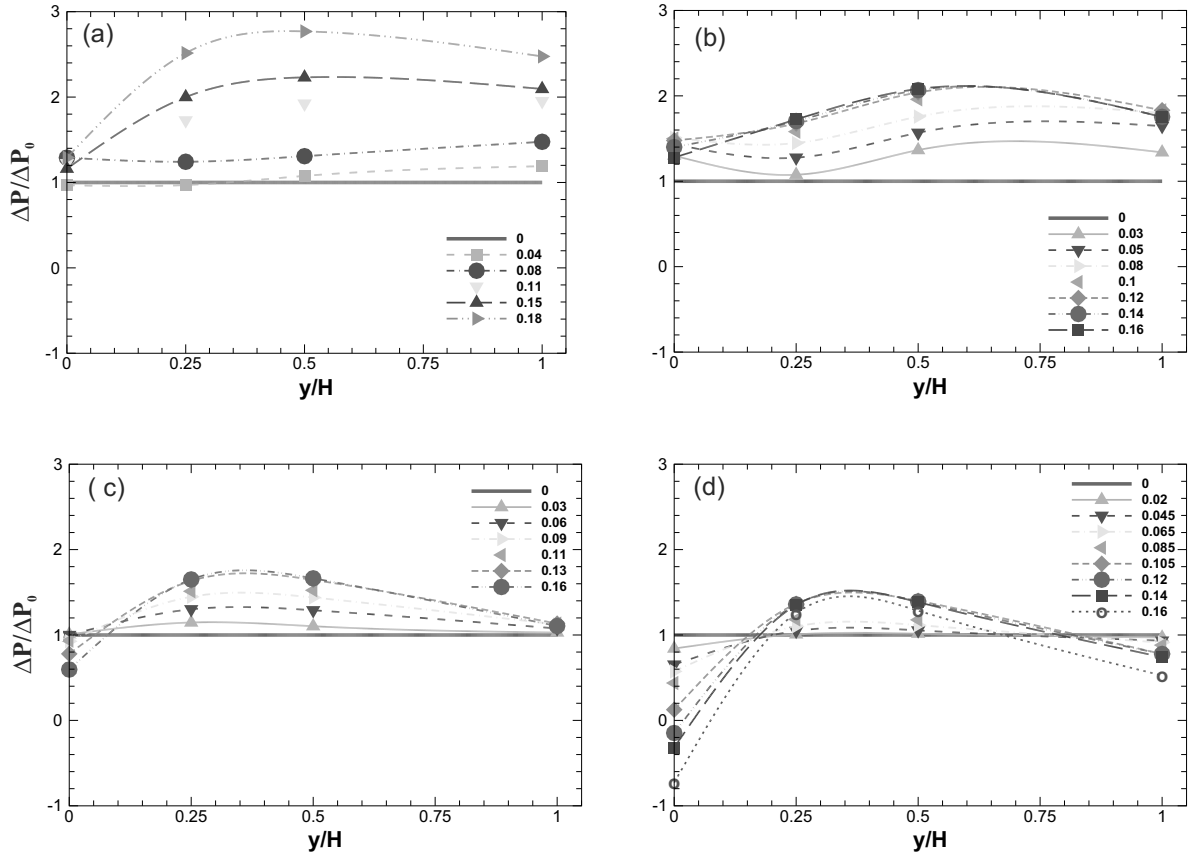

Fig. 5.7 Figure shows the vertical variation of pressure drop non-dimensionalised by the base case pressure drop ($\Delta P/\Delta P_0$), for different void fraction (α) for bottom wall injection. The flow *Re* corresponding to each of the plots is (a) 22500, (b) 43400, (c) 54600, and (d) 67500.

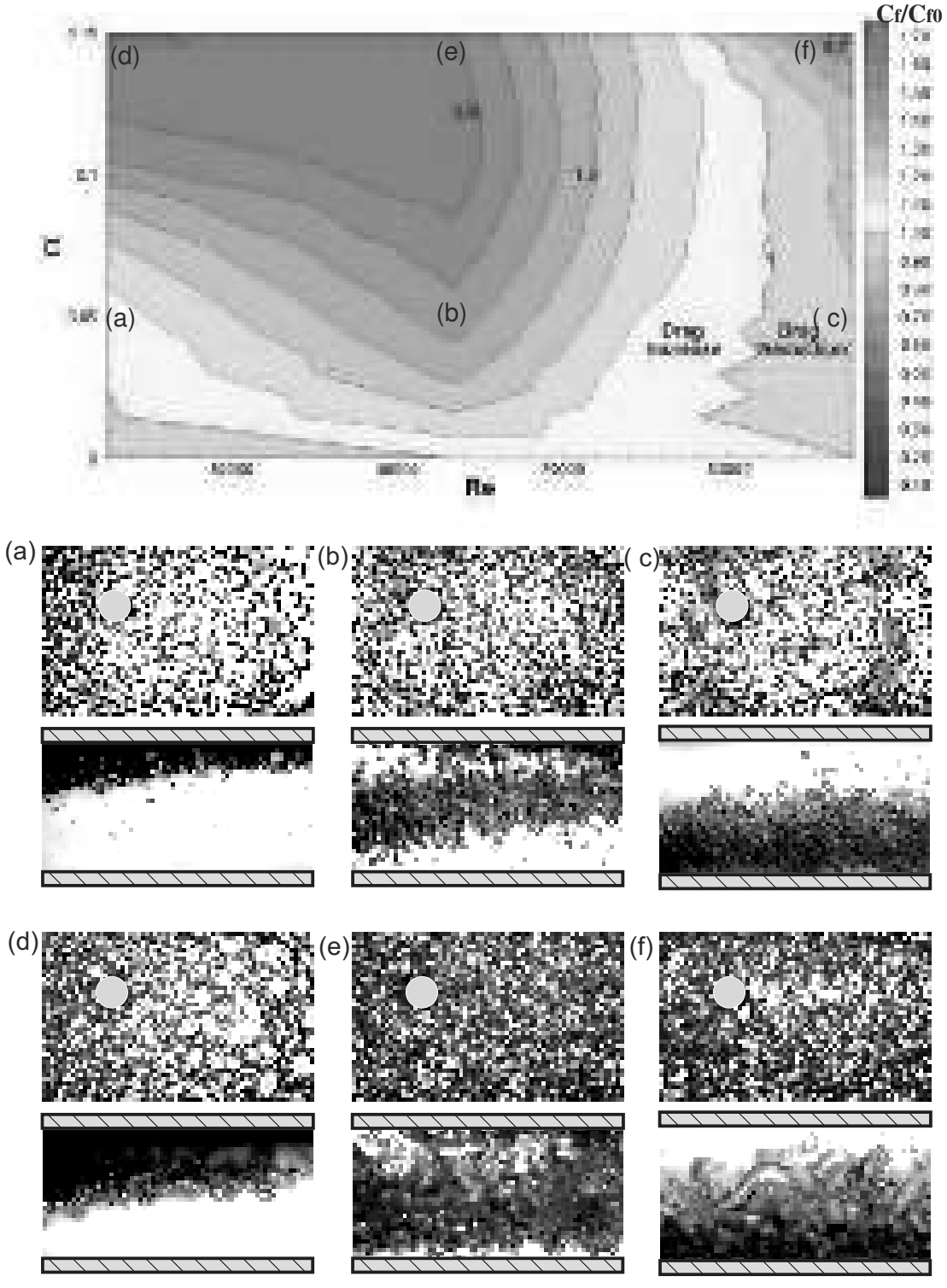

Fig. 5.8 Plot shows the contour of C_f/C_{f0} for the bottom wall injection in the Re - α plane. In most of the Re - α plane, the bubbles in this case lead to drag increase. Drag reduction is only seen at the largest Re cases and is found to increase with α. Bubble visualizations at six conditions marked on the contour plot as (a) to (f) are also shown.

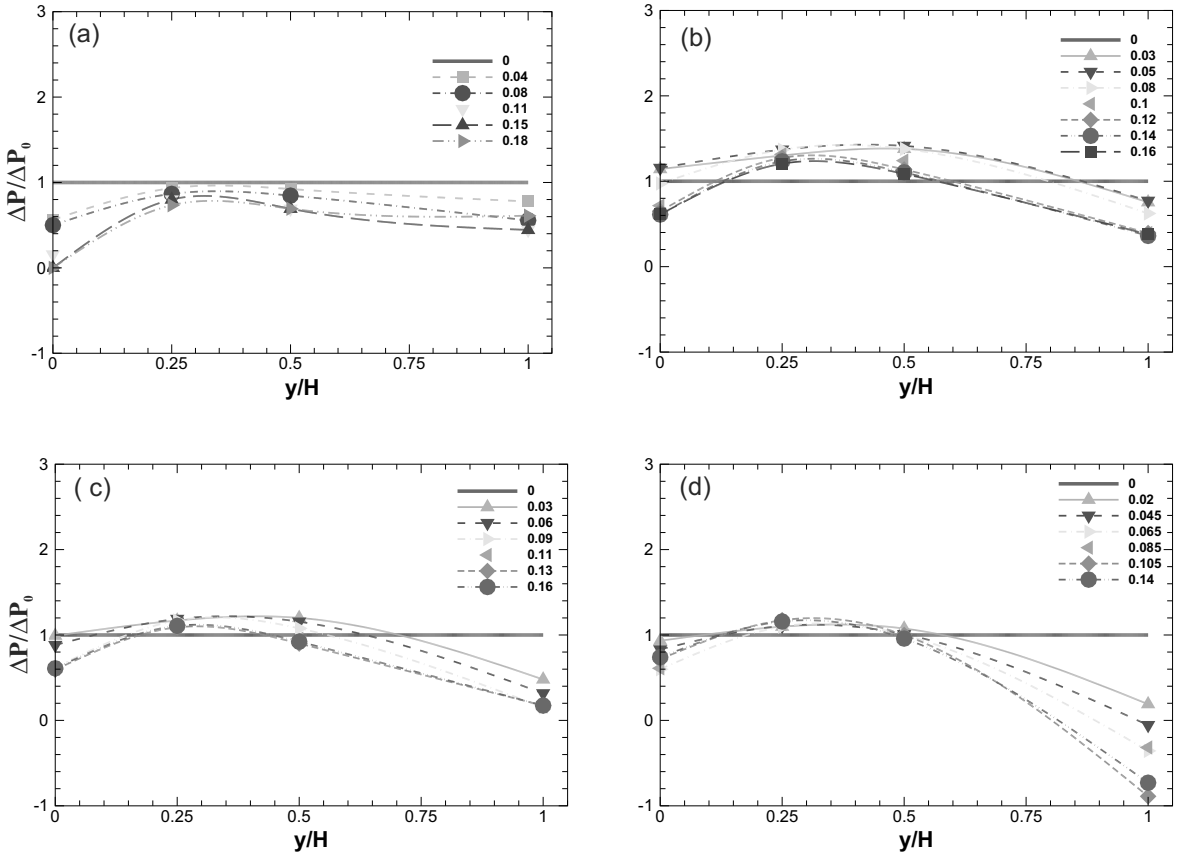

Fig. 5.9 Figure shows the vertical variation of pressure drop non-dimensionalised by the base case pressure drop (dP/dP_0), for different void fraction (α) for top wall injection. The flow *Re* corresponding to each of the plot is (a) 22500, (b) 43400, (c) 54600, and (d) 67500.

and this leads to drag reduction. At higher *Re* of 67,500, we observe small discrete bubbles at low α, which give mild drag reduction. As the void fraction is increased at this *Re*, the air layer forms with bubble waves, and this is found to lead to large drag reductions of about 60%, as may be seen in figure 5.13(d). For *Re* of 67500 and high void fraction, we again observe more than 100% pressure drop reduction locally at the top wall from where bubbles are injected, similar to the bottom wall at same *Re* and about same α. At this *Re* we again observe saturation of drag reduction with increasing α as shown in figure 5.13d and maximum drag reduction of about 50% is observed.

5.2.3 Both wall Injection

We now consider the case of injection from both top and bottom walls, which can be relevant to drag reduction in liquid pipelines. In this case, at *Re* of 22500, all the bubbles injected from the bottom wall reaches the top wall (figure 5.12(a) and (d)) and pressure drop increases for all α as shown in figure 5.11a. Even at the *Re* of 43400, drag increases due to bubbles. For this case, all the bubbles are near the centre or near the top wall. Bubble from the bottom reaches the top wall by disturbing the top wall boundary layer (figure 5.12(b) and (e)). Increasing *Re* to 54600, pressure drop reduces at the top and bottom wall, whereas pressure increases away from the wall (figure 5.11(c)). In the integral sense, there is very little change in drag due to bubble injection at all void fractions at this *Re* of 54,600. With further increase in *Re* to 67500, flow drag starts reducing due to the presence of bubbles. Pressure drop at both top and bottom walls becomes negative for $\alpha \geq 0.12$ as seen in figure 5.11(d). However, in the integral sense, the flow still has wall drag, but much lower than the corresponding base case. Drag reduction increases with increasing void fraction. Bubbles injected at the top wall stay very close to the top wall, and bubbles injected at the bottom wall are distributed between the bottom wall and the centre of the channel (figure 5.12(c) and (f)). At the highest void fraction of 0.14 and *Re* of 67500, we observe a drag reduction of about 60%.

5.3 Discussions

Variations in drag reduction (C_f/C_{f0}) among different experiments are summarised in the review of Ceccio [9]. An overview plot of this data compiled by him shows large variations in drag reduction among different studies in the literature when plotted versus the void fraction. These variations are likely a reflection of the fact that there are many other parameters other than void fraction that can significantly influence the final drag reduction.

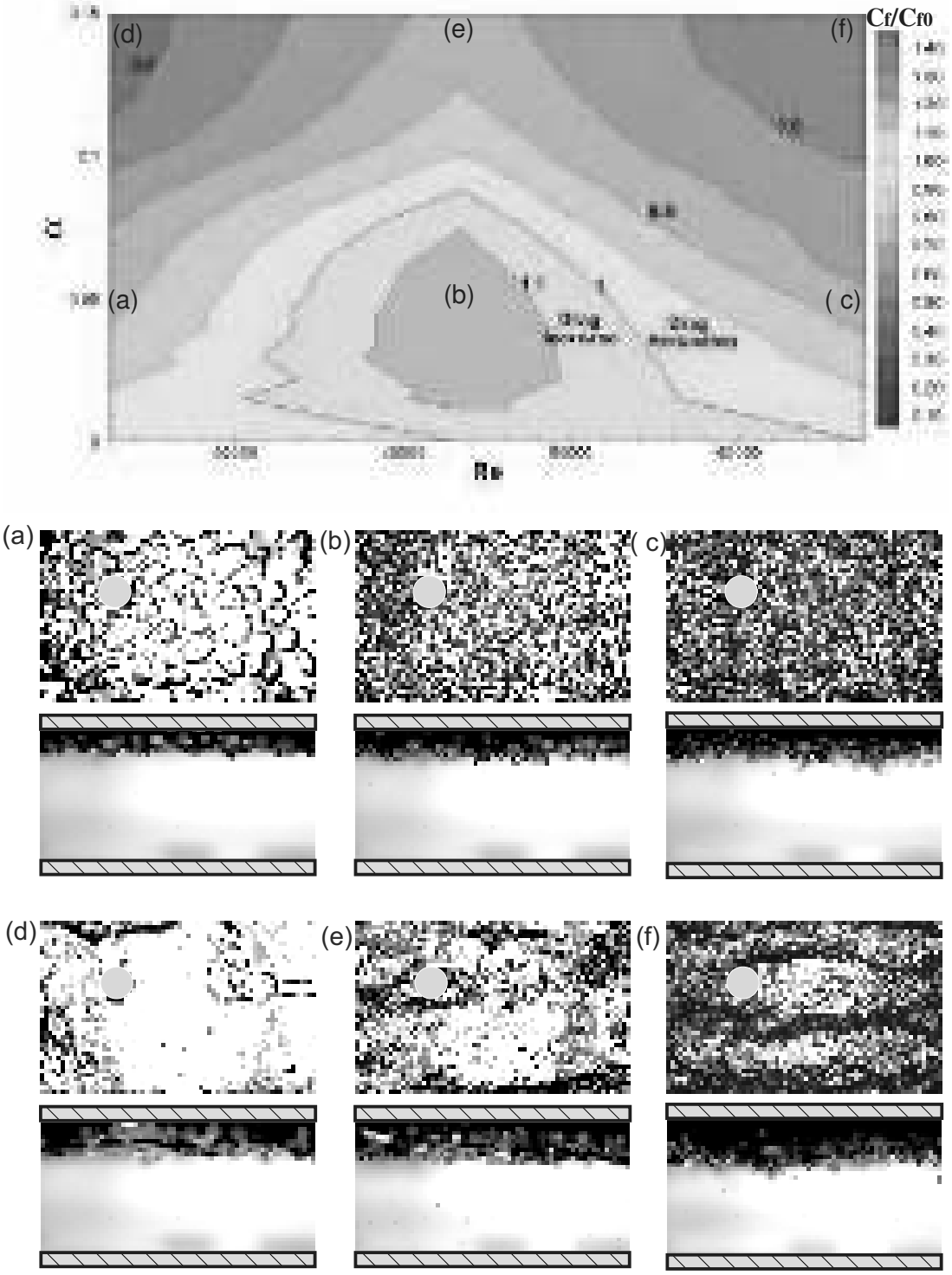

Fig. 5.10 Plot shows the contour of C_f/C_{f0} for the top wall injection in the Re - α plane. In most of the Re - α plane, the bubbles in this case lead to drag reduction. Bubble visualizations at six conditions marked on the contour plot as (a) to (f) are also shown.

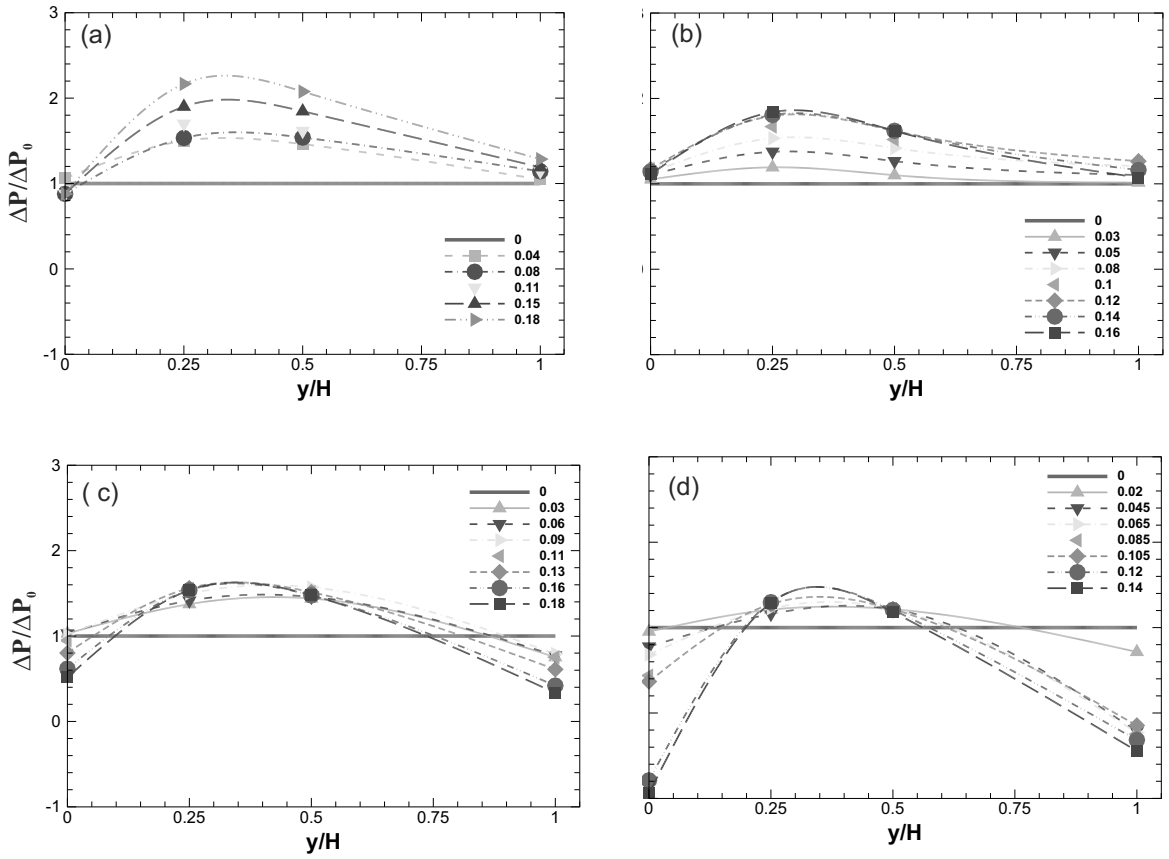

Fig. 5.11 Figure shows the vertical variation of pressure drop non-dimensionalised by the base case pressure drop (dP/dP_0), for different void fraction (α) for both wall injection. The flow *Re* corresponding to each of the plot is (a) 22500, (b) 43400, (c) 54600, and (d) 67500.

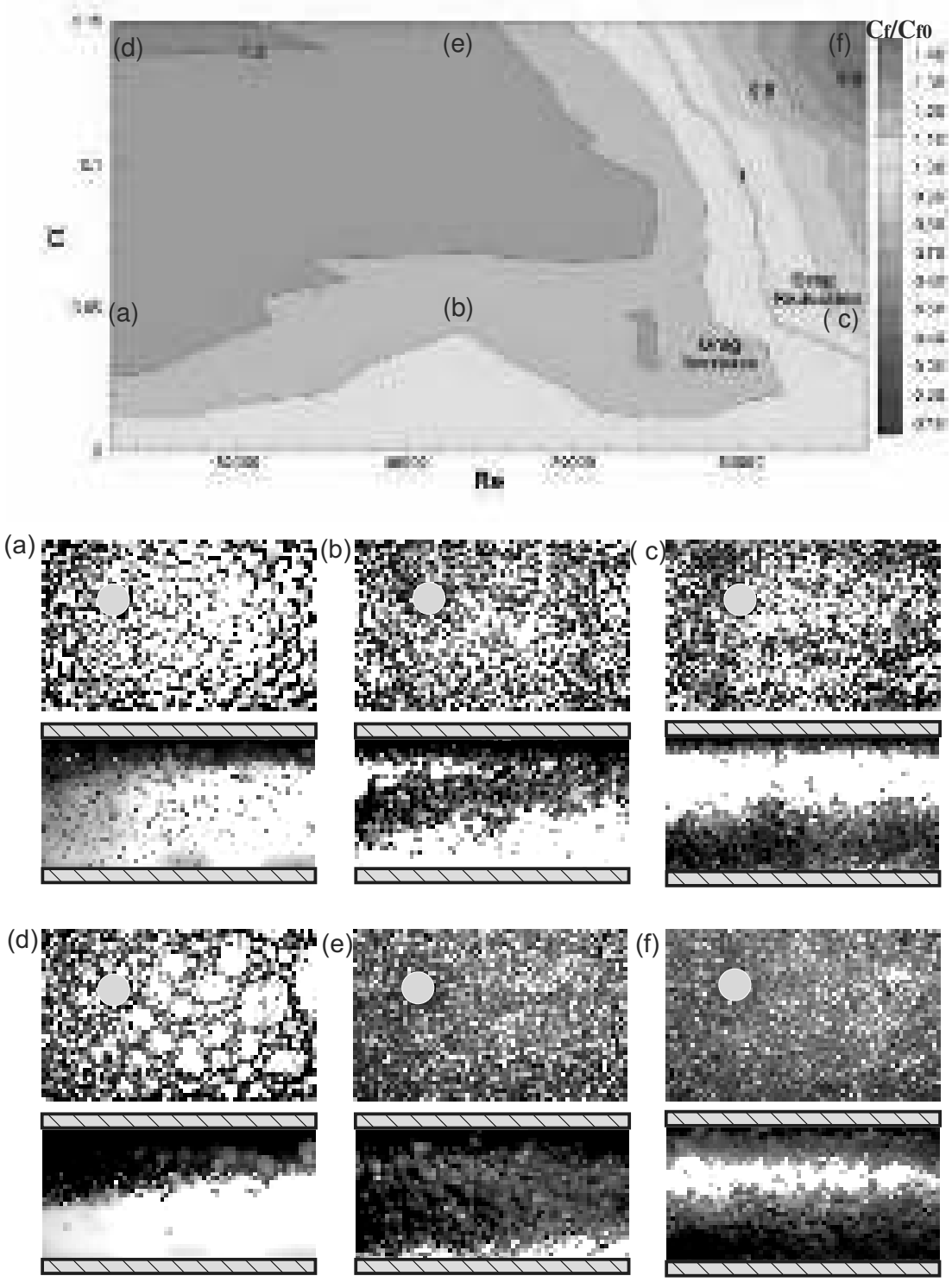

Fig. 5.12 Plot shows the contour of C_f/C_{f0} for the both wall injection in the *Re* - α plane. In most of the *Re* - α plane, the bubbles in this case lead to drag increase. Drag reduction is only seen at the largest *Re* cases and is found to increase with α. Bubble visualizations at six conditions marked on the contour plot as (a) to (f) are also shown.

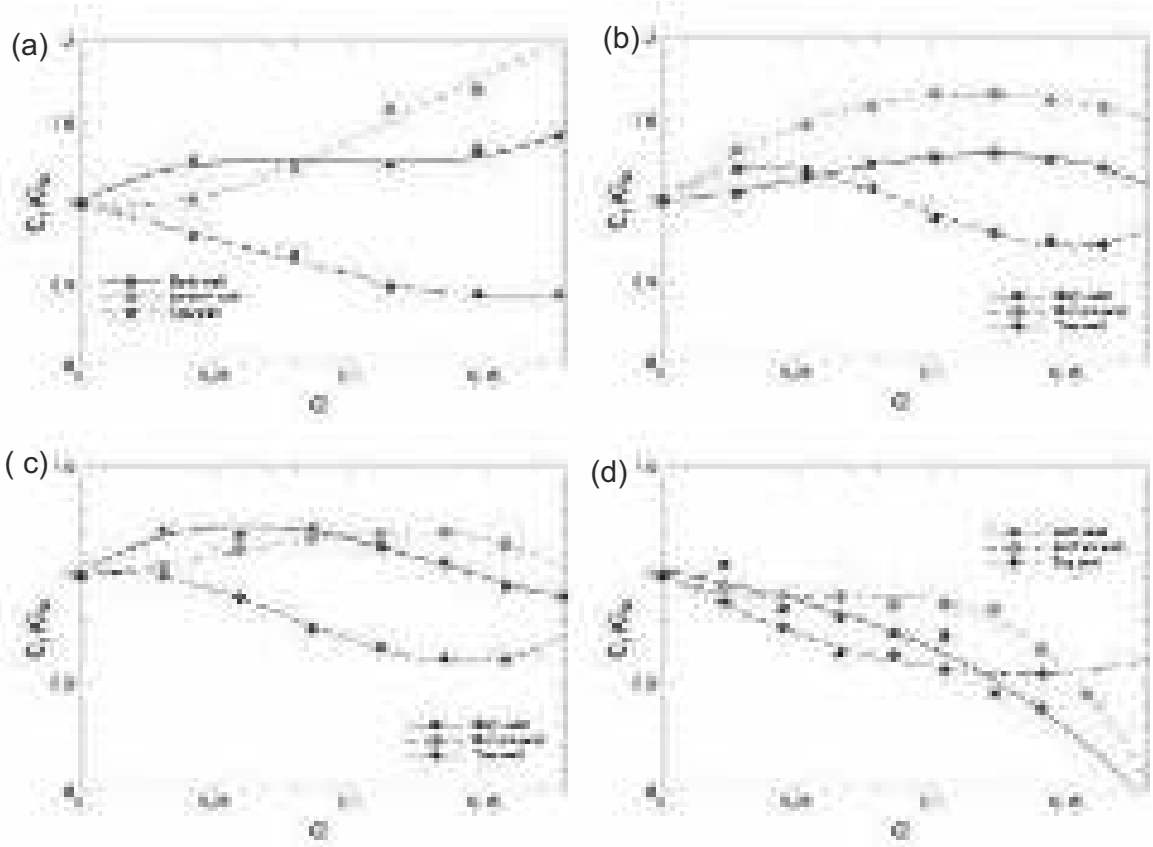

Fig. 5.13 Variation of non-dimensional skin friction co-efficient C_f/C_{f0} with α is plotted for different type of orientation of injection plate. Figure (a), (b), (c), and (d) correspond to flow *Re* of 22500, 43400, 54600, and 67500, respectively.

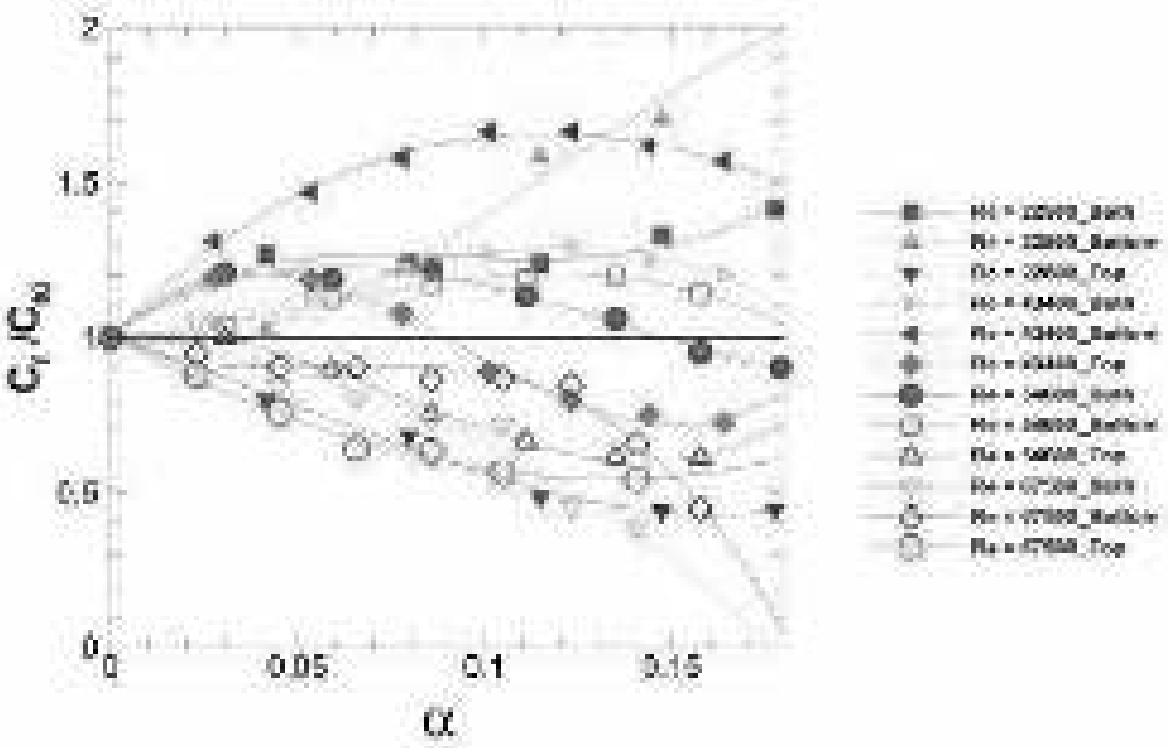

Fig. 5.14 Variation of non-dimensional skin friction co-efficient C_f/C_{f0} with α is plotted for all 84 cases investigated in the present study. One obvious observation is the large scatter in C_f/C_{f0} values seen at the same α due to the very different bubble dynamics regimes.

Case	*Re*	α	*Orientation*	*BubbleDynamicsRegime*	D_b (mm)	C_f/C_{fo}
1	22500	0.05	Bottom	Coalesced bubbles	7.3	1.05
2	22500	0.1	Bottom	Layering	10.9	1.44
3	22500	0.15	Bottom	Layering	15.9	1.71
4	22500	0.05	Top	Coalesced bubbles	7.7	0.771
5	22500	0.1	Top	Layering	37.7	0.56
6	22500	0.15	Top	Layering	84.5	0.44
7	22500	0.05	Both	Coalesced bubbles	6.2	1.271
8	22500	0.1	Both	Layering	8.3	1.227
9	22500	0.15	Both	Layering	9.8	1.33
10	43400	0.05	Bottom	Discrete, not in LWB	2.5	1.45
11	43400	0.1	Bottom	Discrete, in outer log layer	2	1.65
12	43400	0.15	Bottom	Discrete, in inner log layer	2.4	1.6
13	43400	0.05	Top	Coalesced bubbles	4.33	1.189
14	43400	0.1	Top	Layering	29.5	0.907
15	43400	0.15	Top	Layering	90.2	0.742
16	43400	0.05	Both	Discrete, not in LWB	2	1.129
17	43400	0.1	Both	Discrete, in outer log layer	1.9	1.258
18	43400	0.15	Both	Discrete, in outer log layer	2.4	1.236
19	54600	0.05	Bottom	Discrete, in log layer	2.2	1.09
20	54600	0.1	Bottom	Discrete, in log layer	2.2	1.186
21	54600	0.15	Bottom	Discrete, in log layer	2.2	1.172
22	54600	0.05	Top	Discrete	3.3	0.94
23	54600	0.1	Top	Coalesced bubbles	21.9	0.701
24	54600	0.15	Top	Bubble waves along side air layer	116.8	0.61
25	54600	0.05	Both	Discrete, in log layer	2.2	1.199
26	54600	0.1	Both	Discrete, in log layer	2.75	1.18
27	54600	0.15	Both	Discrete, in log layer	1.6	0.985
28	67500	0.05	Bottom	Discrete, near wall also	1.6	0.906
29	67500	0.1	Bottom	Discrete, near wall also	1.8	0.867
30	67500	0.15	Bottom	Discrete, near wall also	2.5	0.547
31	67500	0.05	Top	Discrete	2.65	0.728
32	67500	0.1	Top	Start of layer and bubble waves	42.6	0.583
33	67500	0.15	Top	Bubble waves along side air layer	118.4	0.56
34	67500	0.05	Both	Discrete, near wall also	1.7	0.833
35	67500	0.1	Both	Discrete, near wall also	1.8	0.723
36	67500	0.15	Both	Discrete, near wall also	2	0.432

Table 5.1 Experimental conditions, bubble dynamics regimes, bubble size and drag reduction for 36 cases is summarized.

In the present work, we have used high speed imaging and pressure drop measurements to systematically investigate the different bubble dynamics regimes and have simultaneously obtained drag reduction data. The simultaneously obtained visualizations and data enables connections to be made between the bubble dynamics regimes and drag reduction.

In figure 5.14, we plot variation of non-dimensional skin friction co-efficient C_f/C_{f0} with α for all cases investigated in the present study. This includes *Re*, α and injection orientation variations as discussed in this chapter. One obvious observation is the large scatter in C_f/C_{f0} values seen at the same α due to the very different bubble dynamics regimes depending on the other parameters like *Re* and injection orientation. All experimental conditions and observations are summarized in table 5.1, including observations of bubble dynamics regimes, bubble size and drag reduction. Depending on the conditions, large variations are seen in bubble dynamics regimes and drag reduction data. Large scatter in figure 5.14 points to the fact that there are different physical mechanisms responsible for drag reduction, which are not captured by the void fraction alone. Change in bubble size, shape, relative position of bubbles with respect to wall, and turbulence characteristics are all-seen to affect wall drag. Further, as there is variation in pressure drop in the vertical direction due to asymmetry generated by the bubbles, mean flow streamline are also expected to be curved. Top wall injection is observed to give good drag reductions over a wide range of flow *Re* and α, but is seen to saturate beyond a threshold α. In contrast, the bottom wall injection case shows that drag reduction continuously increases with α at high *Re*. The present study shows a maximum of about 60% increase and a similar 60% reduction in wall drag over the entire range of conditions investigated.

Chapter 6

Conclusions

"I think and think for months and years. Ninety-nine times, the conclusion is false. The hundredth time I am right."

- Albert Einstein

In the present work, we have experimentally studied the interaction of single and multiple bubbles with vortical structures. The study has been broadly divided in to three parts. In the first part, we study the interaction of a single bubble with a single vortical structure, namely a vortex ring, formed in water. This may be thought of as a simplified case of the interaction of bubbles with vortical structures in any turbulent flow. We then increase the complexity and study the interaction of a single bubble with naturally occurring vortical structures present in a fully developed turbulent channel flow, and then finally to the case of a large number of bubbles injected in to a fully developed turbulent channel. The bubble motions and deformations in all three cases are directly imaged using high speed visualizations, while the flow field information is obtained using time-resolved Particle-Image Velocimetry (PIV) in the first two cases, and from pressure drop measurements within the channel in the latter case. We shall now present our conclusions from each of the three studies, providing an overview of how the interaction of bubbles with vortical structures affects both the bubble and the vortical structure.

6.1 Interaction of a single bubble with a vortex ring

In the first part, we have experimentally studied the interaction of a single bubble with a single vortical structure, namely, a vortex ring. In particular, we measure both the bubble dynamics using high-speed imaging, and the vortex dynamics using time-resolved PIV and

show that both can be significantly affected by the other. The experiments are done in water with a vortex ring generated from a piston-cylinder mechanism that interacts with an air bubble.

Two important parameters in this problem are the ratio of the bubble volume to vortex core volume (V_R), and the circulation strength of the vortex (Γ). The latter can be represented in terms of a Weber number ($We = 0.87\rho(\Gamma/2\pi a)^2/(\sigma/D_b)$), along the lines used in Oweis et al. [63], which may be thought of as the ratio of the pressure difference between the core and the far field ($\Delta P = 0.87\rho\,(\Gamma/2\pi a)^2$) to the Laplace pressure (σ/D_b) for a spherical bubble (a = vortex core radius, D_b = bubble diameter, σ = surface tension). Another parameter related to the vortex ring is the non-dimensional core radius (ε) of the ring. In our studies, V_R is maintained to be of the order of 0.1, this being representative of the kind of volume ratio (bubble volume to eddy core volume) seen in bubbly turbulent boundary layers used in drag reduction studies. The *We* number, on the other hand, is varied over a large range from 3 to 406 by changing the circulation (Γ). The main study is done for vortex rings with non-dimensional core radius (ε) of about 0.25, while a few cases have also been done for thicker core rings with ε of about 0.75.

The interaction between the bubble and ring for all *We* cases broadly falls into four stages, which are demarcated on an overview plot (figure 3.5) showing the location of the vortex ring as it interacts with the bubble. In stage I, the bubble is outside the vortex ring, and is pulled in towards the ring with capture of the bubble into the core occurring at the line demarcating stages I and II. Within stage II, the bubble elongates in the azimuthal direction along the core, and then gradually breaks-up into a set of smaller bubbles. In stage III, the break-up is complete and the set of smaller broken bubbles slowly moves around in the azimuthal direction, and finally in stage IV, the bubbles escape from the ring leaving a distorted or fragmented core.

In stage I, where the bubble is drawn into the ring in a spiralling manner, we measure the capture time (t_c), and find that it decreases significantly as the *We* increases. After capture, the bubble reaches an equilibrium radial location within the vortex core, which is found to be displaced from the centre of the vortex at low *We*. At higher *We* numbers, the radial equilibrium location is found to be at the centre of the vortex core, with the vorticity in the water phase being distributed in an annular form around the bubble. The pressure distributions calculated from the velocity field show a large azimuthal pressure difference between the core where the bubble is captured and the other core, which is of the order of $\Delta P = 0.87\rho\,(\Gamma/2\pi a)^2$. This pressure difference causes stretching of the bubble in the azimuthal direction. When time is non-dimensionalized by a time-scale,

$t_p = (0.87\rho\Gamma)/(\Delta P\pi) = \pi(2a)^2/\Gamma$, based on this pressure difference, it is found to collapse the measured elongation rates of the bubble in the azimuthal direction.

By the end of stage II, the bubble is broken up into a number of smaller bubbles, and break-up of the bubble is practically complete. The number of broken smaller bubbles is found to increase with *We* starting from 3 at low *We*, and reaching about 16 at the higher *We* of 406. The number of broken bubbles is not found to be correlated to the measured number of Kelvin waves on the ring. Apart from the Kelvin waves, another possible mechanism that could determine the number of broken bubbles would be the classical Rayleigh-Plateau instability of the stretched cylindrical bubble. The number of these waves that fit into the stretched bubble and their variation with We, is reasonably in agreement with experimental data at low *We* ($We < 150$). At $We > 150$, the visualized number of broken bubbles continues to increase, while the number of instability waves is fixed. The discrepancy between the two continues to increase with *We* and is probably caused by the increased level of turbulence in the higher strength (and *Re*) rings at larger *We*. Associated with this increase in the number of smaller bubbles is a reduction in the average diameter of the bubbles formed (D_m), which is found to vary as $We^{-0.124}$. This value of the exponent (-0.124) may be compared to the well studied case of droplet/bubble break-up due to isotropic turbulence, where Shinnar [72] showed that the average bubble size formed after complete break-up by isotropic turbulence varies as $We^{-0.6}$. It should be noted here that the change in exponent is not unexpected, as in the isotropic turbulence case, the whole process of break-up is considerably more complex due to the multi-scale nature of turbulent structures. The differences between the two can be attributed to the fact that bubble break-up in the turbulent case can occur through the combined action of a succession of different eddies [68], in addition to the fact that the broken bubbles are always exposed to eddies with smaller scales that they can interact with. The vorticity distribution in this stage shows that there are very significant variations between the interacting ring vorticity distribution and the base vortex ring in the absence of the bubble, at similar times. In particular at low *We* ($We \sim 3$), the vortex core appears fragmented with significant shedding of vorticity from the core with the bubble, while we see a clean vortex ring in the base case at similar times. Correspondingly, the convection speed of the ring drops significantly for the interacting case, and the enstrophy shows a large reduction of about 50%. In the higher *We* cases, the drop in convection speed of the ring is very small, and the core is not affected significantly, with almost no change in enstrophy of the ring compared to the base case at similar times.

In the case of thicker core rings with non-dimensional core size (ε) of 0.75, we find more dramatic effects. In this case, at low *We* ($We \sim 3$), the vortex ring interacts with the bubble and almost comes to a stop some time after bubble capture. The vorticity distribution at this

instant shows complete fragmentation of the core into two pieces, and a resultant drop in enstrophy of the ring by about 50%. As in the thinner core ring, at high *We*, the effects on the convection speed are not as significant as at low *We*. It should be mentioned here that in the earlier study of Sridhar and Katz [74] for a ring interacting with a set of smaller bubbles, distortion of the core was noted, but the core returned to its initial state after bubble escape. In the present case, where the bubble size is larger, the core deformation and fragmentation are lasting effects, and the ring is left in a fragmented state after bubble escape.

The drop in convection speed and fragmentation of the core seen in the present experiments at low *We* do not occur at bubble capture, but at times significantly after bubble capture. This suggests that the drop in convection speed and fragmentation of the core may be due to an instability of the modified vorticity distribution after bubble capture, where vorticity is in an annular form around the bubble with sharp density and viscosity changes at the interface. This of course needs further investigation, but it appears that stability analysis of an annular vorticity configuration with an air-water interface would be helpful to understand the fragmentation of the vortex core. Numerical two-phase simulations of this interaction would also be a very useful way to better understand this interaction.

A number of connections can be made between the present experiments and the relatively well studied case of drag reduction through bubble injection into a turbulent flow. The numerical simulations of Lu et al. [46] have shown that drag reduction in turbulent channel flow takes place only when the *We* is sufficient to cause bubble deformation, which they also link to reduction in enstrophy and suppression of vortical structure. This point has also been emphasized by Van Gils et al. [84] for the case of bubbles in turbulent Taylor-Couette flow, who also state that significant drag reduction takes place only when *We* is sufficient to cause deformation of bubbles. In the present idealized study of a vortex ring interacting with a bubble over the *We* range from 3 to 406, we find that bubble deformation occurs in all cases. However, we find that significant reduction in enstrophy and fragmentation of the structure occurs only when $We \sim 3$. Hence, the present experiments suggest that for enstrophy reduction and drag reduction, bubble deformation alone is not sufficient. We find that fragmentation/suppression of the structure is also important, and this is found to occur only at low *We*. Another observation for bubbles in turbulent flow is the enhancement of energy at small scales and reduction in energy at large scales [53, 83]. In the present context, the increase in energy at small scales can be related to the observed increase in shedding behind the vortex ring interacting with a bubble. On the other hand, the reduction in energy at the large scales can be related to our observed fragmentation of the vortex core. These relations between bubbly turbulent flows and the present idealized study suggest that the

present experiments could help to better understand interactions of bubbles with turbulent flows, which occur in many practical applications.

6.2 Interaction of a single bubble with vortical structures in a turbulent channel flow

In this part, we have studied the interaction of a single bubble with naturally occurring vortical structures present in a fully developed turbulent channel flow. We are interested here, as in the previous chapter, with both the bubble dynamics and the effect of the bubble on the vortical structures present in the turbulent channel flow. We therefore investigate both the trajectories of single bubbles injected in to a fully developed turbulent channel flow, and also study the effect that such bubbles have on vortical structures present in these flows. We are particularly interested to see if bubble capture by a vortical structure in the turbulent flow leads to a rapid decrease in enstrophy of the structure, as seen in the previous chapter for a simple vortical structure. Towards these broad goals, we have used high speed visualizations to track injected bubbles in the flow, while simultaneously measuring the velocity/vorticity of the bulk (water) flow using time-resolved Particle Image Velocimetry (PIV). These simultaneous time-resolved measurements have enabled us to connect bubble trajectories with the small scale vortical structures present in the flow. Understanding the interaction of bubbles with vortical structures can help in understanding the modification of statistical/global properties of turbulence due to presence of bubbles.

For the present work, we have designed, fabricated and tested a fully developed horizontal large aspect ratio turbulent channel flow facility. The channel aspect ratio (span/height) was about 12, which is large enough to ensure a nearly two dimensional flow in the mean sense. The mean and fluctuating flow field within this channel in the absence of bubbles has been validated with prior measurements in the literature. We inject single bubbles in to this flow, taking care to minimize any effect on the incoming turbulent boundary layer. The injected single bubble interacts with the multiple vortical structures present in the incoming boundary layer. We measure the bubble trajectories using high speed visualizations, and also extract small scale structures from the instantaneous flow field obtained using time-resolved PIV. The injected bubble size varied from 0.3 to 1.5 mm in a channel of height (H) 27.5 mm. Experiments were done at two channel Reynolds number ($Re = u_m H/\nu$) of 43400 and 67500 (u_m = mean velocity, ν = kinematic viscosity).

From the simultaneously recorded high speed visualizations in two perpendicular views, we have extracted the bubble shape and its location at successive instants in time. These

visualizations show that there are three different types of bubble paths that are seen for the bottom injection case, namely, the bubble sliding along the wall, bouncing motions of the bubble and escape of the bubble from the near wall region. These observed paths are broadly similar to that reported by Felton and Loth (2001) for the case of a bubble in a vertical boundary layer. The main difference is the "escape" path observed here, which is likely linked to buoyancy taking the bubble away from the wall. The bouncing motions of the bubble are likely caused by the interaction of the bubble with the vortical structures within the turbulent channel. Even at the same bubble diameter D_b and channel flow Re, we find that different realizations show considerable variations, with all three types of bubble paths being possible. These variations indicate that the bubble paths are significantly affected by local turbulent structures that can vary considerably. Statistics of bubble path at fixed Re and bubble diameter (D_b) show about 15% variation in the streamwise velocity. The variations in the wall normal (y) direction are much larger, as cases that slide show nearly no vertical migration, while bubbles that escape have relatively large vertical migration away from the bottom wall. As expected, there is a clear increase in probability of escape with increase in bubble diameter. When we reduced the channel Re, the main difference was the larger vertical rise due to lower channel velocities. In contrast to the bottom wall injection case discussed so far, the top wall injection showed only bouncing motions of the bubble. Escape of bubbles is obviously not expected in this case, but perhaps surprisingly even sliding motions of the bubble were not seen for any of the bubble sizes investigated.

Time-resolved measurements of the water (carrier phase) velocity/vorticity field helped in understanding the interaction of vortical structures present in the turbulent channel with the single bubble. For this, we did PIV at 1000 fps, which was adequate to track the temporal evolution of vortical structures in the flow and the bubble. Reynolds decomposition reveals small-scale vortices in the flow, and we study the interaction of the bubble with these small scale structures present in the turbulent channel flow. In the bouncing bubble path case, we find that the bubble convects along with a vortical structure, and then gets captured by it. In general, bubble path can either be affected by single eddy or combination of many eddies. When bubble escapes, we find either that there is either absence of strong structures in the vicinity of the bubble, or that the bubble rises vertically with a structure. Sliding bubble paths were found to be caused either due to the bubble entrained in some vortical structure near the wall or related to the downward Q_3 or Q_4 (sweep) events of the flow.

There are different forces acting on a bubble inside a turbulent boundary layer. There are few forces which one finds even in a laminar boundary layer like lift force (shear lift, Magnus, shedding behind bubble), drag force and added mass force. Presence of vortical structures in a turbulent boundary layer, as in the present case, brings in additional forces.

There is the pressure gradient based force towards the vortex centre, which in the multiple eddies case, results in a force towards each vortex centre. Distribution of structures in a turbulent boundary layer is random, which gives rise to a complex pressure gradient induced force causing complex bubble motions like combination of slide and bounce.

One way to estimate the total strength/life of vortical structures in a turbulent flow is to look at the enstrophy or volume integral of the square of the vorticity of the structures. In the present study, as 2D time resolved PIV measurements have been done, the enstrophy is calculated as the area average of the square of the fluctuating spanwise vorticity, this being representative of the principal vorticity of the structure. For the purpose of enstrophy calculation, a rectangular area that covers the complete vortical structure was used in each time instant. Vortical structures in a boundary layer, in the absence of bubbles, take birth, grow and reach an equilibrium state. At later times, the vortical structure decays down slowly, giving birth to newer structures. This process can be observed in enstrophy plots with time, with the enstrophy increasing to its maximum value, staying there for some time, which we refer to as the lifetime of the structure, and then decaying. For structures in the absence of bubbles, this lifetime of the vortical structure was found to be about 60 wall units in time (t^+). In contrast, we found that when a bubble is trapped within such vortices, the lifetime of the vortical structure is found to be significantly smaller about 30 wall units. This suggests that as in the vortex ring case in chapter 3, we can see reasonably rapid decrease in enstrophy of the structure when it entrains a bubble. The vortical structures in the turbulent channel flow are more complex in structure compared to the vortex ring with large variations between them. Since no two structures are the same, it is not easy to compare the effect of a bubble on such structures, as there is no clear base vortical structure. These observations are therefore not very conclusive, but they do suggest that presence of a bubble can affect vortical structures that capture it, very similar to the idealized vortex ring structure studied in chapter 3.

6.3 Effect of bubble distribution and buoyancy on pressure field and drag in channel flow

In the final part of the study, a large number of bubbles are injected in to the horizontal channel through porous plates fixed at the top and bottom channel walls. We are interested again in both bubble dynamics and in the vortical structures within the flow. In this study, we use pressure drop measurements to ascertain the effect of the bubbles on the vortical structures, as it is not possible to obtain reasonable PIV measurements in flows with large amount of bubbles. The bubble dynamics are however again directly visualized using high

speed visualization as in the previous chapter. The parameters that are varied in this work are the bubble void fraction (α), the channel Reynolds number (Re), and the orientation of injection in to the channel. The bubble void fraction, (α), which is the ratio of the volumetric flow rate of injected air from one wall (Q_a) to that of water flow rate in the channel (Q_w) is varied from 0 to about 0.2, this being measured and controlled by an air controller feeding air to the bubble injection system. Experiments are done at seven bubble void fraction (α) of about 0.025, 0.05, 0.075, 0.1, 0.125, 0.15, and 0.175. The experimental arrangement permits injection of bubbles through porous plates from either only the top wall, or only the bottom wall, or from both walls. We have studied and report results on all these three combinations. In addition, the channel Reynolds number has been varied over the range from about 22,500 to about 67,500 at four Reynolds number ($Re = \mathrm{u}_m\,\mathrm{H}/\nu$) of 22500, 43400, 54600, 67500. In all these cases, we visualize the bubble dynamics in two perpendicular views and also measure the streamwise pressure drop at four vertical locations on the channel. From these systematic measurements over a range of parameters, we attempt to identify different bubble dynamics regimes and relate it to the pressure drop distribution and wall drag within the channel.

Four kinds of bubble dynamics regime was observed depending on incoming flow properties, orientation and α. For low α and high Re, we observed discrete bubble in the flow for either of the wall injection cases, where as for high α, high Re and bottom wall injection, coalesced large bubbles were observed near the channel centre and small bubbles were seen near the wall. The injected bubbles coalesced and formed an intermittent air layer at the top wall for high α, low Re and top wall injection. Bubble/void waves along with the air layer were formed near the top wall for high α, high Re and top wall injection. These bubble waves were found to convect slowly compared to the surrounding air layer.

Bubble injection can either increase or decrease wall drag depending on the final bubble size, shape and relative position of it with respect to the wall. In the present study, pressure drop along the channel was measured to study the effect of bubbles on frictional drag in turbulent channel flow. The measured pressure drop was found to vary significantly in the wall normal vertical direction. Hence, the wall drag was estimated by integrating the measured pressure drop at four vertical locations. Bubbles can reduce the wall drag either due to modification of fluid properties or due to its interaction with turbulence. In order to focus our attention on drag reduction from the more interesting and complex turbulence-bubble interaction, we normalize the wall drag using the modified density and velocity to remove any variations (reductions) caused by these changes in fluid properties. Using this non-dimensionalisation, modification of fluid properties and mean flow velocity is broadly

accounted for, and hence further change in drag is to be attributed to turbulence-bubble interactions.

For the bottom wall injection case, we find that the wall drag increases for most conditions in the *Re*-α plane studied. In these cases, we find that the bubbles have migrated to the top wall from the bottom wall in the time taken by the flow to go from bubble injection to the measurement section. The migration in to the top wall boundary layer appears to disturb it. Besides this, there are also no bubbles in the vicinity of the lower wall either. Hence, we find drag increase in most cases. The exception is at high *Re* values, where the channel speeds are much higher. In this case, the bubbles from the lower wall have not migrated to the top wall, and hence do not disturb the top wall boundary layer. There are also substantial amount of smaller bubbles in this case that are close to the bottom wall, where they appear to reduce drag. The variation of pressure drop in the vertical direction also gives interesting spatial information. For example, at high *Re*, where most of the bubbles are in the bottom wall boundary layer, we still observe a reduction in pressure drop at the top wall. This is probably linked to the fact that in channel flow, boundary layer/vorticity on top and bottom walls mutually affect each other and hence the pressure drop decreases at the top wall despite the absence of bubbles there. Another interesting feature at high *Re* is the measured negative values of pressure drop at the bottom wall for $\alpha \geq 0.12$. This was found to be a repeatable result, and probably means that close to the wall, the bubbles have reduced drag completely and added extra energy to the flow. One possible reason for this may be the energy released during coalescence, which could be added to the flow. This argument is not very conclusive, but it is perhaps one possible mechanism to release the energy in the flow. Although locally near the wall, the pressure drop is negative in this case, the integrated pressure drop or wall drag is positive, but about 60% smaller than the base case.

When bubbles are injected from the top wall, buoyancy force is towards the wall and therefore bubbles stay near the top wall. In this case, the integrated pressure drop or wall drag is reduced compared to the base case for almost all void fractions and *Re* values. Further, the drag reduction is seen to saturate at higher void fractions. This seems to be related to the fact that the injected bubbles form an intermittent air layer on the top wall in this case, and at higher void fractions, only the thickness of the air layer is increased, which has little effect on the drag. This is similar to the observation of Elbing et al. [19] for air layer drag reduction in zero pressure gradient turbulent boundary layer. At high *Re* values, we again observe more than 100% pressure drop reduction locally at the top wall from where bubbles are injected, similar to the bottom wall at same *Re* and about same α. At this *Re* we again observe saturation of drag reduction with increasing α as discussed earlier, and maximum drag reduction of about 50% is observed.

We have also investigated the case when bubbles are injected from both top and bottom walls, which can be relevant to drag reduction in liquid pipelines. In this case, at low *Re* values, all the bubbles injected from the bottom wall reaches the top wall and pressure drop increases for all α similar to the bottom wall injection case. As the *Re* is increased to high values, the bubbles from the bottom wall do not reach the top and disturb the top boundary layer. These bubbles instead stay closer to the bottom wall, where they help in reducing drag. Hence, the drag starts reducing due to the presence of bubbles. Pressure drop at both top and bottom walls becomes negative for $\alpha \geq 0.12$. However, in the integral sense, the flow still has wall drag, but much lower than the corresponding base case. Drag reduction at these large *Re* values is found to increases with increasing void fraction. Bubbles injected at the top wall stay very close to the top wall, and bubbles injected at the bottom wall are distributed between the bottom wall and the centre of the channel. At the highest void fraction of 0.14, we observe a maximum drag reduction of about 60%.

The present experiments show large variations in bubble dynamics regimes and in drag reduction data. The systematic experiments over a range of parameters with simultaneous bubble visualizations and drag enable connections to be made between the two. The results indicate that the drag data is substantially affected by the bubble dynamics regime. It is clear from the data that the void fraction alone is not sufficient to give an idea of the amount of drag reduction. At the same void fraction, other parameters like *Re* and bubble injection orientation can substantially alter the drag reduction obtained. Overall, the present study shows a maximum of about 60% increase and a similar 60% reduction in wall drag over the entire range of conditions investigated.

"Mobility is immortality, mobility is religion. Just look at the treasures of the sun, they have never slept since the inception of creation. So strive forward, strive forward."

- Aitareya Upanishad

References

[1] Adrian, R., Christensen, K., and Liu, Z.-C. (2000a). Analysis and interpretation of instantaneous turbulent velocity fields. *Experiments in fluids*, 29(3):275–290.

[2] Adrian, R. J., Meinhart, C. D., and Tomkins, C. D. (2000b). Vortex organization in the outer region of the turbulent boundary layer. *Journal of Fluid Mechanics*, 422:1–54.

[3] Aliseda, A. and Lasheras, J. (2006). Effect of buoyancy on the dynamics of a turbulent boundary layer laden with microbubbles. *Journal of Fluid Mechanics*, 559:307–334.

[4] Arndt, R. E. A., Arakeri, V. H., and Higuchi, H. (1991). Some observations of tip-vortex cavitation. *Journal of Fluid Mechanics*, 229:269–289.

[5] Balachandar, S. and Eaton, J. K. (2010). Turbulent dispersed multiphase flow. *Annual Review of Fluid Mechanics*, 42:111–133.

[6] Biferale, L., Boffetta, G., Celani, A., Devenish, B., Lanotte, A., and Toschi, F. (2004). Multifractal statistics of lagrangian velocity and acceleration in turbulence. *Physical review letters*, 93(6):064502.

[7] Brücker, C. (1999). Structure and dynamics of the wake of bubbles and its relevance for bubble interaction. *Physics of Fluids (1994-present)*, 11(7):1781–1796.

[8] Carlier, J. and Stanislas, M. (2005). Experimental study of eddy structures in a turbulent boundary layer using particle image velocimetry. *Journal of Fluid Mechanics*, 535:143–188.

[9] Ceccio, S. L. (2010). Friction drag reduction of external flows with bubble and gas injection. *Annual Review of Fluid Mechanics*, 42:183–203.

[10] Chahine, G. L. (1995). Bubble interactions with vortices. In *Fluid Vortices*, pages 783–828. Springer.

[11] Choi, J. and Ceccio, S. L. (2007). Dynamics and noise emission of vortex cavitation bubbles. *Journal of fluid mechanics*, 575:1–26.

[12] Choi, J., Hsiao, C.-T., Chahine, G., and Ceccio, S. (2009). Growth, oscillation and collapse of vortex cavitation bubbles. *Journal of Fluid Mechanics*, 624:255–279.

[13] Cihonski, A. J., Finn, J. R., and Apte, S. V. (2013). Volume displacement effects during bubble entrainment in a travelling vortex ring. *Journal of Fluid Mechanics*, 721:225–267.

[14] Dabiri, J. O., Bose, S., Gemmell, B. J., Colin, S. P., and Costello, J. H. (2013). An algorithm to estimate unsteady and quasi-steady pressure fields from velocity field measurements. *The Journal of experimental biology*, pages jeb–092767.

[15] Dean, R. (1978). Reynolds number dependence of skin friction and other bulk flow variables in two-dimensional rectangular duct flow. *Journal of Fluids Engineering*, 100(2):215–223.

[16] Dennis, D. J. and Nickels, T. B. (2011). Experimental measurement of large-scale three-dimensional structures in a turbulent boundary layer. part 1. vortex packets. *Journal of Fluid Mechanics*, 673:180–217.

[17] Dixit, H. N. and Govindarajan, R. (2011). Stability of a vortex in radial density stratification: role of wave interactions. *Journal of Fluid Mechanics*, 679:582–615.

[18] Dritschel, D. G. (1986). The nonlinear evolution of rotating configurations of uniform vorticity. *Journal of Fluid Mechanics*, 172:157–182.

[19] Elbing, B. R., Mäkiharju, S., Wiggins, A., Perlin, M., Dowling, D. R., and Ceccio, S. L. (2013). On the scaling of air layer drag reduction. *Journal of Fluid Mechanics*, 717:484–513.

[20] Elbing, B. R., Winkel, E. S., Lay, K. A., Ceccio, S. L., Dowling, D. R., and Perlin, M. (2008). Bubble-induced skin-friction drag reduction and the abrupt transition to air-layer drag reduction. *Journal of Fluid Mechanics*, 612:201–236.

[21] Felton, K. and Loth, E. (2001). Spherical bubble motion in a turbulent boundary layer. *Physics of Fluids (1994-present)*, 13(9):2564–2577.

[22] Ferrante, A. and Elghobashi, S. (2004). On the physical mechanisms of drag reduction in a spatially developing turbulent boundary layer laden with microbubbles. *Journal of Fluid Mechanics*, 503:345–355.

[23] Ferrante, A. and Elghobashi, S. E. (2007). On the effects of microbubbles on taylor–green vortex flow. *Journal of Fluid Mechanics*, 572:145–177.

[24] Fritts, D. C., Arendt, S., and Andreassen, Ø. (1998). Vorticity dynamics in a breaking internal gravity wave. part 2. vortex interactions and transition to turbulence. *Journal of Fluid Mechanics*, 367:47–65.

[25] Fukumoto, Y. and Moffatt, H. (2000). Motion and expansion of a viscous vortex ring. part 1. a higher-order asymptotic formula for the velocity. *Journal of Fluid Mechanics*, 417:1–45.

[26] Gabillet, C., Colin, C., and Fabre, J. (2002). Experimental study of bubble injection in a turbulent boundary layer. *International journal of multiphase flow*, 28(4):553–578.

[27] Gan, L., Dawson, J., and Nickels, T. (2012). On the drag of turbulent vortex rings. *Journal of Fluid Mechanics*, 709:85–105.

[28] Gharib, M., Rambod, E., and Shariff, K. (1998). A universal time scale for vortex ring formation. *Journal of Fluid Mechanics*, 360:121–140.

[29] Glezer, A. (1988). The formation of vortex rings. *Physics of Fluids (1958-1988)*, 31(12):3532–3542.

[30] Govindarajan, R. and Sahu, K. C. (2014). Instabilities in viscosity-stratified flow. *Annual Review of Fluid Mechanics*, 46:331–353.

[31] Guin, M. M., Kato, H., Yamaguchi, H., Maeda, M., and Miyanaga, M. (1996). Reduction of skin friction by microbubbles and its relation with near-wall bubble concentration in a channel. *Journal of marine science and technology*, 1(5):241–254.

[32] Haberman, W. and Morton, R. (1953). An experimental investigation of the drag and shape of air bubbles rising in various liquids. Technical report, DTIC Document.

[33] Hara, K., Suzuki, T., and Yamamoto, F. (2011). Image analysis applied to study on frictional-drag reduction by electrolytic microbubbles in a turbulent channel flow. *Experiments in fluids*, 50(3):715–727.

[34] Herpin, S., Stanislas, M., Foucaut, J. M., and Coudert, S. (2013). Influence of the reynolds number on the vortical structures in the logarithmic region of turbulent boundary layers. *Journal of Fluid Mechanics*, 716:5–50.

[35] Hinze, J. (1955). Fundamentals of the hydrodynamic mechanism of splitting in dispersion processes. *AIChE Journal*, 1(3):289–295.

[36] Huang, J., Murai, Y., and Yamamoto, F. (2008). Shallow dof-based particle tracking velocimetry applied to horizontal bubbly wall turbulence. *Flow Measurement and Instrumentation*, 19(2):93–105.

[37] Hutchins, N., Hambleton, W., and Marusic, I. (2005). Inclined cross-stream stereo particle image velocimetry measurements in turbulent boundary layers. *Journal of Fluid Mechanics*, 541:21–54.

[38] Jacob, B., Olivieri, A., Miozzi, M., Campana, E. F., and Piva, R. (2010). Drag reduction by microbubbles in a turbulent boundary layer. *Physics of Fluids (1994-present)*, 22(11):115104.

[39] Joshi, P., Liu, X., and Katz, J. (2014). Effect of mean and fluctuating pressure gradients on boundary layer turbulence. *Journal of Fluid Mechanics*, 748:36–84.

[40] Kolmogorov, A. (1949). On the breakage of drops in a turbulent flow. In *Dokl. Akad. Navk. SSSR*, volume 66, pages 825–828.

[41] La Porta, A., Voth, G. A., Moisy, F., and Bodenschatz, E. (2000). Using cavitation to measure statistics of low-pressure events in large-reynolds-number turbulence. *Physics of Fluids (1994-present)*, 12(6):1485–1496.

[42] Lance, M. and Bataille, J. (1991). Turbulence in the liquid phase of a uniform bubbly air–water flow. *Journal of Fluid Mechanics*, 222:95–118.

[43] Leweke, T. and Williamson, C. (1998). Cooperative elliptic instability of a vortex pair. *Journal of Fluid Mechanics*, 360:85–119.

[44] Linden, P. and Turner, J. (2001). The formation of 'optimal' vortex rings, and the efficiency of propulsion devices. *Journal of Fluid Mechanics*, 427:61–72.

[45] Lo, T., L'vov, V. S., and Procaccia, I. (2006). Drag reduction by compressible bubbles. *Physical Review E*, 73(3):036308.

[46] Lu, J., Fernández, A., and Tryggvason, G. (2005). The effect of bubbles on the wall drag in a turbulent channel flow. *Physics of Fluids (1994-present)*, 17(9):095102.

[47] L'vov, V. S., Ooms, G., and Pomyalov, A. (2003). Effect of particle inertia on turbulence in a suspension. *Phys. Rev. E*, 67:046314.

[48] L'vov, V. S., Pomyalov, A., Procaccia, I., and Tiberkevich, V. (2005). Drag reduction by microbubbles in turbulent flows: The limit of minute bubbles. *Physical review letters*, 94(17):174502.

[49] Madavan, N., Deutsch, S., and Merkle, C. (1985). Measurements of local skin friction in a microbubble-modified turbulent boundary layer. *Journal of Fluid Mechanics*, 156:237–256.

[50] Magnaudet, J. and Eames, I. (2000). The motion of high-reynolds-number bubbles in inhomogeneous flows. *Annual Review of Fluid Mechanics*, 32(1):659–708.

[51] Martínez-bazán, C., Montanes, J., and Lasheras, J. C. (1999). On the breakup of an air bubble injected into a fully developed turbulent flow. part 2. size pdf of the resulting daughter bubbles. *Journal of Fluid Mechanics*, 401:183–207.

[52] Marusic, I. (2001). On the role of large-scale structures in wall turbulence. *Physics of Fluids (1994-present)*, 13(3):735–743.

[53] Mazzitelli, I. M., Lohse, D., and Toschi, F. (2003). On the relevance of the lift force in bubbly turbulence. *Journal of Fluid Mechanics*, 488:283–313.

[54] McCormick, M. E. and Bhattacharyya, R. (1973). Drag reduction of a submersible hull by electrolysis. *Naval Engineers Journal*, 85(2):11–16.

[55] Meng, J. C. and Uhlman, J. (1998). Microbubble formation and splitting in a turbulent boundary layer for turbulence reduction. In *Proceedings of the international symposium on seawater drag reduction*, volume 341355.

[56] Mougin, G. and Magnaudet, J. (2001). Path instability of a rising bubble. *Physical review letters*, 88(1):014502.

[57] Mudde, R., Groen, J., and Van Den Akker, H. (1997). Liquid velocity field in a bubble column: Lda experiments. *Chemical Engineering Science*, 52(21):4217–4224.

[58] Murai, Y. (2014). Frictional drag reduction by bubble injection. *Experiments in Fluids*, 55(7):1–28.

[59] Murai, Y., Oishi, Y., Takeda, Y., and Yamamoto, F. (2006). Turbulent shear stress profiles in a bubbly channel flow assessed by particle tracking velocimetry. *Experiments in Fluids*, 41(2):343–352.

[60] Norbury, J. (1973). A family of steady vortex rings. *Journal of Fluid Mechanics*, 57(03):417–431.

[61] O'Farrell, C. and Dabiri, J. O. (2012). Perturbation response and pinch-off of vortex rings and dipoles. *Journal of Fluid Mechanics*, 704:280–300.

[62] Oishi, Y., Murai, Y., Tasaka, Y., and Yasushi, T. (2009). Frictional drag reduction by wavy advection of deformable bubbles. In *Journal of Physics: Conference Series*, volume 147, page 012020. IOP Publishing.

[63] Oweis, G., Van der Hout, I., Iyer, C., Tryggvason, G., and Ceccio, S. (2005). Capture and inception of bubbles near line vortices. *Physics of Fluids (1994-present)*, 17(2):022105.

[64] Perry, A. and Chong, M. (1982). On the mechanism of wall turbulence. *Journal of Fluid Mechanics*, 119:173–217.

[65] Pope, S. B. (2000). *Turbulent flows*. Cambridge university press.

[66] Revuelta, A. (2010). On the interaction of a bubble and a vortex ring at high reynolds numbers. *European Journal of Mechanics-B/Fluids*, 29(2):119–126.

[67] Richter, D. H. and Sullivan, P. P. (2014). Modification of near-wall coherent structures by inertial particles. *Physics of Fluids (1994-present)*, 26(10):103304.

[68] Risso, F. and Fabre, J. (1998). Oscillations and breakup of a bubble immersed in a turbulent field. *Journal of Fluid Mechanics*, 372:323–355.

[69] Sanders, W. C., Winkel, E. S., Dowling, D. R., Perlin, M., and Ceccio, S. L. (2006). Bubble friction drag reduction in a high-reynolds-number flat-plate turbulent boundary layer. *Journal of Fluid Mechanics*, 552:353–380.

[70] Sene, K., Hunt, J., and Thomas, N. (1994). The role of coherent structures in bubble transport by turbulent shear flows. *Journal of Fluid Mechanics*, 259:219–240.

[71] Shariff, K. and Leonard, A. (1992). Vortex rings. *Annual Review of Fluid Mechanics*, 24(1):235–279.

[72] Shinnar, R. (1961). On the behaviour of liquid dispersions in mixing vessels. *Journal of Fluid Mechanics*, 10(02):259–275.

[73] Sridhar, G. and Katz, J. (1995). Drag and lift forces on microscopic bubbles entrained by a vortex. *Physics of Fluids (1994-present)*, 7(2):389–399.

[74] Sridhar, G. and Katz, J. (1999). Effect of entrained bubbles on the structure of vortex rings. *Journal of Fluid Mechanics*, 397(1):171–202.

[75] Tennekes, H. and Lumley, J. L. (1972). *A first course in turbulence*. MIT press.

[76] Theodorsen, T. (1952). Mechanism of turbulence. In *Proceedings of the Second Midwestern Conference on Fluid Mechanics*, pages 1–18. Ohio State University.

[77] Thorpe, S. (1992). Bubble clouds and the dynamics of the upper ocean. *Quarterly Journal of the Royal Meteorological Society*, 118(503):1–22.

[78] Toschi, F., Biferale, L., Boffetta, G., Celani, A., Devenish, B., and Lanotte, A. (2005). Acceleration and vortex filaments in turbulence. *Journal of Turbulence*, (6):N15.

[79] Toschi, F. and Bodenschatz, E. (2009). Lagrangian properties of particles in turbulence. *Annual Review of Fluid Mechanics*, 41:375–404.

[80] Townsend, A. A. (1980). *The structure of turbulent shear flow*. Cambridge university press.

[81] Tran-Cong, S., Marié, J.-L., and Perkins, R. J. (2008). Bubble migration in a turbulent boundary layer. *International Journal of Multiphase Flow*, 34(8):786–807.

[82] Uchiyama, T. and Kusamichi, S. (2013). Interaction of bubbles with vortex ring launched into bubble plume. *Advances in Chemical Engineering and Science*, 2013.

[83] Van den Berg, T. H., Luther, S., and Lohse, D. (2006). Energy spectra in microbubbly turbulence. *Physics of Fluids*, 18(3):8103.

[84] Van Gils, D. P., Narezo Guzman, D., Sun, C., and Lohse, D. (2013). The importance of bubble deformability for strong drag reduction in bubbly turbulent taylor–couette flow. *Journal of fluid mechanics*, 722:317–347.

[85] Voth, G. A., la Porta, A., Crawford, A. M., Alexander, J., and Bodenschatz, E. (2002). Measurement of particle accelerations in fully developed turbulence. *Journal of Fluid Mechanics*, 469:121–160.

[86] Wei, T. (1987). *Reynolds number effects on the small scale structure of a turbulent channel flow*. PhD thesis, University of Michigan.

[87] Wei, T. and Willmarth, W. (1989). Reynolds-number effects on the structure of a turbulent channel flow. *Journal of Fluid Mechanics*, 204:57–95.

[88] Widnall, S. E., Bliss, D. B., and Tsai, C.-Y. (1974). The instability of short waves on a vortex ring. *Journal of Fluid Mechanics*, 66(01):35–47.

[89] Zanoun, E.-S., Durst, F., and Nagib, H. (2003). Evaluating the law of the wall in two-dimensional fully developed turbulent channel flows. *Physics of Fluids (1994-present)*, 15(10):3079–3089.

[90] Zhou, J., Adrian, R. J., Balachandar, S., and Kendall, T. (1999). Mechanisms for generating coherent packets of hairpin vortices in channel flow. *Journal of Fluid Mechanics*, 387:353–396.

Appendix A

Bubble dynamics in fully developed turbulent channel flow

High speed top and side view of bubble dynamics is captured for the flow *Re* of 22500, 43400, 54600 and 67500, orientation of injection of top, bottom, and both wall, and bubble void fraction (α) of 0.05, 0.1 and 0.15. All this variation constitutes to 36 cases, which is presented below. Scales for each view is constant for all the bubble dynamics presented and can be found from wall to wall distance of 27.52 mm for the side view, where as the scales for top view is 14.32 cm in stream-wise direction and 8.96 cm in span-wise direction. Region marked with hatches in side view are the channel top and bottom wall. A circle filled with ash grey colour seen in top view is used to mask out the pressure port. We shall see that there are different kinds of bubble dynamics, as discussed in chapter 5, depending on the water and air flow conditions. In section A.1, A.2 and A.3 we will present the results for bottom, top and both wall injection respectively. In section A.2, temporal evolution of bubble dynamics at flow *Re* of 67500 and α of 0.15 is also presented at 9 time instances.

A.1 Bottom wall Injection

A.1.1 Effect of Bubble void fraction (α) on bubble dynamics at $Re = 22500$

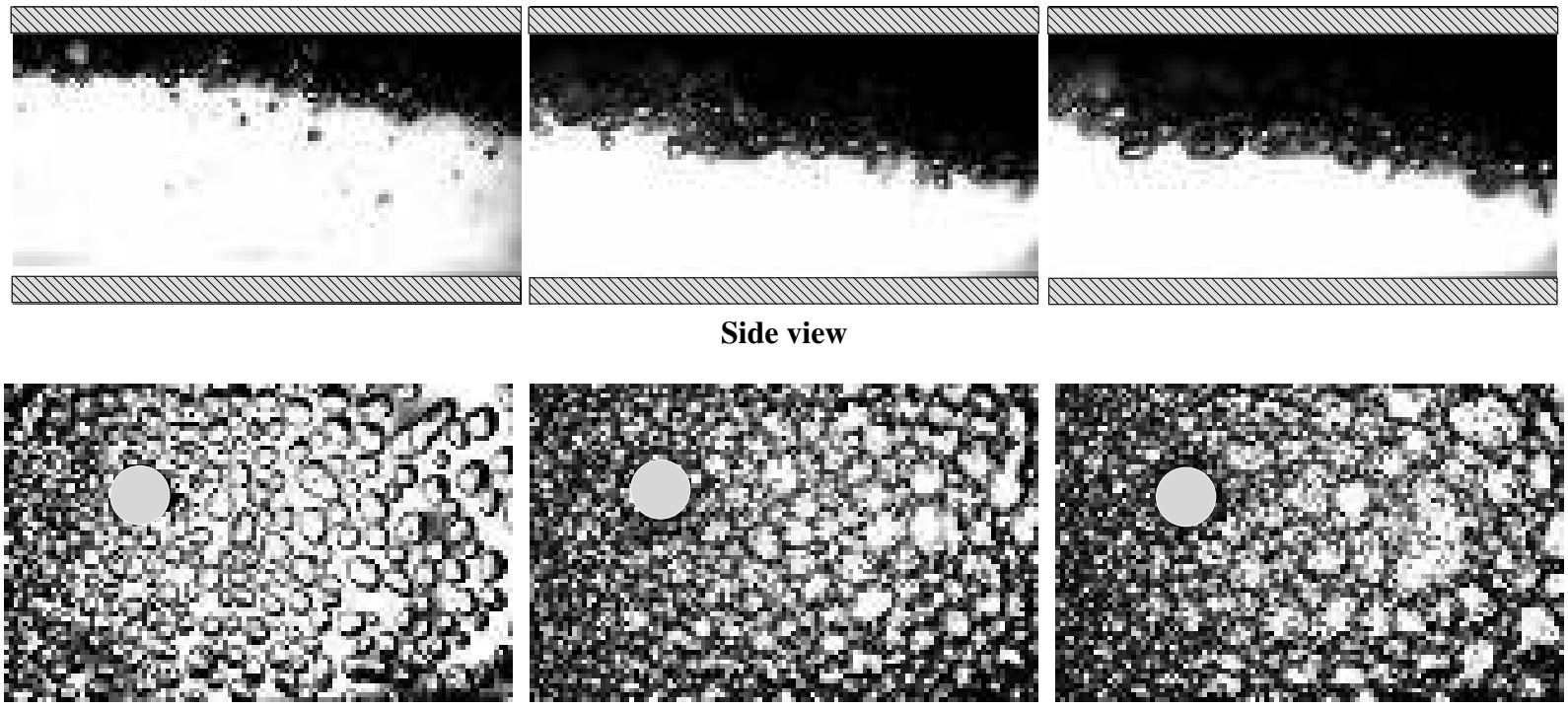

(a) $\alpha = 0.05$ (b) $\alpha = 0.1$ (c) $\alpha = 0.15$

Fig. A.1 Images of bubble dynamics showing effect of bubble void fraction (α) on bubble dynamics at $Re = 22500$ for the bottom wall injection. Scales for side view can be found from wall to wall distance of 27.52 mm, where as the scales for top view is 14.32 cm in stream-wise direction and 8.96 cm in span-wise direction. Region marked with hatches in side view are the channel top and bottom wall. Fluid flow is from left to right for top view and right to left for side view images. A circle filled with ash grey colour seen in top view is used to mask out the pressure port.

A.1.2 Effect of Bubble void fraction (α) on bubble dynamics at $Re = 43400$

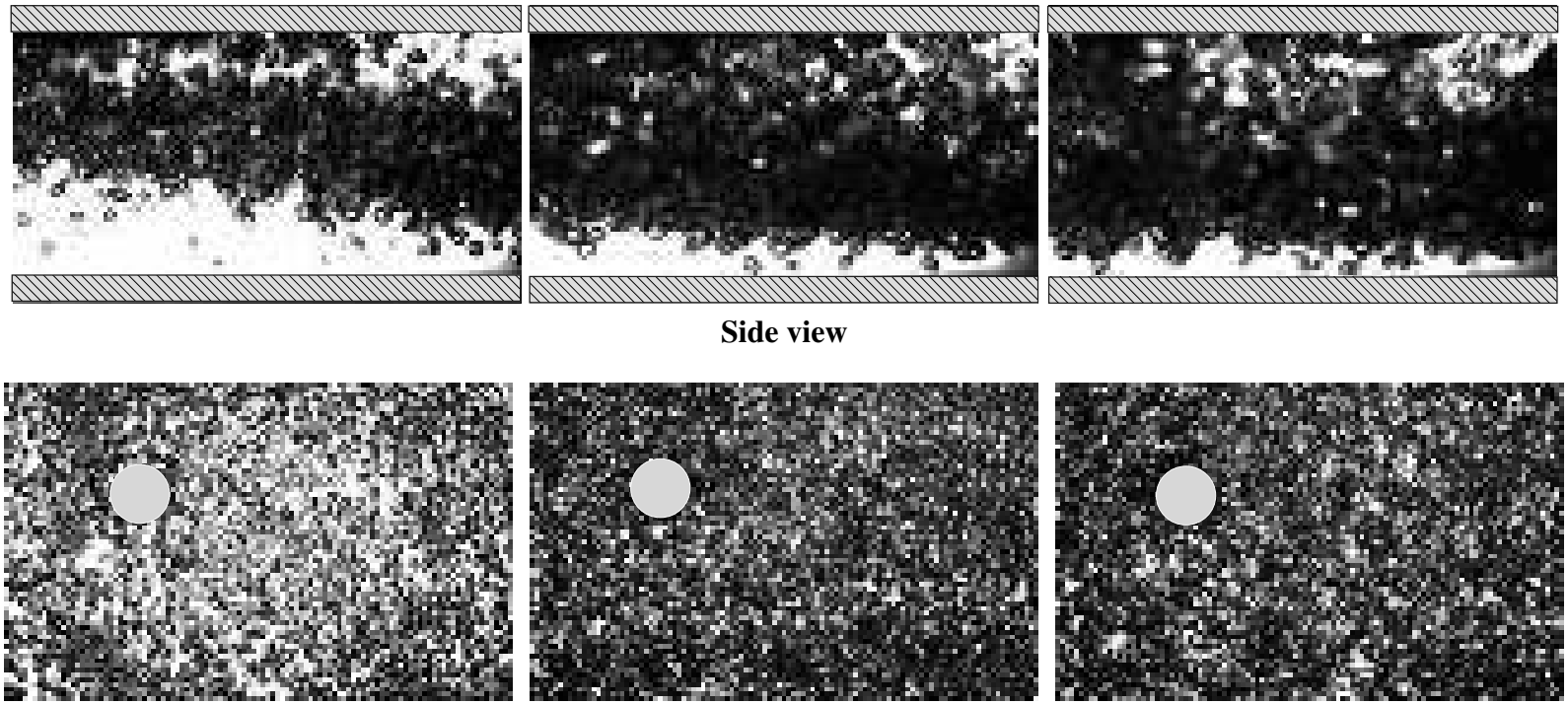

(a) $\alpha = 0.05$ (b) $\alpha = 0.1$ (c) $\alpha = 0.15$

Fig. A.2 Images of bubble dynamics showing effect of bubble void fraction (α) on bubble dynamics at $Re = 43400$ for the bottom wall injection. Scales for side view can be found from wall to wall distance of 27.52 mm, where as the scales for top view is 14.32 cm in stream-wise direction and 8.96 cm in span-wise direction. Region marked with hatches in side view are the channel top and bottom wall. A circle filled with ash grey colour seen in top view is used to mask out the pressure port.

A.1.3 Effect of Bubble void fraction (α) on bubble dynamics at $Re = 54600$

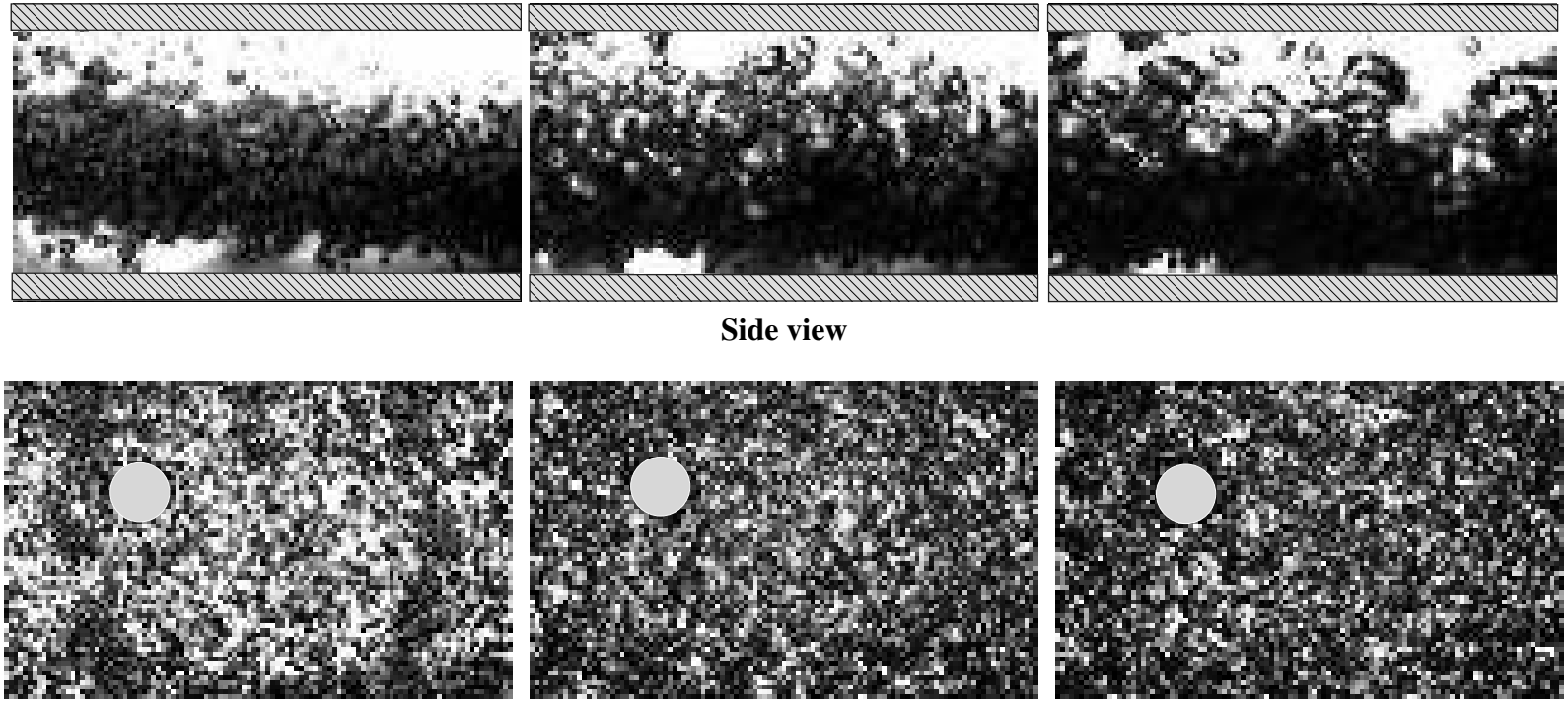

(a) $\alpha = 0.05$ (b) $\alpha = 0.1$ (c) $\alpha = 0.15$

Fig. A.3 Images of bubble dynamics showing effect of bubble void fraction (α) on bubble dynamics at $Re = 54600$ for the bottom wall injection. Scales for side view can be found from wall to wall distance of 27.52 mm, where as the scales for top view is 14.32 cm in stream-wise direction and 8.96 cm in span-wise direction. Region marked with hatches in side view are the channel top and bottom wall. A circle filled with ash grey colour seen in top view is used to mask out the pressure port.

A.1.4 Effect of Bubble void fraction (α) on bubble dynamics at $Re = 67500$

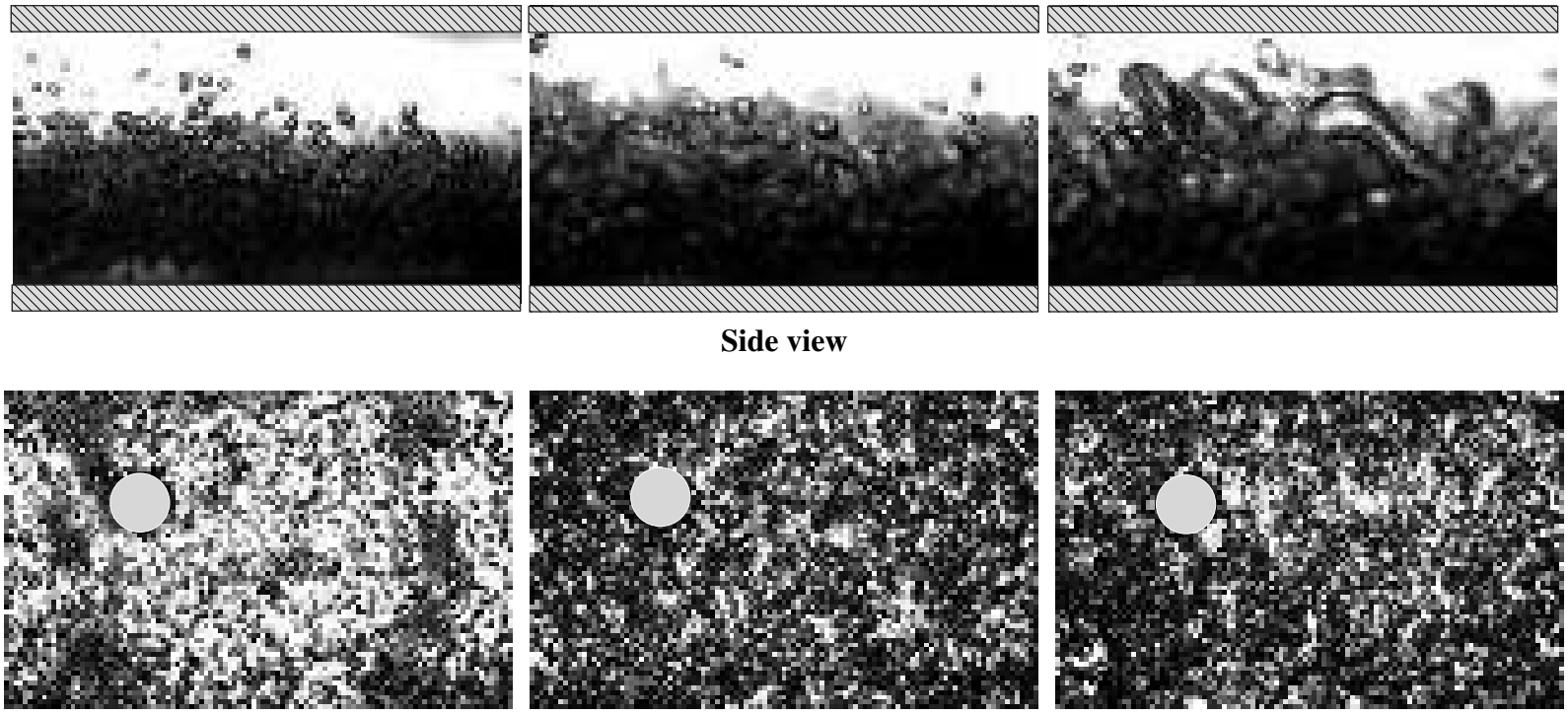

(a) $\alpha = 0.05$ (b) $\alpha = 0.1$ (c) $\alpha = 0.15$

Fig. A.4 Images of bubble dynamics showing effect of bubble void fraction (α) on bubble dynamics at $Re = 67500$ for the bottom wall injection. Scales for side view can be found from wall to wall distance of 27.52 mm, where as the scales for top view is 14.32 cm in stream-wise direction and 8.96 cm in span-wise direction. Region marked with hatches in side view are the channel top and bottom wall. A circle filled with ash grey colour seen in top view is used to mask out the pressure port.

A.2 Top wall Injection

A.2.1 Effect of Bubble void fraction (α) on bubble dynamics at $Re = 22500$

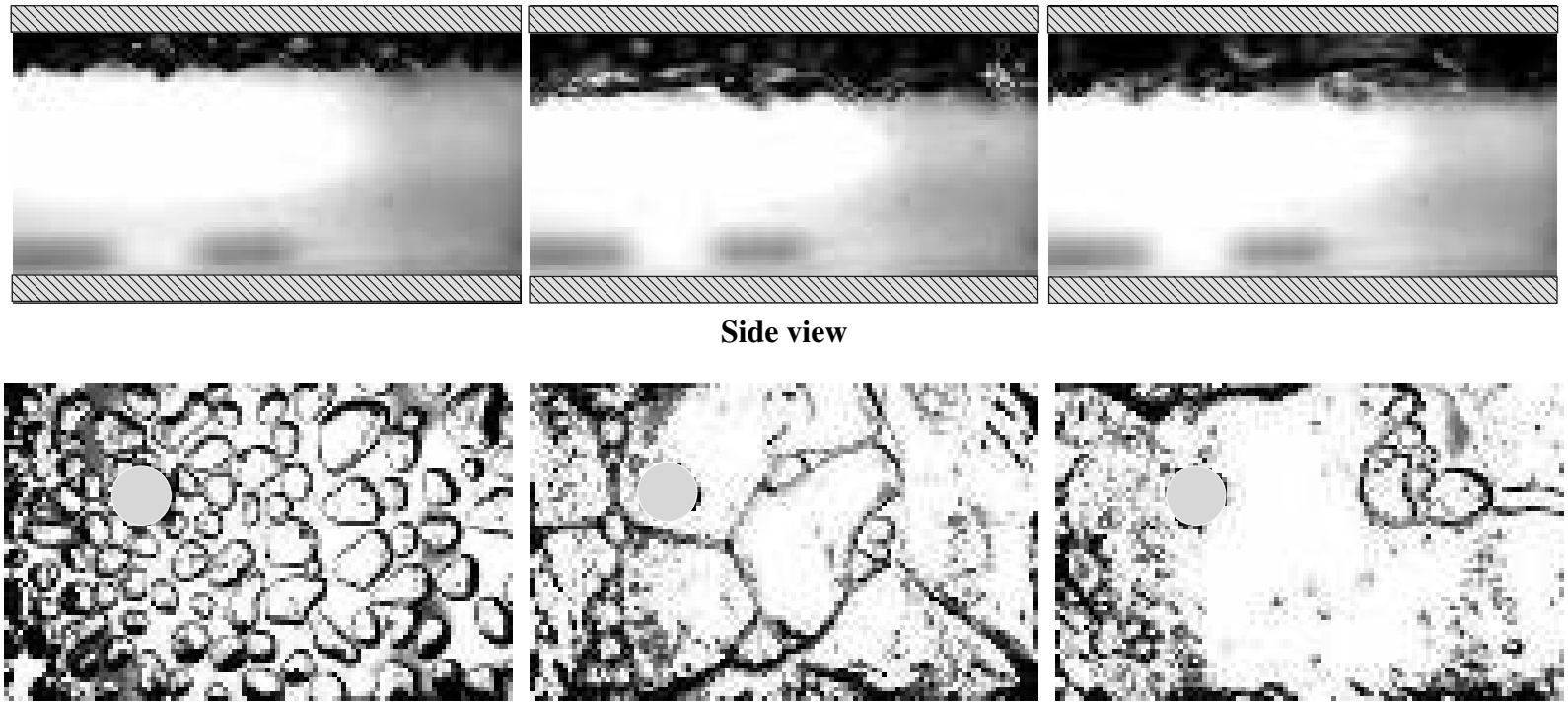

(a) $\alpha = 0.05$ (b) $\alpha = 0.1$ (c) $\alpha = 0.15$

Fig. A.5 Images of bubble dynamics showing effect of bubble void fraction (α) on bubble dynamics at $Re = 22500$ for the top wall injection. Scales for side view can be found from wall to wall distance of 27.52 mm, where as the scales for top view is 14.32 cm in stream-wise direction and 8.96 cm in span-wise direction. Region marked with hatches in side view are the channel top and bottom wall. A circle filled with ash grey colour seen in top view is used to mask out the pressure port.

A.2.2 Effect of Bubble void fraction (α) on bubble dynamics at $Re = 43400$

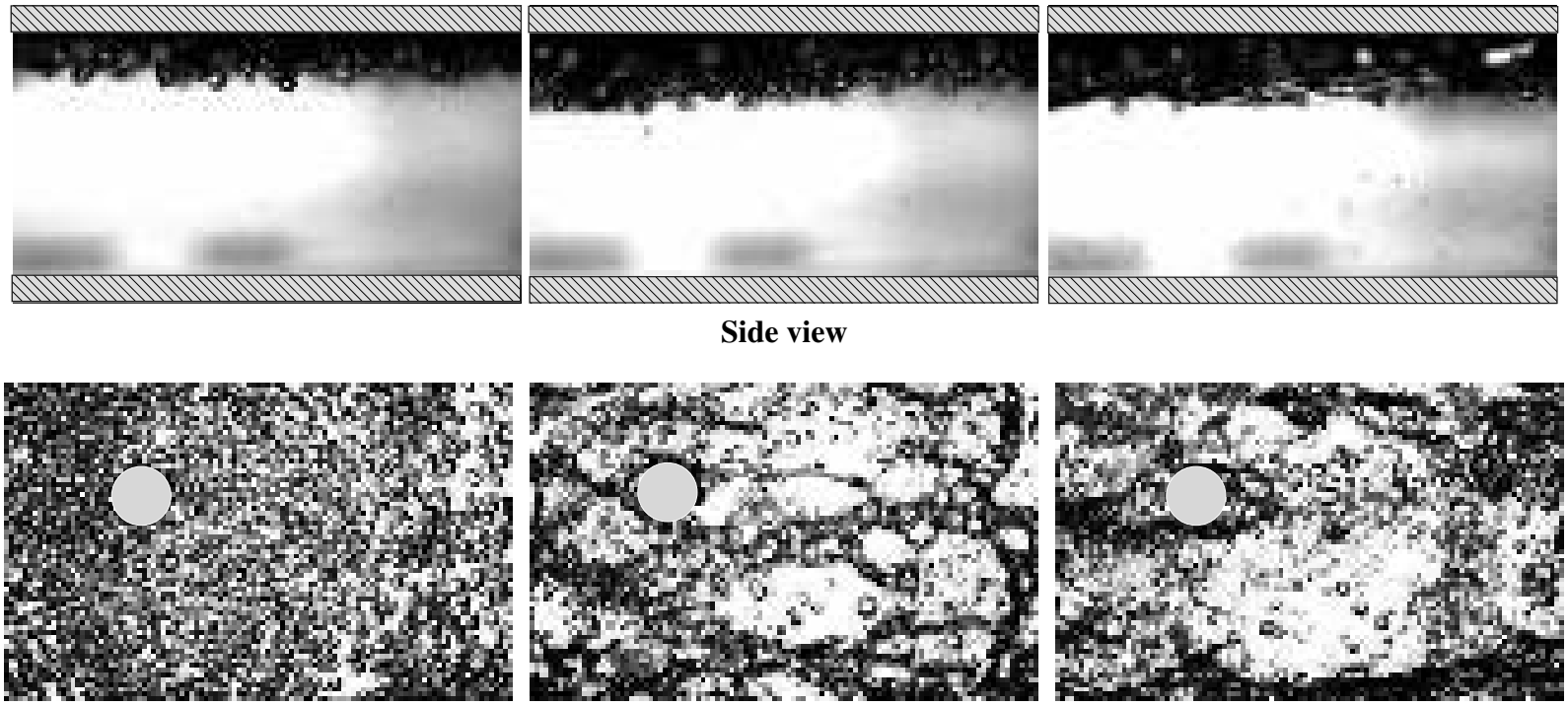

(a) $\alpha = 0.05$ (b) $\alpha = 0.1$ (c) $\alpha = 0.15$

Fig. A.6 Images of bubble dynamics showing effect of bubble void fraction (α) on bubble dynamics at $Re = 43400$ for the top wall injection. Scales for side view can be found from wall to wall distance of 27.52 mm, where as the scales for top view is 14.32 cm in stream-wise direction and 8.96 cm in span-wise direction. Region marked with hatches in side view are the channel top and bottom wall. A circle filled with ash grey colour seen in top view is used to mask out the pressure port.

A.2.3 Effect of Bubble void fraction (α) on bubble dynamics at $Re = 54600$

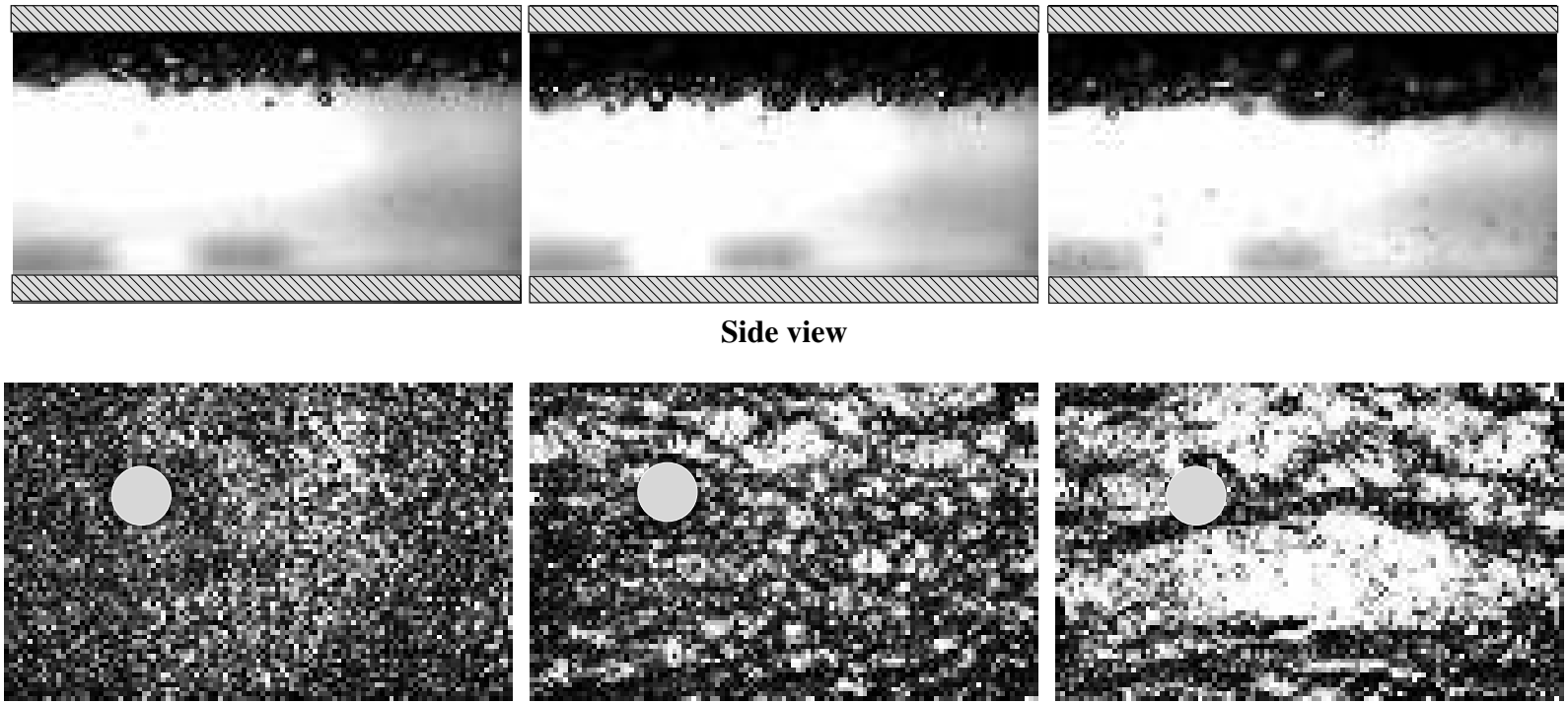

(a) $\alpha = 0.05$ (b) $\alpha = 0.1$ (c) $\alpha = 0.15$

Fig. A.7 Images of bubble dynamics showing effect of bubble void fraction (α) on bubble dynamics at $Re = 54600$ for the top wall injection. Scales for side view can be found from wall to wall distance of 27.52 mm, where as the scales for top view is 14.32 cm in stream-wise direction and 8.96 cm in span-wise direction. Region marked with hatches in side view are the channel top and bottom wall. A circle filled with ash grey colour seen in top view is used to mask out the pressure port.

A.2.4 Effect of Bubble void fraction (α) on bubble dynamics at $Re = 67500$

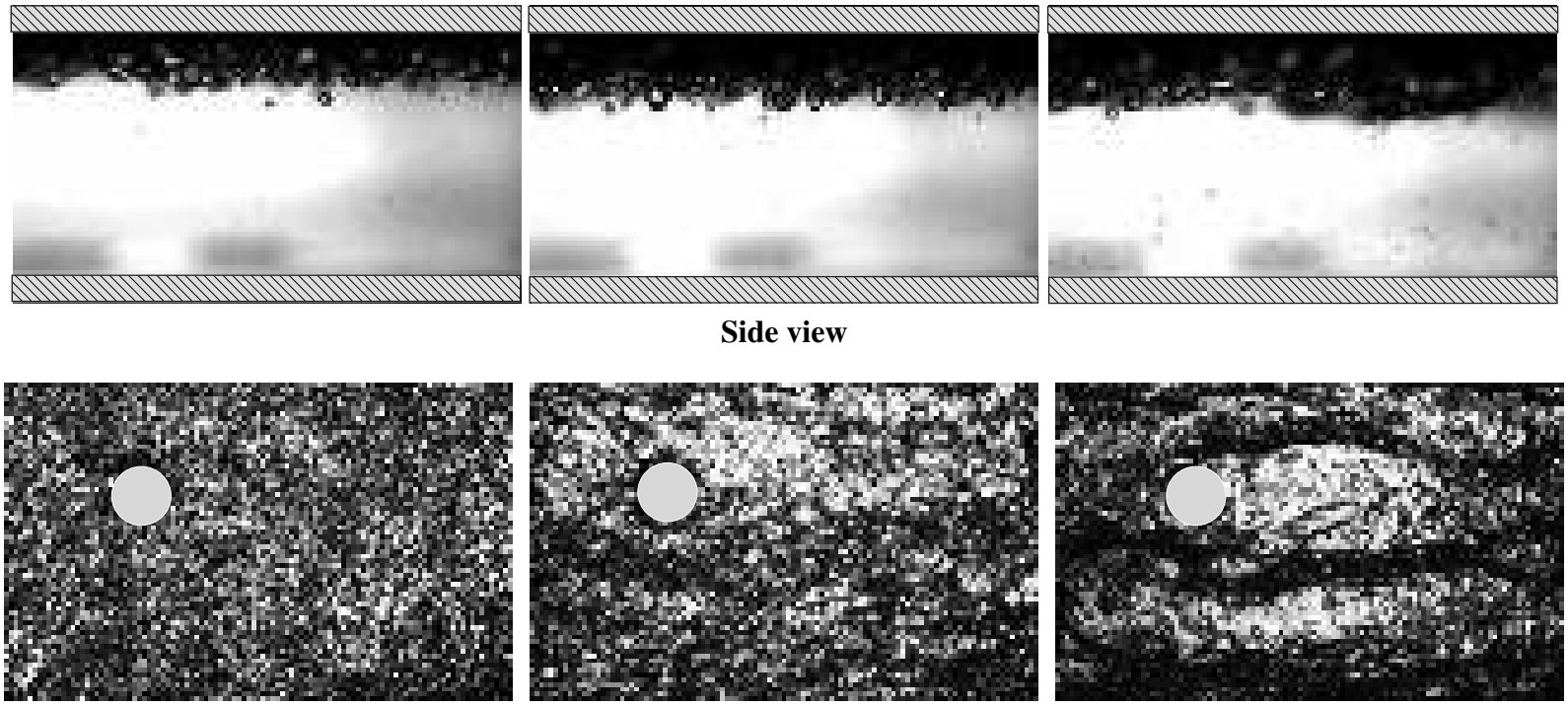

(a) $\alpha = 0.05$ (b) $\alpha = 0.1$ (c) $\alpha = 0.15$

Fig. A.8 Images of bubble dynamics showing effect of bubble void fraction (α) on bubble dynamics at $Re = 67500$ for the top wall injection. Scales for side view can be found from wall to wall distance of 27.52 mm, where as the scales for top view is 14.32 cm in stream-wise direction and 8.96 cm in span-wise direction. Region marked with hatches in side view are the channel top and bottom wall. A circle filled with ash grey colour seen in top view is used to mask out the pressure port.

A.2.5 Temporal evolution of bubble waves

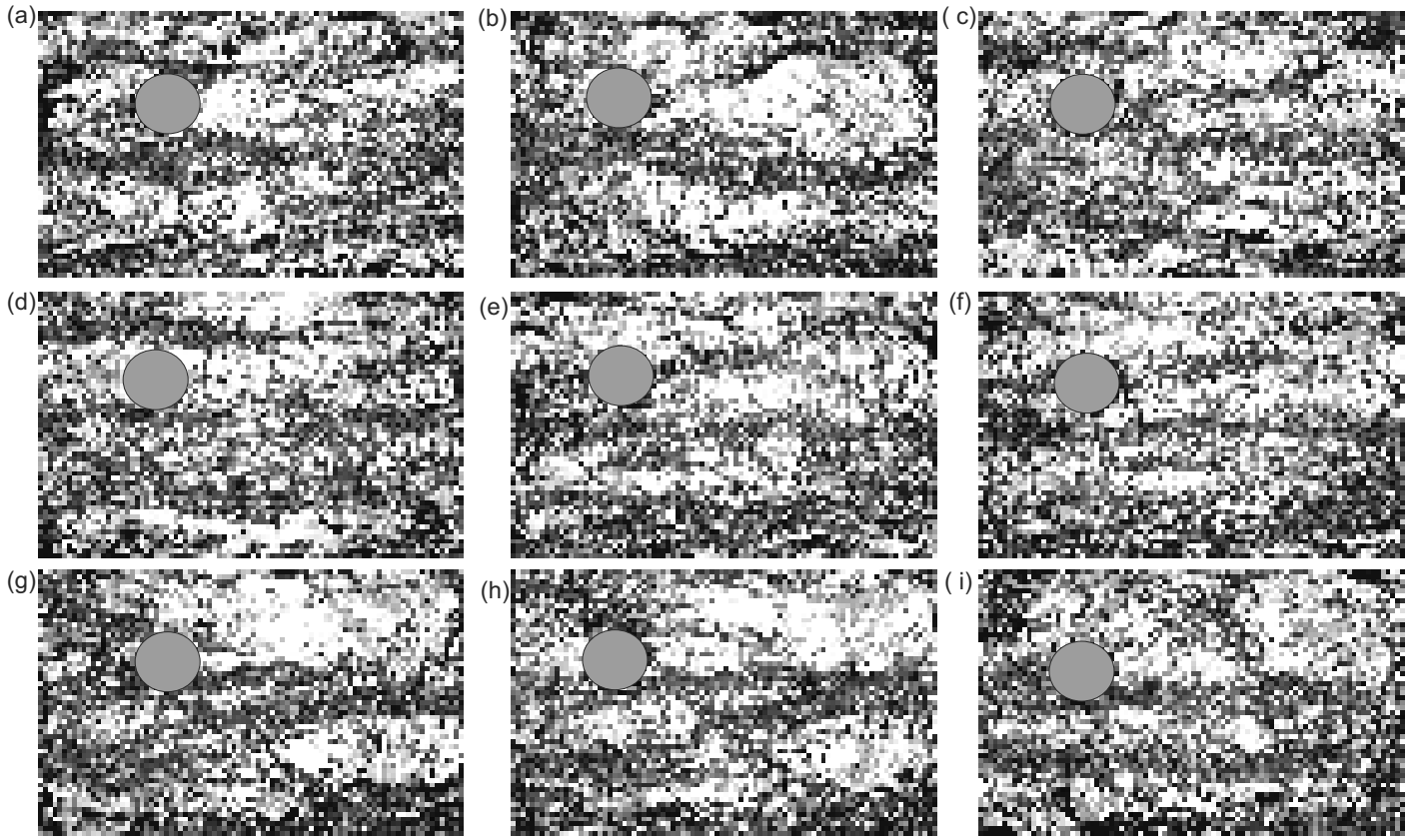

Fig. A.9 Top view images of temporal evolution of bubble dynamics for bubble void fraction (α) of 0.15 and *Re* of 67500 for the top wall injection. Field of view is 14.32 cm in stream-wise direction. There are bubble waves along side the air layer. The time corresponding to each of the images shown is (a) 0, (b) 93.75, (c) 169.375, (d) 213.125, (e) 293.125, (f) 306.875, (g)366.875, (h)381.25 and (i) 448.75 msec.

A.3 Both wall Injection

A.3.1 Effect of Bubble void fraction (α) on bubble dynamics at $Re = 22500$

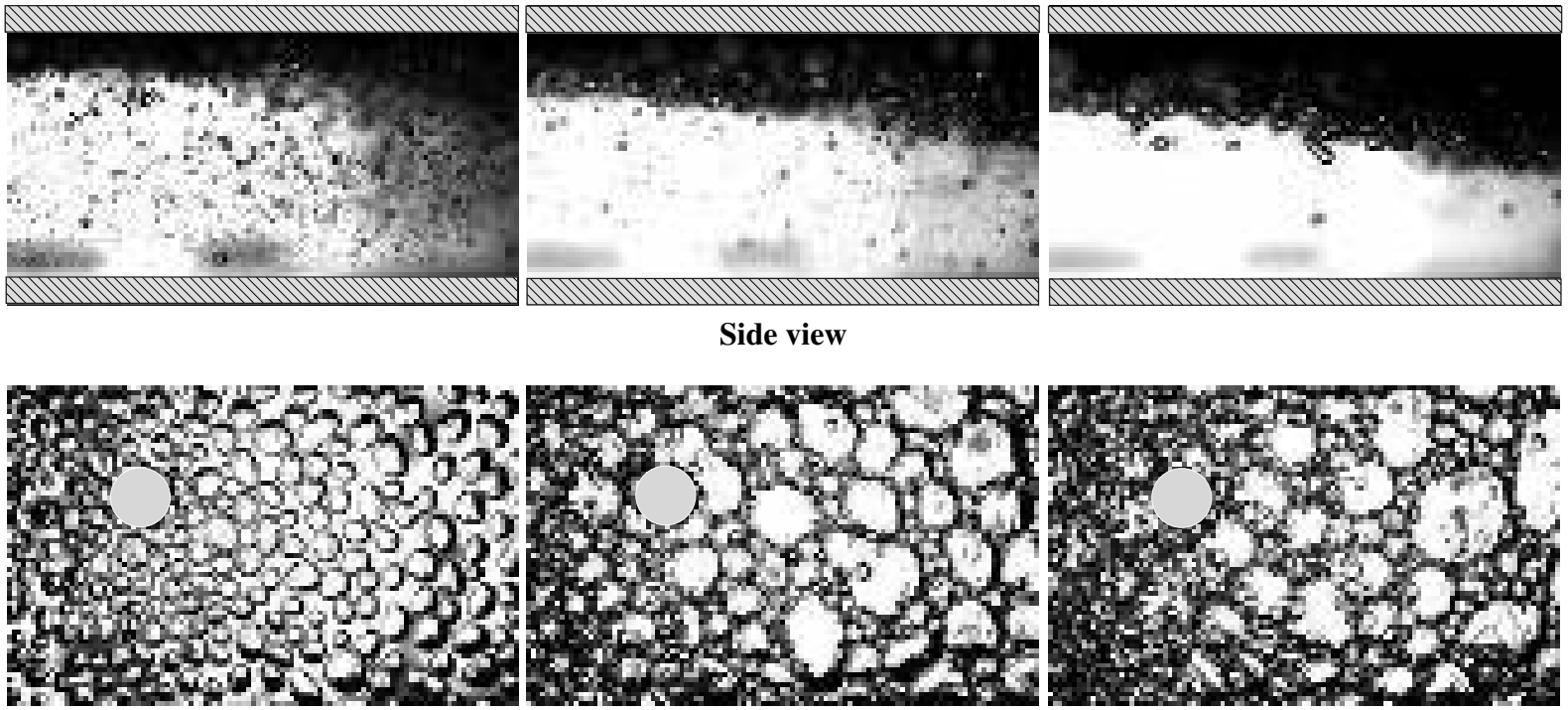

(a) $\alpha = 0.05$ (b) $\alpha = 0.1$ (c) $\alpha = 0.15$

Fig. A.10 Images of bubble dynamics showing effect of bubble void fraction (α) on bubble dynamics at $Re = 22500$ for the both wall injection. Scales for side view can be found from wall to wall distance of 27.52 mm, where as the scales for top view is 14.32 cm in stream-wise direction and 8.96 cm in span-wise direction. Region marked with hatches in side view are the channel top and bottom wall. A circle filled with ash grey colour seen in top view is used to mask out the pressure port.

A.3.2 Effect of Bubble void fraction (α) on bubble dynamics at $Re = 43400$

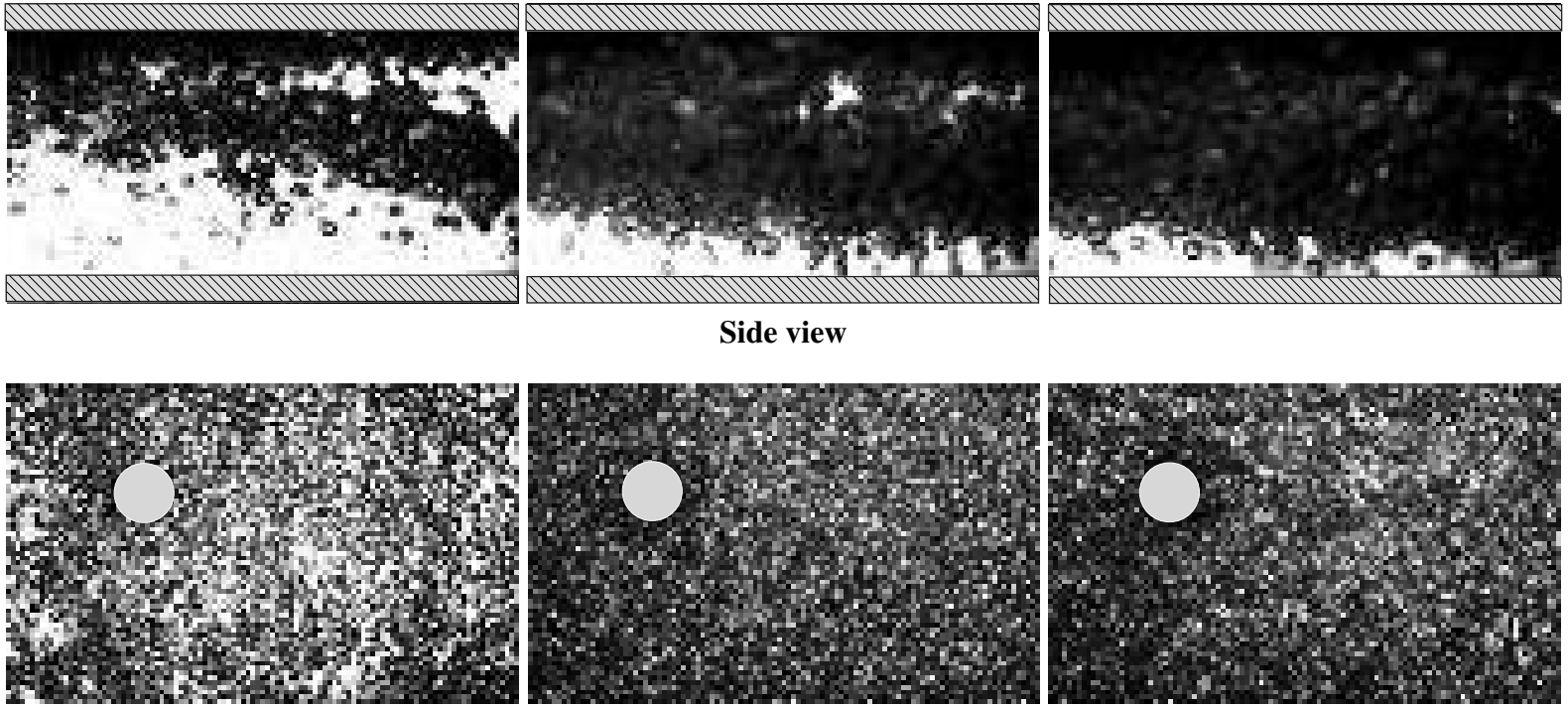

(a) $\alpha = 0.05$ (b) $\alpha = 0.1$ (c) $\alpha = 0.15$

Fig. A.11 Images of bubble dynamics showing effect of bubble void fraction (α) on bubble dynamics at $Re = 43400$ for the both wall injection. Scales for side view can be found from wall to wall distance of 27.52 mm, where as the scales for top view is 14.32 cm in stream-wise direction and 8.96 cm in span-wise direction. Region marked with hatches in side view are the channel top and bottom wall. A circle filled with ash grey colour seen in top view is used to mask out the pressure port.

A.3.3 Effect of Bubble void fraction (α) on bubble dynamics at $Re = 54600$

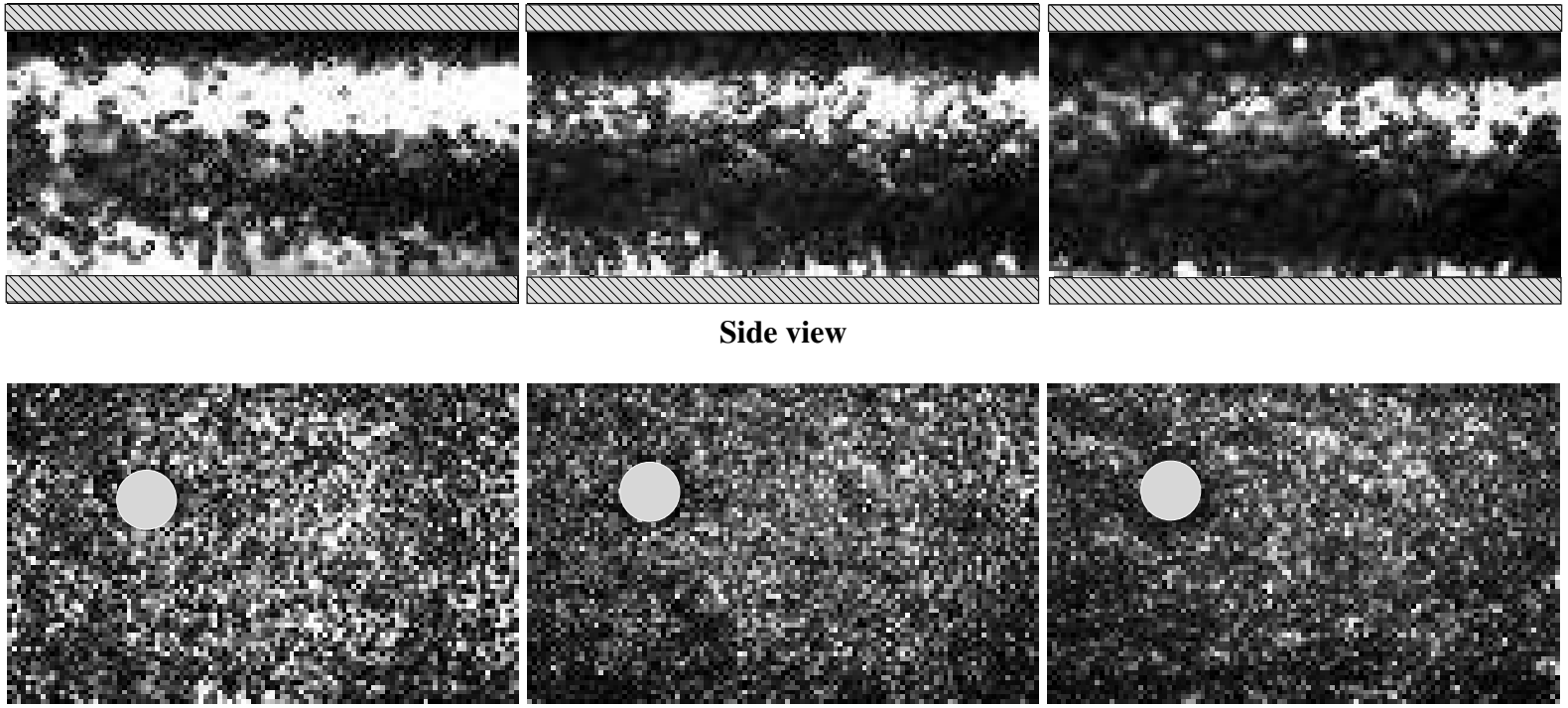

(a) $\alpha = 0.05$ (b) $\alpha = 0.1$ (c) $\alpha = 0.15$

Fig. A.12 Images of bubble dynamics showing effect of bubble void fraction (α) on bubble dynamics at $Re = 54600$ for the both wall injection. Scales for side view can be found from wall to wall distance of 27.52 mm, where as the scales for top view is 14.32 cm in stream-wise direction and 8.96 cm in span-wise direction. Region marked with hatches in side view are the channel top and bottom wall. A circle filled with ash grey colour seen in top view is used to mask out the pressure port.

A.3.4 Effect of Bubble void fraction (α) on bubble dynamics at $Re = 67500$

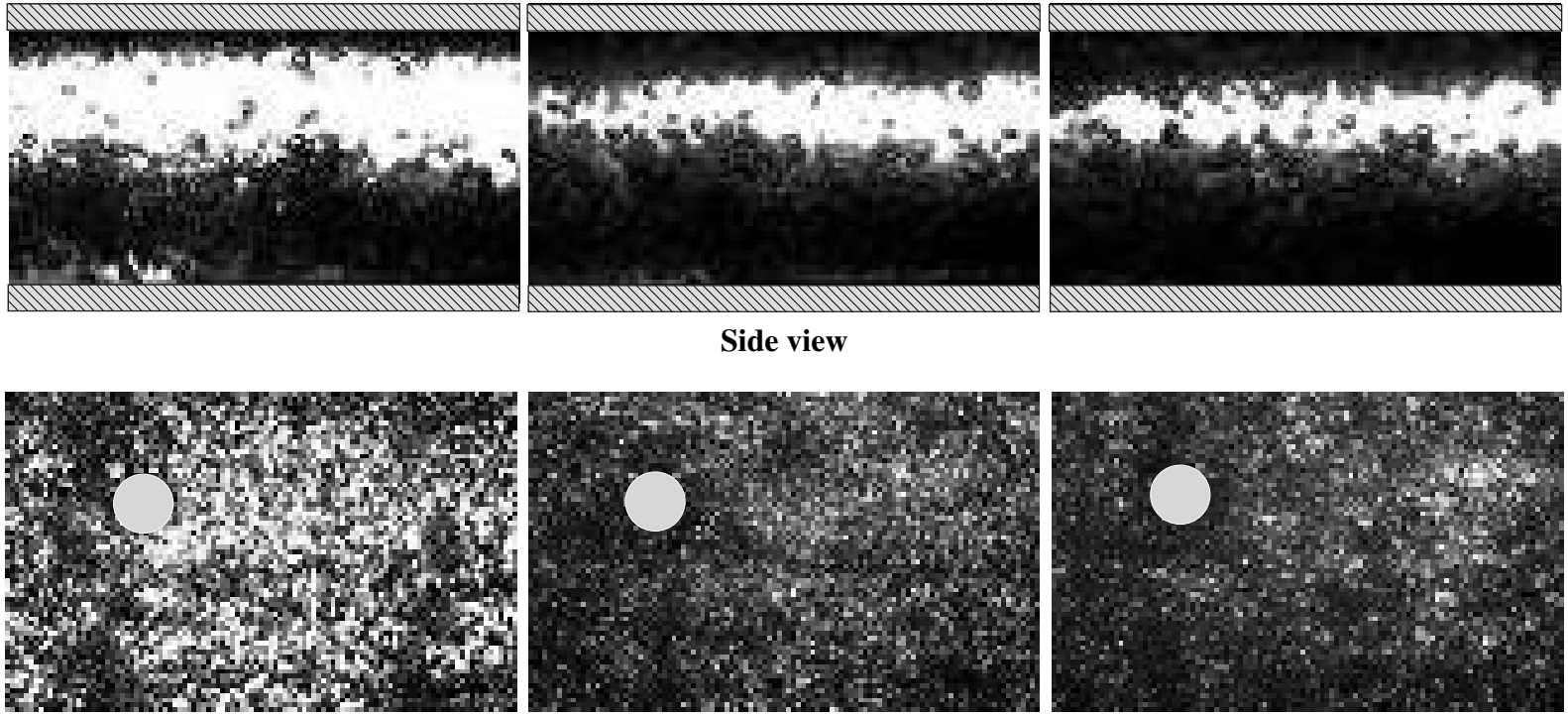

(a) $\alpha = 0.05$ (b) $\alpha = 0.1$ (c) $\alpha = 0.15$

Fig. A.13 Images of bubble dynamics showing effect of bubble void fraction (α) on bubble dynamics at $Re = 67500$ for the both wall injection. Scales for side view can be found from wall to wall distance of 27.52 mm, where as the scales for top view is 14.32 cm in stream-wise direction and 8.96 cm in span-wise direction. Region marked with hatches in side view are the channel top and bottom wall. A circle filled with ash grey colour seen in top view is used to mask out the pressure port.